A Detailed Study of Fan-Shaped Film-Cooling for a Nozzle Guide Vane for an Industrial Gas Turbine

William F. Colban IV

Dissertation submitted to the Faculty of
Virginia Polytechnic Institute and State University
in partial fulfillment of the requirements for the degree of

Doctor of Philosophy
in
Mechanical Engineering

Dr. Karen A. Thole, Advisor and Chair
Dr. Thomas E. Diller
Dr. Wing F. Ng
Dr. Walter F. O'Brien
Dr. Roger L. Simpson

November 28, 2005
Blacksburg, Virginia

Keywords: Gas Turbine, Film-Cooling, Shaped Hole, Vane, Endwall

A Detailed Study of Fan-Shaped Film-Cooling for a Nozzle Guide Vane for an Industrial Gas Turbine

William F. Colban IV

Abstract

The goal of a gas turbine engine designer is to reduce the amount of coolant used to cool the critical turbine surfaces, while at the same time extracting more benefit from the coolant flow that is used. Fan-shaped holes offer this opportunity, reducing the normal jet momentum and spreading the coolant in the lateral direction providing better surface coverage. The main drawback of fan-shaped cooling holes is the added manufacturing cost from the need for electrical discharge machining instead of the laser drilling used for cylindrical holes.

This research focused on examining the performance of fan-shaped holes on two critical turbine surfaces; the vane and endwall. This research was the first to offer a complete characterization of film-cooling on a turbine vane surface, both in single and multiple row configurations. Infrared thermography was used to measure adiabatic wall temperatures, and a unique rigorous image transformation routine was developed to unwrap the surface images.

Film-cooling computations were also done comparing the performance of two popular turbulence models, the RNG-kε and the v^2-f model, in predicting film-cooling effectiveness. Results showed that the RNG-kε offered the closest prediction in terms of averaged effectiveness along the vane surface. The v^2-f model more accurately predicted the separated flow at the leading edge and on the suction side, but did not predict the lateral jet spreading well, which led to an over-prediction in film-cooling effectiveness.

The intent for the endwall surface was to directly compare the cooling and aerodynamic performance of cylindrical holes to fan-shaped holes. This was the first direct comparison of the two geometries on the endwall. The effect of upstream injection and elevated inlet freestream turbulence was also investigated for both hole geometries.

Results indicated that fan-shaped film-cooling holes provided an increase in film-cooling effectiveness of 75% on average above cylindrical film-cooling holes, while at the same time producing less total pressure losses through the passage. The effect of upstream injection was to saturate the near wall flow with coolant, increasing effectiveness levels in the downstream passage, while high freestream turbulence generally lowered effectiveness levels on the endwall.

Preface

This dissertation is composed of four papers that were written to chronicle the performance of film-cooling performance of fan-shaped holes on turbine vane and endwall surfaces. This research was meant to be a comprehensive study, both from a thermal and aerodynamic perspective, incorporating both experimental and computational results. Major areas in the literature that lacked sufficient treatment in the published literature were addressed by this research including the following: high resolution measurements of adiabatic film-cooling effectiveness on a vane for both single and multiple row configurations, computational predictions of a fully-cooled nozzle guide vane, adiabatic film-cooling effectiveness measurements of any kind on a turbine endwall surface with fan-shaped holes, a direct one-to-one comparison between the cooling performance of cylindrical holes versus fan-shaped holes on a vane endwall, and a comparison of the aerodynamic performance of the two hole shapes and their effect on turbine passage secondary flows.

An evaluation of fan-shaped holes at eight individual surface locations on a turbine vane is presented in the first paper. This paper was presented at the International Gas Turbine Institute (IGTI) conference in 2005 in Reno, NV, and was accepted for publication in the Journal of Turbomachinery. The second paper was presented at the International Mechanical Engineering Congress and Exposition (IMECE) in 2005 in Orlando, FL. The multiple-row configuration was presented and compared to computational results using both the RNG-kε and v^2-f turbulence models. The second paper has also been accepted for publication in the Journal of Turbomachinery. The third paper in this dissertation was submitted to the IGTI conference in 2006 in Barcelona, Spain. This paper presents high resolution adiabatic film-cooling measurements on the endwall for cylindrical and fan-shaped holes at low and high freestream turbulence levels. The final paper will be submitted to the 2007 IGTI conference in Montreal, Canada. The fourth paper offers a comparison between fan-shaped and cylindrical holes with and without upstream injection. Aerodynamic measurements of total pressure losses at the exit plane are also presented in the fourth paper comparing the losses generated by the two hole shapes and their effect on the secondary flows that develop in the passage.

There are five appendices included at the end of the dissertation. The first chronicles the design and construction of the unique film-cooling vane and endwall. The second appendix gives a detailed description of the data collection and data analysis procedures, should they ever need to be replicated. An uncertainty analysis, including the method and sample calculations, is offered in the third appendix. The fourth appendix describes the necessity of and method for measuring each film-cooling hole diameter. The final appendix gives and brief overview of the significant results from this research, as well as suggesting several topics for additional investigation into this research area.

Acknowledgments

First and foremost, I owe everything to God. I would also like to thank the people that helped me get through the last three years. My advisor and friend, Dr. Karen Thole, guided me through the project, and taught me a few things along the way. I'm not sure I realized how much she did for me until I was nearly finished. I know I chose the right place to do my PhD in her lab. I also would like to thank my committee members, Dr. Diller, Dr. Ng, Dr. O'Brien, and Dr. Simpson. Thanks for your advice and your patience while I was trying to schedule my prelims and final defense.

I really enjoyed working with everyone that I've gotten to know at VTExCCL. That crazy guy from Arkansas, Andrew Gratton, who turned out to be a great guy and a good friend, and who also really helped me out with my project. My good buddy Sundar (like 'thunder') Narayan, I've really enjoyed our trips together and I look forward to going to India one day. My Snapple cap buddy, Joe 'Guiseppe' Scrittore. Nick '♫Texas…Texas never tasted so good♫' Cardwell and his man-sized therapy dog. Paul 'Siiiiiiick' Sanders. Mike 'International Man of Music' Barringer. Scottie-2-Hottie 'Sand Blaster' Walsh. The ole Pratt guys, Jeff Prausa, Eric Couch, and Jesse Christophel. Erik Hohlfeld, such a funny guy, will definitely never forget the ride to Arkansas and back. Scott 'Don't Scratch my Chevy' Brumbaugh. Mike 'Football Players can Build Pyramids' Lawson. Steve Lynch, Andrew Duggleby, Evan Sewall, Satoshi Hada, Alan Thrift, Cam Land, Angela Morris, Erin Elder, Erik Lyall, Ben Poe, Jamie Archual, Cathy Hill, Kathy Taszarek, Lynne Ellis, and others.

I also want to thank the professors that helped me out during my first teaching experiences, Dr. Karen Thole, Dr. Danesh Tafti, Dr. Dennis Jaasma, Dr. Clint Dancey, and Dr. Mark Paul. My teaching assistants were also a big help and great guys as well, Ali Rozzati and Anant Shah.

Of course my family gave me great support, and was always there for me whenever I needed. Mom, Ellis, E. J., I love and appreciate you guys more than you probably know.

As far as making the project itself possible, I would like to thank Siemens Power for their funding of the research. They gave the research a purpose and direction, as well

as they picked up the tab for the research and my schooling, for which I am extremely grateful. I would particularly like to thank Michael Händler for all of his help guiding the project and reviewing all the papers that Karen and I wrote.

Last and most of all, I would like to thank my fiancé Lauren. She is the single greatest thing that's ever happened to me, I love her more than anything, and I can't wait to get married to her next summer. It was nice having her studio literally 200 ft away, so that whenever I needed a break I could just stop by and see her and take my mind of work and research. We had lots of fun in Blacksburg, Paris, Charleston, and Colorado.

Table of Contents

List of Tables

List of Figures

Paper 1: Heat Transfer and Film-Cooling Measurements on a Stator Vane with Fan-Shaped Cooling Holes

Paper 2: Experimental and Computational Comparisons of Fan-Shaped Film-Cooling on a Turbine Vane Surface

Paper 3: A Comparison of Cylindrical and Fan-Shaped Film-Cooling Holes on a Vane Endwall at Low and High Freestream Turbulence Levels

Paper 4: A Comparison of Cylindrical and Fan-Shaped Film-Cooling Holes on a Vane Endwall with and without Upstream Blowing

Paper 1:
Heat Transfer and Film-Cooling Measurements on a Stator Vane with Fan-Shaped Cooling Holes

Accepted for publication in the *ASME Journal of Turbomachinery*[*]

Abstract

In a typical gas turbine engine, the gas exiting the combustor is significantly hotter than the melting temperature of the turbine components. The highest temperatures in an engine are typically seen by the turbine inlet guide vanes. One method used to cool the inlet guide vanes is film-cooling, which involves bleeding comparatively low-temperature, high-pressure air from the compressor and injecting it through an array of discrete holes on the vane surface. To predict the vane surface temperatures in the engine, it is necessary to measure the heat transfer coefficient and adiabatic film-cooling effectiveness on the vane surface.

This study presents heat transfer coefficients and adiabatic effectiveness levels measured in a scaled-up, two-passage cascade with a contoured endwall. Heat transfer measurements indicated that the behavior of the boundary layer transition along the suction side of the vane showed sensitivity to the location of film-cooling injection, which was simulated through the use of a trip wire placed on the vane surface. Single row adiabatic effectiveness measurements without any upstream blowing showed jet lift-off was prevalent along the suction side of the airfoil. Single row adiabatic effectiveness measurements on the pressure side, also without upstream showerhead blowing, indicated jet lifted-off and then reattached to the surface in the concave region of the vane. In the presence of upstream showerhead blowing, the jet lift-off for the first pressure side row was reduced, increasing adiabatic effectiveness levels.

* Co-authors: Dr. Karen A. Thole, Andrew Gratton, Mechanical Engineering Department, Virginia Tech
Michael Haendler, Siemens Power Generation, Muelheim a. d. Ruhr, Germany

Introduction

In an effort to increase overall efficiency and power output of industrial gas turbines, the combustor exit temperatures have continued to rise. This has placed an ever increasingly difficult task on engine designers to effectively cool turbine components. The turbine inlet guide vanes are subjected to the most extreme conditions and are therefore one of the most difficult components to cool. Most turbine guide vanes contain a complicated internal cooling scheme, as well as external film-cooling holes, which are designed to cover the surface of the vane with a thin protective film of relatively cooler air.

There are three main regions of the vane where film-cooling is used; the leading edge, the pressure side, and the suction side. Multiple rows of cylindrical holes are typically used near the leading edge to make sure that the stagnation region is adequately cooled. On the pressure and suction sides, rows of film-cooling holes are spaced such that the downstream row is placed where the upstream row ceases to be effective. Different film-cooling hole shapes are used in an effort to keep the jet attached to the surface over a range of blowing ratios.

One film-cooling hole shape that is a consideration for a designer is the so-called fan-shaped hole, or laid-back diffuser hole. This hole expands in the lateral direction, effectively reducing the jet's momentum before it ejects onto the downstream surface. The reduced momentum helps the jet stay attached to the surface for high blowing ratios. The fan-shaped hole also promotes lateral spreading of the jet compared with a cylindrical hole, causing the jet to more effectively cover the entire surface.

This study is the first to present parallel heat transfer coefficients and adiabatic film-cooling effectiveness for a scaled up turbine guide vane with fan-shaped film-cooling holes. Heat transfer coefficients are presented for a dry airfoil at different span heights noting the effect of endwall contouring. Heat transfer coefficients are also presented with trip wires used to simulate the boundary layer transition caused by a row of film-cooling holes. Adiabatic effectiveness data is presented for the leading edge as well as eight individual fan-shaped cooling rows on the pressure and suction sides for an engine representative blowing ratios.

Past Studies

Past studies involving surface heat transfer on a gas turbine vane include the effects of Reynolds number, freestream turbulence, acceleration, transition, and surface roughness. The transition location is particularly important because of the increase that occurs in heat transfer coefficients as the boundary layer becomes turbulent. The film-cooling rows on the vane surface also cause the boundary layer to transition from laminar to turbulent.

There have been a few studies investigating the effect of boundary layer transition on vane surface heat transfer using a trip wire to force the boundary layer to transition. Riess and Bölcs [1] used a trip wire on the suction side to transition the boundary layer upstream of a single row of cooling holes and showed a decrease in adiabatic film-cooling effectiveness with an incoming turbulent boundary layer.

Polanka et al. [2] studied leading edge film-cooling experimentally for blowing ratios ranging from 0.3 to 2.9. They had six rows of showerhead holes that were directed along the span of the vane and had a 25º angle relative to the surface. Results from Polanka et al. [2] showed increasing adiabatic effectiveness with increasing blowing ratio. This was attributed to the small surface angle facilitating jet attachment.

There have been many studies investigating the benefits of film-cooling of many different hole shapes on flat plates. Gritsch et al. [3], Yuen et al. [4], and Dittmar et al. [5] all studied fan-shaped film-cooling holes on a flat plate for blowing ratios ranging from 0.33 to 2.83. All reported that fan-shaped film-cooling holes performed better than cylindrical holes for all measured blowing ratios, particularly the higher blowing ratios. The fan-shaped hole performed better because its reduced jet momentum allowed the jet to stay attached to the surface and spread out and cover a larger surface area. Dittmar et al. [6] studied fan-shaped holes on a flat surface designed to simulate the Reynolds number and acceleration parameter distribution along the pressure side of a gas turbine vane. Dittmar et al. [6] showed that fan-shaped holes have higher levels of adiabatic film-cooling effectiveness than cylindrical holes for the same amount of coolant flow, especially at blowing ratios above one.

Film-cooling is a topic that has been studied extensively and yet despite all the work done there has not been much published research with fan-shaped cooling holes on

turbine vanes. Guo et al. [7] studied the adiabatic film-cooling effectiveness on a fully cooled nozzle guide vane with fan-shaped holes in a transonic annular cascade using thin-film technology. On the suction side they found that fan-shaped holes had a consistently higher level of adiabatic film-cooling effectiveness than cylindrical holes. On the pressure side, Guo et al. [7] found that initially downstream of the hole exit the fan-shaped hole had a higher adiabatic film-cooling effectiveness than the cylindrical hole. However, the fan-shaped hole had a much faster decay of adiabatic effectiveness on the pressure side than the cylindrical hole.

Zhang et al. [8] researched vane film-cooling with one row of shaped holes on the suction side using the pressure sensitive paint technique. They found that adiabatic film-cooling effectiveness increased from blowing ratios of 0.5 to 1.5. Zhang et al. [8] also reported that for a blowing ratio of 1.5, a small separation region occurred downstream of the hole exit before the jet reattached. Using the same setup and technique, Zhang and Puduputty [9] studied one row of fan-shaped holes on the pressure side. They found that the adiabatic film-cooling effectiveness decreased as blowing ratios increased from 1.5 to 2.5.

Sargison et al. [10] studied a converging slot-hole design on a flat plate and compared the results with cylindrical and fan-shaped holes. They found that the fan-shaped holes and converging slot-holes had similar adiabatic effectiveness levels downstream of the hole exit, and both performed better than cylindrical holes. Sargison et al. [11] did the same comparison on a transonic nozzle guide vane placed in an annular cascade. Again, fan-shaped holes and converging slot-holes both performed similarly in terms of adiabatic film cooling effectiveness, and both performed better than cylindrical holes at the same blowing ratios.

Schnieder et al. [12] studied vane film-cooling with showerhead blowing and three rows of fan-shaped film-cooling holes on the pressure side. They presented laterally averaged adiabatic effectiveness data for each row for three blowing ratios. Schnieder et al. [12] investigated the superposition approach for individual rows and found that it matched quite well with the complete coverage data. Polanka et al. [13] also examined the effect of showerhead blowing on the first downstream pressure side row. They found that at higher blowing ratios the pressure side row separated without

upstream showerhead cooling. With showerhead cooling, the adiabatic effectiveness downstream of the separating pressure side row increased. This was attributed to the upstream showerhead coolant increasing turbulence levels and dispersing the downstream detached jet down towards the surface.

Despite the work that has been done to study fan-shaped film-cooling on a gas turbine vane, there still is not a complete study offering high resolution measurements of adiabatic film-cooling effectiveness that characterizes the entire pressure and suction side surfaces. The current study offers a complete characterization by giving measurements at eight surface locations for different blowing ratios. It is important to understand the jet-freestream interaction at each location on the vane surface since film-cooling effectiveness is affected by many different factors which vary along the vane surface including surface curvature, acceleration, the state of the boundary layer, and pressure gradient.

Experimental Facilities

The heat transfer on a nozzle guide vane is difficult to predict with boundary layer codes due to factors such as surface curvature, pressure gradients, boundary layer transition location, and freestream turbulence. This study used a large scale test facility to obtain high resolution heat transfer and adiabatic film-cooling effectiveness data. All experiments were done in the low-speed, large-scale, closed-loop wind tunnel shown in Figure 1.1. Heat was removed from the flow by the main heat exchanger before entering

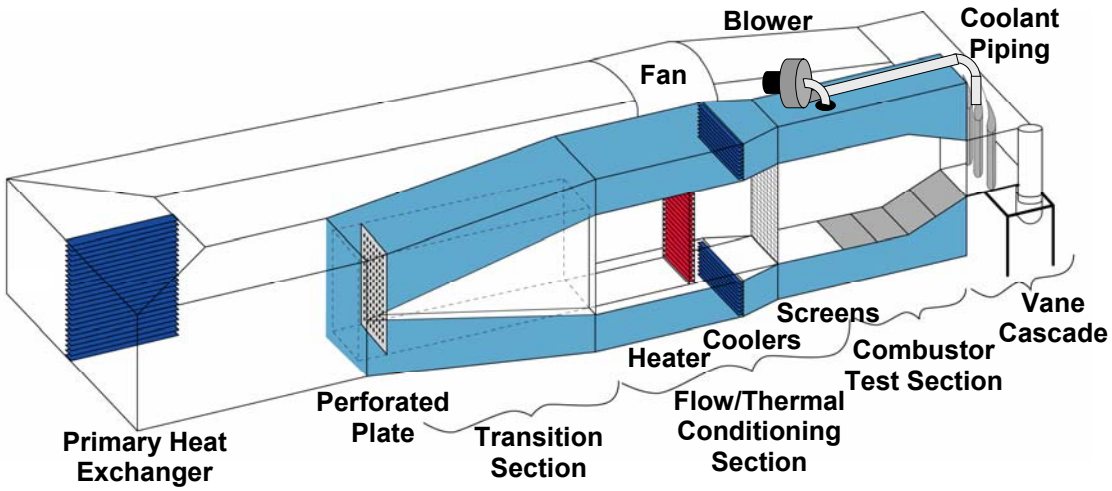

Figure 1.1. Schematic of the low-speed recirculating wind tunnel facility.

the flow split section. A perforated plate provided the correct pressure drop to split the flow into a center flow channel and two secondary channels. The core flow was heated by a 55 kW heater bank, while the outer two channels were cooled by heat exchangers and served as the coolant flow supply. The measurements were taken on the center vane of the two passage cascade (shown in Figure 1.2) which had one contoured endwall. The freestream turbulence level entering the turbine cascade was measured with a hot wire anemometer to be 1.2%. A description of the vane geometry, as well as some nominal operating conditions, is listed in Table 1.1. Inlet temperatures were 30ºC for the heat

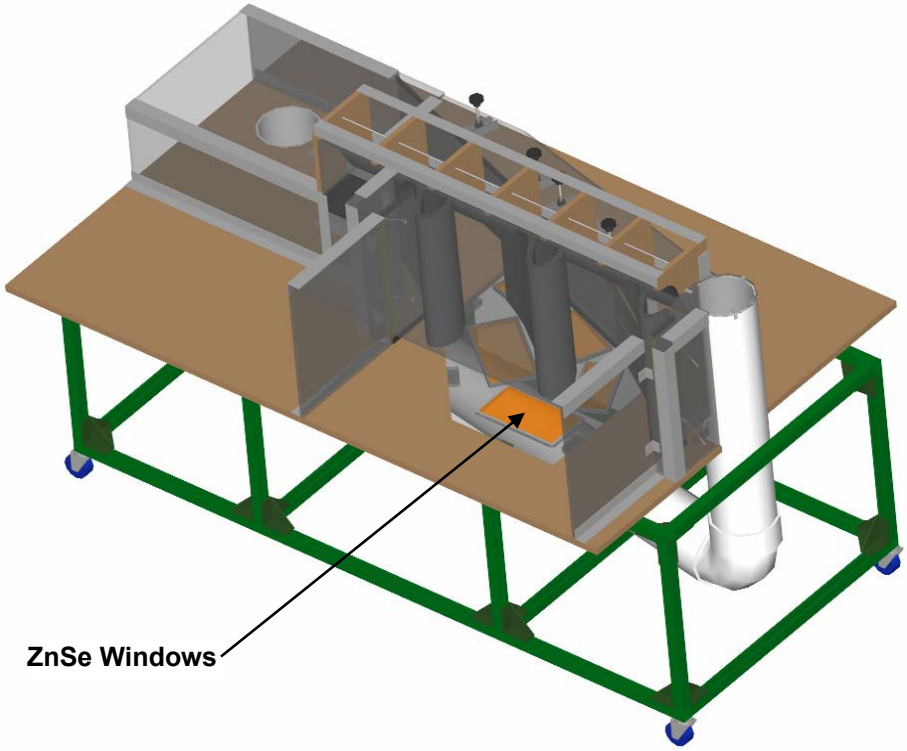

Figure 1.2. Two passage, three vane test section with a contoured endwall.

Table 1.1. Operating Conditions and Vane Parameters

Scale	3X
C (m)	0.53
$Z_{max,inlet}$/C (-)	1.05
$Z_{max,exit}$/C (-)	0.54
$S_{max,PS}$ (m)	0.52
$S_{max,SS}$ (m)	0.68
U_{inlet} (m/s)	10
Re_{inlet} (-)	3.0×10^5
ΔT_{FC} (ºC)	20

transfer coefficient tests and 60ºC for the film-cooling measurements, while inlet pressures were nominally atmospheric.

Vane Test Section Design

Whenever a nozzle guide vane is placed in a low speed experimental facility, the lack of compressibility effects changes the location of the minimum static pressure on the suction surface. There are two options available for doing low speed simulations, the first of which is to redesign the turbine vane profile so that the low speed pressure distribution matches the engine surface pressure distribution. The second option, which was taken in this study, is to incorporate a contoured endwall to accelerate the flow, which maintains the vane's geometric integrity from the engine design. The finished contour is shown in Figure 1.3 non-dimensionalized by the maximum span height. The contraction occurs earlier along the surface of the suction side. Figure 1.4 shows the non-dimensional pressure distribution, Cp, before and after the contoured endwall compared with the engine conditions. The film-cooling hole exit locations are shown in Figure 1.4 as well. The low speed pressure distributions were predicted with Fluent 6.0, a commercially available CFD solver, and verified experimentally.

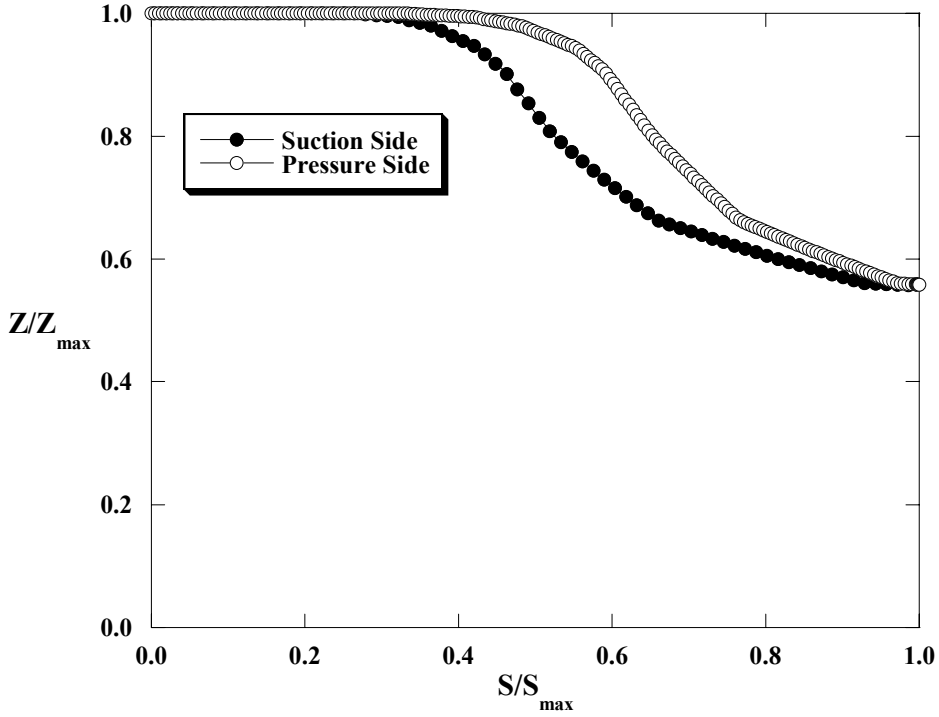

Figure 1.3. Contoured endwall surface definition.

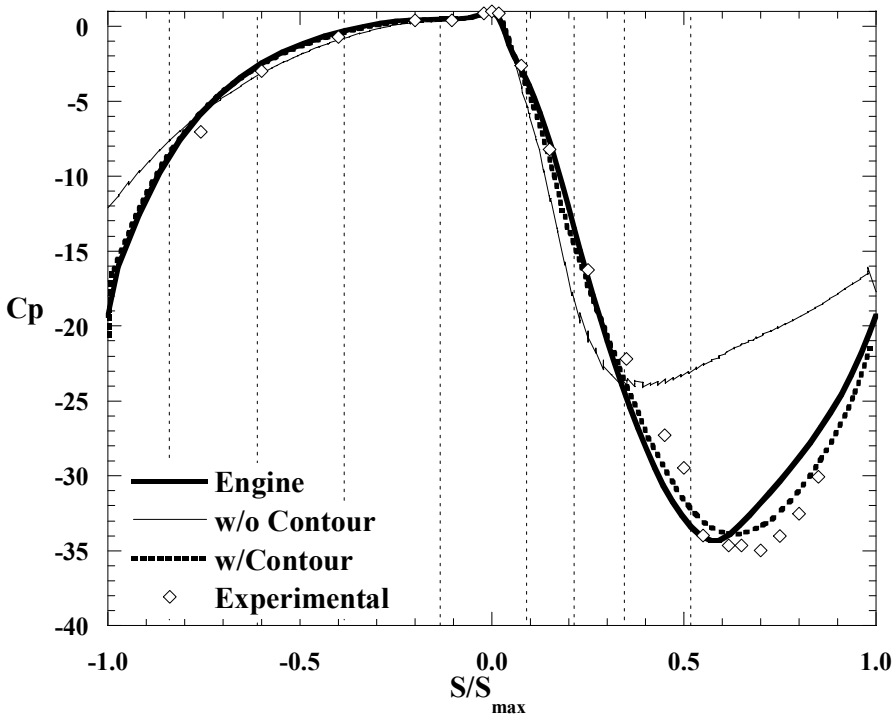

Figure 1.4. Cp distribution around the vane before and after the contoured endwall compared with engine conditions (dashed lines indicate locations of film-cooling rows).

An iterative process was used to design the contour that involved altering the contour shape, modeling the resulting geometry in Fluent, and comparing the modified Cp distribution to the engine Cp distribution. A systematic iterative approach of altering the contour based on the desired difference between pressure distributions was used by implementing the definition of the pressure coefficient as well as Bernoulli's equation. Note that the Cp distribution at the vane midspan was the design location for these iterations. The final contour shape had a sharp contraction, with the span reduced by 46% from the leading edge to the trailing edge the across the vane passage.

The effect of the contour on the pressure distribution can be seen in Figure 1.5 by measurements at three span heights. The Cp distribution at the lowest span height (Z/Z_{max} = 30%) did not vary significantly from the midspan location (Z/Z_{max} = 46%), indicating a nearly two-dimensional flow on the bottom half of the vane. At the highest span height (Z/Z_{max} = 70%) the flow on the suction side initially had a much lower acceleration, indicating a stagnating flow in the region just upstream of the contraction. However, as the contour began to contract the flow showed a much greater acceleration

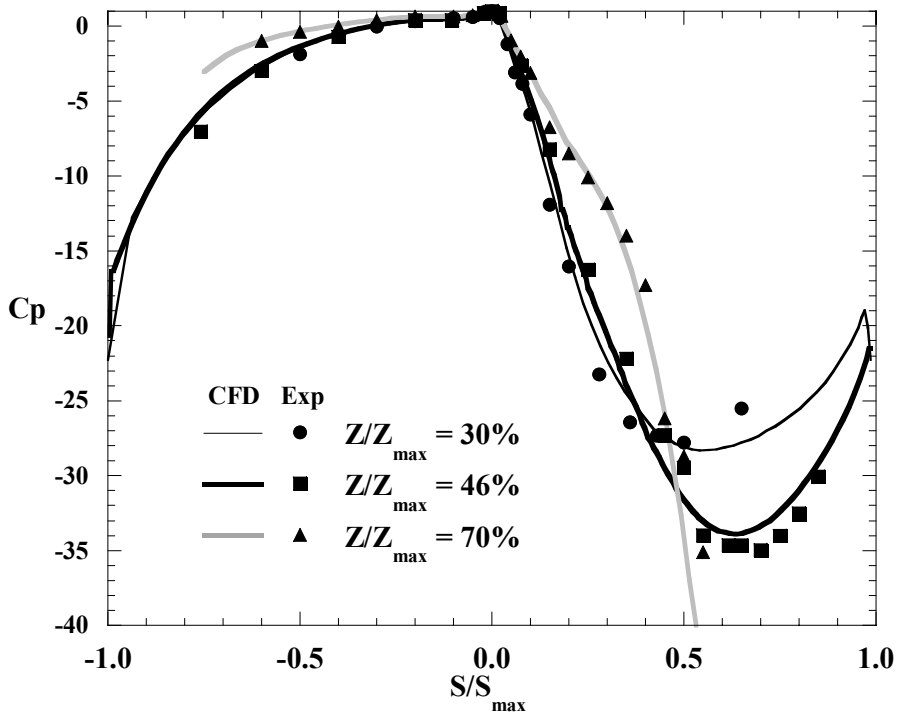

Figure 1.5. The effect of span height on the Cp distribution.

at the 70% span.

Vane Construction

The center vane was made from a low-density foam with a low thermal conductivity (k = 0.028 W/m·K) in order to minimize conduction losses through the surface. For the heat transfer tests, the vane was covered with thirteen Inconel 600 thin metal foils, which provided a constant surface heat flux. Between each foil there was a gap of 0.38 cm, which allowed enough room for pressure taps and insured that current did not conduct between foils. The foils were connected in series, with copper bus bars soldered to the ends of each foil to promote a uniform distribution of the current and insure a good electrical connection. The vane was instrumented with 214 type E thermocouples that were placed just below the heat transfer surface at five span heights to measure the surface temperature. Pressure taps were installed at 74 locations along the vane at three span heights, concentrating them in regions of high pressure gradients as predicted by Fluent.

The convective heat flux was calculated using the total power supplied to the metal foils minus radiation losses and conduction losses and gains. For the radiation

correction the emissivity, $\varepsilon = 0.22$, of the Inconel foils was assumed to be the same value as stainless steel foils (Incropera and DeWitt [14]). The surrounding temperatures were measured and found to agree with the freestream temperature. The radiation losses amounted to 4% of the total heat flux. Conduction corrections were calculated based on a one-dimensional conduction model driven by the temperature difference through the foam vane and accounted for a maximum of about 2% of the total heat flux for the worst case.

Adiabatic film-cooling effectiveness measurements were performed in the same large-scale test facility as the heat transfer measurements. Coolant flow was provided by the upper flow channel of the wind tunnel shown in Figure 1.1, using a blower to increase the coolant supply pressure before it was fed into the film-cooling vane. The temperature difference between the freestream and coolant flows was typically 20°C for the film-cooling tests, yielding density ratios near 1.06. The center vane of the two passage cascade contained five rows of cylindrical showerhead film-cooling holes and eight rows of fan-shaped film-cooling holes, four rows each on the suction and pressure sides. The experimental film-cooling vane is shown in Figure 1.6. A detailed schematic of the fan-shaped film-cooling hole geometry is shown in Figure 1.7, while the important film-cooling parameters are listed in Table 1.2 for both the showerhead and fan-shaped holes. The cylindrical showerhead holes had a 60° surface angle and a 90° compound angle. The centerlines of the fan-shaped holes were angled 30° with respect to the surface. The fan-shaped holes also had a 10° lateral diffusion angle from the hole centerline and a 10°

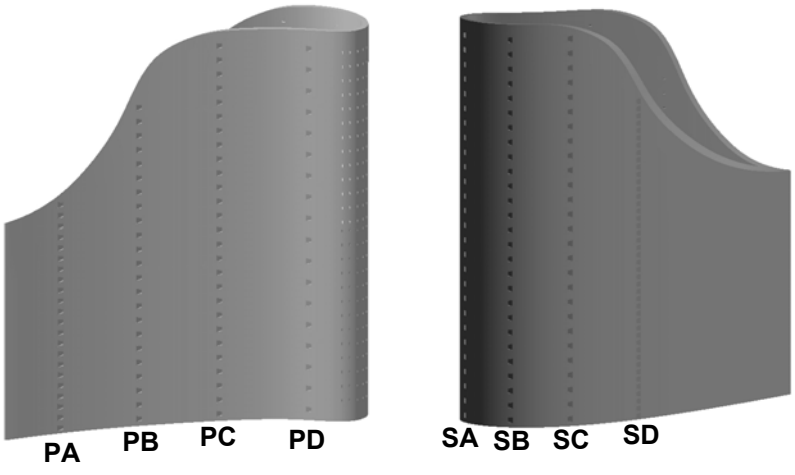

Figure 1.6. Film-cooling vane showing hole designations.

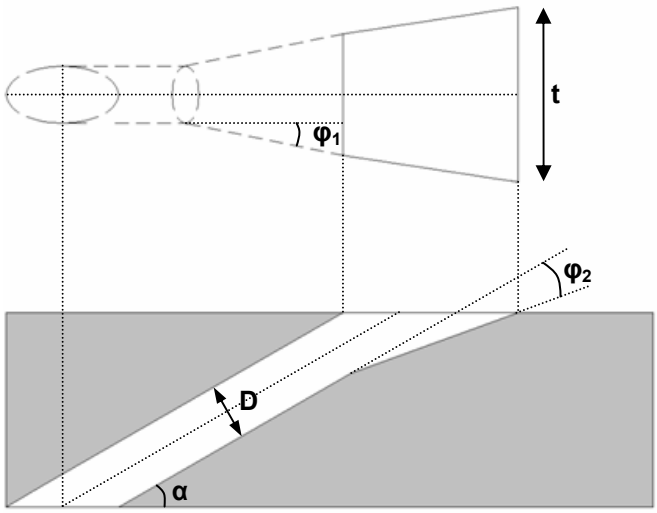

Figure 1.7. Fan shaped cooling hole detailed geometry.

Table 1.2. Film-Cooling Hole Parameters

Fan Shaped			Showerhead	
D (cm)	0.38		**D (cm)**	0.24
α (°)	30		**α (°)**	60
φ_1 (°)	10		**β (°)**	90
φ_2 (°)	10		**t (cm)**	0.48
t (cm)	0.81		**t/P (-)**	0.22
	t/P (-)	**S_{exit}/S_{max} (-)**		
Row PA	0.540	-0.840		
Row PB	0.405	-0.615		
Row PC	0.405	-0.384		
Row PD	0.270	-0.135		
Row SA	0.405	0.090		
Row SB	0.405	0.214		
Row SC	0.405	0.345		
Row SD	0.810	0.519		

forward expansion angle.

The film-cooling vane was also constructed using low thermal conductivity foam (k = 0.028 W/m·K). The film-cooling holes were cut into the foam using a 5-axis water jet cutting machine. The manufacturing process did produce small non-uniformities in the diameter of the cylindrical portion of the hole. Each hole was measured individually to insure the correct flow areas were used in calculating the coolant mass flow. The nominal diameter for the cylindrical portion of the fan-shaped film-cooling hole was 0.38

± 0.015 cm. Four plenums were placed inside the film-cooling vane to allow for the capability of independently varying individual row blowing ratios. To verify to the non-dimensional pressure distribution as discussed previously, pressure taps were placed at 46% span. Type E thermocouples were also placed flush with the surface at various locations for calibration purposes.

To set the desired coolant flows, discharge coefficients were measured for the fan-shaped film-cooling holes and compared to data from Gritsch et al. [15], which had slightly larger lateral diffusion and forward expansion angles of $\varphi_1 = 14^\circ$ and $\varphi_2 = 15^\circ$. Discharge coefficients shown in Figure 1.8 increased with pressure ratio initially before leveling off, with C_D values falling in the range between 0.8 and 0.9. Generally good agreement is shown between most of the rows and also between the current study and Gritsch, et al. [15], with slight differences in C_D attributed to the smaller lateral diffusion and forward expansion angles used in our study. C_D values were further verified by running multiple rows at the same time and comparing the calculated total mass flow rate using pressure ratios and C_D coefficients to the measured total flow rate, showing agreement within 1%.

An infrared camera was used to measure the surface temperature distribution on

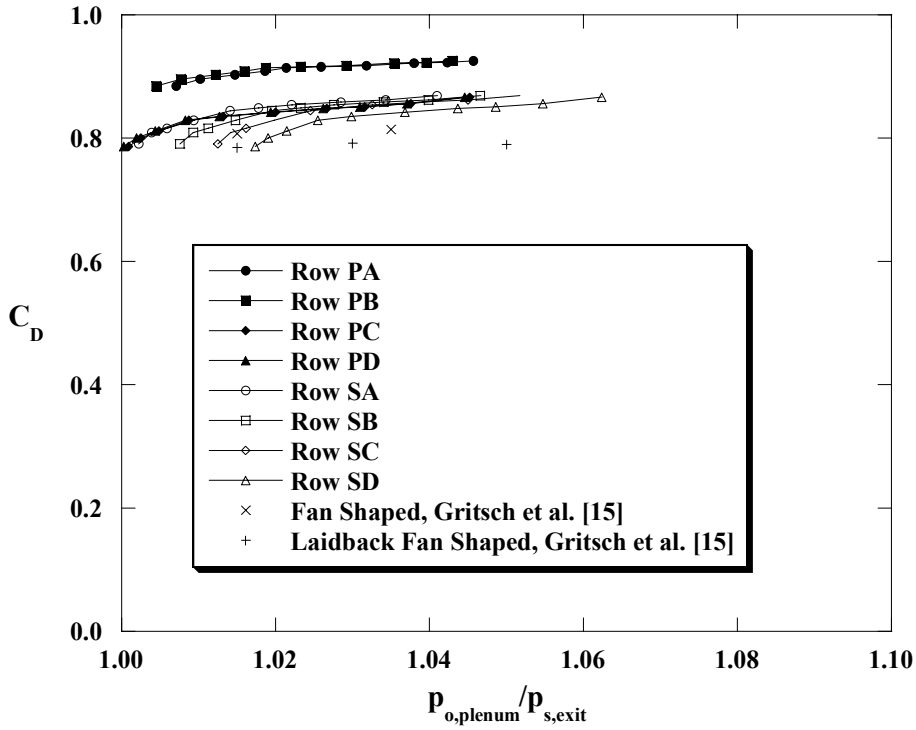

Figure 1.8. Fan-shaped hole discharge coefficients.

the vane during testing. Five images were taken at each location and averaged to minimize experimental uncertainty. Images were taken from beneath the test section through ZnSe windows placed in the lower flat endwall (illustrated in Figure 1.2). For some of the rows, more than one image was necessary to capture the area downstream of the cooling holes. Because of the vane surface curvature and the 45º angle between the IR camera and the surface, the IR images needed to be transformed to accurately represent the true surface distance. Prior to testing, a 1 cm x 1 cm grid was placed on the surface of the vane and an IR image was taken at each viewing location. Next, the grid vertices in each of the images were used to perform a 3rd or 4th order polynomial surface transformation for that image.

The transformed images were then calibrated using type E thermocouples that were placed flush with the vane surface. The infrared camera measures the radiation from the surface, so an accurate knowledge of the surface emissivity and the surrounding ambient temperature yield the correct surface temperature. The values of ε and T_{amb} for each image were deduced by calibrating the image surface temperatures to match the measured thermocouple temperatures over the full measurement range. Values for ε were fairly consistent between image locations, varying from 0.6 to 0.7. The variation resulted because not all of the images were taken at the same viewing angle or the same distance from the surface.

Following the calibration procedure, the surface temperatures were non-dimensionalized and corrected for conduction errors using the method established by Ethridge et al. [16]. Values for η_o ranged from 0.04 to 0.12 around the vane surface, where the highest values occurred just downstream of row PB on the pressure side.

Blowing ratios for this study were defined in two ways, depending on the region. For the showerhead region, blowing ratios are reported based on the inlet velocity, U_{in},

$$M_{\infty} = \frac{m_c}{A_h U_{in} \rho_{in}} \tag{1.1}$$

However, for each row of fan-shaped holes, blowing ratios are reported in terms of the local surface velocity, U_{local},

$$M = \frac{m_c}{A_h U_{local} \rho_{in}} \tag{1.2}$$

Five blowing ratios were tested for the showerhead region, four blowing ratios were tested for each row on the pressure side, and three blowing ratios were tested for each row on the suction side. The range of blowing ratios was chosed to span typical engine operating conditions.

Experimental Uncertainty

The partial derivative and sequential perturbation method given by Moffat [17] were used to calculate uncertainties for the measured values. For a high reported value of St = 0.0093 the uncertainty was ±3.23%, while the uncertainty for a low value of St = 0.0023 was ±2.13%. The uncertainties for the adiabatic effectiveness measurements were ±0.012 for a high value of $\eta_{AW} = 0.9$ and ±0.011 for a low value of $\eta_{AW} = 0.2$.

Experimental Results

Heat transfer results will be discussed first followed by adiabatic effectiveness results and a comparison to existing data from literature.

Heat Transfer Results

Heat transfer results are reported in terms of the Stanton number based on inlet velocity, with results shown in Figure 1.9 for each of the five span locations. There was a local peak in heat transfer at the stagnation region for all span heights, followed by a decrease on the pressure side before Stanton numbers leveled off. On the suction side there was a decrease in heat transfer until the boundary layer transitioned from laminar to turbulent. The transition caused a large increase in heat transfer, followed again by decreasing Stanton numbers as the turbulent boundary layer developed.

A large increase in Stanton numbers also occurred at the higher span locations, which were closer to the contour, but the increase occurred at more upstream locations on the surface ($S/S_{max,SS} = 0.4$ for the 73% span location and $S/S_{max,SS} = 0.3$ for the 88% span location). The sudden increase in Stanton numbers below 50% span was because of the boundary layer transition. However, the effect of the contour was to stagnate the flow in the region just upstream of the contraction, which led to the increase in Stanton numbers for the higher span locations. A midspan comparison with the prediction from the

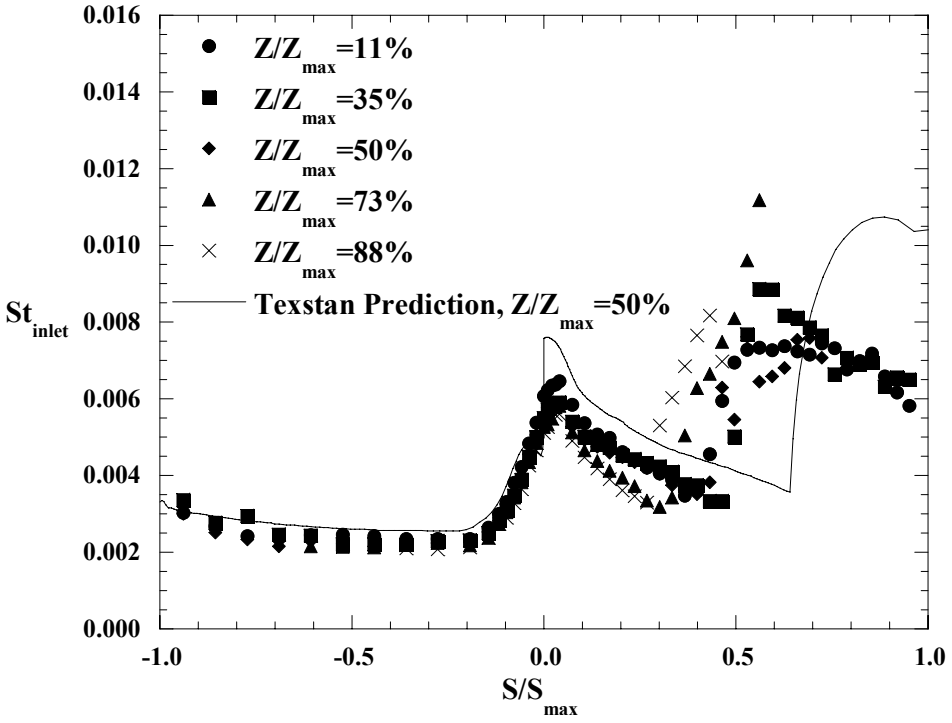

Figure 1.9. Stanton number distribution around the vane for all span heights.

numerical boundary layer code Texstan [18] show the same general trends in Stanton numbers.

Trip wires were used to simulate film-cooling injection along the surface of the vane. The effect of a trip wire on the boundary layer is analogous to a film-cooling hole modifying the boundary layer. The desired effect was that of perturbing the laminar boundary layer and causing it to become turbulent at the trip location. The trip wires consisted of materials that would not conduct current across the heat transfer surface, and were sized based on the criterion by Schlichting [19], which stated that the critical Reynolds number based on the trip diameter should be greater than 900 to cause boundary layer transition. Trip wires were placed at four locations on the suction side as shown in Figure 1.10. The critical Reynolds numbers based on the trip wire diameters and local velocities are also shown in Figure 1.10. Note there were no cooling holes present during these tests but are merely illustrated for reference.

Figure 1.11 shows the effect of the trip wires placed on the suction side in terms of a locally defined Stanton and Reynolds number, along with flat plate correlations for laminar and turbulent flow over a flat plate with constant surface heat flux developed by

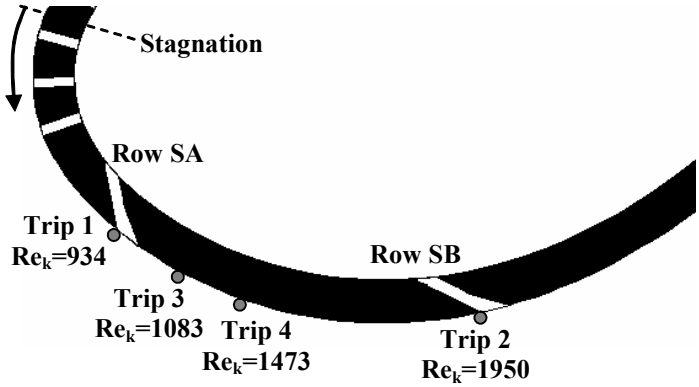

Figure 1.10. Trip wire locations shown relative to hole exit locations on the vane.

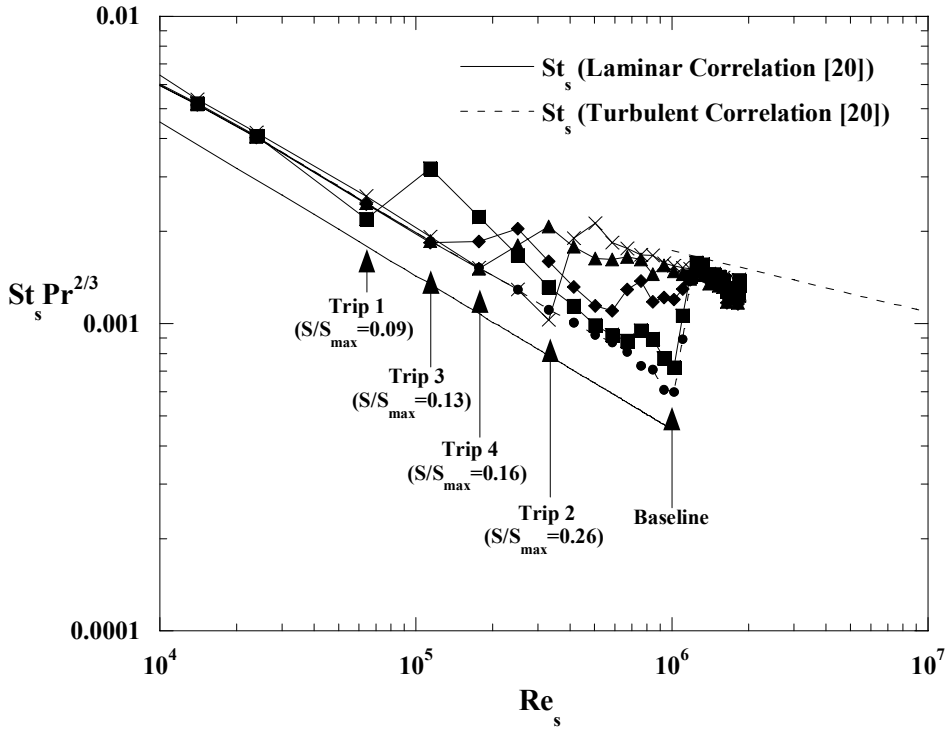

Figure 1.11. Stanton numbers for the four suction side trip cases.

Kays and Crawford [20]. Trip 1, which was placed at the same surface location as the first row of suction side film-cooling holes, caused the boundary layer to transition. However, the boundary layer ultimately relaminarized because of the strong flow acceleration. Further downstream, the boundary layer transitioned at nominally the same location as the no trip case. Trip 2, which was placed at the same surface location as the second row of suction side film-cooling holes, again forced the boundary layer to transition, which was shown by an increase in heat transfer. In this case however, the boundary layer did not relaminarize as for trip 1. A resulting investigation of several

more trip locations defined a critical region along the surface bounded by trips 3 and 4 wherein the boundary layer would transition to turbulent and not relaminarize.

Showerhead Adiabatic Effectiveness Results

Showerhead film-cooling was investigated independently, without downstream blowing, by measuring η_{AW} for five different blowing ratios ranging from M_∞ = 0.6 to 2.9. These blowing ratios are reported as the average M_∞ value of the five showerhead rows when referring to a certain case, although M_∞ values varied slightly between rows. Film-cooling effectiveness contours for the highest and lowest blowing ratio cases are shown in Figure 1.12. As M_∞ increased the jets were directed up the span of the vane and started to lift off. At M_∞ = 0.6 the coolant trickled out causing the jets to spread laterally, while at M_∞ = 2.9 the coolant offered little benefit downstream of the holes.

The pitch-averaged film-cooling effectiveness for the showerhead cases is shown in Figure 1.13. It is interesting to see that the peaks increase with M_∞ while the valleys decrease with M_∞. This is due to the change in jet direction as the blowing ratio increased. Also shown in Figure 1.13 is a comparison to Polanka et al. [2] for blowing ratios of 0.5 and 2.9. The showerhead holes in their study had a shallow surface angle of 25º, as compared with the much sharper 60º surface angle used in this study, although both studies had a 90º compound angle. In addition, the holes in the Polanka et al. [2] study were in a staggered configuration. These differences in geometry allowed the film cooling jets to stay attached to the surface much better, even for the relatively low

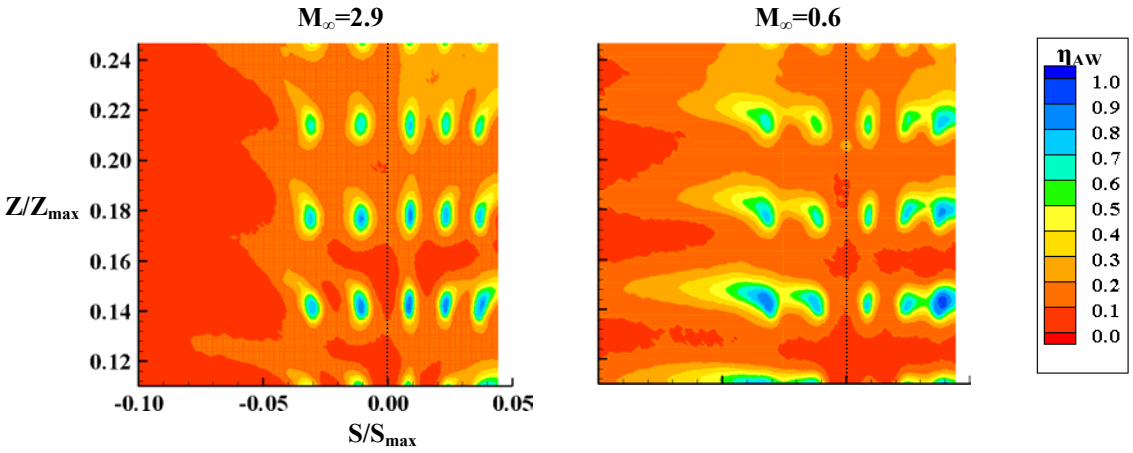

Figure 1.12. Contours of adiabatic effectiveness for the M_∞=2.9 and M_∞=0.6 showerhead cases.

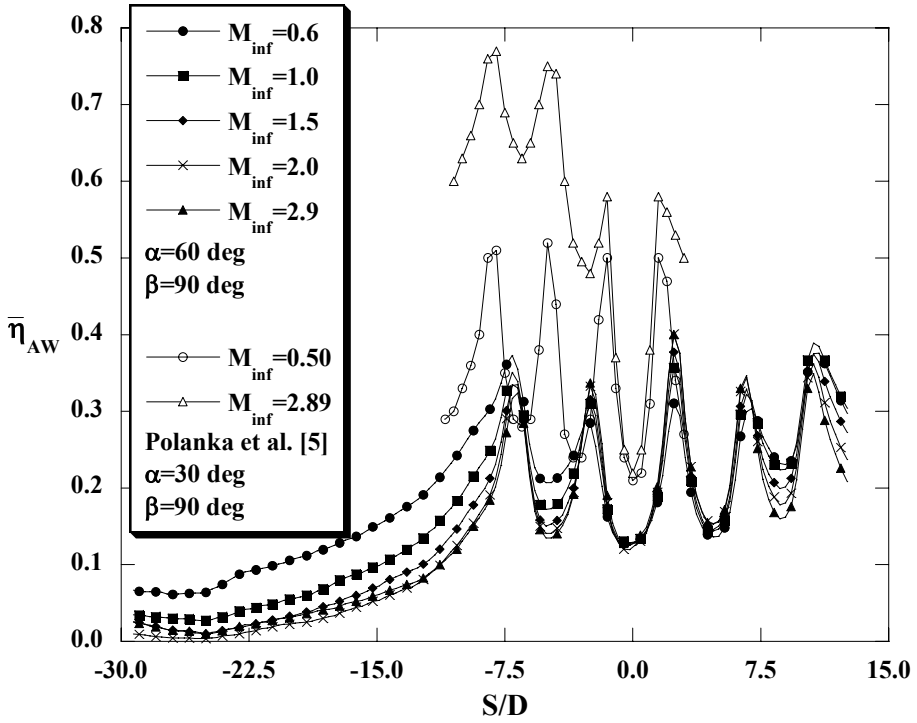

Figure 1.13. Laterally averaged effectiveness for the showerhead cases.

blowing ratio of 0.5, leading to the much greater levels of laterally averaged effectiveness by Polanka et al. [2].

Pressure Side Adiabatic Effectiveness Results

Single row adiabatic film-cooling effectiveness measurements were taken for four rows on the pressure side, without any upstream showerhead blowing. Adiabatic effectiveness contours for the highest (M = 7.4) and lowest (M = 2.9) blowing ratios measured for the first pressure side row (Row PD: $S/S_{max,PS}$ = -0.14) are shown in Figure 1.14. The contours for row PD show a contraction of the jet downstream of the hole exit indicating jet separation. After about 10 hole diameters a large lateral spreading of the jet occurs that yields an increase in both the level of adiabatic effectiveness and jet coverage. Jet separation occurred immediately downstream of the hole location due to relatively high local blowing ratios coupled with a concave surface curvature. However, as the vane surface curved back into the jet trajectory, the jet impinged and spread onto the vane surface. As expected, this phenomenon was accentuated with an increase in blowing ratio, which led to increased separation. Also shown in Figure 1.14 is the laterally averaged effectiveness for row PD. For this configuration, increased blowing led to

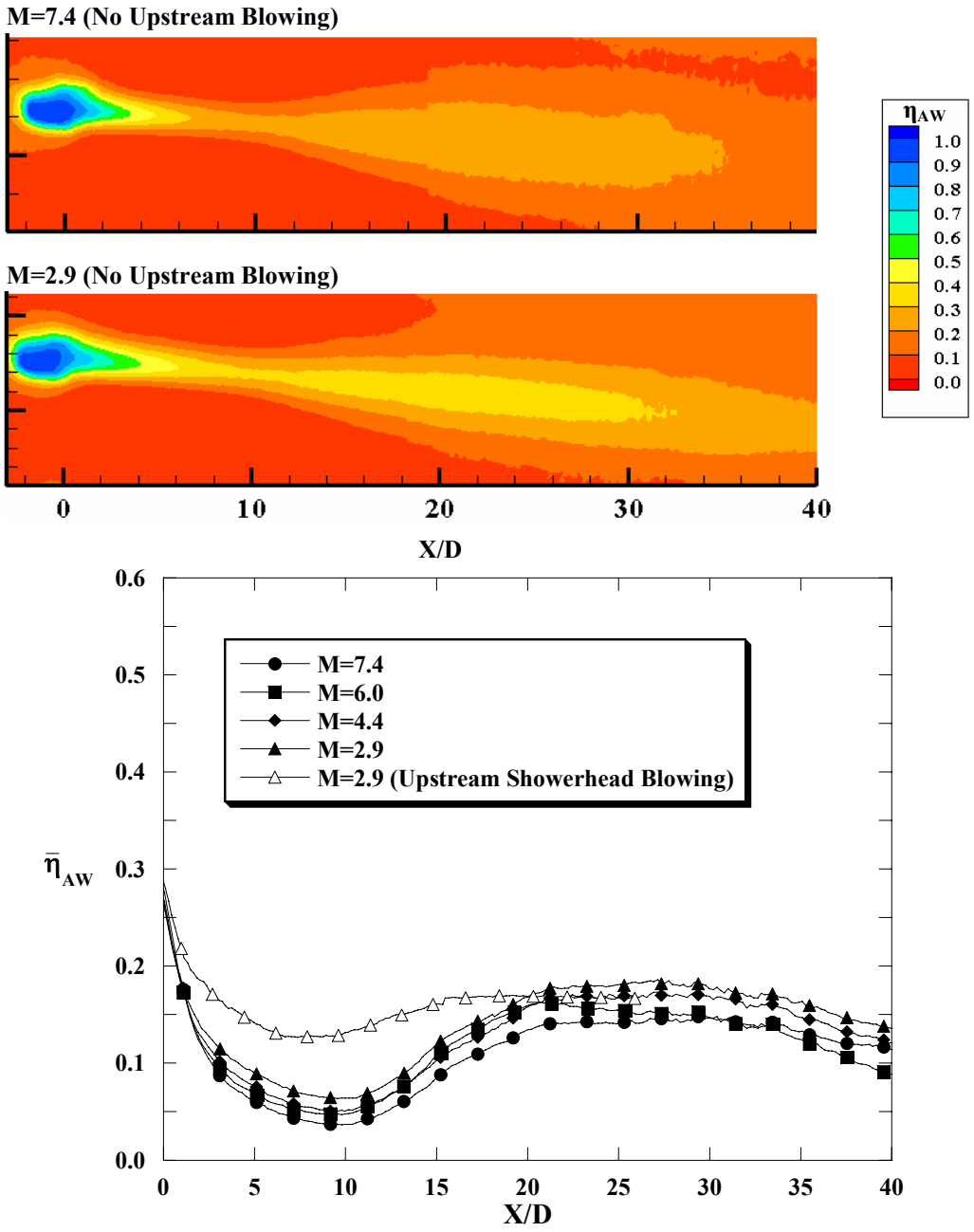

Figure 1.14. Contours of adiabatic effectiveness for high and low blowing ratios for row PD and laterally averaged adiabatic effectiveness for row PD.

lower laterally averaged effectiveness due to the increasing separation.

Also investigated was the effect of upstream showerhead cooling on the first pressure side row of fan-shaped holes. Included in Figure 1.14 is a comparison of the laterally averaged effectiveness for row PD at a blowing ratio of M = 2.9 in which there was upstream showerhead blowing (M_∞ = 2.0). The upstream blowing actually increased

the adiabatic effectiveness downstream of row PD. This is consistent with the findings of Polanka et al. [13], who stated that for high blowing ratios the turbulence generated by the upstream blowing tended to disperse the jet down onto the vane surface making it more effective at cooling the surface.

The other pressure side rows (Row PC: $S/S_{max,PS}$ = -0.38, Row PB: $S/S_{max,PS}$ = -0.61, Row PA: $S/S_{max,PS}$ = -0.84) were located on a relatively flat section of the vane surface. Representative adiabatic effectiveness contours for these three rows for high (Row PC, M = 4.8) and low (Row PC, M = 2.0) blowing ratios are shown in Figure 1.15. The jet contours taper immediately downstream of the holes. These three pressure side rows were located in a region of high acceleration, which tends to provide less resistance to jet lift off. Also shown in Figure 1.15 are laterally averaged effectiveness values for rows PC, PB, and PA, for the highest and lowest measured blowing ratios. Due to jet separation, higher blowing ratios actually reduced the adiabatic effectiveness of the fan-shaped rows.

Suction Side Adiabatic Effectiveness Results

Single row adiabatic film-cooling measurements, without any upstream showerhead blowing, were also made on the suction side for four individual rows. The first three rows on the suction side, rows SA ($S/S_{max,SS}$ = 0.09), SB ($S/S_{max,SS}$ = 0.21), and SC ($S/S_{max,SS}$ = 0.35), were located in a region of high convex curvature and high acceleration. The final suction side row (Row SD: $S/S_{max,SS}$ = 0.52) had much closer hole spacing and was located just upstream of the maximum throat velocity. Representative adiabatic effectiveness contours for high (Row SA, M = 2.8) and low (Row SA, M = 1.1) blowing ratios in the region of high curvature are shown in Figure 1.16. The contours show a large amount of separation with increased blowing. This trend is seen further in the laterally averaged effectiveness values for rows SA, SB, and SC, which are also shown in Figure 1.16 for a high and low blowing ratio. Clearly the separation is due to the severe surface curvature in this region of the suction side. The results indicate that for this region it is more beneficial to eject less flow so that it remains attached to the surface.

A representative contour of adiabatic effectiveness for row SD (also see Figure

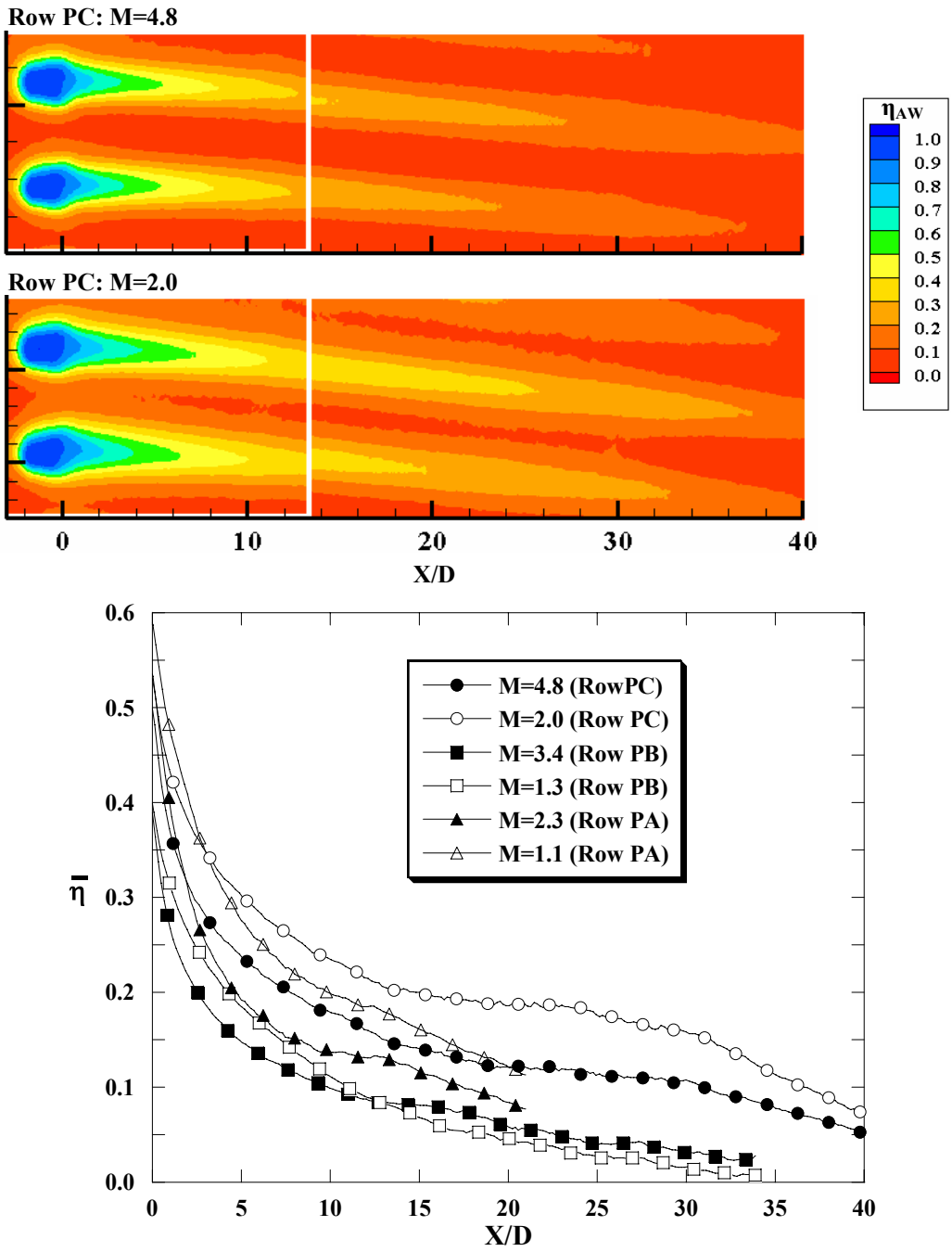

Figure 1.15. Contours of adiabatic effectiveness for high and low blowing ratios for row PC and laterally averaged adiabatic effectiveness for rows PC-PA.

1.16) shows a much higher effectiveness than the other suction side rows, in part because of the hole spacing, but also because of an absence of separation. There was less tapering of the jet contours downstream of the hole exit for row SD, indicating less separation. Individually defined jets are nearly indistinguishable downstream of about 16 hole

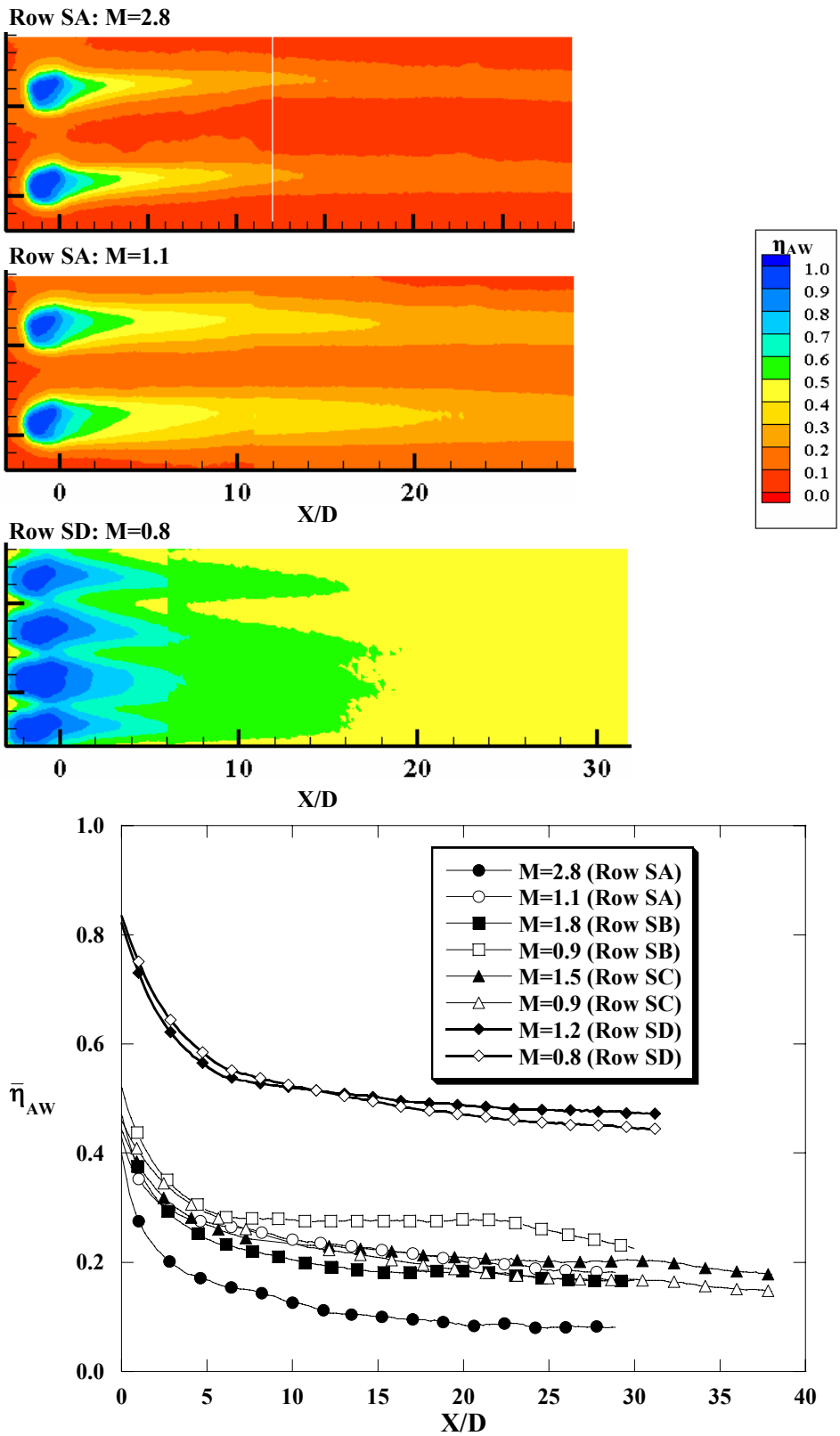

Figure 1.16. Contours of adiabatic effectiveness for high and low blowing ratios for row SA and a representative case for row SD. Also laterally averaged effectiveness for the suction side rows.

diameters, indicating the excellent lateral diffusion typically seen in an attached fan-shaped cooling hole jet. Also shown in Figure 1.16 are the laterally averaged effectiveness levels for row SD. The laterally averaged values are much higher than the separated cooling rows, and level out near a laterally averaged effectiveness value of 0.5.

Comparisons to Literature

A pressure side comparison between cylindrical and fan-shaped cooling holes for a blowing ratio near M = 2.0 is shown in Figure 1.17. The cylindrical holes studied by Zhang and Pudupatty [9] had surface inclination angles of $\alpha = 20°$ and $\alpha = 40°$, while Polanka et al. [13] studied cylindrical holes on the vane pressure side with a surface inclination angle of $\alpha = 30°$ and a compound angle of 45°. Because of differences in hole geometry and spacing, the distance downstream of the hole exit was normalized with respect to the equivalent exit slot width s described by L'Ecuyer and Soechting [21], where s is the ratio of the hole breakout area to the hole spacing P (measured normal to

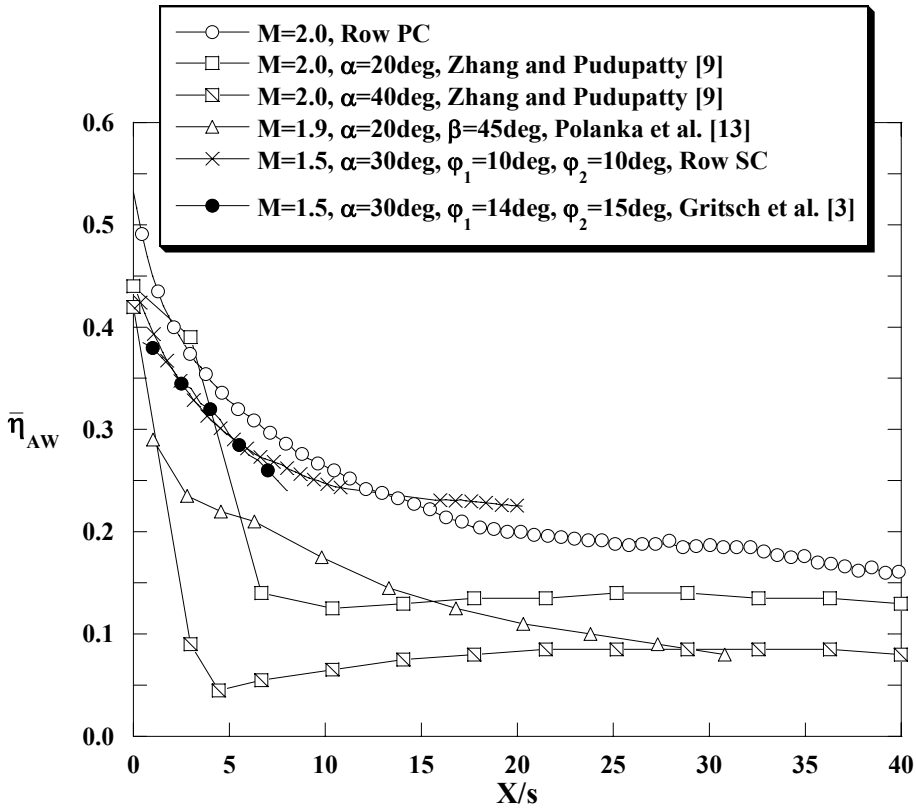

Figure 1.17. Comparisons with published cylindrical hole vane film-cooling data and fan-shaped flat plate data.

the streamwise direction). This comparison shows that the fan-shaped hole geometry offers a significant increase in adiabatic effectiveness over cylindrical holes.

Although there has been some previous studies done with fan-shaped holes on a vane surface, it was not possible to make a direct comparison to these studies, as the equivalent slot width was not able to be determined. For a region on the suction side with relatively low surface curvature, a comparison was made between data from our study and fan-shaped data on a flat plate from Gritsch et al. [3] (also shown in Figure 1.17). The flat plate study by Gritsch et al. [3] featured the same surface inclination angle as our study ($\alpha = 30°$), with slightly larger lateral diffusion and forward expansion angles of $\varphi_1 = 14°$ and $\varphi_2 = 15°$. In this region of relatively low surface curvature on the suction side, very good agreement is shown just downstream of the hole between the current study and the flat plate study by Gritsch et al. [3].

Conclusions

This paper has presented a coupled study of the heat transfer coefficients and adiabatic effectiveness for a large-scale turbine vane under low-speed conditions. A contoured endwall was designed in order to match the engine pressure distribution around the vane. Heat transfer results showed a peak in Stanton numbers near the leading edge. Stanton numbers decreased on the pressure side to a constant value. On the suction side, Stanton numbers decreased until a surface location of $S/S_{max} = 0.5$, where Stanton numbers were increased because of the boundary layer transitioning from laminar to turbulent.

Trip wires were used to simulate the boundary layer transition caused by film-cooling holes on the vane suction side. It was noted that using a trip wire to transition the boundary layer increased the Stanton numbers as if the boundary layer had transitioned naturally. The trip wire placed at the location of the first film-cooling hole row tripped the boundary layer, but the boundary layer relaminarized before the natural transition location. An investigation of trip wire location showed the sensitivity to location in terms of the boundary layer transition and the relaminarizing process. This sensitivity should be considered by engine designers when determining film-cooling hole placement, as this will dictate the laminar to turbulent boundary layer transition.

Adiabatic effectiveness measurements for the showerhead region showed that increasing the blowing ratio changed the direction of the jets and reduced the amount of lateral spreading. Adiabatic film-cooling effectiveness measurements showed that in regions of high curvature just downstream of the leading edge the jets separated from the surface. However, on the pressure side where there was a concave surface curvature near the first cooling hole row, the coolant jets impinged on the surface about ten hole diameters downstream and spread laterally. Along both the suction and pressure sides, increasing the blowing ratio tended to accentuate the jet lift off, reducing overall film-cooling effectiveness. The presence of upstream showerhead blowing on the first pressure side row tended to increase the turbulent diffusion of the jet downwards onto the surface, increasing effectiveness. The suction side was particularly hard to cool due to the jet separation resulting from the convex curvature.

A comparison to previous cylindrical hole vane cooling studies further highlights the cooling benefit from fan-shaped holes over the traditional cylindrical cooling hole shape. This study emphasizes the difficulty of film-cooling hole placement, as there are many effects that play a role in the effectiveness of a cooling jet. These effects include boundary layer transition location, surface curvature, acceleration, hole spacing, and blowing ratio.

Acknowledgments

The authors are grateful to Siemens Power Generation for their funding and support of this project.

Nomenclature

A area

C vane chord

C_D discharge coefficient

C_p specific heat

Cp static pressure coefficient, $Cp = (p_{s,local} - p_{s,in})/0.5\rho_{in}U^2_{in}$

D film-cooling hole diameter

h heat transfer coefficient

k	thermal conductivity
m	mass flow rate
M	blowing ratio using local velocity, $m_c/A_hU_{local}\rho_{in}$
M_∞	blowing ratio using inlet velocity, $m_c/A_hU_{in}\rho_{in}$
p	pressure
P	hole spacing measured normal to streamwise direction
Re	Reynolds number, $Re = U_{in}C/\upsilon$
s	equivalent slot width, A_{break}/P
S	distance along the vane surface
St_{in}	Stanton number using inlet conditions, $St_{in} = h/\rho_{in}C_pU_{in}$
St_s	Stanton number using local conditions, $St_s = h/\rho_{in}C_pU_{local}$
t	hole breakout width
U	velocity
X	distance downstream of the hole exit
Z	distance measured along the vane span

Greek

α	inclination angle
β	compound angle
ε	surface emissivity
η_{AW}	adiabatic film-cooling effectiveness, $\eta_{AW} = (\eta_{meas} - \eta_o)/(1 - \eta_o)$
η_{meas}	effectiveness with blowing, $\eta_{meas} = (T_\infty - T_{surf})/(T_\infty - T_c)$
η_o	effectiveness without blowing, $\eta_o = (T_\infty - T_{surf})/(T_\infty - T_c)$
ρ	density
υ	kinematic viscosity
φ_1	lateral diffusion angle
φ_2	forward expansion angle

Subscripts

amb	ambient
break	hole breakout area

c coolant

h metering area of film-cooling holes based on D

in inlet condition

k critical

local local conditions

max maximum

o total

s static pressure

surf surface

∞ freestream conditions

Overbar

– lateral average

References

[1] Riess, H., and Bölcs, A., 2000, "The Influence of the Boundary Layer State and Reynolds Number on Film-cooling and Heat Transfer on a Cooled Nozzle Guide Vane," 2000-GT-205.

[2] Polanka, M. D., Witteveld, V. C., and Bogard, D. G., 1999, "Film-cooling Effectiveness in the Showerhead Region of a Gas Turbine Vane Part 1: Stagnation Region and Near Pressure Side," 99-GT-48.

[3] Gritsch, M., Schulz, A., and Wittig, S., 1998, "Adiabatic Wall Effectiveness Measurements of Film-Cooling Holes with Expanded Exits," *ASME Journal of Turbomachinery*, vol. 120, pp. 549.

[4] Yuen, C. H. N., Martinez-Botas, R. F., and Whitelaw, J. H., 2001, "Film-cooling Effectiveness Downstream of Compound and Fan-Shaped Holes," 2001-GT-0131.

[5] Dittmar, J., Schulz, A., and Wittig, S., 2002, "Assessment of Various Film-

cooling Configurations Including Shaped and Compound Angle Holes Based on Large Scale Experiments," GT-2002-30176.

[6] Dittmar, J., Schulz, A., and Wittig, S., 2004, "Adiabatic Effectiveness and Heat Transfer Coefficient of Shaped Film-cooling Holes on a Scaled Guide Vane Pressure Side Model," *International Journal of Rotating Machinery*, vol. 10, pp. 345-354.

[7] Guo, S. M., Lai, C. C., Jones, T. V., Oldfield, M. L. G., Lock, G. D., and Rawlinson, A. J., 1998, "The Application of Thin-Film Technology to Measure Turbine-Vane Heat Transfer and Effectiveness in a Film-Cooled, Engine-Simulated Environment," *International Journal of Heat and Fluid Flow*, vol. 19, pp. 594-600.

[8] Zhang, L., Baltz, M., Pudupatty, R., and Fox, M., 1999, "Turbine Nozzle Film-cooling Study Using the Pressure Sensitive Paint (PSP) Technique," 99-GT-196.

[9] Zhang, L., and Pudupatty, R., 2000, "The Effects of Injection Angle and Hole Exit Shape on Turbine Nozzle Pressure Side Film-cooling," 2000-GT-247.

[10] Sargison, J. E., Guo, S. M., Oldfield, M. L. G., Lock, G. D., and Rawlinson, A. J., 2001, "A Converging Slot-Hole Film-Cooling Geometry Part 1: Low-Speed Flat-Plate Heat Transfer and Loss," 2001-GT-0126.

[11] Sargison, J. E., Guo, S. M., Oldfield, M. L. G., Lock, G. D., and Rawlinson, A. J., 2001, "A Converging Slot-Hole Film-Cooling Geometry Part 2: Transonic Nozzle Guide Vane Heat Transfer and Loss," 2001-GT-0127.

[12] Schneider, M., Parneix, S., and von Wolfersdorf, J., 2003, "Effect of Showerhead Injection on Superposition of Multi-Row Pressure Side Film-cooling with Fan-shaped Holes," GT-2003-38693.

[13] Polanka, M. D., Ethridge, M. I., Cutbirth, J. M., and Bogard, D. G., 2000, "Effects of Showerhead Injection on Film-cooling Effectiveness for a Downstream Row of Holes," 2000-GT-240.

[14] Incropera, F. P., and DeWitt, D. P., 1996, *Fundamentals of Heat and Mass Transfer*, 4th ed., New York: J. Wiley & Sons.

[15] Gritsch, M., Schulz, A., and Wittig, S., 1997, "Discharge Coefficient Measurements of Film-Cooling Holes with Expanded Exits," 97-GT-165.

[16] Ethridge, M. I., Cutbirth, J. M., and Bogard, D. G., 2000, "Scaling of Performance for Varying Density Ratio Coolants on an Airfoil with Strong Curvature and Pressure Gradient Effects," 2000-GT-239.

[17] Moffat, R. J., 1988, "Describing the Uncertainties in Experimental Results," *Experimental Thermal and Fluid Science*, vol. 1, pp. 3-17.

[18] Crawford, M. E., 1986, "Simulation Codes for Calculation of Heat Transfer to Convectively-Cooled Turbine Blades," 130 pp., a set of four lectures in Convective Heat Transfer and Film-cooling in Turbomachinery, T. Arts, ed., Lecture Series 1986-06, von Karman Institute for Fluid Dynamics, Rhode-Saint-Genese, Belgium.

[19] Schlichting, H., 1979, *Boundary Layer Theory, 7th Edition*, McGraw-Hill, New York.

[20] Kays, W. M., and Crawford, M. E., 1991, *Convective Heat and Mass Transfer*, McGraw-Hill, New York.

[21] L'Ecuyer, M. R., and Soechting, F. O., 1985, "A Model for Correlating Flat Plate Film-cooling Effectiveness for Rows of Round Holes," *Heat Transfer and*

Cooling in Gas Turbines, AGARD CP-390, Paper 19.

Paper 2:
Experimental and Computational Comparisons of Fan-Shaped Film-Cooling on a Turbine Vane Surface

Accepted for publication in the *ASME Journal of Turbomachinery*[*]

Abstract

The flow exiting the combustor in a gas turbine engine is considerably hotter than the melting temperature of the turbine section components, of which the turbine nozzle guide vanes see the hottest gas temperatures. One method used to cool the vanes is to use rows of film-cooling holes to inject bleed air that is lower in temperature through an array of discrete holes onto the vane surface. The purpose of this study was to evaluate the row-by-row interaction of fan-shaped holes as compared to the performance of a single row of fan-shaped holes in the same locations.

This study presents adiabatic film-cooling effectiveness measurements from a scaled-up, two-passage vane cascade. High resolution film-cooling measurements were made with an infrared (IR) camera at a number of engine representative flow conditions. Computational fluid dynamics (CFD) predictions were also made to evaluate the performance of some of the current turbulence models in predicting a complex flow such as turbine film-cooling. The RNG k-ε turbulence model gave a closer prediction of the overall level of film-effectiveness, while the v^2-f turbulence model gave a more accurate representation of the flow physics in some regions.

* Co-authors: Dr. Karen A. Thole, Mechanical Engineering Department, Virginia Tech
Michael Haendler, Siemens Power Generation, Muelheim a. d. Ruhr, Germany

Introduction

The nozzle guide vanes in a gas turbine, located directly downstream of the combustion section, are particularly susceptible to thermal failure, with gas temperatures commonly reaching levels above component latent melting temperatures. Combustion temperatures continue to rise in an effort to increase the efficiency and power output from gas turbine engines. This rise has led to the increased demand to devise better cooling schemes and more resilient materials from which to manufacture the turbine vanes. Many cooling strategies are typically used at the same time; including impingement cooling, internal passage cooling, and external film-cooling. While designing various cooling configurations, consideration must also be given to the structural integrity of the vanes, since turbine vanes are under extremely high thermal stresses.

Ideally, film-cooling aims to inject cooler temperature fluid over the surface of the vane, shielding it from the high temperature freestream gases. This goal is sometimes difficult to achieve, however, as the nature of the flow through the turbine passage tends to be uncompromising with conditions including high freestream turbulence, secondary flows, high surface curvature, rapid flow acceleration, and high pressure gradients, all of which have been shown to affect cooling performance. Film-cooling offers the engine designer an enticing way to extend part life, however, the use of too much coolant flow from the compressor takes a toll on the overall engine efficiency. To counteract this consequence, engine designers are constantly on the lookout for ways to maintain or even increase the cooling performance but with less coolant.

Alternative hole geometries are sometimes used by engine designers, such as the diffused or so-called fan-shaped holes, to maximize the performance of the injected coolant. By expanding the exit of the cooling hole in the lateral direction, the effective momentum of the surface coolant can be reduced prior to injection. Goldstein et al. [1] showed that fan-shaped holes provide better surface attachment at higher blowing ratios, as well as better lateral spreading of the coolant than cylindrical holes. A slight deviation of this design is the laidback fan-shaped hole, wherein a forward expansion is also included, further inhibiting jet liftoff. The major drawback for non-cylindrical hole geometries is increased initial manufacturing costs. The benefits however, of fan-shaped holes are many, including increased part life (fewer replacements needed), less required

coolant (increased engine efficiency), and fewer holes needed (increased structural stability of the vane).

CFD is becoming an essential design tool in the gas turbine industry, because it is both cheaper and faster than performing experiments. However, in order to rely on CFD results it is first necessary to validate the predictions with measurements to ensure computational reliability. In this study, detailed comparisons of the measured adiabatic effectiveness data are made with CFD predictions using both the RNG k-ε and v^2-f turbulence models.

The standard k-ε turbulence model is a Reynolds Averaged Navier-Stokes (RANS) model with two transport equations – one for the turbulent kinetic energy (k) and one for the eddy viscosity (ε) – which are used to approximate the turbulent viscosity (μ_t). The RNG k-ε model involves renormalization group theory and adds a term to the eddy viscosity transport equation, which makes the model better for high strain flows than the standard k-ε model. One major drawback of the RNG k-ε model in wall-bounded flows such as film-cooling is the assumption of isotropic turbulence. The existence of the wall introduces anisotropy in the normal fluctuations, the presence of which are not accounted for in the wall functions used to approximate the behavior in the boundary layer in the k-ε turbulence models. Wall functions lose their reliability in 3D or separated flow regimes such as sometimes seen in film-cooling.

Durbin [2] incorporated turbulence anisotropy in the near wall region into the existing k-ε RANS model by adding two transport equations – one for the normal fluctuations (v^2) and one for an elliptic relaxation function (f) – and effectively removed the necessity of wall functions. The v^2-f turbulence model correctly models the blocking phenomenon near the wall that is responsible for attenuating the normal turbulent fluctuations, eliminating the requirement of damping functions in wall bounded flows.

Film-cooling effectiveness has been predicted using both the RNG k-ε and the v^2-f turbulence models in our paper. The complete passage, including the contoured endwall was modeled in the RNG k-ε simulation for a baseline case. A spanwise periodic section of the vane passage was modeled using the v^2-f turbulence model for the same blowing ratios that were measured experimentally.

This study is the first to present detailed high-resolution adiabatic film-cooling

effectiveness measurements for a turbine vane with multiple rows of fan-shaped film-cooling holes at engine representative blowing ratios. Contours and laterally averaged values of adiabatic film-cooling effectiveness are presented for both the pressure and suction sides. Adiabatic film-cooling effectiveness data is critical information for engine designers, necessary to predict not only metal temperatures but also to validate CFD predictions.

Past Studies

Because of its crucial role in preventing thermal failure in gas turbine engines, film-cooling has been an extensively researched topic over the last 30 to 35 years ([3],[4]). Flat plate studies have encompassed a variation of every possible geometrical parameter; including surface angle, entrance length, hole spacing, compound angle, lateral expansion angle, forward expansion angle, area ratio, and multiple row configurations. External conditions have also been thoroughly investigated for flat plates; including such effects as turbulence intensity, pressure gradient, and the state of the approaching boundary layer. An excellent review of the relevant shaped hole literature, which primarily focused on flat-plate studies, was given by Bunker [5]. Although flat plate studies are a key first step in understanding the flow physics for a given cooling hole geometry, to completely understand the flow physics and evaluate a given film-cooling design, it must be tested on the actual turbine vane. It stands to reason that the flow physics on a highly curved surface such as a turbine vane, coupled with multiple cooling row interaction, could yield results that are different from the flat plate special case. Some studies have presented results for partially and/or fully cooled nozzle guide vanes, but the deficiency of many of those studies is the lack of high resolution effectiveness measurements.

Studies involving a single row of fan-shaped cooling holes on a vane surface have been performed by Zhang et al. [6], Zhang and Pudupatty [7], and Colban et al. [8]. Using the same experimental procedure and facilities for both studies, effectiveness measurements were made with fan-shaped holes on the suction side by Zhang et al. [6] and on the pressure side by Zhang and Pudupatty [7]. Results indicated an increase in effectiveness on the suction side for the blowing ratio range from 0.5 to 1.5 and a

decrease in effectiveness on the pressure side for the blowing ratio range from 1.5 to 2.5. Colban et al. [8] presented adiabatic effectiveness measurements for eight single rows of fan-shaped holes on both the pressure and suction sides in the same facilities as this paper. Their results indicated that in regions of high convex curvature, particularly on the suction side near the leading edge, jet lift-off was prevalent, and increased with blowing ratio. Colban et al. [8] also noted a decrease in effectiveness with increased blowing on the pressure side, which was attributed to partial jet lift-off and hot gas entrainment.

Despite the knowledge gained by studying single row cooling on the vane, it is still necessary to study multiple row film-cooling on the vane. Goldstein et al. [9] showed that on a flat plate a single row of cooling holes separated with increasing blowing ratio, resulting in decreased film-effectiveness. However, with a double row cooling configuration, the upstream row provided the impetus for the downstream row to stay attached to the surface. This resulted in an increased film-effectiveness with blowing ratio. The study by Goldstein et al. [9] suggested that an accurate study of vane film-cooling would not be complete unless all of the engine-present film-cooling rows were tested together.

Effectiveness measurements were made by Guo et al. [10] in a transonic facility for a turbine airfoil with multiple rows of fan-shaped holes. Results showed higher values of effectiveness for fan-shaped holes than for cylindrical holes. However, the decay in effectiveness on the pressure side was faster for fan-shaped than for cylindrical holes, which was most likely the result of a better lateral coverage for the fan-shaped holes. Sargison et al. [11] also measured effectiveness in an annular turbine cascade with multiple rows of cylindrical, fan-shaped, and converging slot holes. They reported similar levels of performance for the fan-shaped and converging slot holes, both of which had superior performance than cylindrical holes.

Effectiveness measurements on the pressure side were made for three rows of fan-shaped holes and isothermal showerhead blowing by Schnieder et al. [12]. They reported that the presence of isothermal showerhead blowing caused increased mixing of the first pressure side row, lowering effectiveness. However, with showerhead cooling, perhaps the increased mixing of the first pressure side row might actually improve effectiveness. Polanka et al. [13] also studied the effect of showerhead blowing on the first downstream

pressure side row, using cylindrical instead of fan-shaped holes. They reported that showerhead blowing caused the jets to stay attached, where they would normally separate without upstream blowing. Polanka et al. [13] suggested that increased turbulent mixing caused by the showerhead dispersed the jet towards the wall, reducing lift-off.

Colban et al. [8] presented effectiveness for fan-shaped holes combined with upstream showerhead blowing. Their results indicated that upstream showerhead blowing increased jet dispersion towards the vane surface for the first row of film-cooling holes downstream on the pressure side, a result consistent with the results of Polanka et al. [13]. Although Colban et al. [8] presented a complete set of high resolution data for single row fan-shaped holes on a turbine vane, it is further necessary to understand the row-to-row interaction, as the state of the approaching boundary layer has been shown to have a significant effect on the performance of a film-cooling jet [14].

There have been a limited number of computational studies involving shaped hole film-cooling on a flat plate. Kohli and Thole [15] used the standard k-ε model with non-equilibrium wall functions to show the importance of modeling the interior plenum conditions correctly. A similar flat-plate study was performed by Hyams and Leylek [16] who investigated the effect of hole geometry on the thermal and flow field using the high Reynolds number k-ε model with generalized wall functions. They showed that laterally diffused shaped holes had the highest adiabatic effectiveness levels downstream of the hole exit location.

Computational film-cooling studies on a turbine vane surface with fan-shaped holes have been done by Hildebrandt et al. [17], Ferguson et al. [18] and Heidmann et al. [19]. Only Heidmann et al. [19] however, modeled more than one row of holes on the vane. Their study used the k-ω model to simulate a periodic section of the vane with six staggered rows of cylindrical showerhead holes, four rows of fan-shaped holes on the pressure side, and two rows of cylindrical holes on the suction side. The numerical results presented by Heidmann et al. [19] were not validated with experiments, so the validity of the method was not established. The single row numerical results of Ferguson et al. [18] showed good agreement with experimental results for blowing ratios less than 1.5 using the RNG k-ε model with a two-layer wall treatment. Above a blowing ratio of 1.5, the agreement was not so good.

Nothing, to the author's knowledge, as of yet has been published applying the v^2-f turbulence model to film-cooling flow applications. However, because the v^2-f model is valid all the way to the wall, with no need for wall functions or damping models in the viscous sublayer, it stands to reason that it should be expected to perform at least as good as the existing two-equation models if not better. The v^2-f model has been used with success in modeling three-dimensional turbulent boundary layers (Parneix et al. [20]) as well as separated flow conditions such as the backward facing step and vortex shedding flows (Durbin [21]).

Of the previous fan-shaped film-cooling studies that have been performed on a vane, the obvious deficiency is for high resolution data for the fully cooled situation. This study offers the first completely cooled turbine vane study with fan-shaped film-cooling giving detailed experimental adiabatic film-cooling effectiveness results. Similarly, past computational studies of film-cooling have been limited in their scope.

Experimental Facilities

The experiments were performed in the VTExCCL large-scale, low-speed, recirculating wind tunnel facility shown in Figure 2.1. This facility was identical to the one used by Colban et al. [8], and was described in detail by that study. The main features of the facility were a flow split section that divided the flow into two channels; one which was heated to by a 55 kW heater bank and used as the mainstream combustor exit flow and the other which was cooled using a 40 kW chiller in series with a heat

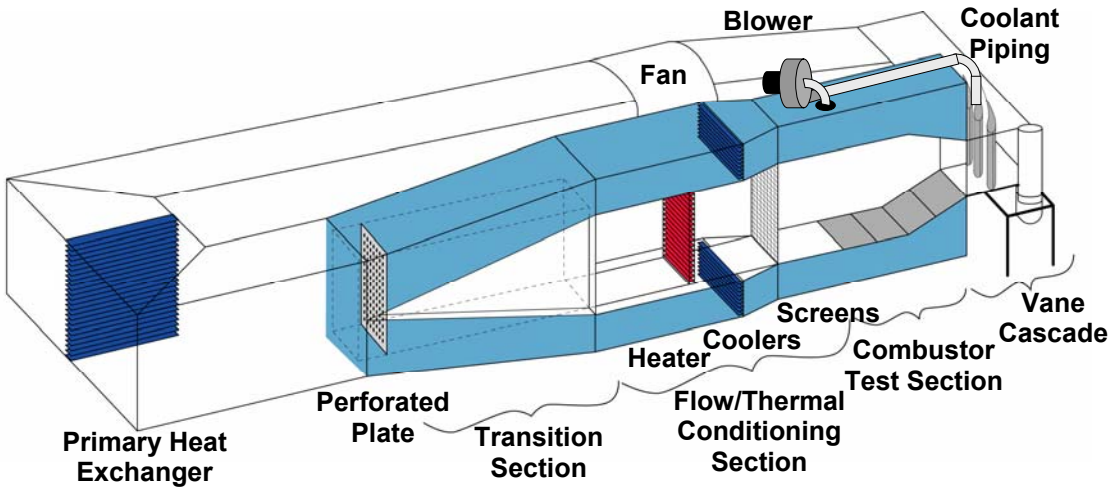

Figure 2.1. Schematic of the low-speed recirculating wind tunnel facility.

exchanger and used as coolant flow.

The test section was a linear, two-passage cascade with a contoured upper endwall. The inlet freestream turbulence intensity was measured to be 1.2% a distance of 0.2 C upstream of the vane leading edge with a hot wire anemometer. Typical mainstream temperature was 60ºC, with a nominal difference between the mainstream and coolant of 20ºC, yielding a density ratio of 1.06. The pressure at the test section inlet was nearly atmospheric. A list of pertinent geometrical parameters for the test section is given in Table 2.1, along with certain relevant inlet conditions.

Test Section Design

To match the engine static pressure distribution around the vane to that found in the engine, a contoured surface was implemented for the upper endwall. The contoured endwall, which contracted to roughly 54% of the inlet span height, is shown schematically and graphically in Figure 2.2. A detailed account of the contour design was given by Colban et al. [8]. The contoured endwall resulted in an excellent match of the experimental static pressure distribution at the midspan to that of the engine. Also, since this investigation was not focused on any three-dimensional effects of the contour on the vane cooling, a rigorous investigation, including CFD predictions and experimental examination, was used to verify the presence of a two-dimensional flow regime in the area where the measurements were taken. All of the film-cooling effectiveness measurements were made between 5% and 32% span, while the flow was essentially two-dimensional below 40% span.

A schematic of the vane test section is shown in Figure 2.3. Bleed valves were used to ensure flow periodicity between the two passages, and the flexible wall was used

Table 2.1. Operating Conditions and Vane Parameters

Scale	3X
C (m)	0.53
$S_{max,PS}$ (m)	0.52
$S_{max,SS}$ (m)	0.68
U_{in} (m/s)	10
Re_{in}	3.0×10^5
ΔT_{FC} (ºC)	20
Vane Pitch (m)	0.465

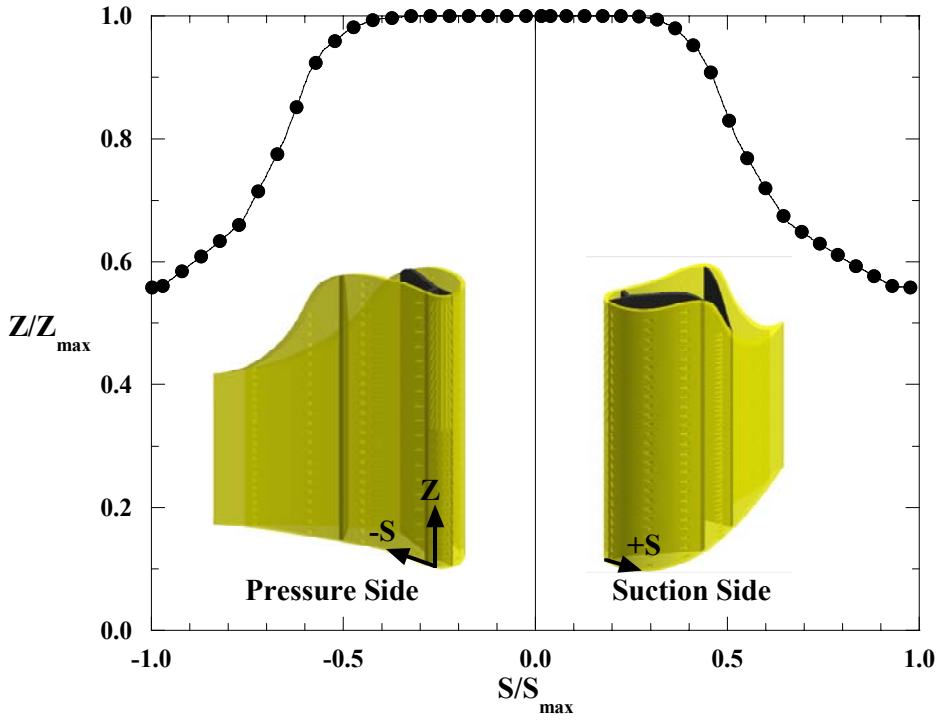

Figure 2.2. Contoured endwall surface definition.

to make minor adjustments to the flow distribution around the center vane. Also shown in Figure 2.3 are the plenum locations relative to the holes, as well as the hole designations, to be used throughout the rest of the report.

A detailed discussion of the vane design and construction was given by Colban et al. [8]. The vane contained four interior plenums, which allowed for flow rate control amongst the rows of holes to obtain the desired blowing ratio distribution. Coolant was

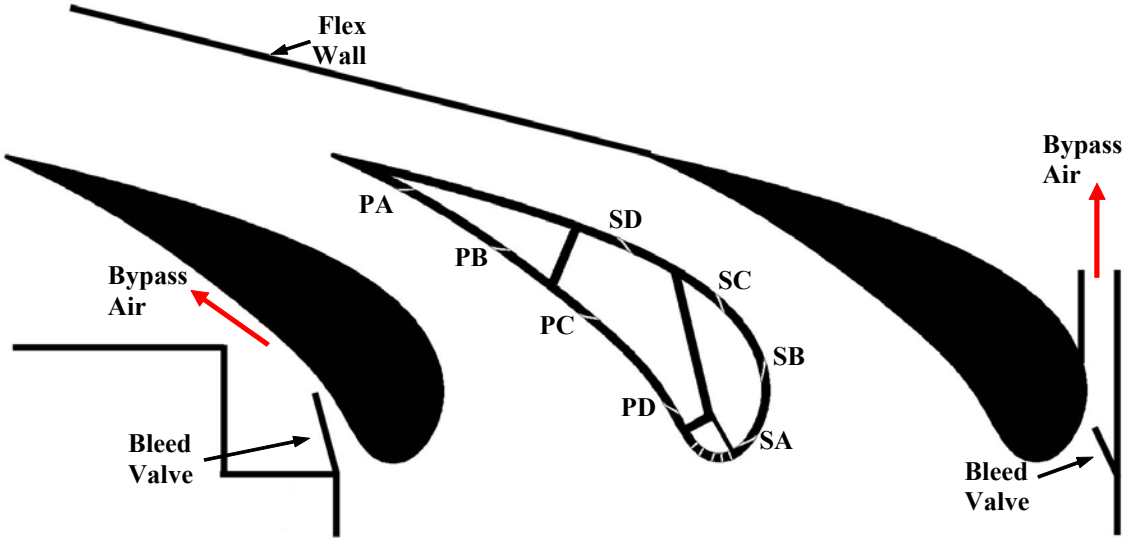

Figure 2.3. Schematic of experimental test section.

supplied to the plenums from the upper channel in the wind tunnel using the blower shown in Figure 2.1. Discharge coefficients, which were presented in the study of Colban et al. [8], were used to set the combined flow rates through each plenum based on the desired blowing ratios.

The test vane contained showerhead cooling with five in-line rows, four fan-shaped pressure side rows, and four fan-shaped suction side rows of film-cooling holes. The diameter of the cylindrical inlet section of the fan-shaped holes was 0.38 ± 0.015 cm. The diameters of each hole were measured to verify that the correct flow area was used to determine the total mass flow rate and individual blowing ratios because of slight manufacturing variation resulting from the five-axis water-jet machining process. Slight variations did occur in fan-shape of the holes as a result of the manufacturing process. Some hole-to-hole variation can be seen in the effectiveness contours, which were attributed to variation in hole shape as well as experimental uncertainty. An illustration of the fan-shaped hole geometry is shown in Figure 2.4, and relevant parameters for the film-cooling holes are listed in Table 2.2. The cylindrical showerhead holes had fairly high surface inclination angle of 60° along with a 90° compound angle. The fan-shaped holes had a surface inclination angle of 30° and lateral and forward expansion angles of 10°.

High resolution surface temperature measurements were obtained with an IR camera. Thermocouples placed in the vane surface were used to calibrate the images,

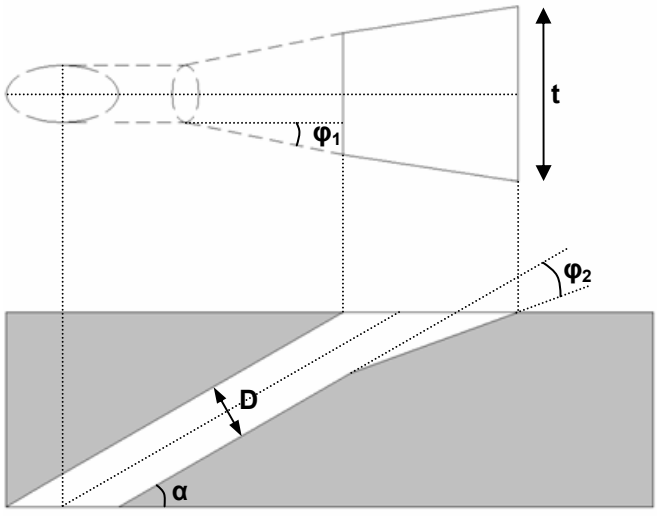

Figure 2.4. Fan shaped cooling hole detailed geometry.

Table 2.2. Film-Cooling Hole Parameters

Fan Shaped			Showerhead	
D (cm)	0.38		**D (cm)**	0.24
α (°)	30		**α (°)**	60
φ_1 (°)	10		**β (°)**	90
φ_2 (°)	10		**t (cm)**	0.48
t (cm)	0.81		**t/P (-)**	0.22
	t/P (-)	**S_{exit}/S_{max} (-)**		
Row PA	0.540	-0.840		
Row PB	0.405	-0.615		
Row PC	0.405	-0.384		
Row PD	0.270	-0.135		
Row SA	0.405	0.090		
Row SB	0.405	0.214		
Row SC	0.405	0.345		
Row SD	0.810	0.519		

which were taken from below the test section at 45° relative to the surface for optical access. Post-processing of the images required a three-dimensional transformation, calibration, conduction correction, and assembly. A detailed description of the complete measurement technique can be found in Colban et al. [8].

Two blowing ratios were defined for this study. For the showerhead region, blowing ratios are reported based on inlet velocity, U_{in},

$$M_{\infty} = \frac{\dot{m}_c}{A_h U_{in} \rho_{in}} \tag{2.1}$$

For the fan-shaped holes however, it is more appropriate to report blowing ratios in terms of local velocity, U_{local},

$$M = \frac{\dot{m}_c}{A_h U_{local} \rho_{in}} \tag{2.2}$$

Three sets of blowing ratios were measured for the fan-shaped holes, while the showerhead blowing ratio of $M_{\infty} = 2.0$ was held constant for all cases. The range of measured blowing ratios, shown in Figure 2.5, was chosen to encompass typical operating conditions in an industrial gas turbine. As described earlier, blowing ratios were set by using previously measured discharge coefficients.

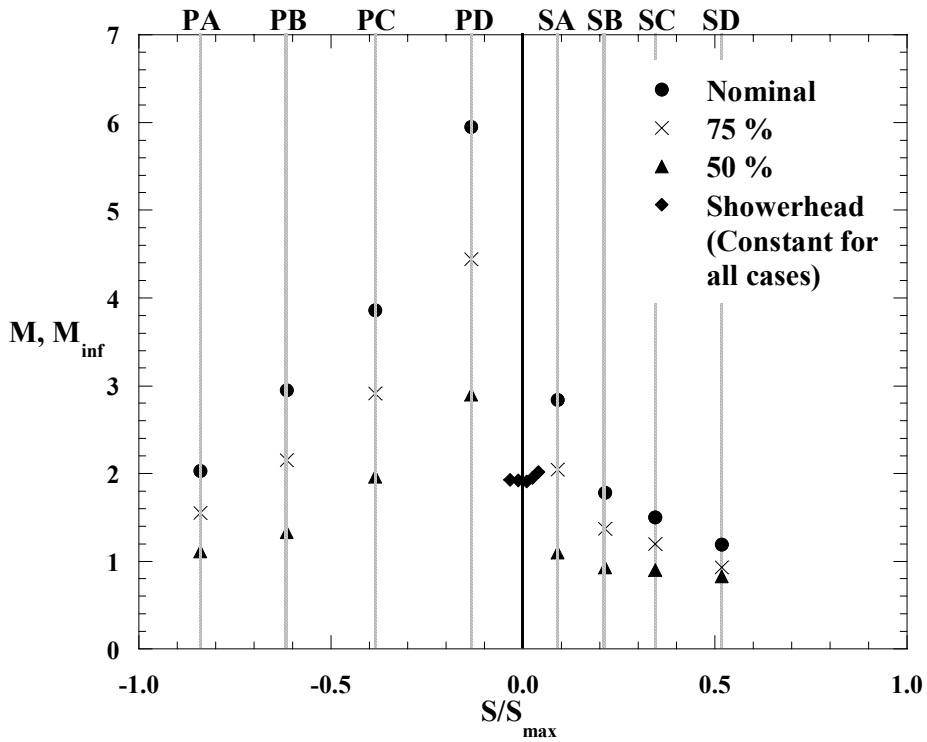

Figure 2.5. Test matrix of blowing ratios for each case.

Experimental Uncertainty

Surface temperatures were measured for a reference case with hot mainstream flow and cool plenum flow, but no surface film-cooling. This procedure yielded values of surface effectiveness without blowing betweeen 0.04 and 0.12. A one-dimensional conduction correction was then applied to the data using the reference values as described in Etheridge et al. [22]. The partial derivative and sequential perturbation method as explained by Moffat [23] was used to determine uncertainties for the experimentally reported effectiveness values. High values of $\eta = 0.9$ had uncertainties of ± 0.012, while low values of $\eta = 0.2$ had an uncertainty of ± 0.011.

Computational Methodology

CFD predictions were done with both the RNG k-ε and v^2-f [2] turbulence models. The RNG k-ε was chosen because it is perhaps the most common turbulence model currently used in industry, and serves as a baseline computational comparison for the v^2-f model. The v^2-f model was chosen to see if the improvements made in the near-wall modeling would offer a significant improvement in predictive capability over the current

industry standard. The constraints of the two models dictated different approaches in selecting the computational domain and in meshing. All of the CFD predictions were done using Fluent 6.0.1, a commercially available CFD solver with a special module for the v^2-f model.

RNG k-ε Model

The computational domain for the RNG k-ε simulation consisted of one periodic vane passage. A two-dimensional view of the domain is shown in Figure 2.6. The domain began one chord length upstream of the vane leading edge, using a velocity inlet condition. The exit boundary was located 1.5 C downstream of the trailing edge, a

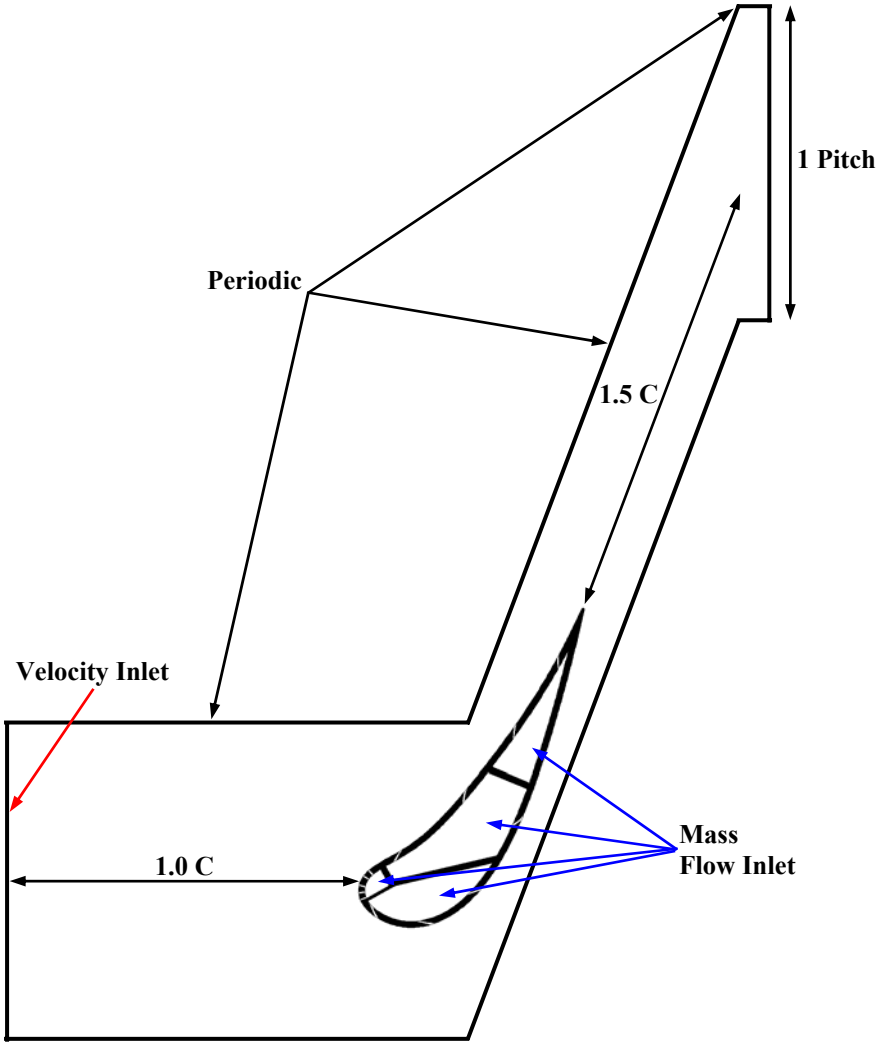

Figure 2.6. 2D view of the CFD domain (the RNG k-ε model featured the entire span and contour, while the v^2-f prediction featured only a 6 cm spanwise periodic section).

distance suggested by Hermanson and Thole [24] so as not to affect the upstream flow field. The interior plenum geometry was consistent with the experimental setup, using mass flow inlet boundaries. The mass flow rates were specified such that the average blowing ratios exiting the holes would correspond to the experimentally desired values. The contoured endwall was also modeled to see how far down the vane span the effects of the contour reached. The RNG k-ε domain included the entire vane height and all of the cooling holes, 215 of which were fan-shaped holes and 130 of which were cylindrical showerhead holes.

Approximately 2.2 million unstructured tetrahedral cells were used to mesh the domain. This resulted in approximately 1500 volumetric cells to define each fan-shaped hole (Figure 2.7a), and approximately 400 volumetric cells to define each cylindrical hole. Because the RNG k-ε turbulence model is not valid within the laminar sublayer, non-equilibrium wall functions were used to model the viscous effects of the boundary layer near the wall. This required cells with centroids located within a range of $30 < y^+ < 60$ near the vane surface. Convergence required approximately 1000 iterations on 4 parallel processors. The simulations took approximately two days to converge. Convergence was determined not only from residuals, but also by monitoring area-averaged surface temperatures on both the suction and pressure sides. The drag coefficient around the vane was also monitored as a check on aerodynamic convergence. A grid independence study was also performed by adapting the grid up to 3.9 million cells, but no significant change in results was observed so the initial grid size of 2.2 millions cells was deemed sufficient.

v^2-f Model

Unlike the RNG k-ε model, the v^2-f model is valid to the wall. This required a

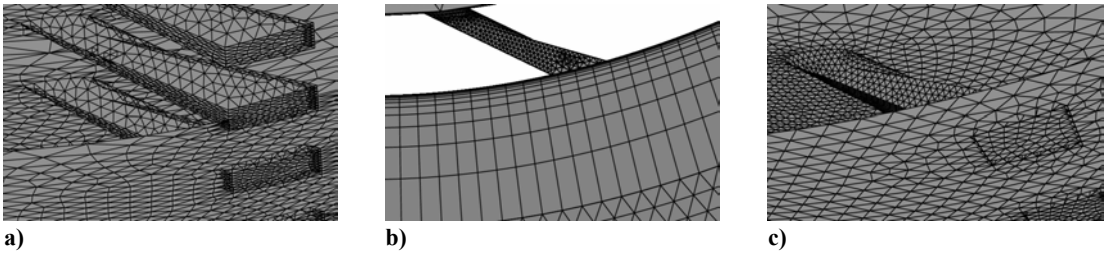

Figure 2.7. Computational grid sample of (a) the RNG k-ε surface mesh, (b) the v^2-f boundary layer mesh, and (c) the v^2-f surface mesh.

structured grid in the vicinity of the wall, resolving the boundary layer to within $y^+ < 3$. Consequently, modeling the entire span was not a possibility for the v^2-f model due to the higher cell density required near the wall. For this reason, only a 6 cm spanwise periodic section was included in the computational domain, which is shown schematically in Figure 2.6. Both the experimental results and the RNG k-ε CFD results showed periodicity below the midspan, so it was valid to model only the small periodic section, thus making the computations feasible.

The v^2-f model grid contained approximately 1.6 million cells in order to get the near wall resolution. The vane surface was meshed with an unstructured grid, and a boundary layer mesh was applied to the vane surface (shown in Figure 2.7b). Consequently, there were prismatic cells to a distance of 1.5 cm from the wall, at which point the remainder of the domain was meshed with unstructured tetrahedral cells. The surface mesh resolution is shown for the v^2-f simulations in Figure 2.7c. Solutions were run for 500 iterations on a first order upwind scheme, before being switched over to a second order upwind scheme with SIMPLEC coupling for 1500 iterations. The v^2-f model computations were run on 3 parallel processors and required approximately 3 days to reach convergence. As with the RNG k-ε model, the surface temperatures and drag coefficient were monitored as additional convergence criteria.

Results

Prior to performing the multiple row adiabatic film-cooling measurements, the experimental method and data reduction procedure were validated for a single row and compared to existing published data. Figure 2.8 shows laterally averaged single row effectiveness downstream of row SC, a row which was located in a relatively flat region of the vane. Because of differences in hole geometry and spacing, the distance downstream of the hole exit was normalized with respect to the equivalent exit slot width s, where s was the ratio of the hole breakout area to the hole spacing P. The results show excellent agreement with the flat plate study by Gritsch et al. [25], thus validating both the experimental and data reduction methods.

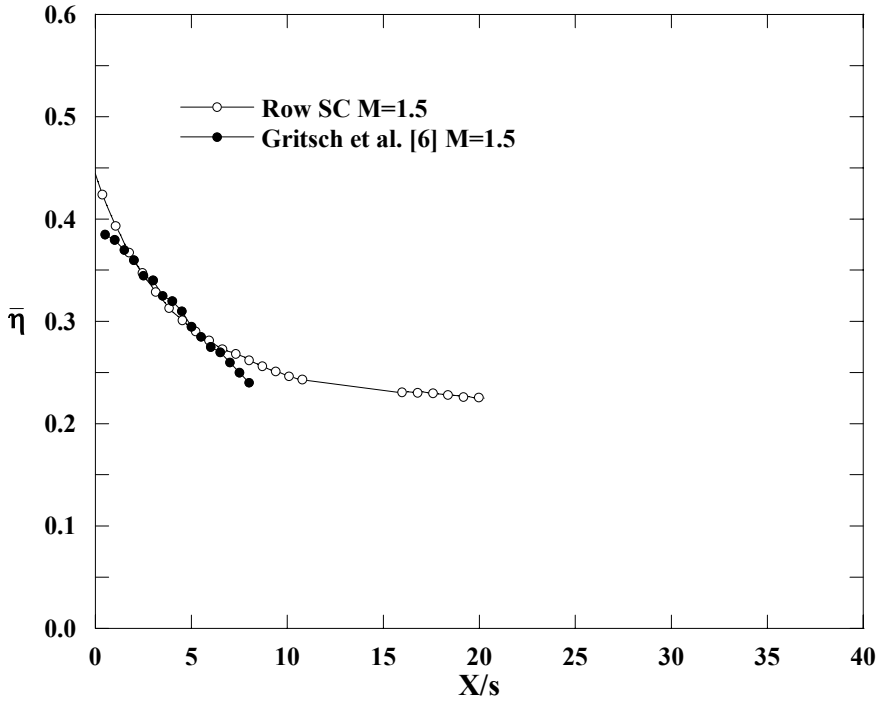

Figure 2.8. Comparison of results with previously published data.

Pressure Side

Adiabatic film-cooling effectiveness contours for each case are shown in Figure 2.9 for the pressure side. In total, five images were required to completely capture the pressure side, with measurements taken in the nominally 2-D flow region of the vane. The showerhead cooling was largely ineffective at cooling the leading edge region, which Colban et al. [8] attributed to jet lift-off from the high surface angle. The first row of fan-shaped holes showed lift-off by a narrowing in the jet contour just downstream of the hole exit. However, downstream near $S/S_{max} = -0.20$, the jets began to spread laterally. This was a result of the holes in row PD being placed in a region of concave curvature on the pressure side. The jets lifted off initially, but downstream they impinged on the vane surface, which caused lateral spreading. These results were consistent with the cylindrical film-cooling study performed by Ito et al. [26] on a concave pressure surface.

Overall, there was an increase in η with distance from the leading edge, which is evident from the increased η levels between the jets in rows PC, PB, and PA. Laterally averaged η values (shown in Figure 2.10) also show an increase in cooling effectiveness with increased blowing. This result differs from the single row results for the pressure side (Colban et al. [8]), which showed a decrease in film-effectiveness with increased

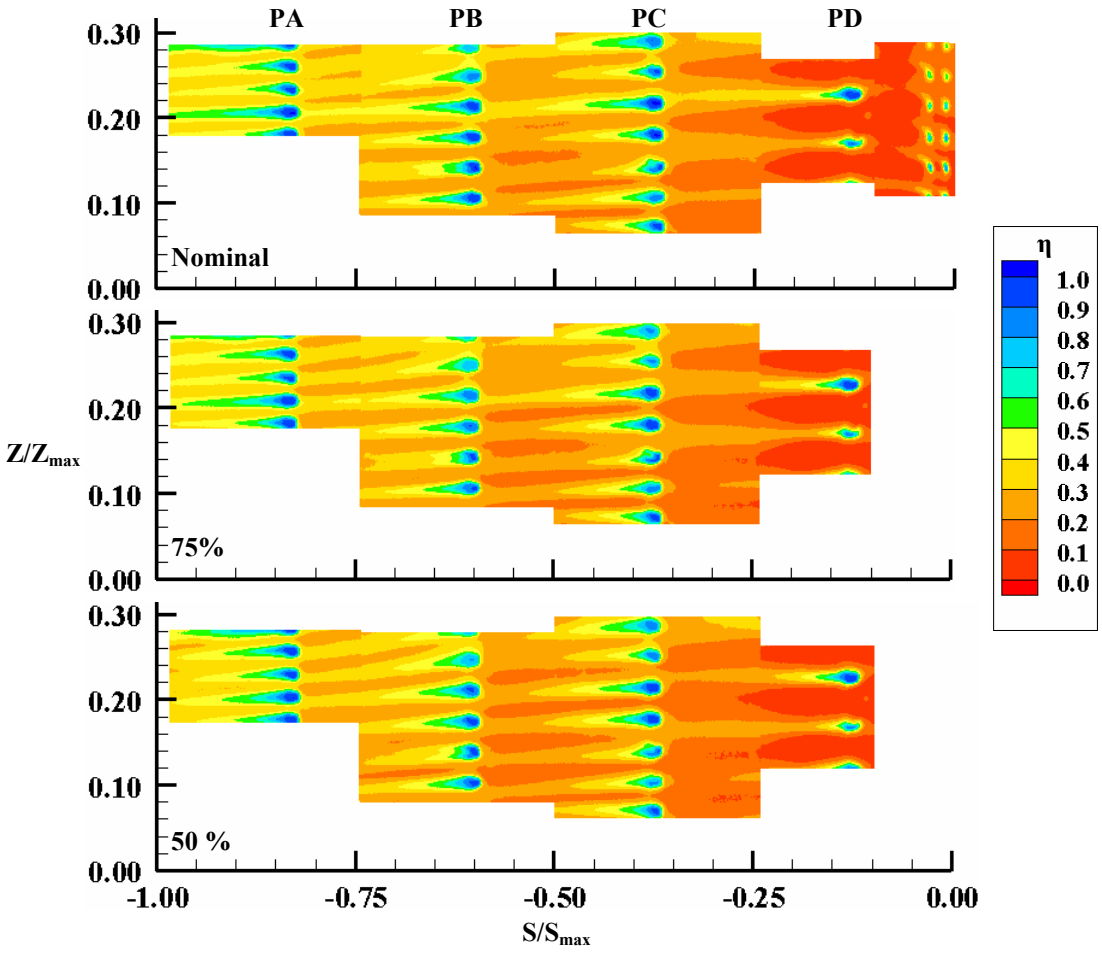

Figure 2.9. Pressure side experimental results.

blowing. The belief is that the upstream coolant caused increased turbulent mixing in the downstream jet (both laterally and normal to the surface). The enhanced mixing coupled with the upstream coolant caused better film-cooling jet diffusion and consequently more effective surface cooling. Figure 2.11 shows the single row data from Colban et al. [8] plotted with the multi-row data for the nominal case. The multi-row data has overall much higher η, which became increasingly pronounced with surface distance. The increase in η from single row cooling to multi-row cooling is due to a combination of two effects. First, the upstream coolant filled in the gaps or spaces between the downstream rows, leading to a greater cooled surface area. Secondly, as mentioned before, the upstream film-cooling makes the downstream row more effective by increasing the amount of turbulent mixing and reducing the normal momentum. This was particularly evident for row PD, which separated from the surface for both the single row and multi-row tests. The difference however, was that the amount of lift-off was significantly

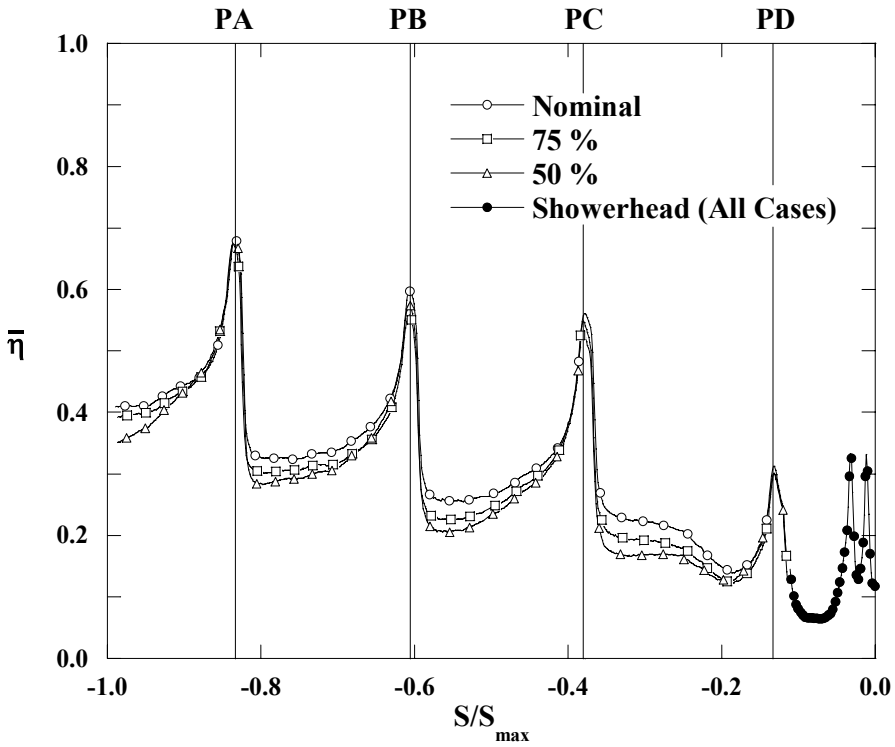

Figure 2.10. Experimental laterally averaged adiabatic film-cooling effectiveness on the pressure side.

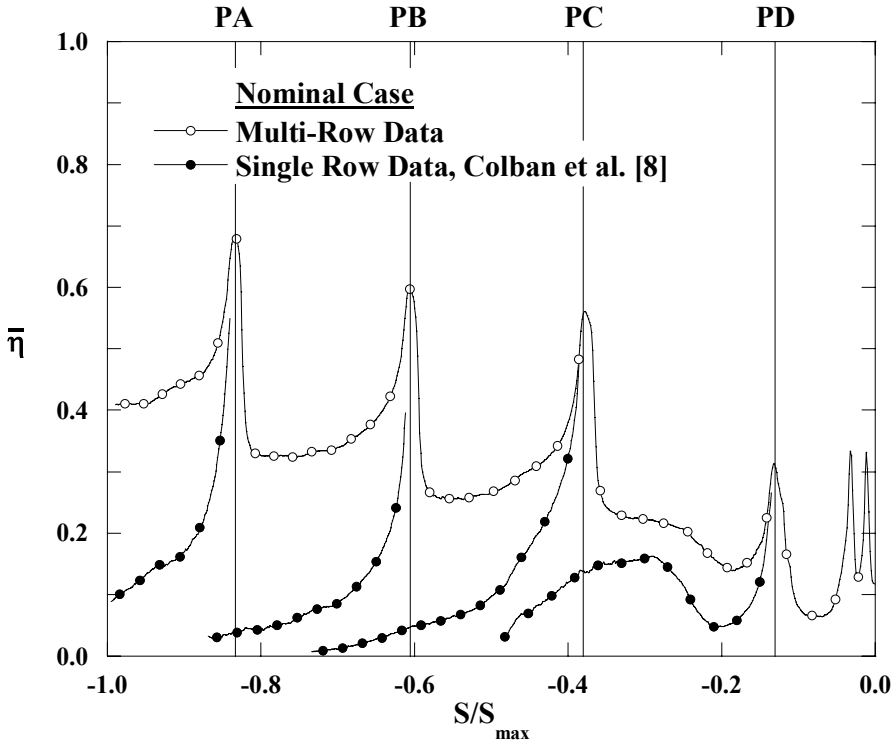

Figure 2.11. Comparison of multi-row and single row data on the pressure side at nominal conditions.

reduced for the multi-row cases, indicating that the upstream showerhead blowing had the effect of keeping the jets attached to the surface. This finding was consistent with the flat-plate study of Goldstein et al. [9] and the airfoil study of Polanka et al. [13], both of which used cylindrical holes.

Computational film-cooling effectiveness contours are shown in Figure 2.12 for the pressure side. Results from both turbulence models show a spanwise skewness in jet trajectory for row PD (row PC as well for the v^2-f model). This directionality was caused by the orientation of the showerhead cooling. However, the experimental results did not indicate a directional influence from the showerhead on the downstream rows (Figure 2.9).

Differences between the two models show that the RNG k-ε predictions were more accurate in terms of the overall level of film-cooling effectiveness. However, the RNG k-ε prediction showed a wider coolant footprint than the experimental results, while the v^2-f predictions showed a much narrower coolant footprint downstream of the hole. Another physical trend shown by the v^2-f that was not picked up by the RNG k-ε prediction was the spreading of the coolant downstream of the first fan-shaped row due to

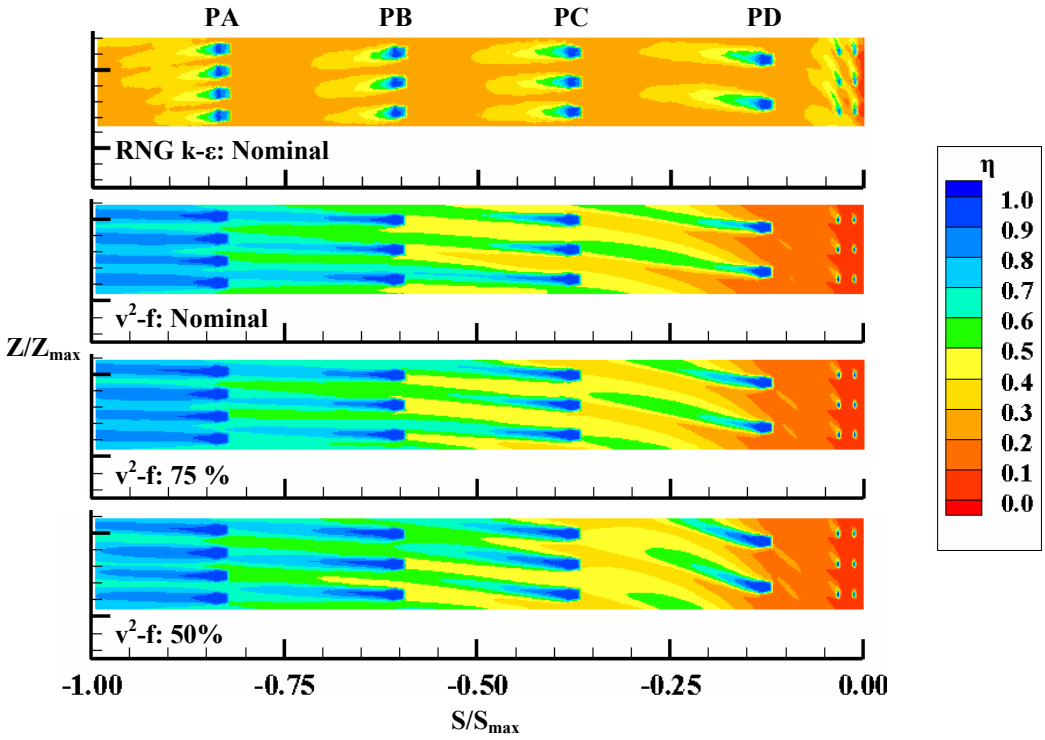

Figure 2.12. CFD contours for the pressure side.

lift-off and reattachment. Neither model accurately predicted the showerhead behavior. The RNG k-ε model under-predicted the showerhead lift-off, while the v^2-f model over-predicted the amount of lift-off in the showerhead region. Perhaps the deficiency in the v^2-f model lies in the spanwise fluctuations. The lateral spreading of the cooling jets downstream of the hole exit was not predicted correctly by the v^2-f model, which led to a gross over-prediction of film-cooling effectiveness.

A comparison of laterally averaged effectiveness at nominal conditions between the experimental results and both computational models is shown in Figure 2.13. Again, the RNG k-ε model more accurately predicted the overall levels of η, while the v^2-f model grossly over-predicted η on the pressure side. It is interesting to note that the v^2-f model predicted a continual rise in effectiveness, indicating a build-up of coolant from upstream rows. The RNG k-ε model however, showed no row-to-row increase in effectiveness, which can be seen not only in the laterally averaged values of Figure 2.13, but in the contour of Figure 2.12.

The difference in behavior between the two models in the near leading edge region can be seen by examining the streamlines. Streamlines for the nominal blowing

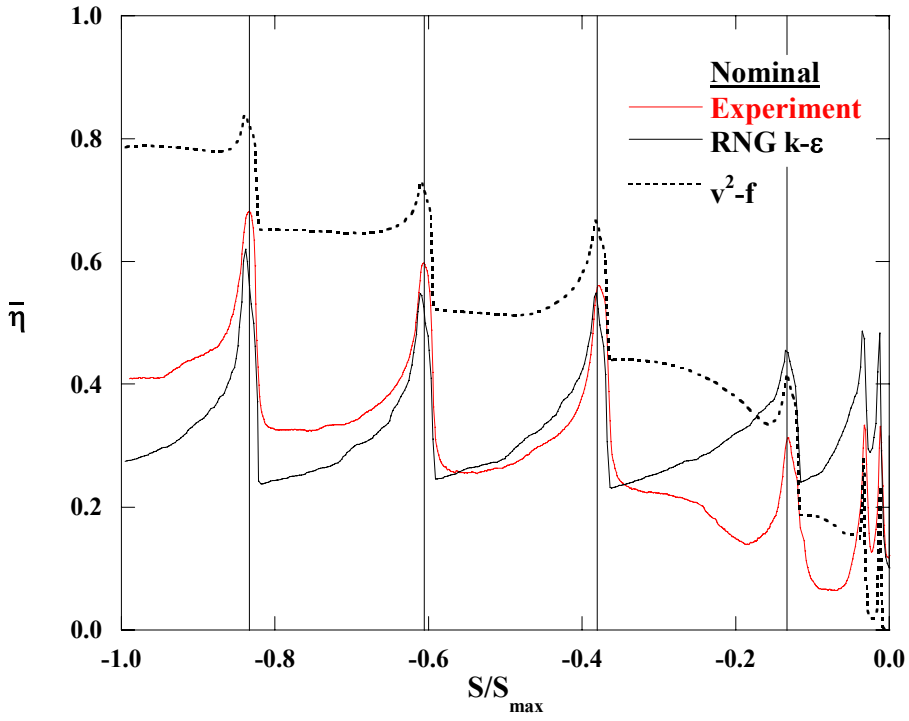

Figure 2.13. Pressure side comparison of laterally averaged film-effectiveness with computations.

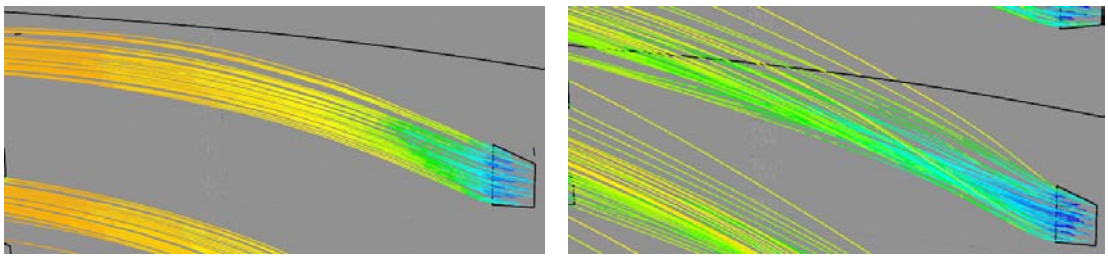

a) b)

Figure 2.14. Streamlines near the leading edge for (a) RNG k-ε and (b) v^2-f models at nominal conditions.

conditions are shown in Figure 2.14 for both turbulence models. The RNG k-ε model showed the streamlines stay attached to the surface with little lateral spreading, while the v^2-f model showed greater lateral spreading after an initial jet lift-off. Also, the skewness in the jets for both models was illustrated by the streamlines as a compound effect from the showerhead film-cooling, which had a 90º compound angle with respect to the main flow.

Suction Side

Contours of η are shown for the experimental results on the suction side in Figure 2.15. Significant showerhead lift-off occurred, as on the pressure side, causing poor leading edge region cooling. The jets on the first two suction side rows (SA and SB) separated from the surface at high blowing ratios due to the high curvature and acceleration in that region. Overall, η increased with surface distance from the stagnation line on the suction side, as seen from the laterally averaged η values in Figure 2.16. Near the leading edge, η decreased with blowing ratio because of the jet separation. However, as we progress along the suction side, the curvature decreases, and the amount of lift-off consequently also decreases. This led to a reversal in trend of η with blowing rates by the end of the suction side.

The effect of multiple cooling rows as opposed to the single row results of Colban et al. [8] for the nominal flow conditions are shown in Figure 2.17. In contrast to the pressure side, where showerhead lift-off also occurred, the effect of the showerhead on the first suction side row was not as significant. On the suction side, the separated showerhead coolant could not remain close enough to the surface to have an effect on the

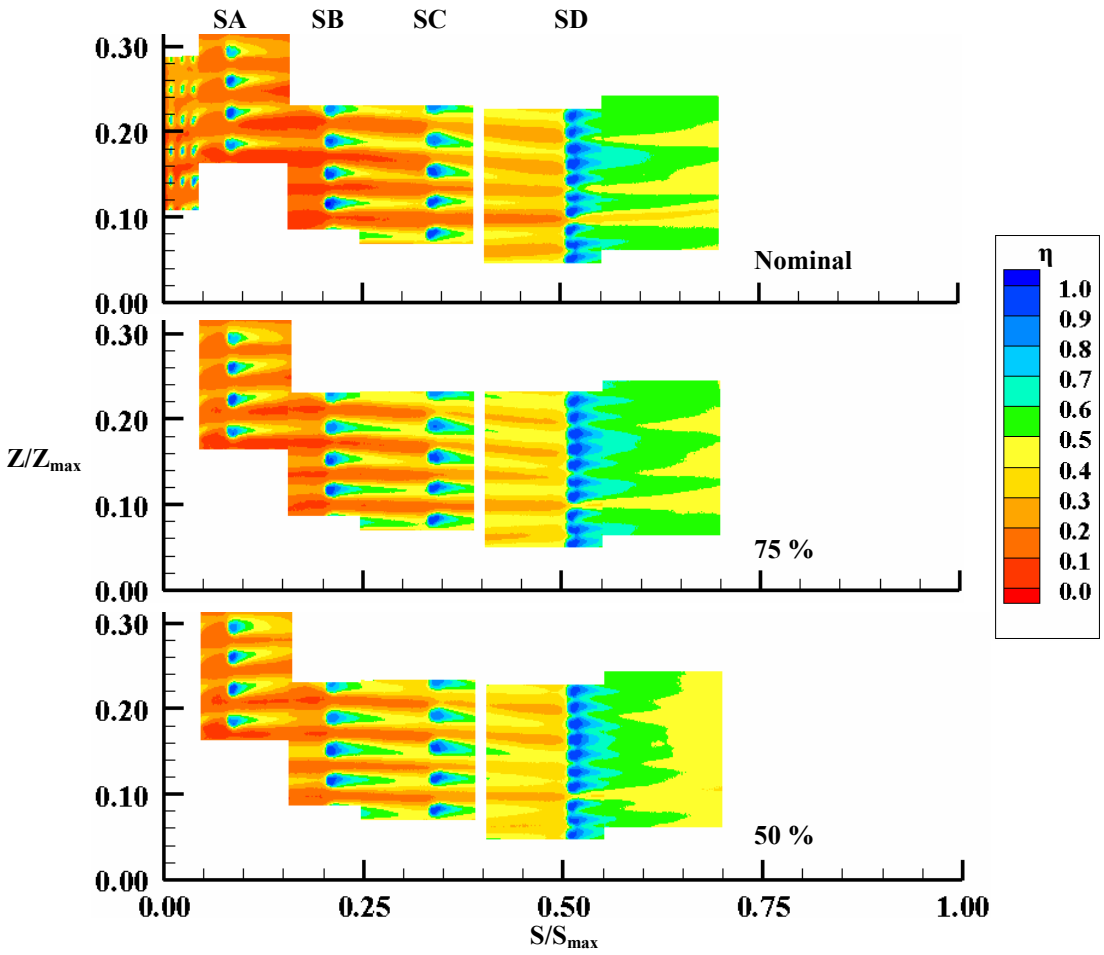

Figure 2.15. Experimental results on the suction side.

downstream rows because of the severe surface curvature. Row SB and SC show a more significant effect of upstream cooling, with results mirroring the trends observed on the pressure side. Further downstream, row SD showed little effect of upstream cooling. This was because of the extremely close hole spacing for row SD, there was no room for extra coolant between the holes.

Contours of η are shown in Figure 2.18 for the CFD results on the suction side. Just as row PD on the pressure side, row SA was directionally influenced by the showerhead cooling. The v^2-f results mimic the experimental results near the leading edge in that they also predicted lift-off for the first two rows of fan-shaped holes, and that lift-off also increases with blowing ratio. The v^2-f model also closely predicts the amount of lift-off in the showerhead region. Again, as on the pressure side, the lateral spreading of the v^2-f model was not predicted correctly, which led to a severe over-prediction of

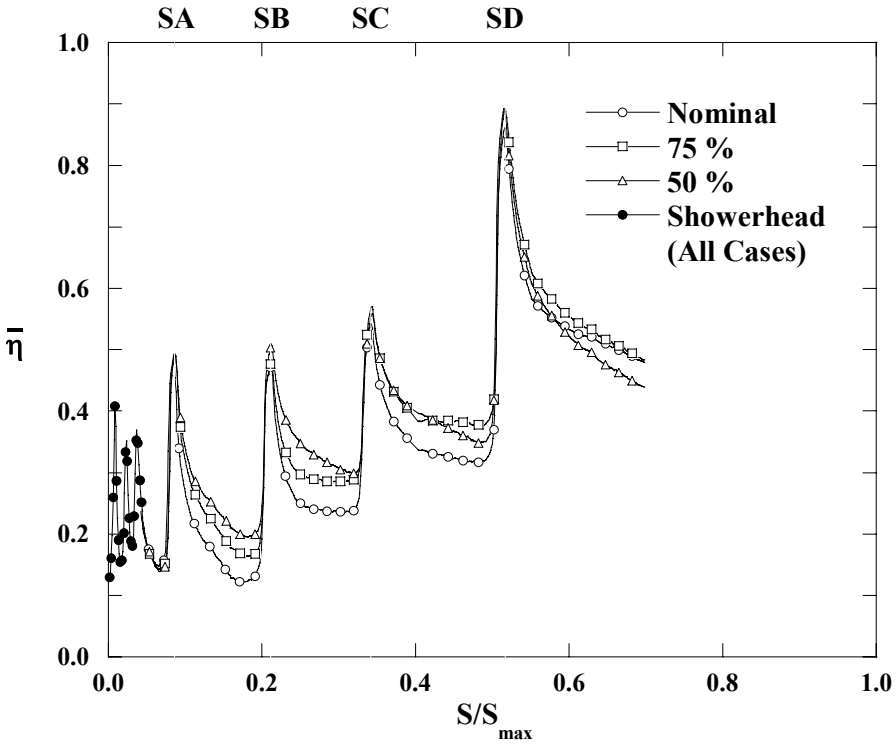

Figure 2.16. Experimental laterally averaged adiabatic film-cooling effectiveness on the suction side.

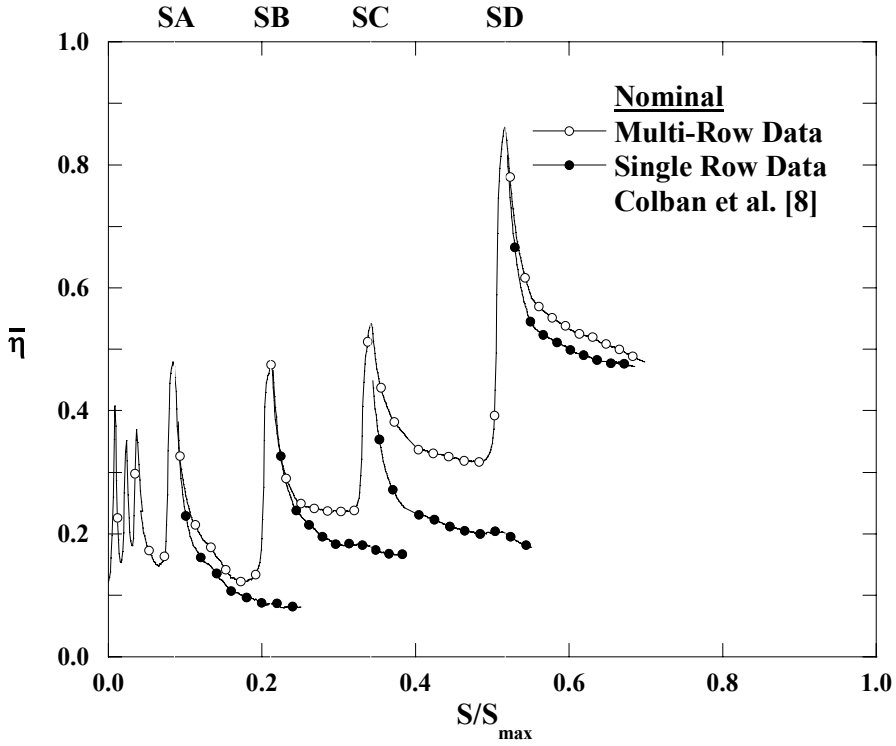

Figure 2.17. Comparison of multi-row and single row data on the suction side at nominal conditions.

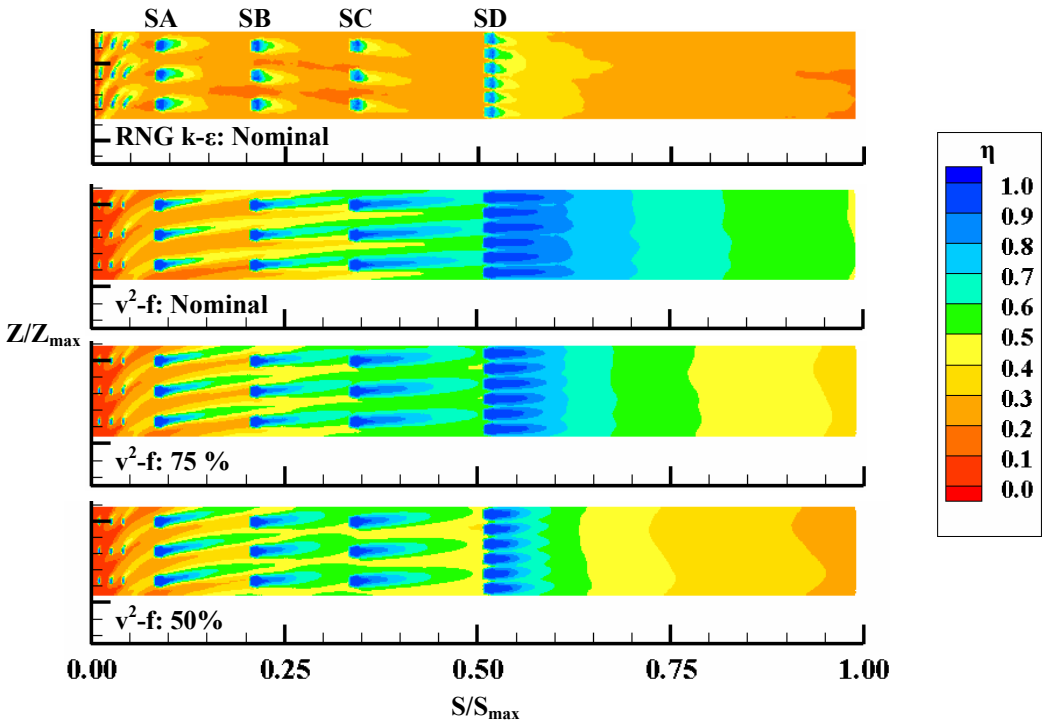

Figure 2.18. CFD contours for the suction side.

film-cooling effectiveness. As shown in the laterally averaged η values for the nominal case in Figure 2.19, the RNG k-ε model exhibits a much faster decay in η downstream of the attached fan-shaped rows than was measured in the experiments. On the other hand, the v^2-f model exhibits more lateral spreading of the attached jets than was measured experimentally, leading to less decay in η with distance downstream. The streamlines on the suction side (Figure 2.20) also show the greater lateral spreading of the fan-shaped holes predicted by the v^2-f model as compared to the RNG k-ε model.

Conclusions

This study presented a detailed experimental and computational investigation of film-cooling on a gas turbine vane with fan-shaped holes. Multi-row data was presented at a range of engine representative blowing ratios on both the pressure and suction sides, and compared to CFD predictions using both the RNG k-ε and v^2-f turbulence models.

Experiments showed that on the pressure side the showerhead blowing was not very effective, with excessive lift-off leading to little cooling in that region. Downstream, the first pressure side fan-shaped row exhibited lift-off and reattachment, as evidenced by

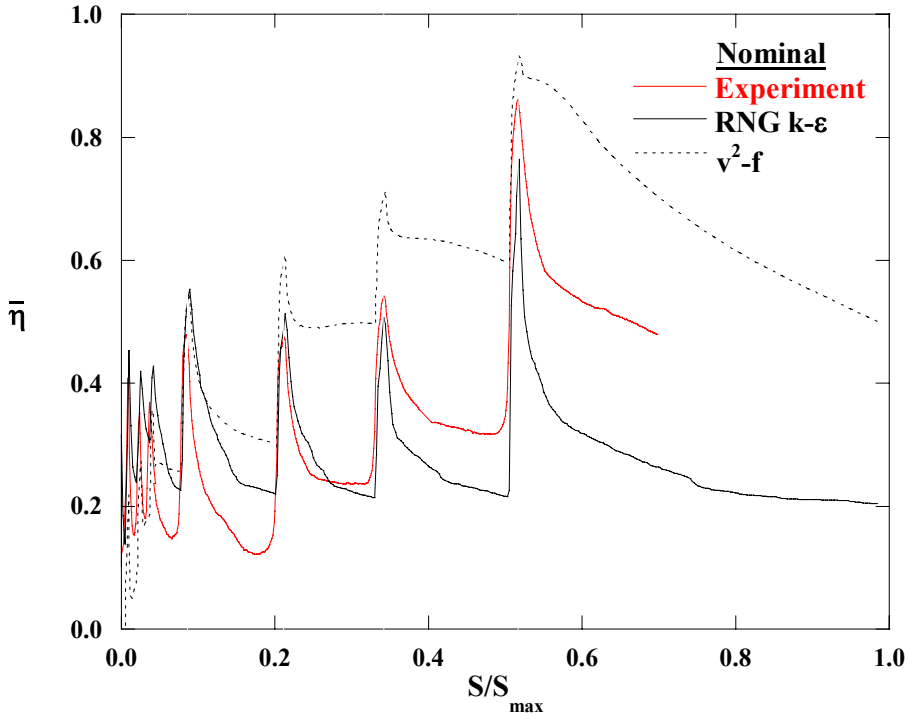

Figure 2.19. Suction side comparison of laterally averaged film-effectiveness with computations.

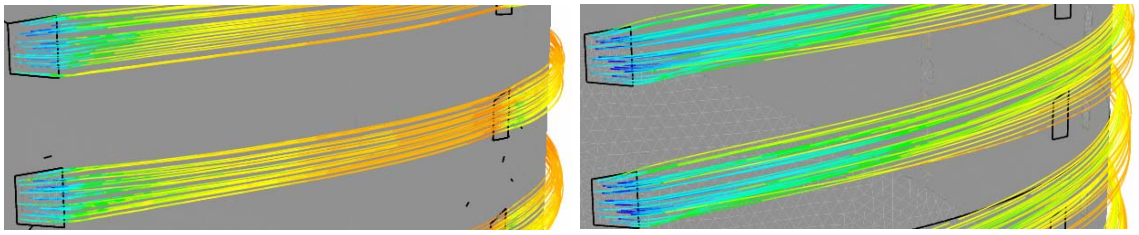

Figure 2.20. Streamlines near the leading edge for (a) RNG k-ε and (b) v^2-f models at nominal conditions.

a narrowing and widening in jet contours, although the lift-off was not as significant as the single row case. Overall, η levels increased on the pressure side with both surface distance and blowing ratio.

Showerhead blowing was also relatively ineffective on the suction side, again exhibiting substantial lift-off and low film-cooling effectiveness. In the near leading edge region of high curvature on the suction side, jet lift-off was accentuated by blowing ratio yielding much lower levels of η at high blowing rates.

The CFD predictions did not agree well with the experimental results for the most part, at best capturing either the correct η levels or some of the correct physics, but not both. The v^2-f model more nearly predicted the actual flow physics in terms of separation, however it had difficulty in accurately predicting the lateral spreading correctly leading of over-predictions of film-cooling effectiveness. The RNG k-ε model, on the other hand, offered a better match with the experimental data in terms of correct effectiveness levels. Although there have been matching CFD predictions for flat plate film-cooling, clearly more advances in CFD turbulence modeling are required before the highly complex flow of film-cooling on a gas turbine vane can be modeled accurately.

Acknowledgments

The authors are grateful to Siemens Power Generation for their funding and support of this project.

Nomenclature

A	area
C	vane true chord
C_D	discharge coefficient
D	film-cooling hole diameter
f	elliptic relaxation function
k	turbulent kinetic energy
k_{cond}	thermal conductivity
$\dot{m}$	mass flow rate
M	blowing ratio using local velocity, $M = m_c/A_h U_{local} \rho_{in}$
M_∞	blowing ratio using inlet velocity, $M_\infty = m_c/A_h U_{in} \rho_{in}$
P	hole spacing measured normal to streamwise direction
P	vane pitch
Re	Reynolds number, $Re = U_{in} C/\nu$
s	equivalent slot width, $s = A_{break}/P$
S	distance along the vane surface
t	hole breakout width

T temperature

U velocity

v^2 normal velocity fluctuations

X distance downstream of the hole exit

y^+ wall coordinate

Z distance measured along the vane span

Greek

α inclination angle

β compound angle

ε eddy viscosity, surface emmissivity

μ_t turbulent viscosity

ν kinematic viscosity

η adiabatic film-cooling effectiveness, $\eta = (T_\infty - T_{ad})/(T_\infty - T_c)$

ρ density

φ_1 lateral diffusion angle

φ_2 forward expansion angle

Subscripts

ad adiabatic

break hole breakout area

c coolant

exit hole exit

h metering area of film-cooling holes based on D

in inlet condition

local local conditions

max maximum

plenumplenum conditions

surf surface

∞ freestream conditions

References

[1] R. J. Goldstein, E. R. G. Eckert, and F. Burggraf, "Effects of Hole Geometry and Density on Three-Dimensional Film Cooling," ASME Journal of Heat and Mass Transfer, vol. 17, pp. 595-607, 1974.

[2] P. A. Durbin, "Near-Wall Turbulence Closure Modeling Without 'Damping Functions'," Theoretical and Computational Fluid Dynamics, vol. 3, pp. 1-13, 1991.

[3] D. M. Kercher, Film-Cooling Bibliography: 1940-2002: Private publication, 2003.

[4] D. M. Kercher, Film-Cooling Bibliography Addendum: 1999-2004: Private publication, 2005.

[5] R. S. Bunker, "A Review of Shaped Hole Turbine Film-Cooling Technology," ASME Journal of Heat Transfer, vol. 127, pp. 441-453, 2005.

[6] L. Zhang, M. Baltz, R. Pudupatty, and M. Fox, "Turbine Nozzle Film-Cooling Study Using the Pressure Sensitive Paint (PSP) Technique," 99-GT-196, 1999.

[7] L. Zhang and R. Pudupatty, "The Effects of Injection Angle and Hole Exit Shape on Turbine Nozzle Pressure Side Film-cooling," 2000-GT-247, 2000.

[8] W. Colban, A. Gratton, K. A. Thole, and M. Haendler, "Heat Transfer and Film-Cooling Measurements on a Stator Vane with Fan-Shaped Cooling Holes," GT2005-68258, 2005.

[9] R. J. Goldstein, E. R. G. Eckert, H. D. Chiang, and E. Elovic, "Effect of Surface Roughness on Film Cooling Performance," ASME Journal of Engineering for Gas Turbines and Power, vol. 107, pp. 111-116, 1985.

[10] S. M. Guo, C. C. Lai, T. V. Jones, M. L. G. Oldfield, G. D. Lock, and A. J. Rawlinson, "The Application of Thin-Film Technology to Measure Turbine-Vane Heat Transfer and Effectiveness in a Film-Cooled, Engine-Simulated Environment," International Journal of Heat and Fluid Flow, vol. 19, pp. 594-600, 1998.

[11] J. E. Sargison, S. M. Guo, M. L. G. Oldfield, G. D. Lock, and A. J. Rawlinson, "A Converging Slot-Hole Film-Cooling Geometry Part 2: Transonic Nozzle Guide Vane Heat Transfer and Loss," 2001-GT-0127, 2001.

[12] M. Schnieder, S. Parneix, and J. von Wolfersdorf, "Effect of Showerhead Injection on Superposition of Multi-Row Pressure Side Film-Cooling with Fan Shaped Holes," GT2003-38693, 2003.

[13] M. D. Polanka, M. I. Ethridge, J. M. Cutbirth, and D. G. Bogard, "Effects of Showerhead Injection on Film Cooling Effectiveness for a Downstream Row of Holes," 2000-GT-240, 2000.

[14] H. Riess and A. Bölcs, "The Influence of the Boundary Layer State and Reynolds Number on Film-cooling and Heat Transfer on a Cooled Nozzle Guide Vane," 2000-GT-205, 2000.

[15] A. Kohli and K. A. Thole, "A CFD Investigation on the Effects of Entrance Crossflow Directions to Film-Cooling Holes," 32nd National Heat Transfer Conference, vol. 12, pp. 223-232, 1997.

[16] D. G. Hyams and J. H. Leylek, "A Detailed Analysis of Film Cooling Physics Part III: Streamwise Injection with Shaped Holes," 97-GT-271, 1997.

[17] T. Hildebrandt, W. Ganzert, and L. Fottner, "Systematic Experimental and Numerical Investigations on the Aerothermodynamics of a Film Cooled Turbine

Cascade with Variation of the Cooling Hole Shape Part II: Numerical Approach," 2000-GT-298, 2000.

[18] J. D. Ferguson, J. H. Leylek, and F. A. Buck, "Film Cooling on a Modern HP Turbine Blade Part III: Axial Shaped Holes," GT-2002-30522, 2002.

[19] J. D. Heidmann, A. J. Kassab, E. A. Divo, F. Rodriguez, and E. Steinthorsson, "Conjugate Heat Transfer Effects on a Realistic Film-Cooled Turbine Vane," GT2003-38553, 2003.

[20] S. Parneix, P. A. Durbin, and M. Behnia, "Computation of 3-D Turbulent Boundary Layers Using the V2F Model," Flow, Turbulence, and Combustion, vol. 60, pp. 19-46, 1998.

[21] P. A. Durbin, "Separated Flow Computations with the k-e-v2 Model," AIAA Journal, vol. 33, pp. 659-664, 1995.

[22] M. I. Ethridge, J. M. Cutbirth, and D. G. Bogard, "Scaling of Performance for Varying Density Ratio Coolants on an Airfoil with Strong Curvature and Pressure Gradient Effects," 2000-GT-239, 2000.

[23] R. J. Moffat, "Describing the Uncertainties in Experimental Results," Experimental Thermal and Fluid Science, vol. 1, pp. 3-17, 1988.

[24] K. S. Hermanson and K. A. Thole, "Effect of Inlet Conditions on Endwall Secondary Flows," Journal of Propulsion and Power, vol. 16, pp. 286-296, 2000.

[25] M. Gritsch, A. Schulz, and S. Wittig, "Adiabatic Wall Effectiveness Measurements of Film-Cooling Holes With Expanded Exits," ASME Journal of Turbomachinery, vol. 120, pp. 549-556, 1998.

[26] S. Ito, R. J. Goldstein, and E. R. G. Eckert, "Film Cooling of a Gas Turbine Blade," Journal of Engineering for Power, vol. 100, pp. 476-481, 1978.

Paper 3:
A Comparison of Cylindrical and Fan-Shaped Film-Cooling Holes on a Vane Endwall at Low and High Freestream Turbulence Levels

Submitted to the 2006 *ASME Turbo Expo*[*]

Abstract

Fan-shaped film-cooling holes have been shown to provide superior cooling performance to cylindrical holes along flat-plates and turbine airfoils over a large range of different conditions. Benefits of fan-shaped holes include less required cooling air for the same performance, increased part lifetime, and fewer required holes. The major drawback however, is increased manufacturing cost and manufacturing difficulty, particularly for the vane platform region.

To this point, there have only been extremely limited comparisons between cylindrical and shaped holes on a turbine endwall at either low or high freestream turbulence conditions. This study presents film-cooling effectiveness measurements on an endwall surface in a large-scale, low-speed, two-passage, linear vane cascade. Results showed that film-cooling effectiveness decreased with increasing blowing rate for the cylindrical holes, indicating jet lift-off. However, the fan-shaped passage showed increased film-cooling effectiveness with increasing blowing ratio. Overall, fan-shaped holes increased film-cooling effectiveness by an average of 75% over cylindrical holes.

* Co-authors: Dr. Karen A. Thole, Mechanical Engineering Department, Virginia Tech
Michael Haendler, Siemens Power Generation, Muelheim a. d. Ruhr, Germany

Introduction

The primary goal of turbine cooling research during the past years was to develop cooling methods in which the amount of coolant could be decreased with at least the same, if not better, cooling performance. Fan-shaped holes have provided this opportunity to engine designers by providing significantly better cooling performance compared to cylindrical holes over a large range in blowing ratios and other conditions. However, the main drawback in implementing fan-shaped holes into current engine designs comes from the manufacturing side. Fan-shaped holes are on the order of four to eight times more expensive to manufacture than cylindrical holes on a per hole basis, depending on the technique. Fan-shaped holes are generally made using the electro-discharge machining technique, which is much more expensive than the cheaper laser-drilling methods typically used to manufacture cylindrical holes.

The benefits of shaped hole cooling over cylindrical hole cooling for flat-plates and airfoils were reviewed by Bunker [1]. Lateral expansion of the coolant promotes a better coverage of surface area downstream of the hole. Exit momentum of the jet is reduced as a result of the hole expansion, which keeps the jet attached to the surface. Both of these benefits were illustrated by the flow visualization study of Goldstein et al. [2].

Although shaped cooling holes have been widely used on the airfoil surface, manufacturing difficulties have limited their use on the vane platform region. For this reason, the majority of endwall cooling studies have used cylindrical cooling holes. However, recent advances in manufacturing coupled with the desire for more efficient cooling, have allowed shaped holes to be used in the platform region. Unlike the majority of the airfoil surface, the endwall is a highly three-dimensional region, with intense secondary flows caused by the approaching boundary layer and cross-passage pressure gradient. This inevitably makes endwall film-cooling more challenging to design and to predict.

This study was spawned from the lack of research of shaped hole endwall film-cooling. It was necessary to directly compare the performance of shaped to cylindrical cooling holes, since cylindrical holes provide most of the current research. This study contained two separate vane passages, one with cylindrical endwall film-cooling holes,

and the other with shaped endwall film-cooling holes. A double row of staggered cylindrical film-cooling holes was located upstream of both passages. Comparisons were directly made based on matching coolant mass flow rates between the two passages. The effect of freestream turbulence was also investigated because today's gas turbines can have a range of different freestream turbulence levels exiting the combustor.

Past Studies

Film-cooling has been studied at great length over the past 50 years (Kercher [3], [4]). Excellent reviews of film-cooling research can be found in Goldstein [5], Bogard and Thole [6], and for shaped film-cooling holes by Bunker [1]. A fair amount of endwall film-cooling research has been done using slots and discrete cylindrical holes, however, only the studies by Vogel et al. [7], Vogel [8], and Barrigozzi [9] have employed shaped holes.

One of the main influences on endwall film-cooling is the passage vortex and subsequent cross passage flow. This tends to sweep the coolant away from the pressure side towards the suction side. This effect has been shown for upstream slot cooling by Blair [10], Granser and Schulenberg [11], Colban et al. [12], and Knost and Thole [13] and for cylindrical film-cooling holes by Harasgama and Burton [14] and Nicklas [15].

Not only does the endwall secondary flow affect the film-cooling, but the film-cooling also has an effect on the secondary flow field. Increased film-cooling has been shown to reduce the strength of the passage vortex, as well as reduce the amount of cross passage flow. This effect has been shown by Sieverding and Wilputte [16] and Kost and Nicklas [17] for endwall cooling injection and Colban et al. [18] for upstream slot injection from a backward-facing step.

Friedrichs et al. [19] studied cylindrical endwall cooling in a rig specially designed to generate stronger secondary flows in order to isolate the effect of the secondary flow field on endwall cooling. They identified barriers to the endwall coolant flow in the form of three-dimensional separation lines on the endwall formed by the secondary flow structures. Coolant ejected near these separation lines was swept off the endwall surface, providing little cooling benefit. However, cooling ejection farther from the secondary flow separation lines provided better cooling. They also reported that the

addition of film-cooling had an effect on the near wall secondary flow structures, redirecting the cross passage flow in the direction of the inviscid streamlines. Friedrichs et al. [19] also found that the coolant trajectories were in large part dictated by the direction of the near wall flow, not the ejection angle of the hole. The insensitivity of the jet trajectory to the hole orientation angle has also been verified by Knost and Thole [20].

Studies of double rows of staggered cylindrical holes upstream of the leading edge have been performed by Oke et al. [21], Zhang and Jaiswal [22], and Zhang and Moon [23]. Oke et al. [21] measured thermal and velocity profiles in the vane passage downstream of 45º holes. Their results showed jet lift-off just downstream of the holes, which resulted in high mixing of the jets with the freestream. Both Zhang and Jaiswal [22] (using 45º holes) and Zhang and Moon [23] (using 30º holes) showed that at low flow rates the majority of the coolant was swept away from the pressure side towards the suction side because of the cross passage flow. However, they found that at higher flow rates, the coolant ejection suppressed the endwall secondary flow, leading to both thermal and aerodynamic benefits.

To date, only the studies by Vogel et al. [7], Vogel [8], and Barigozzi et al. [9] have featured shaped hole film-cooling on the endwall. The first two studies were primarily focused on the development of a unique experimental technique. However, a number of conclusions can be made about the behavior of shaped cooling holes on an endwall from the images presented in that work. The lateral spreading of coolant typically seen on flat-plate and airfoil surfaces with fan-shaped film-cooling also occurred on the endwall. The coolant was still largely affected by the cross-passage flow, and was directed away from the pressure side towards the suction side. Also, jets that were located directly downstream of other coolant trajectories tended to provide the best film-effectiveness.

Barigozzi et al. [9] measured film-effectiveness, total pressure loss, flow field, and thermal field data for an endwall cooled with cylindrical holes and conical diffuser shaped holes. However, their comparison between cylindrical and conical shaped holes was not exact, since there were different hole patterns. Barigozzi et al. [9] showed that the size and vorticity of the passage vortex actually increased with decreasing film-cooling mass flow rates. As the flow rate increased above 1%, the passage vortex

diminished in size and strength until it was no longer recognizable. The endwall cross flow was also eliminated at the highest mass flow rate (MFR), resulting in a nearly uniform two-dimensional exit flow. This result was confirmed with the film-effectiveness measurements, which showed that at low flow rates the jets were deflected towards the suction side, while at high flow rates the jets followed the potential flow streamlines. At low flow rates the cylindrical holes performed slightly better than the conical shaped holes, because the lower momentum jets exiting the shaped holes were more affected by the secondary flows. However, at higher flow rates, the conical shaped holes provided much better cooling than the cylindrical holes, in part because of the increased coverage and reduced exit momentum.

Experimental Facilities

The experiments were performed in the Virginia Tech Experimental and Computational Convection Laboratory low-speed, large-scale, recirculating wind tunnel facility shown in Figure 3.1. The wind tunnel featured a flow split section, which divided the flow into three separate channels. The air in the center channel was heated by a 55 kW heater bank to simulate the combustor core flow, and then passed through a series of flow straighteners before entering the test section. The air in the two outer channels was cooled using heat exchangers supplied by a 44 kW chiller, and then used as supply coolant. The coolant was delivered to the endwall plenum by a 2 hp blower situated atop the wind tunnel. This process resulted in temperature differences between the coolant

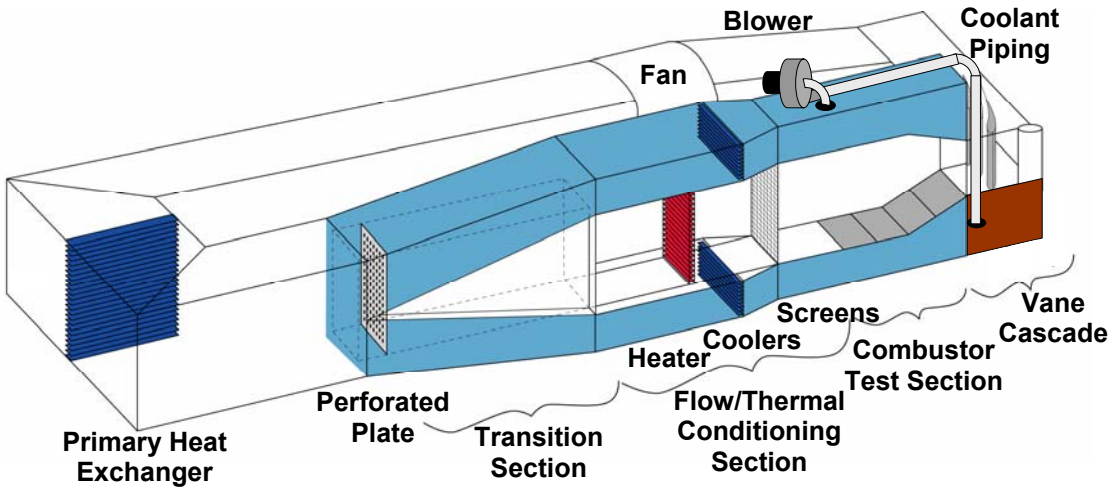

Figure 3.1. Schematic of the low-speed recirculating wind tunnel facility.

and mainstream of approximately 20ºC.

The Reynolds number based on true vane chord and inlet velocity was $3.4x10^5$ for all tests. Profiles of temperature and velocity were made upstream of each passage prior to testing to ensure periodicity amongst both passages. The tests were essentially incompressible, with a jet-to-freestream density ratio of approximately 1.06. The inlet turbulence intensity was measured at a location of X/C = -0.3 upstream of the test section with a hot wire anemometer. Turbulence intensity for the low freestream conditions was measured to be 1.2%. High freestream turbulence was generated using three 7.2 cm diameter normal jets in crossflow, which were located 2.7 chord lengths upstream of the vane leading edge. This resulted in 8.9% turbulence intensity with a length scale of $\Lambda_x/P = 0.15$. The approaching boundary layer thickness was also measured to be $\delta/Z_{max} = 0.12$ at a distance X/C = -0.3 upstream of the vane leading edge. A summary of important inlet conditions and geometrical parameters is given in Table 3.1.

Test Section Design

The two-passage linear vane cascade test section described in detail by Colban et al. [24] was used. A contoured upper endwall was designed to ensure the engine static pressure distribution around the vane surface was matched. It was critical to match the static pressure distribution around the vane surface, as the location of minimum static pressure has a significant effect on the development of the passage secondary flows. The pressure coefficient distributions around the vane at engine conditions and in the low speed facility both with and without the contour are shown in Figure 3.2. The contoured vane was aft-loaded, which leads to weaker secondary flows since the minimum driving pressure is further from the leading edge. Without the contoured endwall, the vane was

Table 3.1. Operating Conditions and Vane Parameters

Scale	3X
C (m)	0.53
$S_{max,PS}$ (m)	0.52
$S_{max,SS}$ (m)	0.68
U_{in} (m/s)	10
Re_{in} (-)	3.4×10^5
ΔT_{FC} (ºC)	20
Vane Pitch (m)	0.465

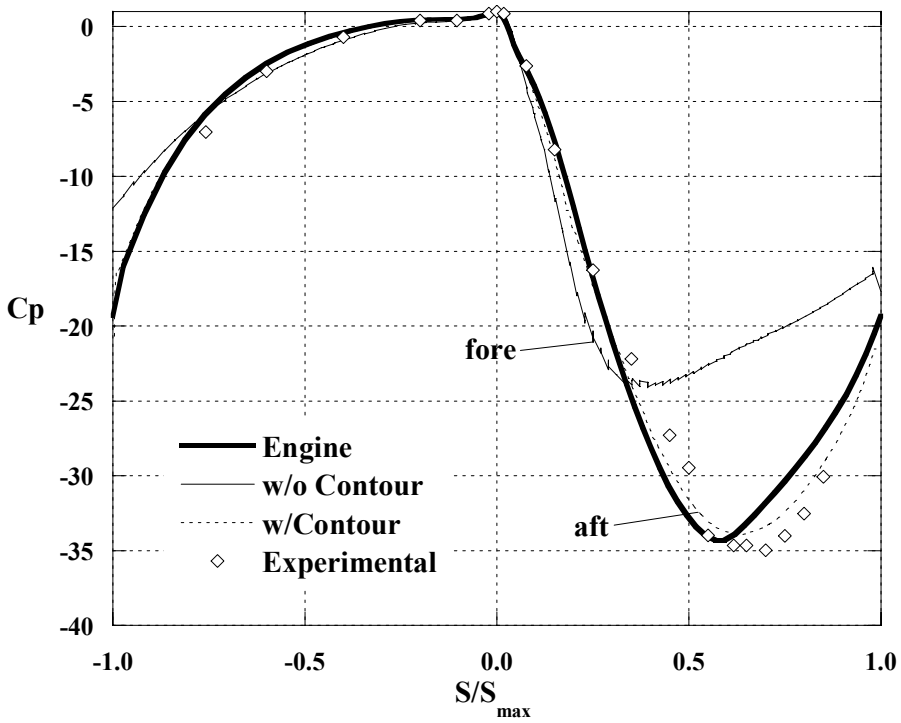

Figure 3.2. Static pressure distribution around the center vane.

more fore-loaded, which tends to strengthen the secondary flow structures because of a larger driving pressure difference in the passage. Clearly with the contoured endwall, the pressure distribution around the vane was very similar to the engine conditions, which led to closely simulated engine representative secondary flows in the vane cascade.

Some modifications to the previously described [24] test section were made. A film-cooled endwall surface was placed on the lower flat platform, and a feed plenum was constructed below. The inner passage of the cascade featured cylindrical holes, while the outer passage featured fan-shaped holes. Figure 3.3 shows the hole layout on the endwall, including the two rows of staggered cylindrical holes that were placed upstream of each passage. The layout of the film-cooling holes was identical for each passage, which allowed a direct comparison of the respective cooling performance of each hole geometry.

The endwall was constructed from medium density foam with a low thermal conductivity (k = 0.028 W/m·K) to allow adiabatic film-cooling effectiveness measurements and it was manufactured using a five-axis water jet cutting machine. The relevant geometrical parameters of the film-cooling holes are summarized in Table 3.2. All of the holes had a cylindrical diameter of 0.26 ± 0.015 cm. The two upstream rows of

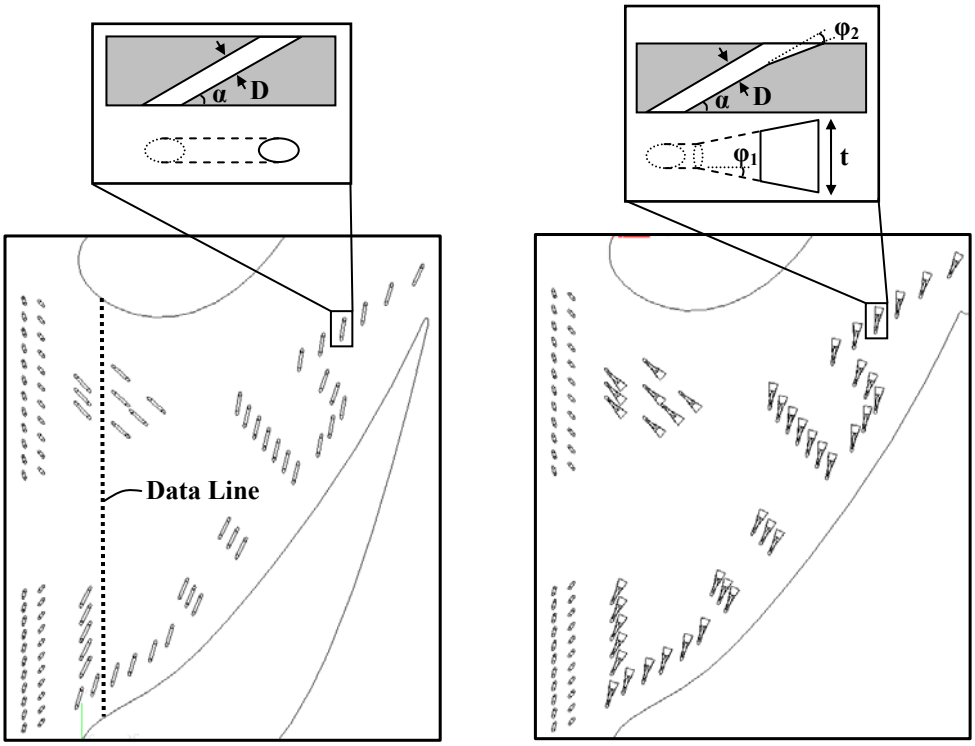

Figure 3.3. Film-cooling hole layout and specifications.

Table 3.2. Film-Cooling Hole Parameters

	Upstream	Cylindrical	Shaped
D (cm)	0.26±0.015	0.26±0.015	0.26±0.015
α (º)	60	35	35
φ_1 (º)	0	0	10
φ_2 (º)	0	0	10

holes had a surface angle of 60º, while the holes in the passage had a surface angle of 35º. The fan-shaped holes had both a 10° lateral and forward expansion angle. The vane-endwall junction was fitted with an elliptical manufacturing fillet, which extended out a distance of 10D normal to the vane surface and to a span height of 12D normal to the endwall surface.

Each passage could be sealed off from below, so that it was possible to provide film-cooling to a single passage individually. This allowed for the total coolant flow rate to be measured directly with a laminar flow element (LFE) placed upstream of the plenum. Coolant flow rates are reported in this study in terms of percent coolant mass flow rate per total passage mass flow rate for one vane pitch (MFR).

Surface temperature measurements were taken for each passage using an IR camera positioned atop the test section. The IR camera was perpendicular to the surface for five of the seven images required to capture the complete endwall. The remaining two pictures were taken at an angle with respect to the surface, which required a linear surface transformation for those images. The IR camera provided an image resolution of 240x320 pixels, while the spatial resolution of the camera was approximately 0.72 mm/pixel (0.28D) at the measurement distance.

A one-dimensional conduction correction, described by Etheridge et al. [25], was applied to the film-effectiveness measurements to obtain the final adiabatic film-cooling effectiveness. This method involved measuring the endwall surface effectiveness with coolant inside the plenum but no blowing and using those values to correct the ultimate measured values of film-cooling effectiveness. The uncooled effectiveness ranged from 0.06 to 0.15 with the highest values occurring near the entrance to the passage.

Experimental Uncertainty

The partial derivative and sequential perturbation method given by Moffat [26] was used to calculate uncertainties for the measured values. For the nominal case with MFR = 0.73%, the uncertainty was calculated to be ± 0.0024% for the cylindrical passage at low freestream turbulence. The uncertainties for the adiabatic effectiveness measurements were ± 0.012 for a high value of $\eta = 0.9$ and ± 0.011 for a low value of $\eta = 0.2$.

Test Design

This study was designed to independently investigate the effect of three separate variables; (1) coolant flow rate, (2) cooling hole shape, and (3) freestream turbulence intensity. The test matrix for this study is shown in Table 3.3, and contained a total of 12

Table 3.3. Test Matrix for Endwall Cases (shaded values are nominal operating conditions)

	Cylindrical MFR			Fan-Shaped MFR		
TI=1.2%	0.55%	0.73%	0.93%	0.54%	0.73%	0.92%
TI=8.9%	0.56%	0.73%	0.93%	0.55%	0.74%	0.92%

cases. The mass flow rates were representative of engine conditions and are reported in terms of MFR. Keep in mind that in actual engines both the inner and outer shrouds would be film-cooled, so the values shown in Table 3.3 are representative of approximately half of the actual coolant rates. Nominal conditions were defined by the shaded values of Table 3.3, and will be used as the baseline to show effectiveness augmentations for both an increase and decrease in MFR.

Local inviscid blowing ratios and local inviscid momentum flux ratios were computed for each hole. Local values mean that the local velocity in the freestream was used in the scaling. An inviscid calculation was used to compute the coolant exit velocity using the measured plenum-total to inlet-static pressure difference, along with the static pressure distribution on the endwall from a 3D CFD prediction without film-cooling in FLUENT 6.1.2. Local freestream velocities on the endwall were also calculated using the CFD static pressure distribution, and the mainstream and coolant densities were measured during testing. The resulting blowing ratios and momentum flux ratios are presented in the form of contours shown in Figures 3.4a and b for the nominal MFR = 0.73% conditions, with the hole locations outlined as well. Figures 3.4a and b are essentially design maps, showing the resulting blowing ratio at any location on the endwall. As expected, blowing ratios are highest at the inlet to the passage, especially near the stagnation point, where the freestream velocity is lowest. Fairly uniform blowing ratios of approximately M = 3.0 are seen in the two upstream rows nearest the

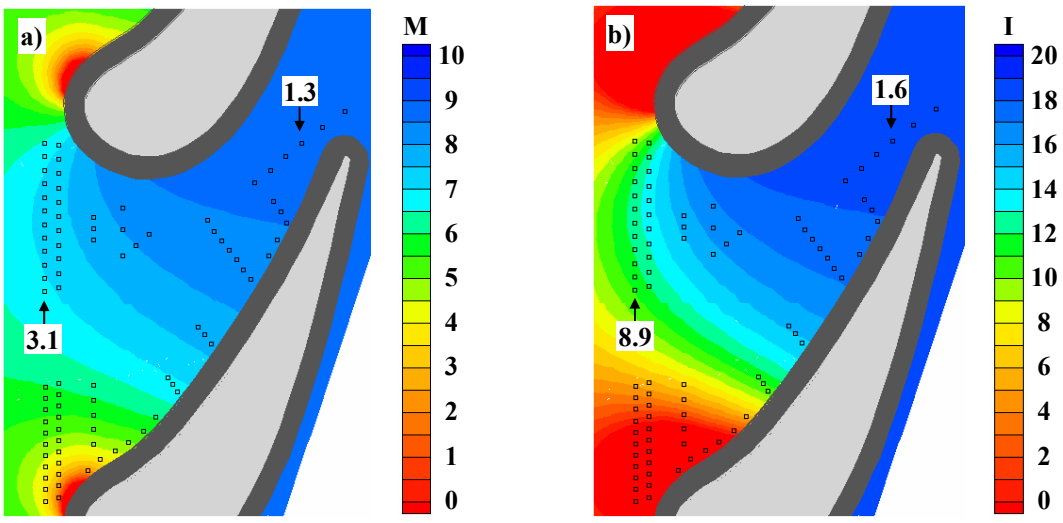

Figure 3.4. Contours of calculated (a) blowing ratio and (b) momentum flux ratio for nominal MFR = 0.73% conditions.

suction side, while the blowing ratios on the two upstream rows nearest the pressure side vary from M = 2.8 to M = 5.9. The blowing ratios for the majority of the holes in the passage are less than 2.0, as the flow accelerates to nearly five times the inlet velocity in the throat region.

Experimental Results

Results are presented in terms of adiabatic film-cooling effectiveness. Contours are shown in Figures 3.5a-f for the low freestream turbulence cases and in Figures 3.6a-f for the high freestream turbulence cases. Analysis plots of laterally-averaged and area-averaged effectiveness are also given along with film-effectiveness augmentation plots of laterally-averaged effectiveness, which show the effects of blowing ratio, hole shape, and freestream turbulence.

Cylindrical Holes at Low Freestream Turbulence

The adiabatic effectiveness contours for the cylindrical passage at low freestream turbulence are shown in Figures 3.5a-c. Overall, effectiveness levels were very low, especially in the region downstream of the double rows of holes at the entrance to the passage, which had a steeper surface angle than the passage holes (60º as opposed to 35º for the passage). Nearly all of the cooling flow from those two rows lifted off the surface, which is not surprising considering that blowing ratios for these holes ranged from 2.8 to 5.9. Only for the lowest flowrate (MFR = 0.55%), were slight cooling footprints visible downstream of the double cylindrical rows.

The row of pressure side holes running along the edge of the fillet just downstream of the leading edge separated completely. Blowing ratios for the holes in that region were extremely high between M = 3.9 and 8.5 (see Figure 3.4a), which is well above the range for cylindrical jet attachement.

The majority of the cooling footprints showed individual jets, indicating that there was not good lateral spreading downstream of most of the cylindrical holes. Most of the holes had a hole-to-hole spacing of greater than five hole diameters, which is generally too large to show significant jet merging. The exception was the first row of holes on the pressure side (X/C = 0), which seemed to have relatively good lateral spreading despite a

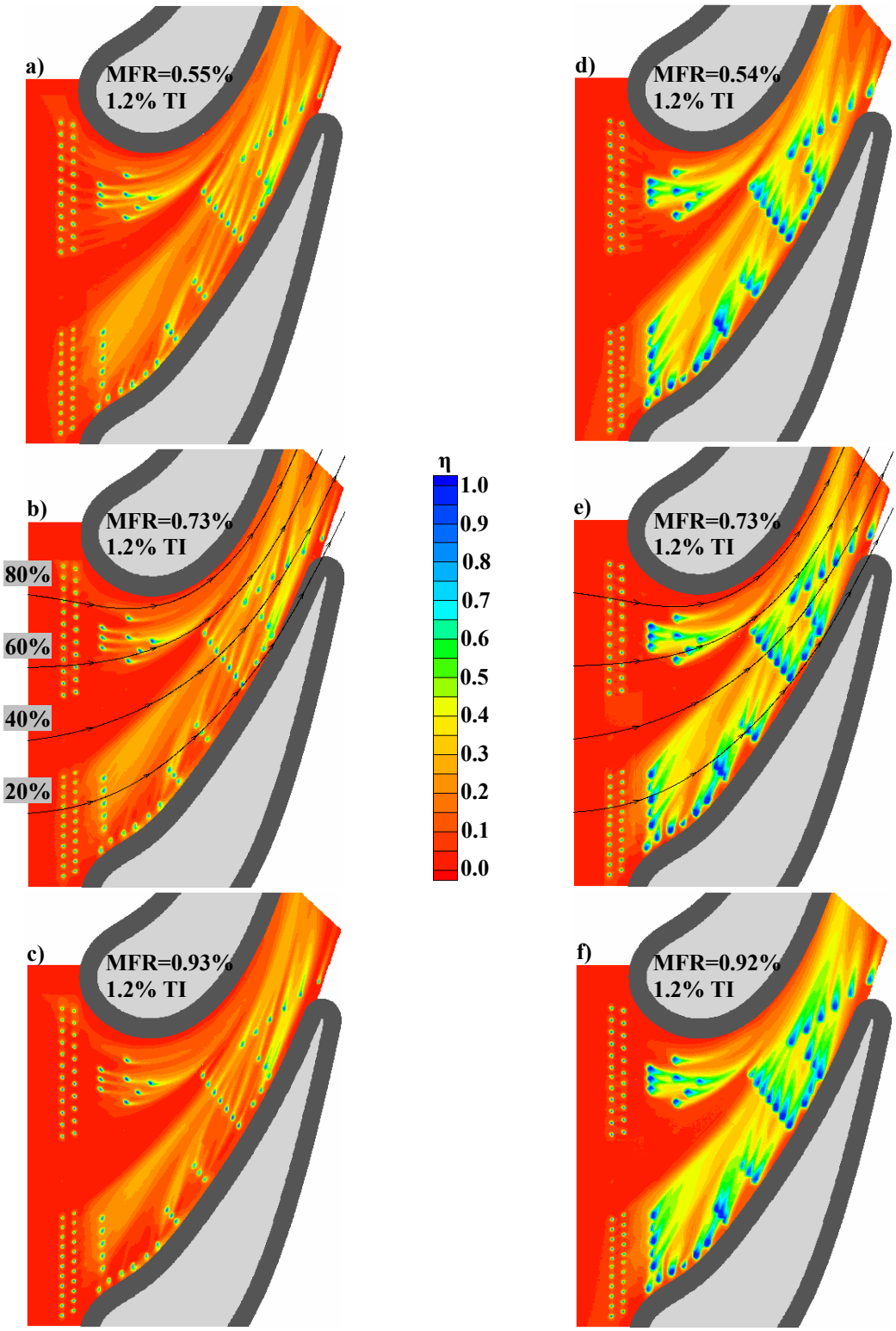

Figure 3.5. Effectiveness contours at low freestream turbulence for the cylindrical passage (a-c) and fan-shaped passage (d-f).

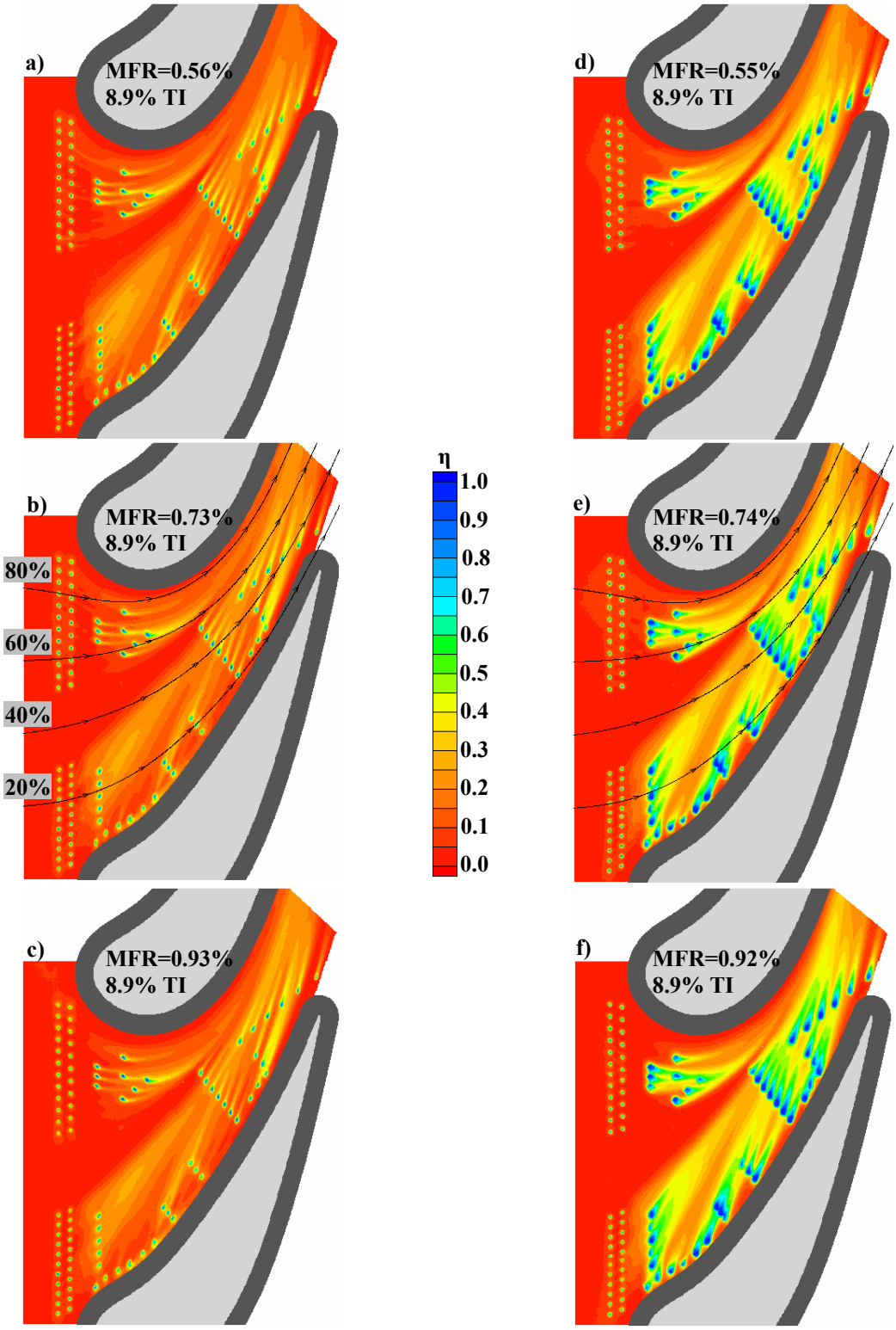

Figure 3.6. Effectiveness contours at high freestream turbulence for the cylindrical passage (a-c) and fan-shaped passage (d-f).

hole-to-hole spacing of 6.2. This spreading was perhaps due to the effect of the upstream double row of holes.

Holes placed directly upstream of other holes seemed to increase the cooling benefit from that downstream hole. This phenomenon has been seen on the vane surface in the near pressure side region as well by Colban et al. [27], where the upstream cooling prevented the natural jet lift-off that would occur otherwise.

Streamlines are shown for the nominal contour in Figure 3.5b. The streamlines were calculated from the velocity vectors at 2% span from a 3D CFD computation in FLUENT 6.1.2. Near the suction side, the holes were clearly swept in the direction of the streamlines, despite their orientation angles towards the pressure side. This partially confirms the observances of Friedrichs et al. [19] and Knost and Thole [20] that the coolant trajectories of the film-cooling holes are primarily dictated by the near-wall streamlines and not by the hole orientations. However, near the pressure side region, the orientation angles of the holes were in the direction of the cross passage pressure gradient, and not in line with the streamline. The coolant in this case followed the orientation angle direction and not the near-wall streamline direction. These results seem to modify the suggestions of the previous studies, such that the injected coolant will follow the near-wall streamline direction unless it is oriented in the direction of the cross-passage pressure gradient.

To quantify the development of the coolant through the passage, and examine the effect of MFR on effectiveness, pitch-wise lateral averages were done for each data set. Figure 3.7 shows $\overline{\eta}$ for the nominal (MFR = 0.73%) cylindrical case at low freestream turbulence. The two spikes in $\overline{\eta}$ were caused by the leading edge rows, but overall the leading edge rows had very little effect on increasing $\overline{\eta}$. Beginning at X/C = 0.0, there was a continual increase in $\overline{\eta}$ throughout the passage by the addition of coolant from each successive row.

Also shown in Figure 3.7 is the augmentation in $\overline{\eta}$ for the MFR = 0.93% and MFR = 0.55% cases relative to the MFR = 0.73% case. It is immediately evident that better cooling performance was achieved at the lower mass flow rate, with a continual decrease in $\overline{\eta}$ with increased blowing. This was a result of jet lift-off from the

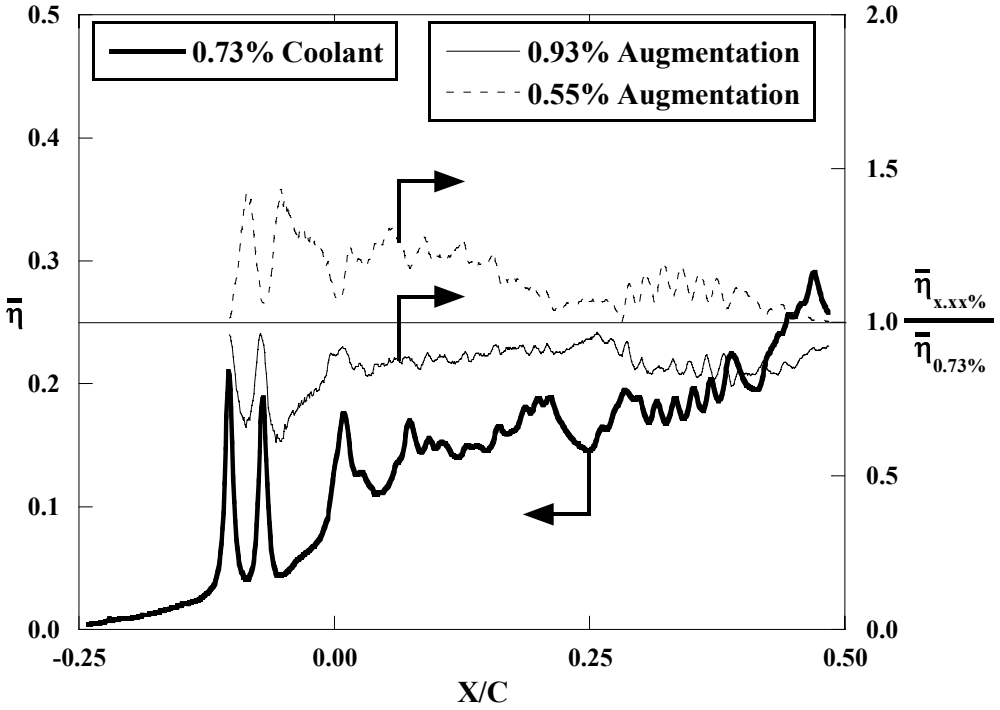

Figure 3.7. Laterally averaged effectiveness for the 0.73% case and augmentation of laterally averaged effectiveness for the 0.55% and 0.93% cases on the cylindrical passage.

cylindrical holes. The same trend of increased cylindrical jet lift-off with increased blowing ratio was also observed in the work done by Jabbari et al. [28].

Fan-Shaped Holes at Low Freestream Turbulence

The effectiveness contours for the fan-shaped passage at low turbulence are shown in Figures 3.5d-f. It is immediately obvious that the fan-shaped cooling holes provided much better cooling to the endwall than their cylindrical counterparts for the same MFR. Specifically, the fan-shaped holes had much better lateral spreading, which allowed the jets to stay attached to the surface because of the reduction in jet momentum. It should be pointed out that the blowing ratios given in the contour in Figure 3.4a are valid for the cylindrical metering area of fan-shaped holes, and that the effective blowing ratio at the fan-shaped hole exit would be approximately half, corresponding to an area ratio of two for the fan-shaped holes.

It is interesting to note that in the area of highest blowing ratio near the pressure side leading edge next to the fillet some of the jets appear to be lifting off, just as in the cylindrical passage. This seems to suggest that the lift-off in that region was not only due

to high blowing ratios, but also because of strong secondary flows. Again, the holes near the suction side were swept towards the suction side following the near-wall streamlines, while the holes near the pressure side were directed along the path dictated by their orientation angles.

Upon closer examination of Figure 3.5e for an MFR of 0.73%, the region shown in Figure 3.8 near the pressure side leading edge displayed an interesting physical phenomenon. The jets in the first pressure side row exhibited an alternating pattern of separation and attachment. The first hole (labeled P1) produced a typical coolant footprint downstream of a fan-shaped hole. However, the next hole in the line, P2, lifted off of the surface entirely. The following hole, P3, again produced a coolant footprint typical of a fan-shaped hole, as did P5. However, as with P2, P4 again lifted off of the surface completely. Because of the orientation angle and close hole spacing, the jet from P2 was blocked by the coolant exiting P1. This caused jet P2 to flow up and over jet P1 and lift off of the surface. Because jet P2 did not stay attached to the surface, jet P3 had a clear path and behaved normally. However, the path of jet P4 was again blocked by the downstream jet from P3, causing jet P4 to lift off of the surface. This alternating pattern of flow blockages was caused by the combination of compound angle and hole spacing.

To evaluate the cooling development through the passage, $\overline{\eta}$ values for the

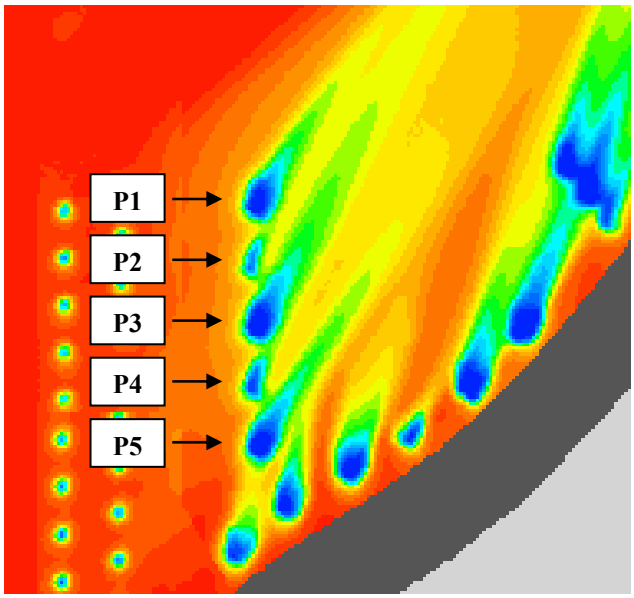

Figure 3.8. Close-up view of region near the pressure side leading edge (MFR = 0.73%).

nominal fan-shaped passage are shown in Figure 3.9. As with the cylindrical passage, the upstream double row of holes had little cooling benefit for the endwall surface, and was mainly wasted in mixing with the freestream. $\overline{\eta}$ was seen to increase continually throughout the passage, reaching a consistent level as high as $\overline{\eta}$ = 0.45 near the end of the passage.

Also shown in Figure 3.9 are the augmentations of $\overline{\eta}$ for the MFR = 0.54% and MFR = 0.92% cases in the fan-shaped passage relative to the case with MFR = 0.73%. In comparison with the cylindrical passage, changing the MFR did not elicit nearly as large of an effect on $\overline{\eta}$ for the fan-shaped holes, causing only a minor increase in cooling performance with increased MFR. The relative insensitivity to MFR was perhaps because of the lateral jet spreading witnessed with the fan-shaped holes, which allowed the fan-shaped holes to provide excellent coverage for all blowing rates. Similar results of small increases in cooling performance with increased blowing were reported for the vane surface with full coverage fan-shaped film-cooling by Colban et al. [27].

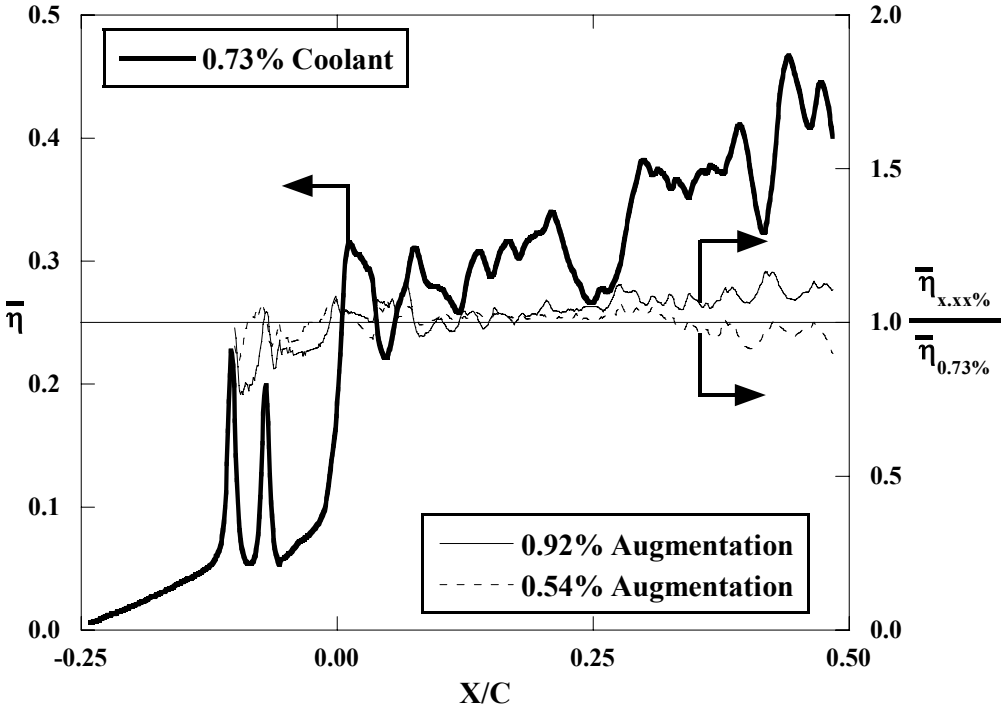

Figure 3.9. Laterally averaged effectiveness for the 0.73% case and augmentation of laterally averaged effectiveness for the 0.54% and 0.92% cases on the fan-shaped passage.

Hole Geometry Comparison at Low Turbulence

As stated previously, the primary goal of this study was to quantify the thermal benefit of using fan-shaped holes instead of cylindrical holes on the endwall. Figure 3.10 shows the augmentation in $\overline{\eta}$ at all three MFR for fan-shaped holes over cylindrical holes. The benefits in film-cooling effectiveness were both substantial and remarkable. Depending on location in the passage and flow rate, increases in $\overline{\eta}$ were seen anywhere from 50% to 150% from the cylindrical cases to the fan-shaped cases. The highest increases in $\overline{\eta}$ were observed just downstream of the hole exits. The highest MFR yielded the largest increases in $\overline{\eta}$ augmentation, in part because of the relative insensitivity to MFR by the fan-shaped passage coupled with the jet lift-off observed in the cylindrical passage.

Effects of High Freestream Turbulence

The many different combustor arrangements used in industry lead to a wide range of turbulence intensity levels somewhere between 5% and 20% entering the turbine section (Goebel et al. [29]). For this reason, we also performed the same measurements

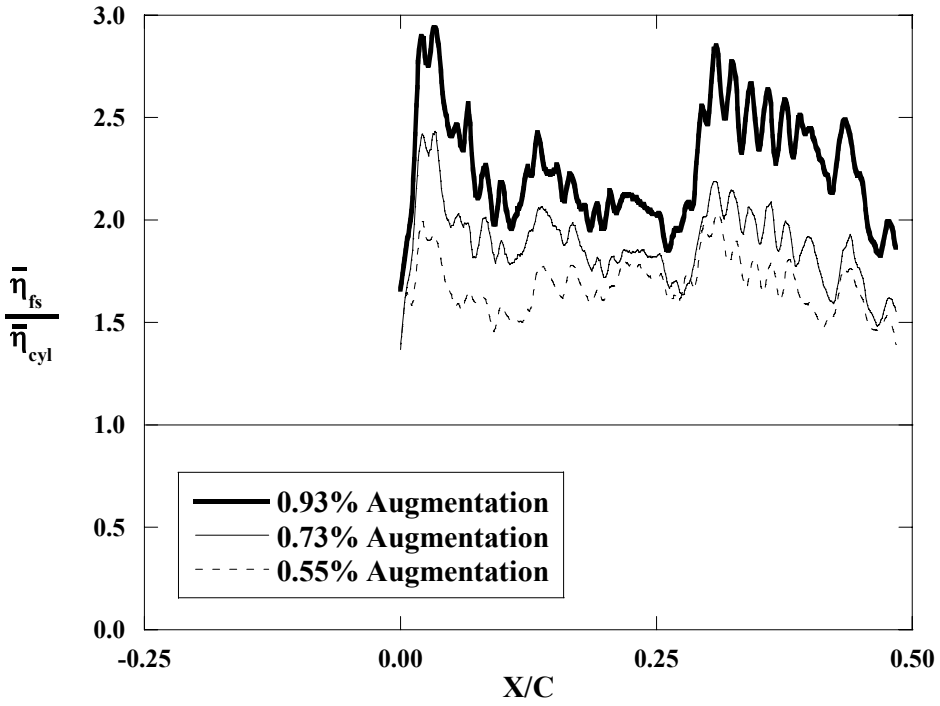

Figure 3.10. Augmentation of laterally-averaged film-cooling effectiveness for fan-shaped cooling holes over cylindrical cooling holes.

of adiabatic film-cooling effectiveness for both passages at a comparably high freestream turbulence level of TI = 8.9%. The contours of film-cooling effectiveness for the cylindrical passage at high freestream turbulence are shown in Figures 3.6a-c. Overall, the general patterns look quite similar to the cases with low turbulence (Figures 3.5a-c). To quantify the effects of elevated levels of turbulence intensity, augmentation levels of $\overline{\eta}$ for the high turbulence condition over the low turbulence condition are shown in Figure 3.11 for the cylindrical passage. High freestream turbulence reduced film-effectiveness for the MFR = 0.56% case near the entrance to the passage, likely as a result of increased mixing with the freestream. The nominal flow case showed little effect from elevated turbulence levels. The MFR = 0.93% case at high freestream turbulence showed a slight augmentation near the entrance to the passage, indicating that the extreme lift-off seen at low turbulence was somewhat counteracted by the high levels of turbulence, making the coolant more effective.

The effectiveness contours for the fan-shaped passage at high freestream turbulence are shown in Figures 3.6d-f. Increased freestream turbulence had no noticeable effect on the overall flow pattern for the fan-shaped passage. Augmentations

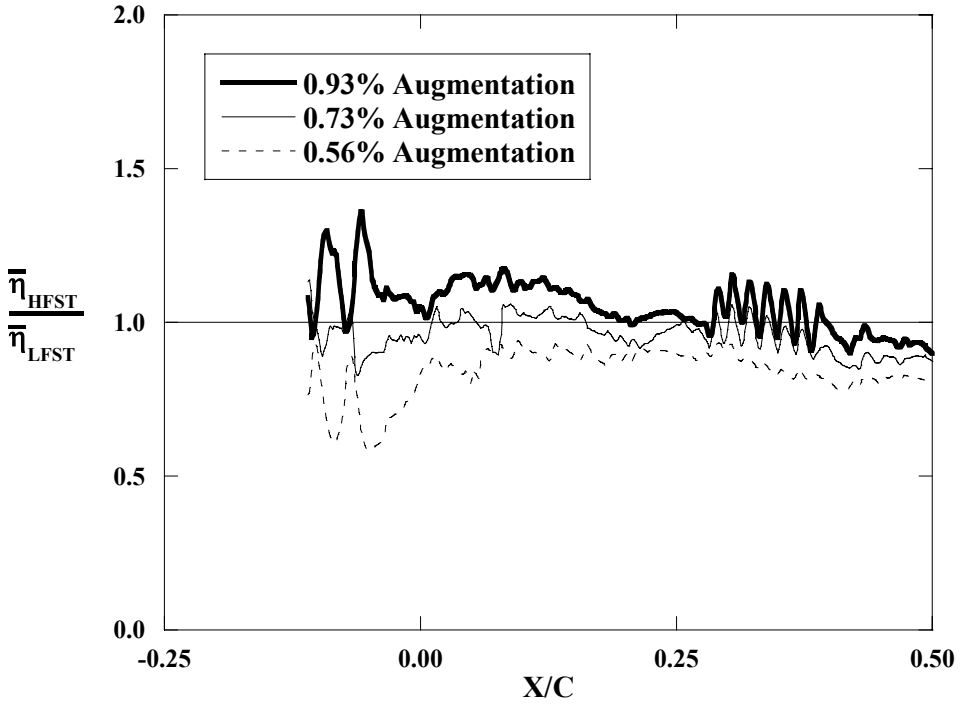

Figure 3.11. Augmentation of laterally-averaged film-cooling effectiveness for the cylindrical passage at high freestream turbulence.

in $\overline{\eta}$ for the fan-shaped passage at high freestream turbulence are shown in Figure 3.12 for all three MFR values. No significant change can be seen from the results, indicating that fan-shaped film-cooling is relatively insensitive to the level of turbulence entering the turbine section.

As a way to further evaluate the effect of both hole shape and turbulence intensity, segments of effectiveness along the data line shown in Figure 3.3 are shown in Figure 3.13 for each of the nominal cases. Again, the superior performance of the fan-shaped holes to the cylindrical holes is immediately evident from the elevated effectiveness levels. The effect of high freestream turbulence on the fan-shaped holes nearest the pressure side ($0.10 < y/P_{loc} < 0.40$) was to decrease the peak-to-valley distance in effectiveness, or essentially smear out the coolant from elevated turbulent mixing.

Another way to visualize the results is in terms of the effectiveness along streamlines released from different vane pitch locations. The nominal contours shown in Figures 3.5b and 3.5e and Figures 3.6b and 3.6e each include four streamlines released from Y/P = 0.2, 0.4, 0.6, and 0.8. The streamlines were taken from a CFD prediction without film- cooling in FLUENT 6.1.2 at 2% span. The effectiveness along the 40%

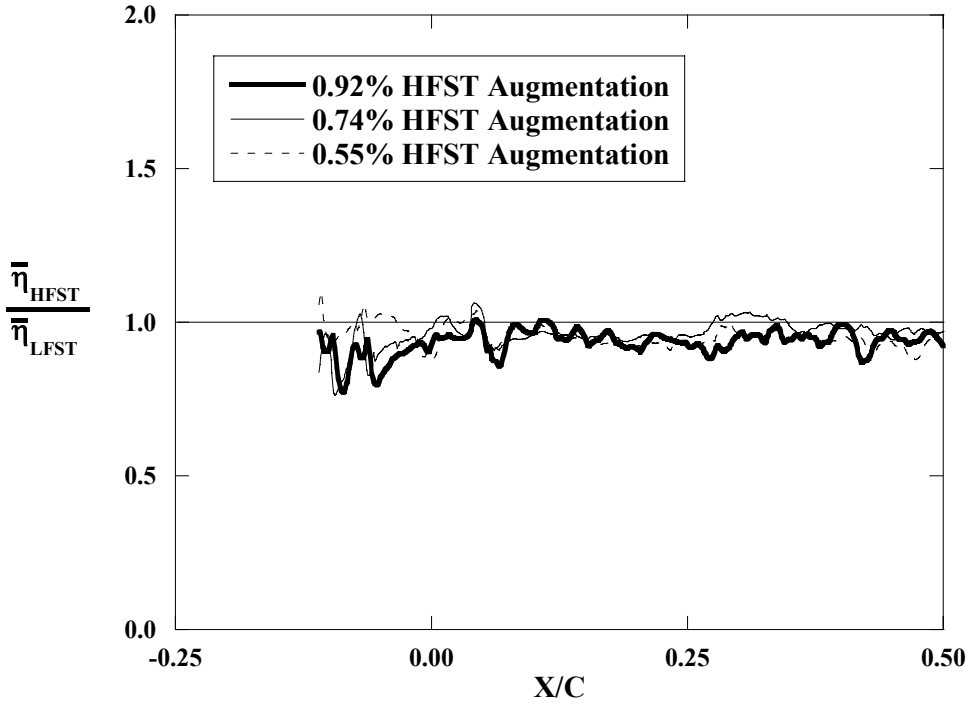

Figure 3.12. Augmentation of laterally-averaged film-cooling effectiveness for the fan-shaped passage at high freestream turbulence.

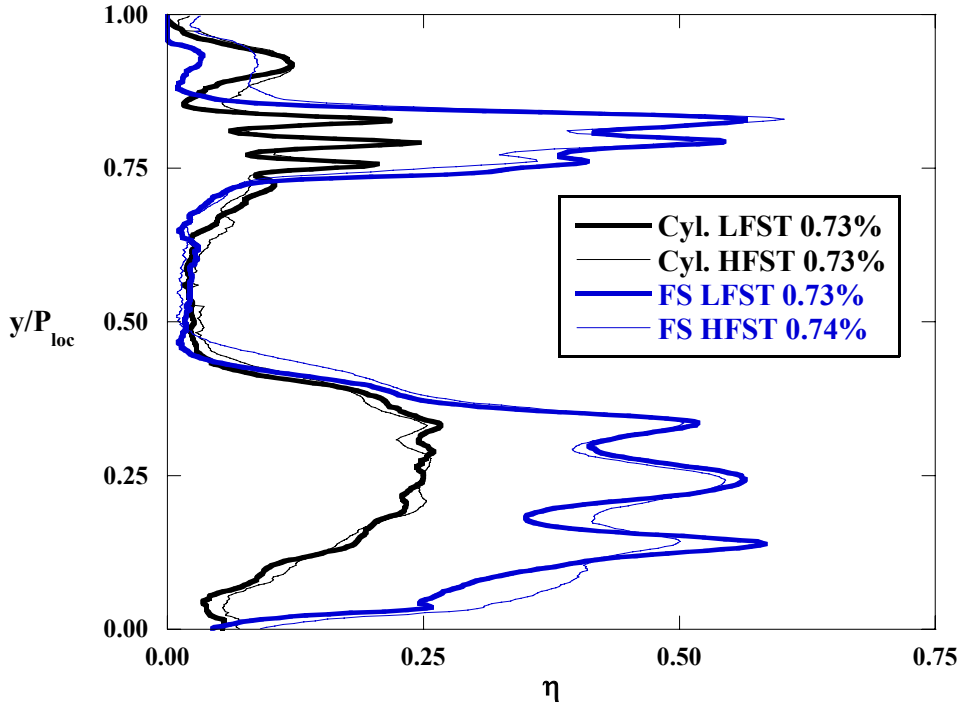

Figure 3.13. Effectiveness along the data line shown in Figure 3.3 for each nominal case (MFR = 0.73%).

and 80% streamlines for each nominal case are shown in Figures 3.14 and 3.15. For the streamlines released from Y/P = 0.4, the benefit from the fan-shaped holes is clear and fairly consistent throughout the passage. However, the streamline at 80% pitch, which follows very close to the vane suction side, gives nearly the same levels for both hole geometries.

Area-Averaged Film-Cooling Effectiveness

To quantify the cooling benefit for the entire endwall surface, area-averaged values of adiabatic film-cooling effectiveness were calculated for each case. The area included in the calculation encompassed one vane pitch, beginning at a distance of X/C = -0.25 upstream of the vane leading edge and ending at the vane trailing edge (X/C = 0.5). Area-averaged values are shown in Figure 3.16 for each case listed in Table 3.3. The superior cooling performance of the fan-shaped holes is clear, with area-averaged film-effectiveness values 75% higher than for the cylindrical cases across the full range of flow rates. The effect of freestream turbulence was to decrease the film-effectiveness by an average of 6% for the fan-shaped passage. Freestream turbulence had a stronger effect

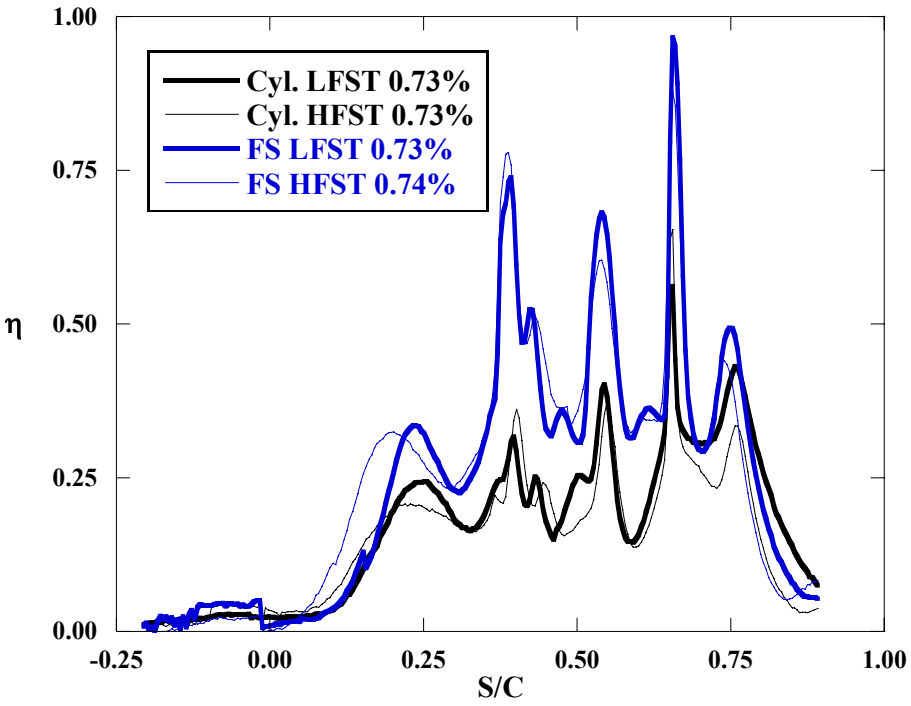

Figure 3.14. Effectiveness along a streamline released from 40% pitch for each nominal case (MFR = 0.73%).

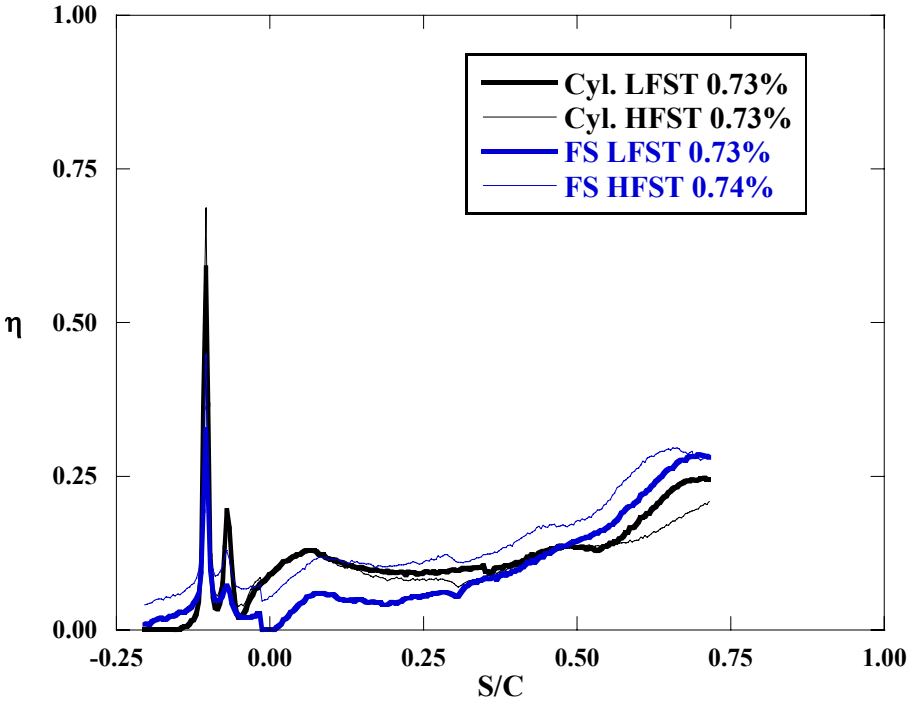

Figure 3.15. Effectiveness along a streamline released from 80% pitch for each nominal case (MFR = 0.73%).

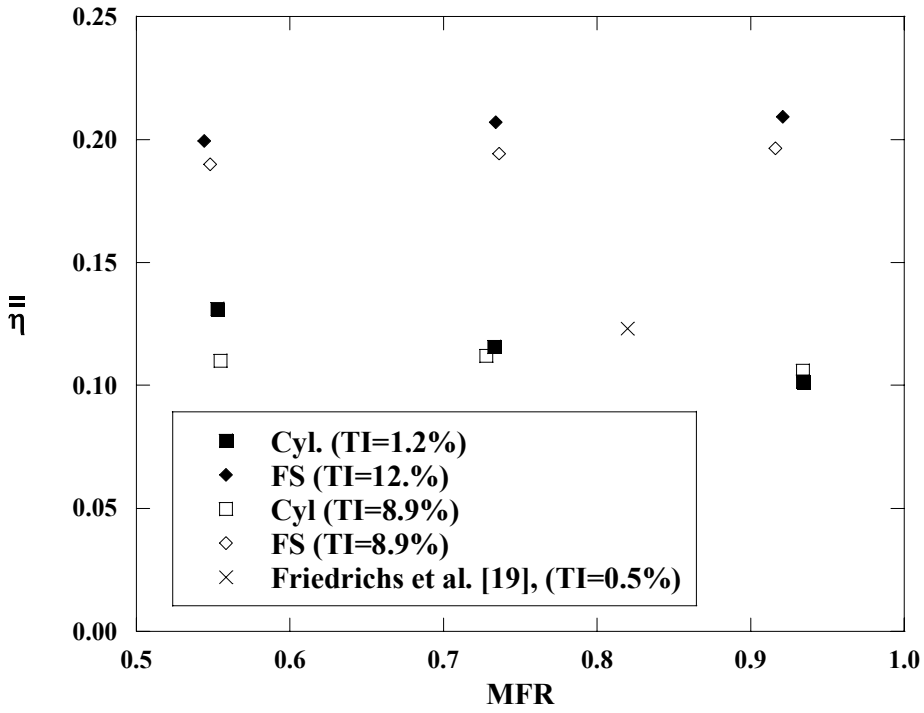

Figure 3.16. Area-averaged film-cooling effectiveness for all cases including results from Friedrichs et al. [19].

on the cylindrical passage because it changed the dependency of film-effectiveness on flow rate. For low freestream turbulence, film-effectiveness in the cylindrical passage decreased with flow rate as a result of coolant lift-off. However, at high freestream turbulence, a slight increase in film-effectiveness was observed with flow rate as a result of increased jet mixing that led to coolant spreading. Overall, the effect of turbulence on the cylindrical passage was to reduce the sensitivity of effectiveness to MFR.

As a point of reference for the hole layout, the area-averaged film-cooling effectiveness from the study by Friedrichs et al. [19] is also shown in Figure 3.16. The value falls nearly on the line formed by the cylindrical passage. The hole pattern used in the study of Friedrichs et al. [19] was very different from the pattern used in this study. They had four rows of holes located at axial positions of X/C ≈ 0, 0.3, 0.6, and 0.9. The difference in cooling hole layout between the two studies suggests that even though local effectiveness may vary significantly, perhaps there is an insensitivity of area-averaged effectiveness to hole layout. More investigation into this hypothesis will be needed.

Conclusions

This paper has presented high resolution measurements of adiabatic film-cooling effectiveness for both cylindrical and fan-shaped holes on a turbine vane endwall surface. Results were presented at both high and low values of freestream turbulence. The measurements were performed in a large-scale, low-speed, two-passage, linear turbine vane cascade, with the identical cooling hole pattern in each passage but with different hole shapes.

The major conclusion from this work was a superior performance of fan-shaped holes in the platform region was found relative to cylindrical holes. An increase in film-effectiveness of 75% based on area averages was seen by using fan-shaped holes instead of cylindrical holes. The effect of high freestream turbulence was to reduce cooling performance by 6% in the fan-shaped passage, and to change the dependency of film-effectiveness on flow rate for the cylindrical passage.

Little benefit from a cooling standpoint was seen from the double row of staggered cylindrical holes placed upstream of each passage. Further work is planned to investigate the effect of the upstream blowing on the cooling performance of the downstream holes. Work is also planned to compare the aerodynamic performance of the two hole shapes.

Acknowledgments

The authors are grateful to Siemens Power Generation for their funding and support of this project.

Nomenclature

C true vane chord

Cp static pressure coefficient, $Cp = (p_{s,loc} - p_{s,in})/0.5\rho_{in}U^2_{in}$

D film-cooling hole diameter

I local momentum flux ratio, $I = \rho_c U_c^2/\rho_{in}U_{in}^2$

k thermal conductivity

M local blowing ratio, $M = \rho_c U_c/\rho_{in}U_{in}$

MFR % total coolant mass flow per total passage mass flow

p	pressure
P	vane pitch
Re	Reynolds number, $Re = U_{in}C/\nu$
t	hole breakout width
s	distance measured along a streamline
S	streamwise distance around the vane
T	temperature
TI	turbulence intensity
U	velocity
X	axial coordinate measured from the vane stagnation
y	local pitchwise coordinate
Y	pitchwise coordinate

Greek

α	inclination angle
δ	boundary layer thickness
ν	kinematic viscosity
η	adiabatic film-cooling effectiveness
Λ_x	integral length scale
ρ	density
φ_1	lateral diffusion angle
φ_2	forward expansion angle

Subscripts

c	coolant
cyl	cylindrical holes
fs	fan-shaped holes
HFST	high freestream turbulence condition (TI = 8.9%)
in	inlet condition
LFST	low freestream turbulence condition (TI = 1.2%)
loc	local value

max maximum value of given variable at that location

s static

Overbar

– lateral average

= area average

References

[1] Bunker, R. S., "A Review of Shaped Hole Turbine Film-Cooling Technology," ASME Journal of Heat Transfer, vol. 127, pp. 441-453, 2005.

[2] Goldstein, R. J., Eckert, E. R. G., and Burggraf, F., "Effects of Hole Geometry and Density on Three-Dimensional Film Cooling," ASME Journal of Heat and Mass Transfer, vol. 17, pp. 595-607, 1974.

[3] Kercher, D. M., Film-Cooling Bibliography: 1940-2002: Private publication, 2003.

[4] Kercher, D. M., Film-Cooling Bibliography Addendum: 1999-2004: Private publication, 2005.

[5] Goldstein, R. J., "Film Cooling," Advances in Heat Transfer, vol. 7, pp. 321-379, 1971.

[6] Bogard, D. G. and Thole, K. A., "Gas Turbine Film Cooling," to appear in the AIAA Journal of Propulsion, 2006.

[7] Vogel, G., Wagner, G., and Bölcs, A., "Transient Liquid Crystal Technique Combined with PSP for Improved Film Cooling Measurements," The 10th International Symposium on Flow Visualization, vol. F0109, 2002.

[8] Vogel, G., "Experimental Study on a Heavy Film Cooled Nozzle Guide Vane with Contoured Platforms," PhD Dissertation, École Polytechnique Fédérale de Lausanne, 2002.

[9] Barigozzi, G., Benzoni, G., Franchini, G., and Perdichizzi, A., "Fan-Shaped Hole Effects on the Aero-Thermal Performance of a Film Cooled Endwall," GT2005-68544, 2005.

[10] Blair, M. F., "An Experimental Study of Heat Transfer and Film Cooling on Large-Scale Turbine Endwalls," ASME Journal of Heat Transfer, vol. 96, pp. 524-529, 1974.

[11] Granser, D. and Schulenberg, T., "Prediction and Measurement of Film Cooling Effectiveness for a First Stage Turbine Vane Shroud," 90-GT-95, 1990.

[12] Colban, W., Thole, K. A., and Zess, G., "Combustor Turbine Interface Studies - Part 1: Endwall Effectiveness Measurements," ASME Journal of Turbomachinery, vol. 125, pp. 193-202, 2003.

[13] Knost, D. G. and Thole, K. A., "Computational Predictions of Endwall Film-Cooling for a First Stage Vane," GT2003-38252, 2003.

[14] Harasgama, S. P. and Burton, C. D., "Film Cooling Research on the Endwall of a Turbine Nozzle Guide Vane in a Short Duration Annular Cascade: Part 1-Experimental Technique and Results," ASME Journal of Turbomachinery, vol. 114, pp. 734-740, 1992.

[15] Nicklas, M., "Film-Cooled Turbine Endwall in a Transonic Flow Field: Part II - Heat Transfer and Film-Cooling Effectiveness," 2001-GT-0146, 2001.

[16] Sieverding, C. H. and Wilputte, P., "Influence of Mach Number and Endwall

Cooling on Secondary Flows in a Straight Nozzle Cascade," ASME Journal of Engineering for Gas Turbines and Power, vol. 103, pp. 257-264, 1981.

[17] Kost, F. and Nicklas, M., "Film-Cooled Turbine Endwall in a Transonic Flow Field: Part I - Aerodynamic Measurements," 2001-GT-0145, 2001.

[18] Colban, W., Lethander, A. T., Thole, K. A., and Zess, G., "Combustor Turbine Interface Studies - Part 2: Flow and Thermal Field Measurements," ASME Journal of Turbomachinery, vol. 125, pp. 203-209, 2003.

[19] Friedrichs, S., Hodson, H. P., and Dawes, W. N., "Distribution of Film-Cooling Effectiveness on a Turbine Endwall Measured Using the Ammonia and Diazo Technique," ASME Journal of Turbomachinery, vol. 118, pp. 613-621, 1995.

[20] Knost, D. G. and Thole, K. A., "Adiabatic Effectiveness Measurements of Endwall Film-Cooling for a First Stage Vane," ASME Journal of Turbomachinery, vol. 127, pp. 297-305, 2005.

[21] Oke, R. A., Burd, S. W., Simon, T. W., and Vahlberg, R., "Measurements in a Turbine Cascade over a Contoured Endwall: Discrete Hole Injection of Bleed Flow," 2000-GT-214, 2000.

[22] Zhang, L. J. and Jaiswal, R. S., "Turbine Nozzle Endwall Film Cooling Study Using Pressure-Sensitive Paint," ASME Journal of Turbomachinery, vol. 123, pp. 730-738, 2001.

[23] Zhang, L. and Moon, H. K., "Turbine Nozzle Endwall Inlet Film Cooling - The Effect of a Back-Facing Step," GT2003-38319, 2003.

[24] Colban, W., Gratton, A., Thole, K. A., and Haendler, M., "Heat Transfer and Film-Cooling Measurements on a Stator Vane with Fan-Shaped Cooling Holes,"

GT2005-68258, 2005.

[25] Ethridge, M. I., Cutbirth, J. M., and Bogard, D. G., "Scaling of Performance for Varying Density Ratio Coolants on an Airfoil with Strong Curvature and Pressure Gradient Effects," 2000-GT-239, 2000.

[26] Moffat, R. J., "Describing the Uncertainties in Experimental Results," Experimental Thermal and Fluid Science, vol. 1, pp. 3-17, 1988.

[27] Colban, W., Thole, K. A., and Haendler, M., "Experimental and Computational Comparisons of Fan-Shaped Film-Cooling on a Turbine Vane Surface," IMECE2005-79596, 2005.

[28] Jabbari, M. Y., Marston, K. C., Eckert, E. R. G., and Goldstein, R. J., "Film Cooling of the Gas Turbine Endwall by Discrete-Hole Injection," 94-GT-67, 1994.

[29] Goebel, S. G., Abauf, N., Lovett, J. A., and Lee, C.-P., "Measurements of Combustor Velocity and Turbulence Profiles," 93-GT-228, 1993.

Paper 4:
A Comparison of Cylindrical and Fan-Shaped Film-Cooling Holes on a Vane Endwall with and without Upstream Blowing

To be submitted to the 2007 *ASME Turbo Expo*[*]

Abstract

In the push for more efficient and powerful gas turbines, combustor exit temperatures continue to rise. This requires active cooling for the downstream turbine section to avoid thermal failure. Film-cooling has long been an integral part of turbine cooling schemes. Cooling the endwall is particularly difficult as much of the coolant is swept across the passage endwall by secondary flows.

This study investigated the effect of upstream blowing from two rows of film-cooling holes on the endwall secondary flows. Flow-field measurements are presented at the passage exit plane both with and without blowing from the upstream rows. Adiabatic effectiveness measurements of the endwall surface are also presented to quantify the cooling performance with and without upstream blowing. Two commonly used film-cooling hole geometries were investigated; cylindrical holes in one passage and fan-shaped holes in the other passage.

Results showed that film-cooling increases the aerodynamic losses at the exit plane, with fan-shaped holes showing lower losses than cylindrical holes. Fan-shaped holes also provided better adiabatic film-cooling effectiveness on the endwall than cylindrical holes. In general, upstream blowing increased aerodynamic losses, due to the increased mixing with the freestream. Although the upstream blowing did not show an immediate benefit near the injection location because of separation, a significant cooling benefit was observed further downstream for the passage film-cooling holes because of the large amount of coolant in the passage from the upstream holes.

* Co-authors: Dr. Karen A. Thole, Mechanical Engineering Department, Virginia Tech
Michael Haendler, Siemens Power Generation, Muelheim a. d. Ruhr, Germany

Introduction

Increasing energy demands require more powerful and more efficient industrial gas turbine engines. One means of achieving this goal is to increase the combustion temperature, resulting in higher temperatures at the inlet of the turbine. Although this is beneficial in terms of power output, it is anything but beneficial in terms of part life. Turbine inlet temperatures are so high in today's gas turbine engines that in the absence of complex cooling schemes the turbine components would completely melt. Ultimately, engine designers aim to accomplish two seemingly opposed tasks; to provide better cooling to the critical surfaces while at the same time reducing the total amount of coolant used. Coolant comes at a cost to an engine's overall efficiency, as it is bled from one of the compressor stages (the necessary injection pressure and temperature determine exactly which compressor stage), so there is a trade-off in the cooling scheme design process.

In addition to the high operating temperatures, the endwall platform region typically has secondary flows, which tend to sweep coolant flow away from critical surfaces and replace it with hot mainstream gases. Methods of reducing harmful secondary flows include endwall profiling, upstream injection, and endwall contouring. Morris and Hoare [1] showed that with a single contoured endwall, similar to this study, the secondary flow losses near the flat endwall were reduced, while the secondary flow losses near the contoured endwall were increased. A reduction in secondary flows resulting from endwall contouring follows from an analysis of the static pressure distribution around the vane. Implementing a contoured endwall pushes the minimum static pressure towards the trailing edge, causing the airfoil to be more aft-loaded and ultimately delaying the onset of the development of secondary flows.

Another method that has been used to try and diminish the strength of secondary flows is to implement coolant ejection upstream of the first vane row. Coolant ejection reenergizes the boundary layer and reduces the strength of the pressure gradients that lead to the formation of passage secondary flows. Although the main purpose of the high-momentum high-angle upstream injection is to actively control the formation of secondary flows, that injection can also provide some additional cooling benefit.

The purpose of this study was two-fold. The first goal was to investigate the

effect of coolant injection on the development of the passage secondary flows. The second objective was to quantitatively evaluate the effect of hole geometry on the exit plane flowfield as well as the cooling performance on the endwall. A five-hole total pressure probe was used to measure total pressure losses and all three velocity components at the passage exit plane for cases with and without upstream injection. Also, endwall adiabatic film-cooling effectiveness was measured using an infrared camera with and without upstream injection. Two different cooling designs were investigated – one with cylindrical holes and the other with fan-shaped holes – in order to compare the relative performance of two different commonly used hole geometries.

Past Studies

Because of the absolute necessity of effective turbine cooling in gas turbine engines, film-cooling has been researched exhaustively for the last 50 years (Kercher [2], [3]). Among the topics studied are hole geometry variations and internal and external conditions such as blowing ratio, density ratio, turbulence level, surface curvature, pressure gradient, cross-flow (internal and external), surface roughness, and hole location. Two excellent reviews on the development of film-cooling technology over the years are offered by Goldstein [4] and Bogard and Thole [5], with a third more specific review for shaped film-cooling holes by Bunker [6]. In terms of hole location, the endwall region is a particularly difficult region for film-cooling designers, partly because of secondary flows, but also partly because of manufacturing difficulties.

Perhaps the most difficult obstacle facing film-cooling designers in the endwall region is the cross-passage flow. The pressure gradient that develops across the passage from the pressure to suction sides has severe cooling consequences. Coolant is swept away from the near wall region, exposing the endwall surface to hot gas flow. This effect has been documented for upstream slot flow cooling by Blair [7], Granser and Schulenberg [8], Colban et al. [9], Knost and Thole [10], and Knost and Thole [11]. Other studies, such as those by Harasgama and Burton [12] and Nicklas [13], have also verified this effect for endwall film-cooling located in the vane passage.

In addition to the thermal penalties associated with the nozzle guide vane secondary flows, there are also aerodynamic penalties that accompany secondary flows in

the form of total pressure losses and non-uniform flow turning. Langston et al. [14], in a study performed without endwall blowing, showed a significant loss in total pressure corresponding to the center of the passage vortex as it migrated through the passage. They showed that at the exit plane, the location of the passage vortex and the corresponding loss core had migrated to the suction side of the vane and had risen off of the endwall.

A number of studies, including Sieverding and Wilputte [15], Friedrichs et al. [16], Kost and Nicklas [17], and Barigozzi et al. [18] have reported aerodynamic benefits associated with endwall film-cooling in the form of reduction of the size and strength of the passage vortex and a reduction in strength of the cross passage flow. However, there is an aerodynamic downside to film-cooling injection, as Friedrichs et al. [19] reported that film-cooling ultimately increases the total pressure losses through the passage. They showed that the additional losses generated within the hole and the losses generated by coolant mixing with the freestream outweigh the reduction in losses associated with a reduction in secondary flows.

Both passive and active solutions to the problems associated with passage secondary flows are being implemented into nozzle guide vanes. Passive solutions include endwall contouring (Oke et al. [20]) and leading edge fillet designs, such as those presented by Zess and Thole [21], Lethander and Thole [22], Becz et al. [23], and Mahmood et al. [24]. One active solution that is currently employed in some designs is to inject high momentum coolant upstream of the vane passage, in many cases in a double row staggered configuration. Zhang and Jaiswal [25] measured endwall film-cooling effectiveness on an endwall downstream of two staggered rows of 45º cylindrical holes placed upstream of the vane passage. They showed that at low injection rates the coolant was swept towards the suction side, indicating a strong cross-passage flow. As the injection rate was increased, the cross-passage flow was diminished, and a more complete cooling coverage was seen on the endwall. Using 30º cylindrical holes upstream of a contoured endwall, Zhang and Moon [26] showed similar results, showing less cross-passage flow at higher injection rates.

A study comparing total pressure losses between an uncooled endwall, a cooled endwall with cylindrical holes, and a cooled endwall with shaped holes was performed by

Barigozzi et al. [18]. They reported that there was no significant difference between the secondary flow field with cylindrical holes versus conical diffuser shaped holes. They showed that for low injection rates, the magnitude of the total pressure losses in the loss core of the passage vortex increased relative to the uncooled case. In addition, the location of the center of the passage vortex and its associated loss core shifted positions. For higher injection rates, the passage vortex migrated towards the pressure side and nearly vanished at the highest injection rate, yielding a nearly two-dimensional loss distribution at the exit plane. Barigozzi et al. [18] reported almost the same performance in terms of film-cooling effectiveness for the two different hole shapes at low mass flow rates, but reported significantly better cooling performance by the shaped holes at high mass flow rates. Note that their study featured different hole patterns in each passage, which meant that it was not a direct one-to-one comparison.

In a parallel study to this paper, Colban et al. [27] compared the film-cooling performance of cylindrical holes and fan-shaped holes on a turbine vane endwall. They had the same experimental setup as the current study, with two passages having the same layout, one with cylindrical holes and the other with fan-shaped holes. Both passages had upstream injection from two staggered rows of cylindrical holes. Colban et al. [27] reported an average augmentation in film-cooling effectiveness of nearly 75% for the fan-shaped passage over the cylindrical passage. The coolant in the fan-shaped passage stayed attached to the surface for the mass flow rates that were tested, while the coolant in the cylindrical passage did not.

The missing element in the research that has been performed is the investigation into the effect of high momentum coolant injection using holes upstream of the vane passage on the downstream endwall film-cooling. The studies so far have either looked at upstream injection alone, or endwall passage film-cooling alone, but the interaction between the two has heretofore not been investigated. This study presents total pressure losses for two passages – one with cylindrical holes and the other with fan-shaped holes – both with and without upstream coolant injection. All four cases are compared to the solid endwall case with no film-cooling. In addition, film-cooling effectiveness measurements on both endwalls are presented at three different mass flow rates both with and without upstream coolant injection.

Experimental Facilities

All experiments were performed in the low-speed, large scale, recirculating wind tunnel facility shown in Figure 4.1 at the Virginia Tech Experimental and Computational Convection Laboratory (VTExCCL). The flow was split into three separate channels, with the center channel being heated to represent the combustor core flow using a 55 kW bank of strip heaters. The lower channel was blocked for this study, while the upper channel was cooled using a 44 kW chiller and used to provide film-cooling for the endwall in the vane cascade test section. The temperature difference between the heated mainstream and the film coolant that was achieved for the heated flow adiabatic effectiveness tests was on the order of 20ºC. The flow field measurements were unheated, with both the coolant and the mainstream at the same temperature.

The relevant inlet conditions for the tests are listed in Table 4.1, along with important geometric parameters. An engine representative inlet Reynolds number of

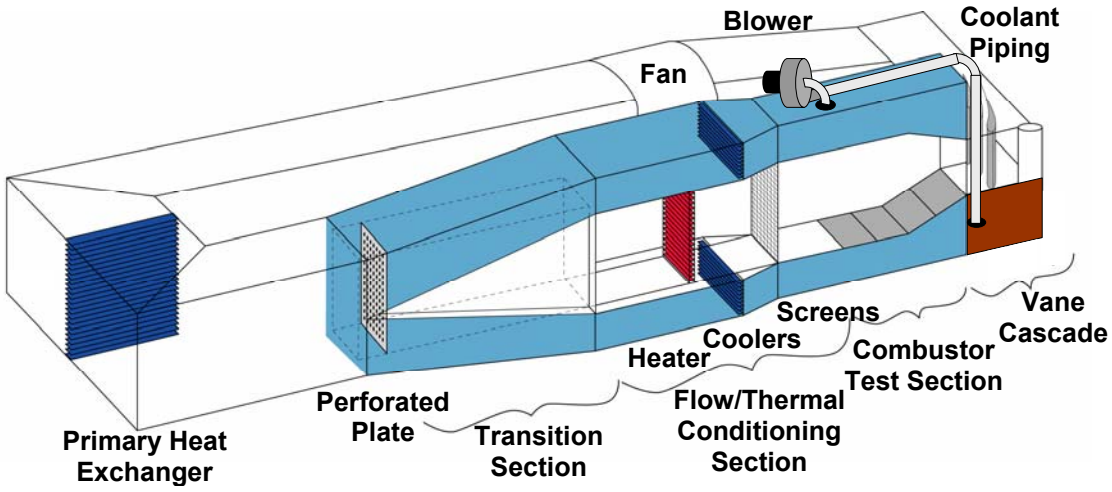

Figure 4.1. Diagram of the large-scale, low-speed, recirculating wind tunnel facility.

Table 4.1. Operating Conditions and Vane Parameters

Scale	3X
C (m)	0.53
$S_{max,PS}$ (m)	0.52
$S_{max,SS}$ (m)	0.68
U_{in} (m/s)	9.41
Re_{in} (-)	3.4×10^5
ΔT (ºC)	20
P (m)	0.465

$3.4x10^5$ based on the true vane chord and the inlet velocity was maintained for all tests. The nozzle guide vanes were scaled up by a factor of three from the engine. Inlet velocity and total pressure profiles where taken at several pitch locations a distance of one chord length upstream of the vane stagnation to ensure periodic inlet conditions and also to measure the reference mass-averaged total pressure used in the total pressure loss calculations. The mass averaged inlet velocity was 9.4 m/s for all experiments. A hot wire anemometer was used to measure the turbulence intensity at the inlet, which was 1.2%. The heated tests were nominally incompressible, with a coolant-to-mainstream density of nearly 1.06.

Test Section Design

The test section, described in detail by Colban et al. [27], was a two-passage linear vane cascade with one contoured endwall and one flat endwall. The upper endwall was contoured in order to match the non-dimensional static pressure distribution at low speed test conditions to that found in the engine at high speed operating conditions. This was important because the static pressure distribution around the vane has a strong influence on the development of secondary flows through the vane passage, both on the strength and location. The development and design of the contoured endwall was also documented by Colban et al. [28] and featured a 40% contraction of the span from the leading edge to the trailing edge. Both experimental results (Colban et al. [28]) and computational predictions (Colban et al. [29]) of the passage flow field show a nearly two-dimensional pressure distribution below 40% of the inlet span height.

The vane cascade featured two periodic passages, each with an identical film-cooling hole pattern, but with a different film-cooling hole geometry. The film-cooling hole layout is shown in Figure 4.2, with a callout and details of each cooling hole shape. The specific geometric parameters for each cooling hole shape are given in Table 4.2. The diameter of all the holes (including the entrance length for the fan-shaped holes) was 2.6 ± 0.15 mm. The double rows of upstream holes were oriented in a staggered array. The surface angle of the upstream holes was 60º from horizontal and each hole had an orientation angle that was directed towards the center of the passage. All of the holes in the passage had a shallower surface angle of 35º and were angled nominally in the

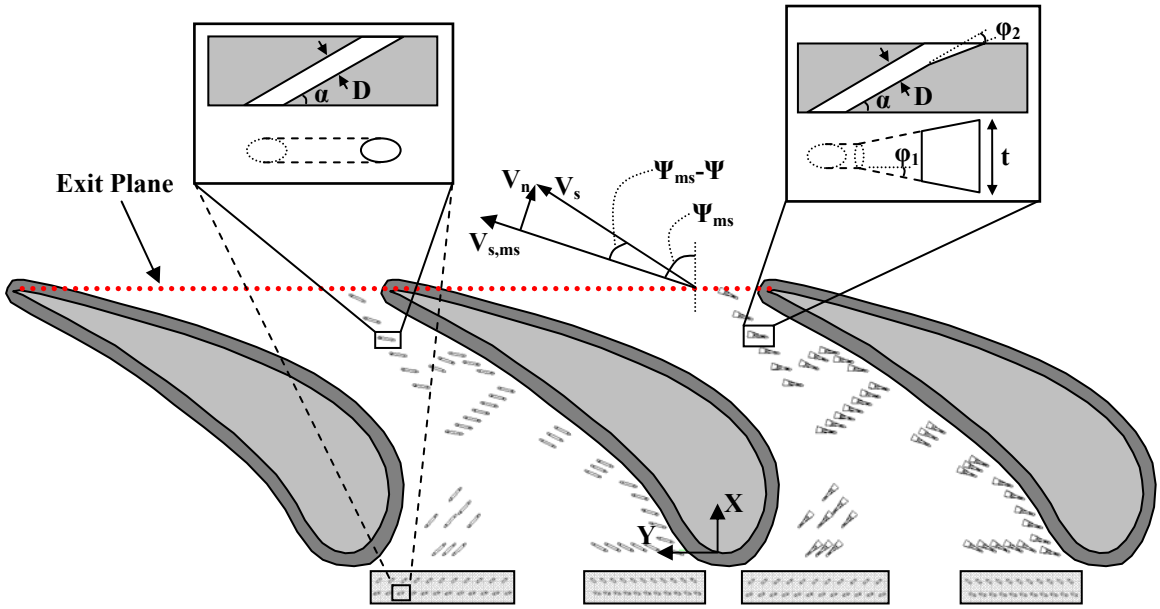

Figure 4.2. Film-cooling hole layout and specifications. Upstream injection holes are highlighted as well as the exit plane, which stretches from trailing edge to trailing edge.

Table 4.2. Film-Cooling Hole Parameters

	Upstream	Cylindrical	Shaped
D (cm)	0.26±0.015	0.26±0.015	0.26±0.015
α (°)	60	35	35
φ_1 (°)	0	0	10
φ_2 (°)	0	0	10

direction of the inviscid streamline at that location. The holes in the fan-shaped passage also featured a lateral diffusion angle of 10º and a forward diffusion angle of 10º.

A single plenum, which provided coolant to supply the entire endwall, was located beneath the test section. The capability was available to block off each passage individually, as well as the rows of upstream holes, and measure exactly the amount of coolant mass flow delivered to the entire endwall using a laminar flow element. The amount of coolant in this study is reported in terms of mass flow rate (MFR), and is defined as a percentage of the total passage mass flow rate for one vane pitch.

The endwall was constructed from a medium density foam material using a five-axis water jet for high geometrical integrity of the hole design and pattern. The foam had a low thermal conductivity (k = 0.028 W/m·K) such that the conduction losses laterally

throughout the foam as well as from the surface into the plenum were minimal. A manufacturing fillet was also implemented, circumnavigating the vane at the vane/endwall junction. The fillet was an elliptical design and extended a distance 12D up the vane span and 10D normal to the vane.

A five-hole total pressure probe with a 2.4 mm tip was used to measure all three components of velocity and the total pressure at the exit plane. The exit plane is shown schematically in Figure 4.2, and it extends from one trailing edge to the other and covers the entire pitch at the exit. The five-hole probe measured streamwise velocity, yaw angle, pitch angle, and total pressure directly.

Data Analysis and Experimental Uncertainty

In order to get an accurate view of the secondary flow vectors in the exit plane, the components were transformed into the coordinates shown in Figure 4.2. The streamwise velocity, V_s, was measured directly with the five-hole probe. The horizontal velocity component, V_n, in the exit plane was calculated normal to the streamline at the midspan according to Equation 4.1,

$$V_n = V_s \sin(\Psi_{ms} - \Psi) \tag{4.1}$$

where $(\Psi_{ms} - \Psi)$ is the deviation in flow turning angle from the midspan. The vertical velocity component, V_z, in the exit plane was calculated using the measured pitch angle, Φ, according to Equation 4.2,

$$V_z = V_s \sin(\Phi) \tag{4.2}$$

Five measurements, each being an average of 4000 data points taken over 4 seconds, were taken at every location in the exit plane, and averaged to give the reported values. Approximately 240 locations were taken for each of the five cases presented in this study, with higher resolution in areas with larger gradients.

Total pressure loss coefficients were calculated according to the method laid out by Friedrichs et al. [19], where the total pressure loss coefficient given by Equation 4.3,

$$Y_o = \frac{P_{o,ref} - P_{o,exit}}{P_{o,ref} - P_{s,exit}} \tag{4.3}$$

where $P_{o,exit}$ and $P_{s,exit}$ were the total and static pressures at the exit. $P_{o,ref}$ was calculated using two different methods. The first way of calculating $P_{o,ref}$ incorporates the additional

total pressure and energy added to the passage flow as a result of the addition of film-coolant. The mass-averaged calculation of $P_{o,ref}$ is given by Equation 4.4,

$$P_{o,ref} = \frac{P_{o,in}\,\dot{m}_{in} + P_{o,cool}\,\dot{m}_{cool}}{\dot{m}_{in} + \dot{m}_{cool}} \tag{4.4}$$

The second definition used for $P_{o,ref}$ in Equation 4.4 was just to set $P_{o,ref} = P_{o,in}$, the mass-averaged inlet stagnation pressure. This definition was used for the uncooled case, in which case Equation 4.4 simplifies to that result, and was also calculated for the other flowfield cases. The second definition neglects the total pressure additions from the film-cooling flow, and can be misleading for that reason because it typically yields lower Y_o values than by using the definition for $P_{o,ref}$ in Equation 4.4.

Mass-averaged values of the total pressure loss coefficients were also computed in the exit plane in order to give an overall comparison of each case in terms of complete total pressure loss. The mass-averaging was done according to Equation 4.5,

$$\overline{\overline{Y}}_o = \frac{\int\int_{Z\,Y} Y_o V_s \rho dY dZ}{\int\int_{Z\,Y} V_s \rho dY dZ} \tag{4.5}$$

although the density term cancelled out of Equation 4.5 because the tests were incompressible, being unheated and at low speed.

Endwall surface temperatures were measured using an infrared camera and converted to adiabatic film-cooling effectiveness. Eight image locations were necessary to map the entire endwall surface for each passage. Five images were taken and averaged at each location. A FLIR P20 infrared camera was used with an image resolution of 240 x 320 pixels, which gave an image resolution of approximately 0.28D per pixel. Each image was calibrated using thermocouples embedded flush with the endwall surface, and then corrected for conduction losses. A one-dimensional conduction correction was applied to the measured film-cooling effectiveness to give the reported adiabatic film-cooling effectiveness. The uncooled effectiveness, η_o, varied between 0.06 and 0.15, and depended on the location on the endwall.

Uncertainty estimates were made using the technique described by Moffat [30], which is a partial derivative and sequential perturbation method. The uncertainty in MFR

for the 0.73% case was determined to be ± 0.0024% for the cylindrical passage. This value is representative of the other reported MFRs. A reported value of $Y_o = 0.15$ for the cylindrical passage with upstream blowing yielded an uncertainty of ± 0.001, with $P_{o,ref}$ being the mass-averaged total pressure including coolant addition as defined by Equation 4.4. The uncertainty in adiabatic film-cooling effectiveness was also calculated for high and low reported values. For a high value of $\eta = 0.9$, the uncertainty was ± 0.012, while a lower value of $\eta = 0.2$ had an uncertainty of ± 0.011.

Test Design

The test matrix is shown in Table 4.3 and includes a total of 13 cases (baseline case with no blowing is not shown). Adiabatic film-cooling effectiveness measurements were made for all cases shown in Table 4.3. The cases for which flow field measurements were taken at the exit plane are highlighted in the test matrix. One other case was measured for the exit plane, and that was a case with no blowing, which was meant to be a baseline case for the flow field measurements. Also, note both the inner and outer endwalls are typically cooled in an actual engine, so the MFR values in Table 4.3 are representative of approximately half of the actual value per vane pitch. The MFRs for the six cases without upstream injection were determined by matching the pressure ratio between the endwall plenum total pressure and the vane stagnation total pressure to the cases with upstream injection. In this way, the passage endwall film-cooling holes had nominally the same MFR in both the upstream and no upstream blowing cases.

To determine the distribution of blowing ratios and momentum ratios for the endwall film-cooling holes, inviscid calculations were done using a computationally predicted static pressure distribution on the endwall with no film-cooling along with the

Table 4.3. Test Matrix (shaded values indicate cases for which the exit plane flow field was measured)

	Cylindrical Passage MFR			Fan-Shaped Passage MFR		
Upstream	0.55%	0.73%	0.93%	0.54%	0.73%	0.92%
No Upstream	0.36%	0.44%	0.55%	0.35%	0.45%	0.56%

measured pressure difference between the plenum total pressure and the upstream endwall surface static pressure. The results are shown in terms of a contour map in Figures 4.3a and b. One could also think of Figures 4.3a and b as design maps with which to predict the blowing ratio and momentum ratio for a hole placed at a given location on the endwall. The highest blowing ratios were near the vane stagnation and resulted from the relatively low local velocity at that location. The lowest blowing ratios occurred in the vane passage at the throat region, where local velocities were highest.

Experimental Results

The total pressure loss measurements at the exit plane will be presented first. That will be followed by an analysis of the adiabatic film-cooling effectiveness measurements.

Exit Plane Flow Field

A five-hole pressure probe was used to measure total pressure losses and all three components of velocity at the exit plane shown in Figure 4.2. The streamwise velocity distribution was nearly the same for all five cases except near the wall, so it is shown in Figure 4.4 only for the uncooled case. The strong downward velocity near the exit midspan was a result of the upper contoured endwall contraction. Both the streamwise velocity and the secondary flow vectors have been non-dimensionalized by the mass-

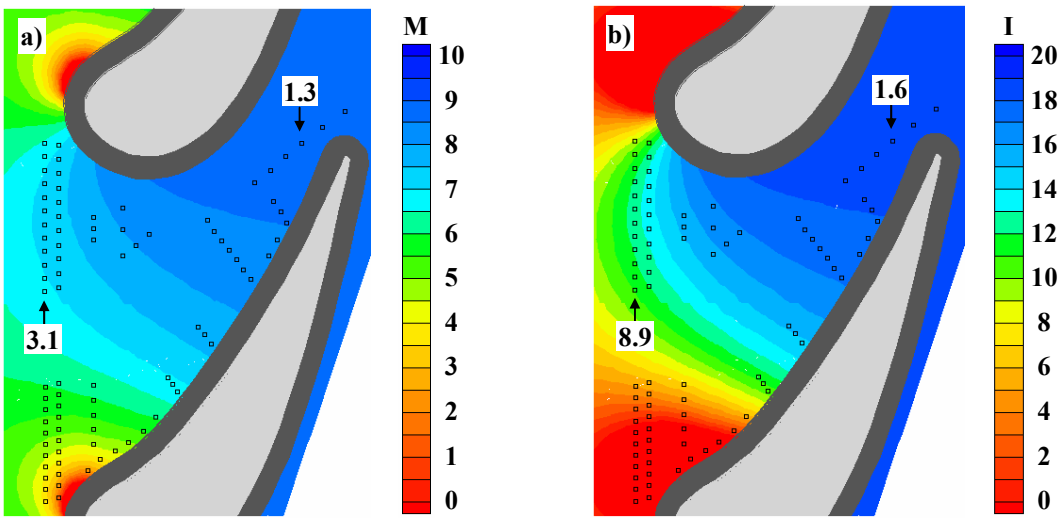

Figure 4.3. Contours of calculated (a) blowing ratio and (b) momentum flux ratio for MFR = 0.73% conditions.

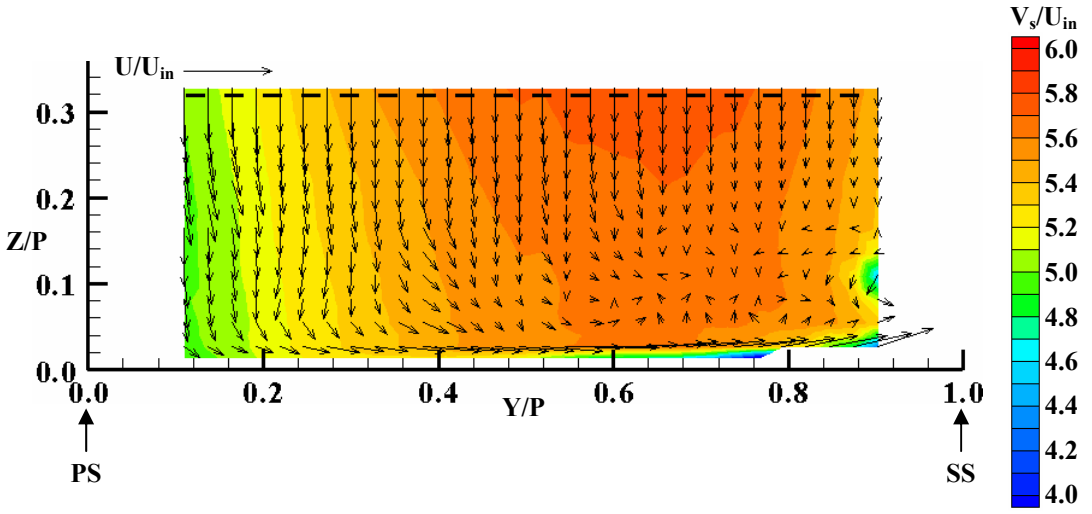

Figure 4.4. Contour of streamwise velocity in the exit plane for the uncooled case with superimposed secondary flow vectors.

averaged inlet velocity to the cascade. Figure 4.4 shows that the streamwise velocity is nearly two-dimensional across most of the exit plane. There was a local minimum nonuniformity in streamwise velocity corresponding to the location of the center of the passage vortex near the suction side at Y/P = 0.9 and Z/P = 0.1. A strong cross passage flow was seen near the wall from the pressure to the suction sides.

Normalized total pressure losses are shown in Figures 4.5a-e. For the baseline uncooled case, the reference total pressure in Equation 4.3 was taken as the mass-averaged inlet total pressure, while for the other cases, the reference total pressure was mass-averaged including the coolant flow to incorporate the losses due to film-cooling addition. Upon examining the uncooled case in Figure 4.5a, the most noticeable feature was the loss core associated with the passage vortex, located at Y/P = 0.9 and Z/P = 0.1. The passage vortex was the most dominant loss generator in the uncooled passage. As with the streamwise velocity shown in Figure 4.4, the secondary flow vectors are superimposed onto the total pressure loss contours in Figure 4.5a-e. There was also a region of high losses near the endwall at the suction side corner. Langston et al. [14] noticed the same phenomenon for an uncooled endwall and attributed it to the separation of the endwall boundary layer.

Figure 4.5b shows the total pressure losses in the exit plane for the cylindrical passage with upstream injection. Two major changes occurred from the uncooled case. First, the location of the passage vortex shifted away from the suction side, perhaps due

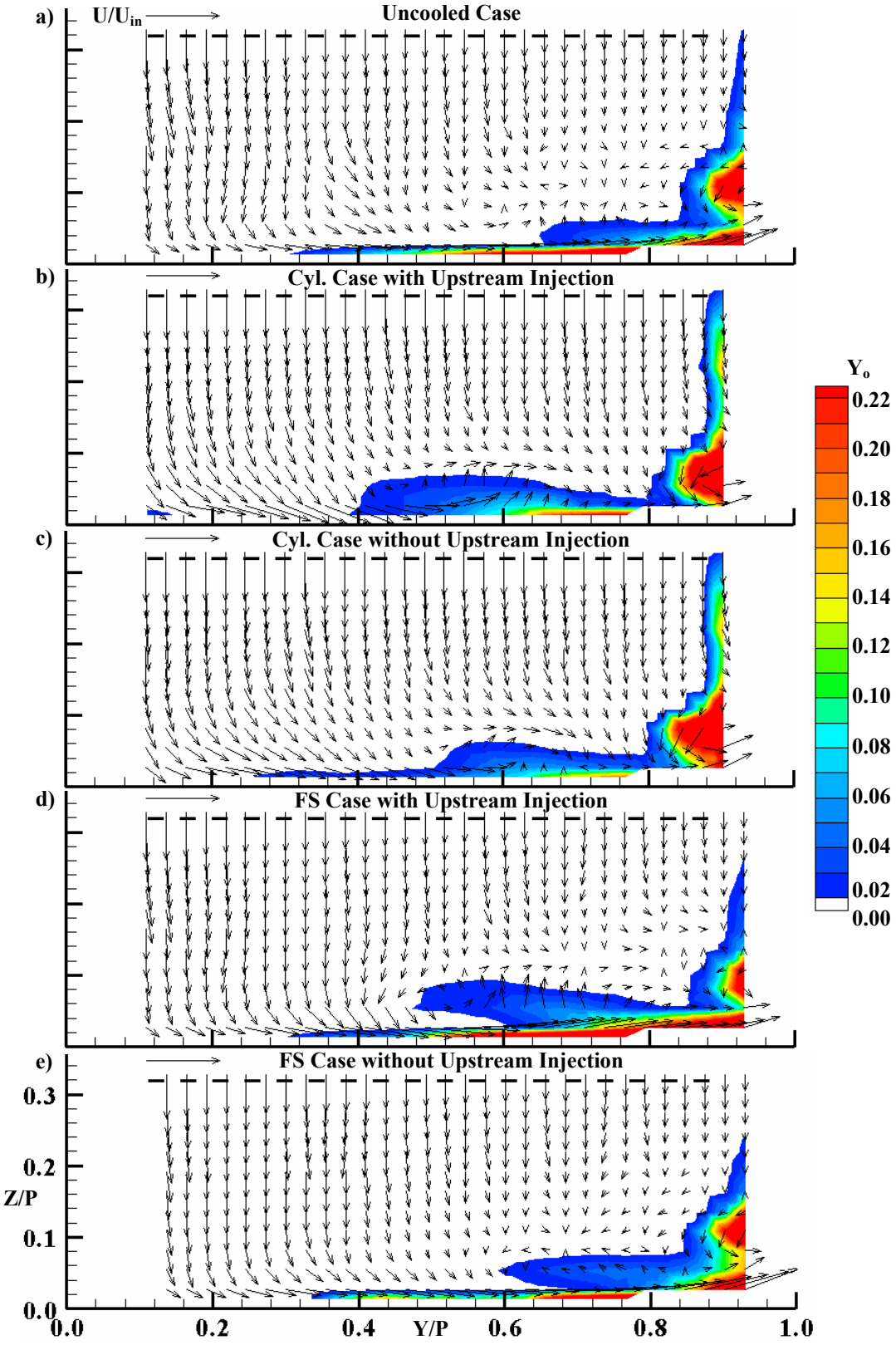

Figure 4.5. Contours of total pressure loss measured at the exit plane.

to a reduction in strength of the cross passage flow. Secondly, there was a region of high total pressure loss near the endwall wall extending from Y/P = 0.4 to Y/P = 0.7. These losses were undoubtedly a result of film-cooling jets mixing with the freestream. It is interesting to note that the secondary flow vectors along the wall near Y/P = 0.5 appear to be cutting under the mixed out film-cooling region and lifting it away from the surface.

The total pressure loss contour and secondary flow vectors for the cylindrical passage without upstream injection are shown in Figure 4.5c. The same general trends as for the case with upstream injection were seen, including the change in location of the passage vortex and the high losses near the wall from jet/freestream mixing. The main difference was that the mixing losses near the wall were not as great for the case without upstream injection. This suggests that the region of high mixing losses near the wall was partly caused by the upstream injection, in addition to the passage film-cooling.

Total pressure losses for the fan-shaped passage are shown in Figures 4.5d (upstream injection) and 4.5e (no upstream injection). For the case with upstream coolant injection, the position of the passage vortex remained unchanged from the uncooled case. The total pressure losses generated near the endwall for the fan-shaped passage had a strikingly different pattern than for the cylindrical passage. In the region from Y/P = 0.5 to Y/P = 0.75, the losses near the endwall in the fan-shaped passage decreased with span up to a height of approximately Z/P = 0.04. At that height, the losses increased again and showed a relative maximum at Z/P = 0.06. This pattern suggests that the film-cooling flow stays attached to the surface, with less loss in that region. The losses centered at Z/P = 0.06 would then be caused by the shear between the coolant layer and the freestream. Again, as with the cylindrical passage, some of the near wall losses appear to be a result of upstream injection, as they were greater for the case with upstream injection. The secondary flow vectors in the fan-shaped passage, although they indicated a stronger cross flow, did not seem to show the lift-off of near wall flow as with the cylindrical passage.

It is also useful to examine the change in total pressure losses that result from the addition of film-cooling. Figures 4.6a-d show the change in total pressure loss coefficient from the uncooled case to each film-cooled case. Note that a negative value of $(Y_o - Y_{o,base})$ indicated a decrease in total pressure relative to the uncooled case, while

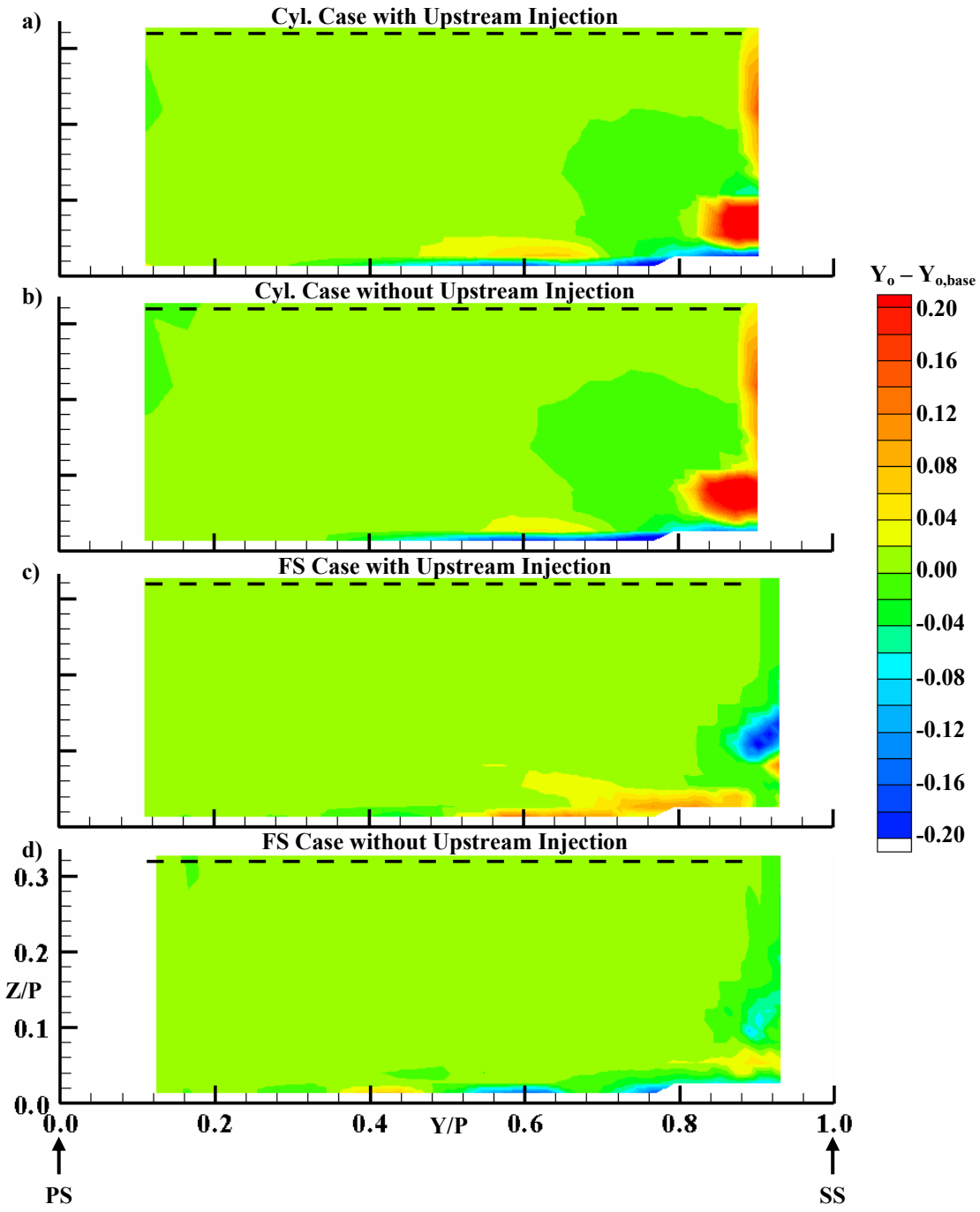

Figure 4.6. Contours of change in total pressure loss coefficient from the uncooled case measured at the exit plane.

a positive value of ($Y_o - Y_{o,base}$) meant there was an increase in total pressure. For all film-cooled cases, the majority of the passage shows virtually no change in total pressure loss from the uncooled case. Both cylindrical hole cases showed a large increase in total pressure in the region of the passage vortex. The increase was partially attributable to the

shift in location of the loss core away from the suction surface for the two cylindrical cases. However, it is likely that the maximum loss associated with the passage vortex was also enhanced. Barigozzi et al. [18] also reported an increase in total pressure loss generated by the passage vortex for a similar MFR with cylindrical hole film-cooling relative to the uncooled case.

For the fan-shaped passage, ($Y_o - Y_{o,base}$) values increased for the upstream injection case in the shear layer mixing region, as shown in Figure 4.6c. However, the upstream injection seemed to reduce the losses associated with the passage vortex for the fan-shaped case. The fan-shaped case without upstream cooling was the most similar to the uncooled case in terms of total pressure loss. There was very little change in either magnitude or distribution of the total pressure losses from the uncooled case to the fan-shaped case without upstream injection, with only a slight reduction in losses associated with the passage vortex and a slight increase in losses because of mixing and shear within the passage.

Because the main purpose of the nozzle guide vanes is to turn the flow as it enters the downstream first blade row, which extracts energy from the expanding hot gases, the exit angle of the flow through the passage is extremely important. Secondary flows such as the near wall cross flow decrease the overall efficiency of the engine because they alter the exit flow angles. Engine designers would like to have as uniform an exit flow angle as possible, or else the blade design must include these flow angles. Figure 4.7 shows pitch-averaged flow angles at the exit plane for each of the five cases as the difference from the midspan flow turning angle. The uncooled case had very little variation above $Z/Z_{max} = 0.1$. Both fan-shaped cases had a similar distribution of flow-turning angles along the span, with slightly higher turning near the wall. The cylindrical cases had significantly less turning in the near wall region, which means that the endwall cross flow was reduced. This corresponds to the shift in location of the passage vortex towards the pressure side from the uncooled case (Figures 4.5a-c). Although the cylindrical passage cases had less endwall cross flow, they did have a higher flow turning angle than the uncooled case from $Z/Z_{max} = 0.1$ to $Z/Z_{max} = 0.25$. The difference in flow turning angles between the uncooled cases and the cases with film-cooling stresses the importance of incorporating the changes in flowfield that are brought upon by film injection into the

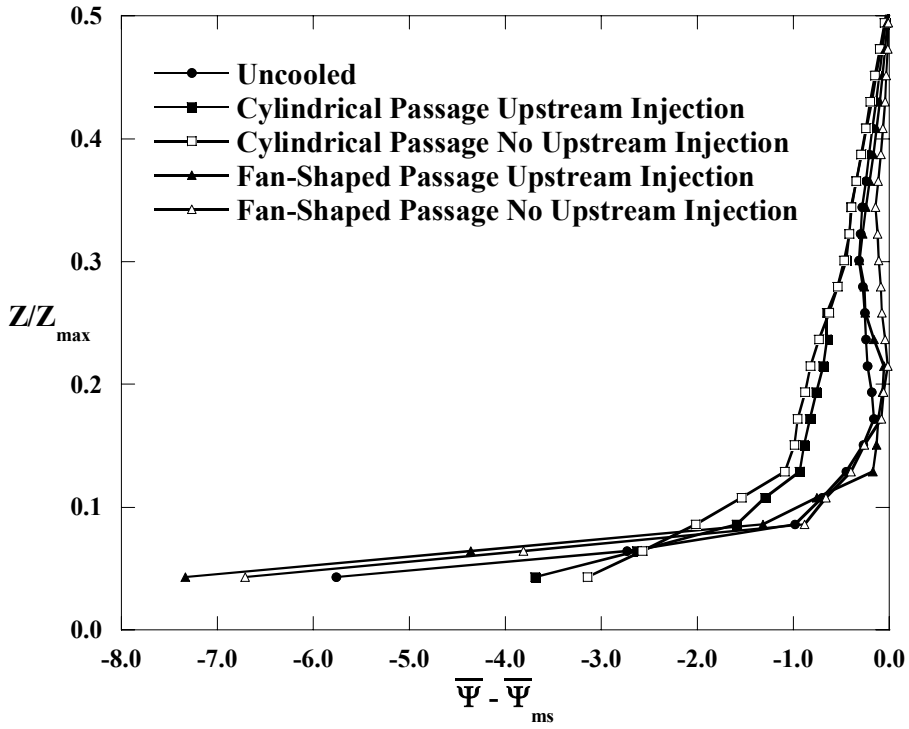

Figure 4.7. Pitch-averaged exit flow angles for each flow field case.

aerodynamic portion of the airfoil design.

Total pressure losses were mass-averaged according to Equation 4.3 using the two different definitions of $P_{o,ref}$, and those values are shown in Figure 4.8 for each flow case. The most obvious conclusion from the mass-averaged total pressure losses in Figure 4.8 is that cylindrical film-cooling greatly increased the total pressure losses through the vane passage, both with and without upstream blowing. Friedrichs et al. [19] also noted an increase in overall total pressure loss through the turbine cascade for cylindrical hole cooling. The results from this study verify the findings of Friedrichs et al. [19] for cylindrical holes, but suggest something different for fan-shaped holes. The mass-averaged total pressure losses through the turbine cascade for fan-shaped holes were only slightly higher than the uncooled case for the case without upstream injection. Even the fan-shaped case with upstream injection had a lower mass-averaged total pressure loss than the cylindrical case without upstream injection. The main reason for this, despite the added mixing losses generated from the upstream blowing, was the reduction in losses associated with the passage vortex. Because the fan-shaped holes did not separate from the endwall surface as the cylindrical holes did, there was less interaction with the freestream and subsequently less mixing losses in the fan-shaped passage.

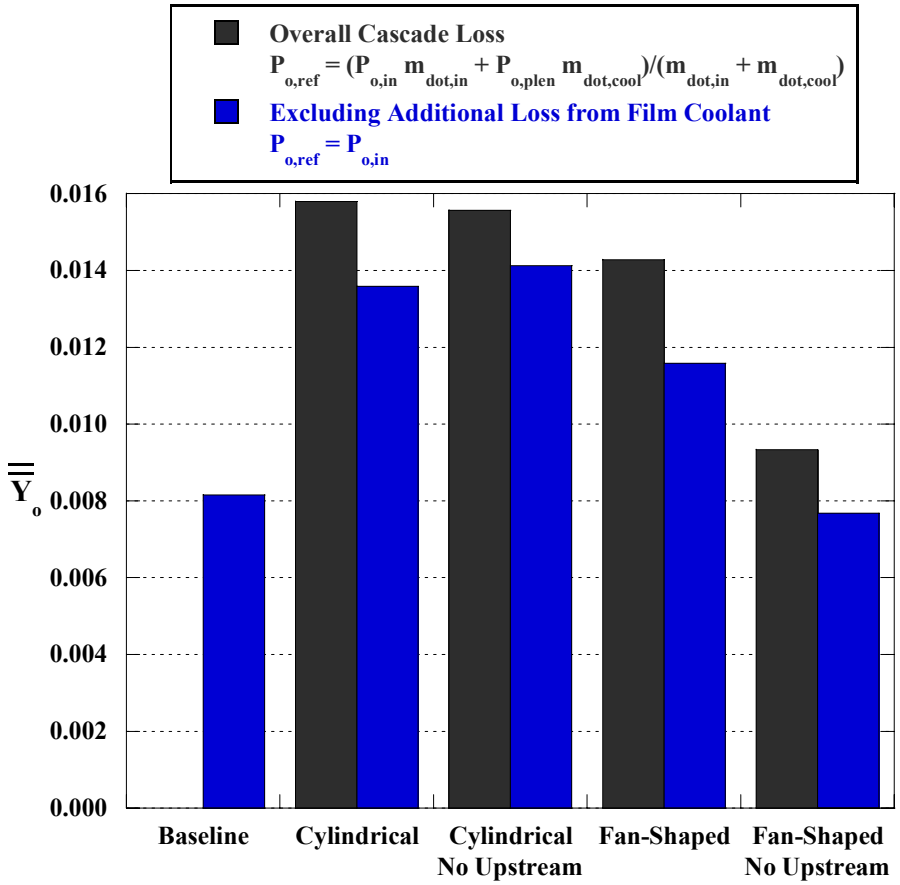

Figure 4.8. Mass-averaged total pressure loss for each flow field case.

Using the inlet stagnation pressure as the reference stagnation pressure rather than Equation 4.4 in the definition of the total pressure loss coefficient resulted in lower $\overline{\overline{Y}}_o$ values for each film-cooled case (shown in Figure 4.8). The reason is that although Equation 4.4 incorporated the additional energy being added to the passage flow by the coolant, it also included the losses that occur within the film-cooling holes.

The effect of upstream injection on the mass-averaged total pressure loss through the cascade depends on the film-cooling hole shape. With cylindrical holes, only a slight increase in $\overline{\overline{Y}}_o$ was seen. The reason was that the cylindrical holes in the passage separate and generate a large amount of mixing within the passage. Any additional mixing caused by the upstream blowing does not significantly add to the total pressure loss. The fan-shaped holes, on the other hand, do not separate and therefore do not generate large mixing losses by themselves. For this reason the mixing losses generated by the upstream blowing in the fan-shaped passage were much more significant in terms of raising the overall losses. The reduction in passage vortex losses for the fan-shaped

passage also contributed to the lower mass-averaged $\overline{\overline{Y}}_o$ values than for the cylindrical passage. The study by Barigozzi et al. [18] showed little difference between the losses generated for their fan-shaped passage versus their cylindrical passage. This however, was attributed to the different number of holes between the the two passages. At the same mass flow rate, fewer holes in the fan-shaped passage caused higher jet velocities, leading to higher losses inside the hole than what would be seen if there had been a one-to-one comparison.

Adiabatic Film-Cooling Effectiveness Measurements

Adiabatic film-cooling effectiveness measurements are shown in Figures 4.9a-f for the cases with upstream coolant injection and in Figures 4.10a-f for the cases without upstream injection. The cases shown in Figures 4.9a-f with upstream injection were described in detail by Colban et al. [27] and are shown in this paper for comparison purposes. It is particularly interesting that the upstream rows provided no immediate cooling benefit to the endwall surface in any of the contours in Figure 4.9. All of the coolant ejected from the upstream holes was completely separated from the surface, even at the lowest tested MFRs due to the high surface angle.

In examining the differences between the cases without upstream coolant (shown in Figure 4.10) and the cases with upstreamcoolant (shown in Figure 4.9), it is immediately obvious that the overall levels of film-cooling effectiveness for the cases without upstream injection were much lower. This is interesting given the fact that the upstream holes offer no visible cooling benefit themselves, one would not expect levels further downstream to be greatly reduced in the absence of upstream injection, although certainly some of the improvement was probably due to a cooler near wall fluid from the upstream blowing. Pressure ratios were matched between cases shown in Figures 4.9 and 4.10, so for instance, the passage film-cooling flow in Figures 4.9a and 4.10a are directly comparable. In Figure 4.10a, the MFR is 0.36% for the passage film-cooling holes, while in Figure 4.9a, the MFR was 0.36% for the passage film-cooling holes and 0.19% for the upstream holes (making 0.55% total MFR for the case in Figure 4.9a). Considering the fact that the amount of coolant issued from the film-cooling holes within the passage was the same for the cases in both Figure 4.9 and Figure 4.10, it is suggested and confirmed

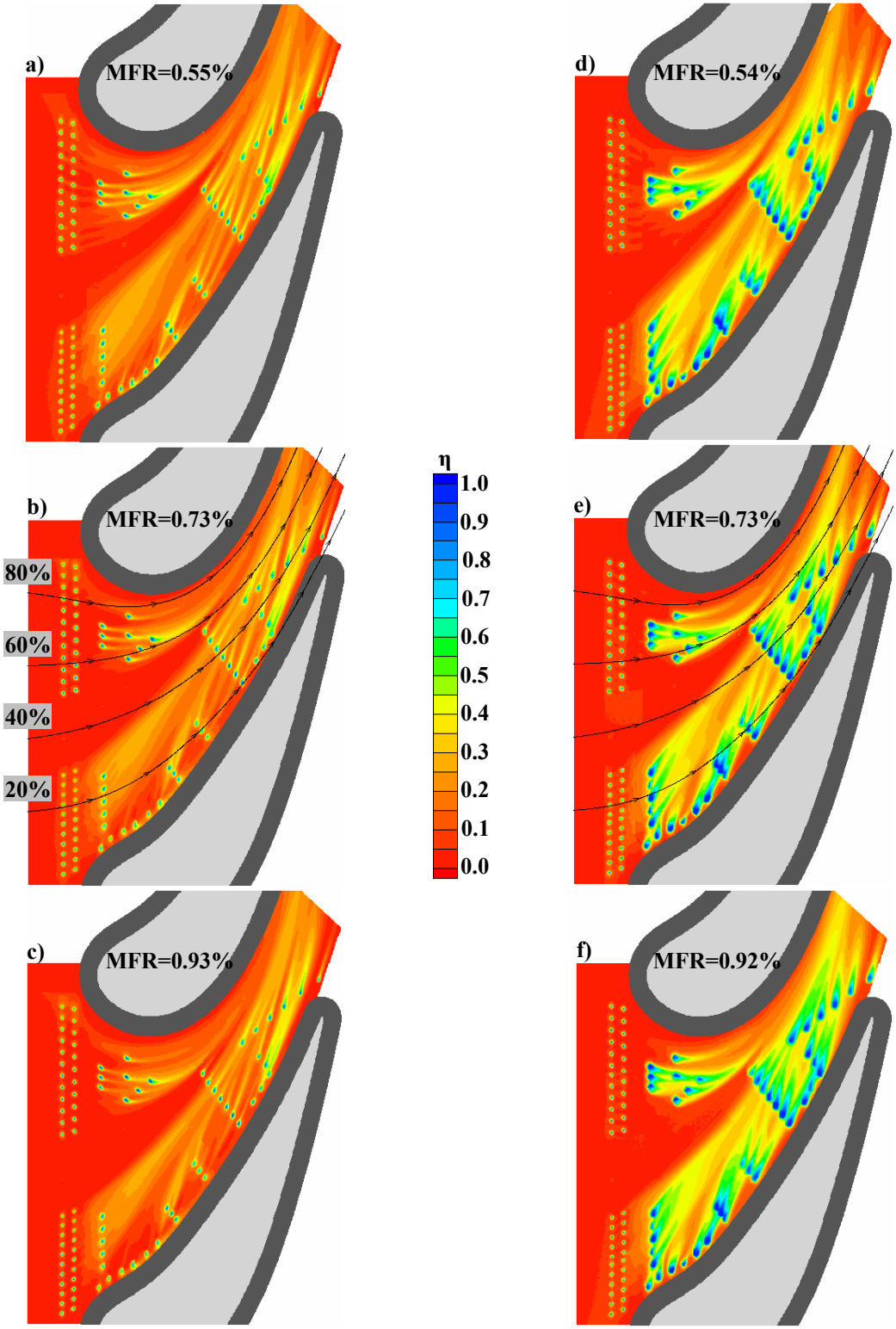

Figure 4.9. Effectiveness contours with upstream coolant injection for the cylindrical (a-c) and fan-shaped passage (d-f).

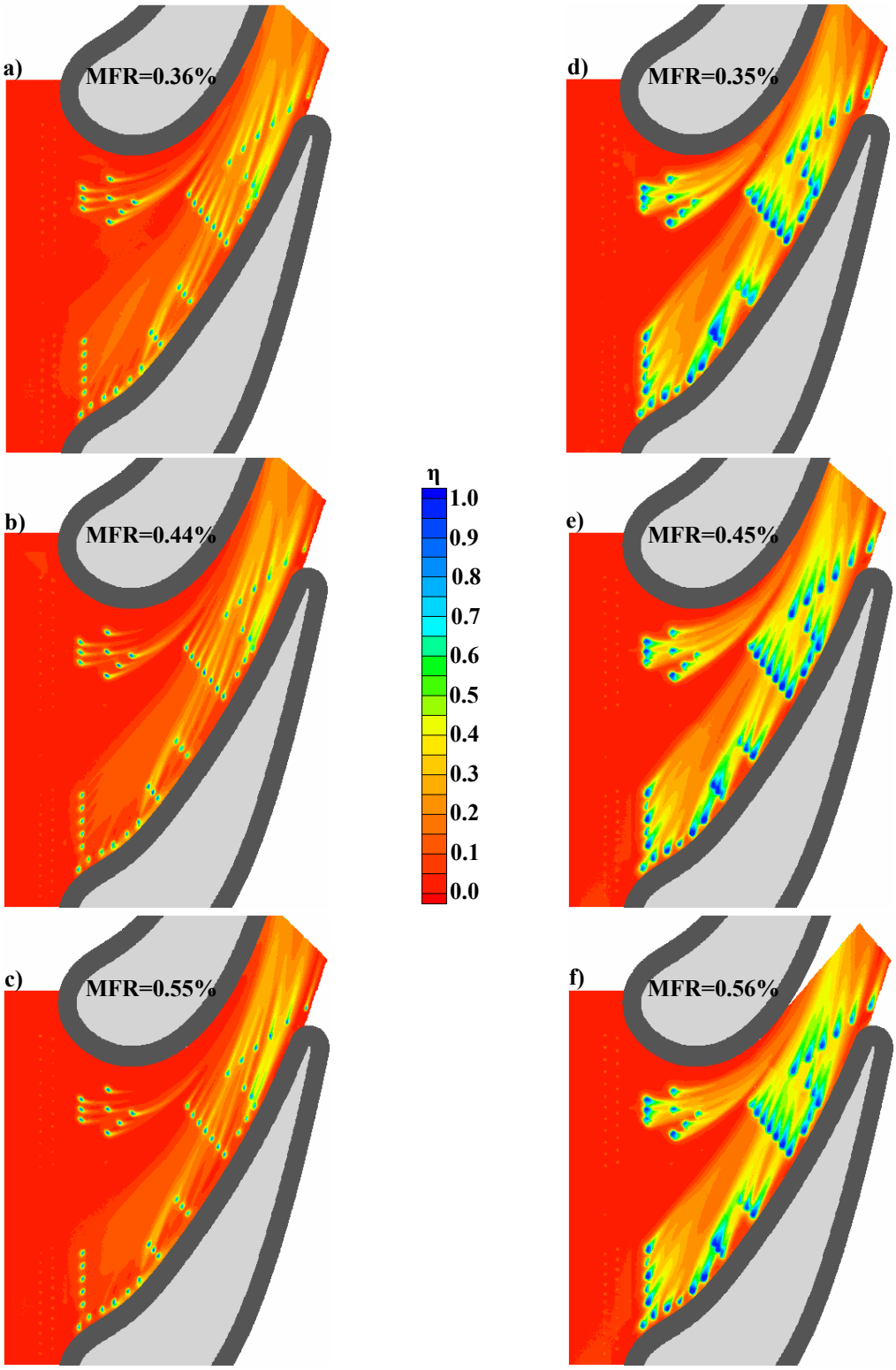

Figure 4.10. Effectiveness contours without upstream coolant injection for the cylindrical (a-c) and fan-shaped passage (d-f).

by the flowfield measurements that upstream coolant injection must alter the passage flow field in such a way as to make downstream endwall film-cooling more effective.

Figure 4.11 shows the laterally averaged effectiveness in the cylindrical passage for the MFR = 0.44% case without upstream injection cooling. The general trend is increased $\overline{\eta}$ throughout the passage, indicating that film-cooling had a beneficial compounding effect. Also shown in Figure 4.11 is the augmentation in laterally averaged film-cooling effectiveness for the MFR = 0.36% and MFR = 0.55% cases with respect to the MFR = 0.44% case. Just as for the case with upstream injection ([27]), $\overline{\eta}$ decreased with increased MFR. The reason for this was that the cylindrical jets separated from the surface rendering inefficient endwall cooling, and the separation got worse with increasing MFR.

The laterally averaged film-cooling effectiveness and augmentation are shown for the fan-shaped passage with no upstream injection in Figure 4.12. Again, $\overline{\eta}$ increased throughout the passage, with overall levels of $\overline{\eta}$ being much higher than the cylindrical passage without upstream injection (Figure 4.11). The effect of increasing MFR on the fan-shaped passage was opposite to the cylindrical passage. Because the fan-shaped

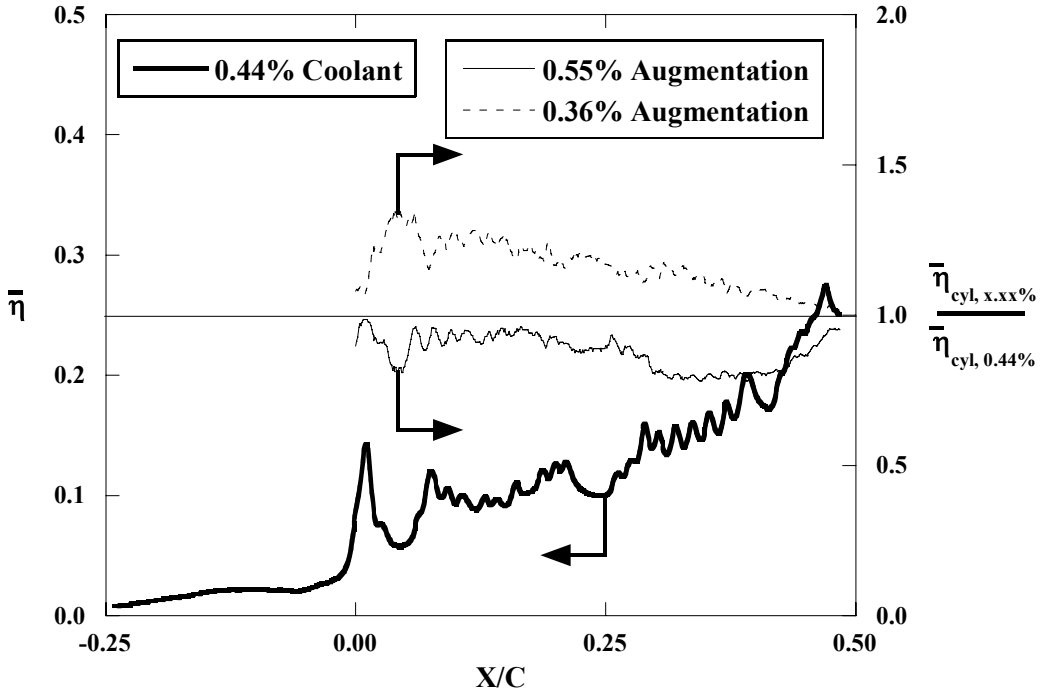

Figure 4.11. Laterally averaged effectiveness for the MFR = 0.44% case and augmentation of laterally averaged effectiveness for the MFR = 0.36% and MFR = 0.55% cases on the cylindrical passage with no upstream cooling.

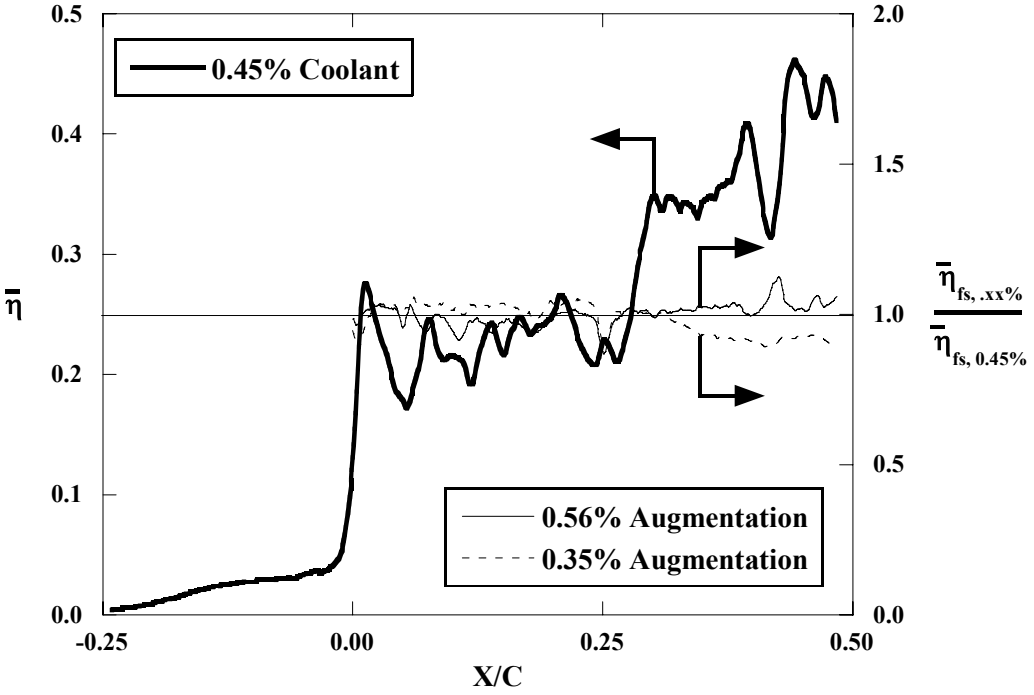

Figure 4.12. Laterally averaged effectiveness for the MFR = 0.45% case and augmentation of laterally averaged effectiveness for the MFR = 0.35% and MFR = 0.56% cases on the fan-shaped passage with no upstream cooling.

holes diffused the coolant jet as it exited the hole, it was not prone to separation as was the cylindrical hole jet. For this reason, $\overline{\eta}$ increased with increasing MFR, yielding the intuitive result of increased cooling performance with increased MFR.

Figures 4.13 and 4.14 both show the augmentation, or lack thereof, in $\overline{\eta}$ without upstream coolant injection versus with upstream coolant injection. For both the cylindrical (Figure 4.13) and the fan-shaped (Figure 4.14) passage, it is clear that upstream coolant injection yielded a significant increase in $\overline{\eta}$. This effect was seen fairly uniformly across all measured MFRs.

The augmentation in $\overline{\eta}$ for the fan-shaped passage versus the cylindrical passage without upstream coolant injection is shown in Figure 4.15. Just as with upstream coolant injection ([27]), the fan-shaped cooling holes offered significantly better film-cooling performance than their cylindrical counterparts. The augmentation in $\overline{\eta}$ increased with MFR as a result of the opposite influence of MFR on the $\overline{\eta}$ performance between the two passages.

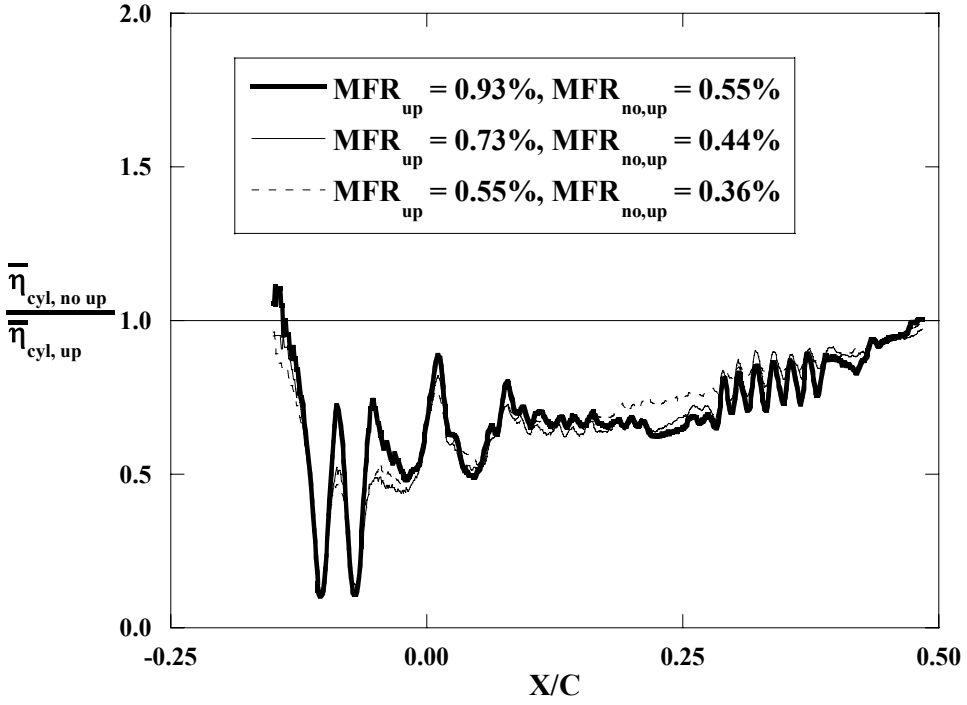

Figure 4.13. Augmentation of laterally-averaged film-cooling effectiveness for the cylindrical passage with and without upstream cooling.

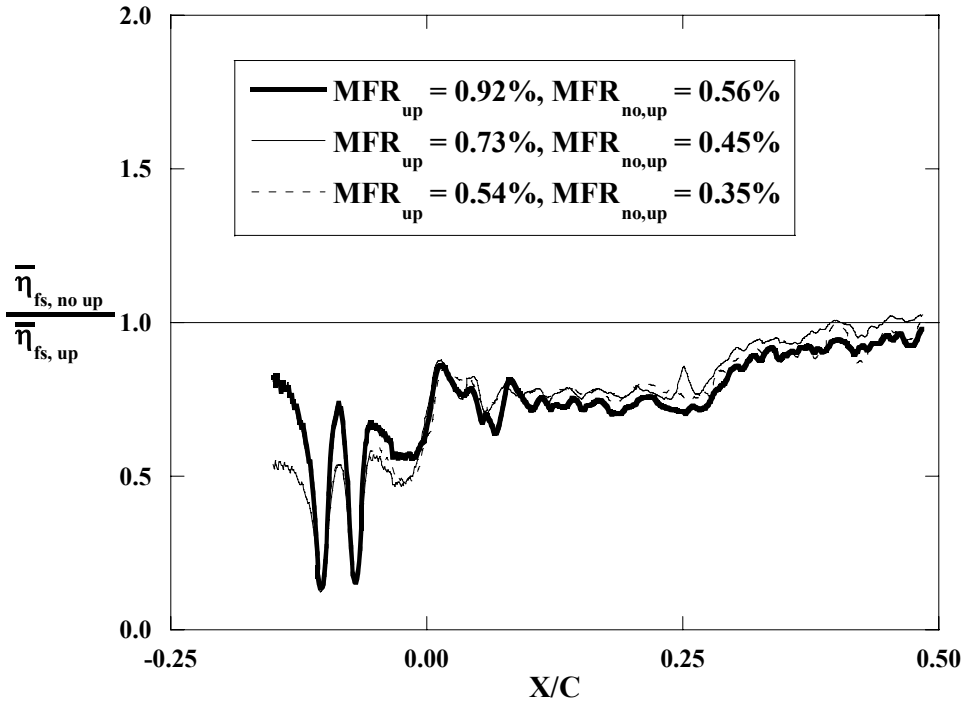

Figure 4.14. Augmentation of laterally-averaged film-cooling effectiveness for the fan-shaped passage with and without upstream cooling.

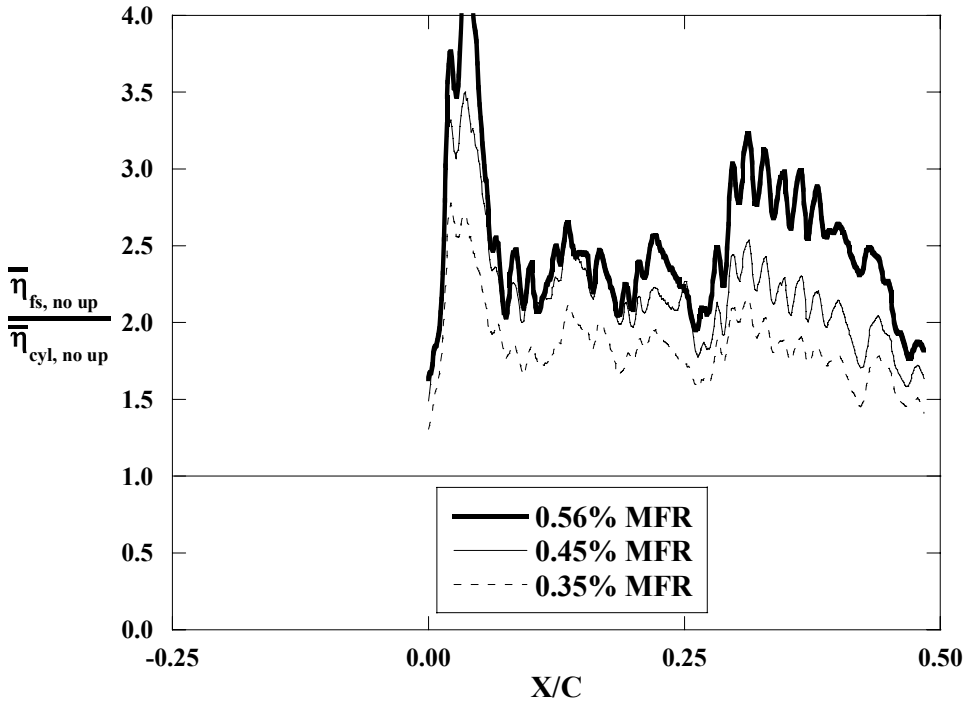

Figure 4.15. Augmentation of laterally-averaged film-cooling effectiveness for fan-shaped cooling holes over cylindrical cooling holes without upstream injection.

Area-Averaged Film-Cooling Effectiveness

Area-averaged values of adiabatic film-cooling effectiveness were calculated over the endwall from X/C = -0.25 to X/C = 0.5 (the vane trailing edge) across one vane pitch. Area-averaged effectiveness offered a sense of the benefit gained by the entire endwall surface in any given cooling configuration (geometry and flow condition). Figure 4.16 shows the area-averaged film-cooling effectiveness for each case reported in Table 4.3. The trends of increasing effectiveness with MFR for the fan-shaped passage, and decreasing effectiveness with MFR for the cylindrical passage can be seen clearly. The trend between the cases with and without upstream coolant injection was not linear, which suggests that the upstream coolant injection altered the flowfield in such a way as to allow the downstream film-cooling to be more effective. Also shown for comparison purposes is a data point from Friedrichs et al. [16]. This point fell nearly on the line for the cylindrical passage with upstream cooling. Their study had a very different cooling hole pattern from the one used in this study. Although they used cylindrical holes, they had four rows of holes located at axial positions of X/C = 0.0, 0.3, 0.6, and 0.9. The first row at X/C = 0 in the study by Friedrichs et al. [16] could act the same as the upstream

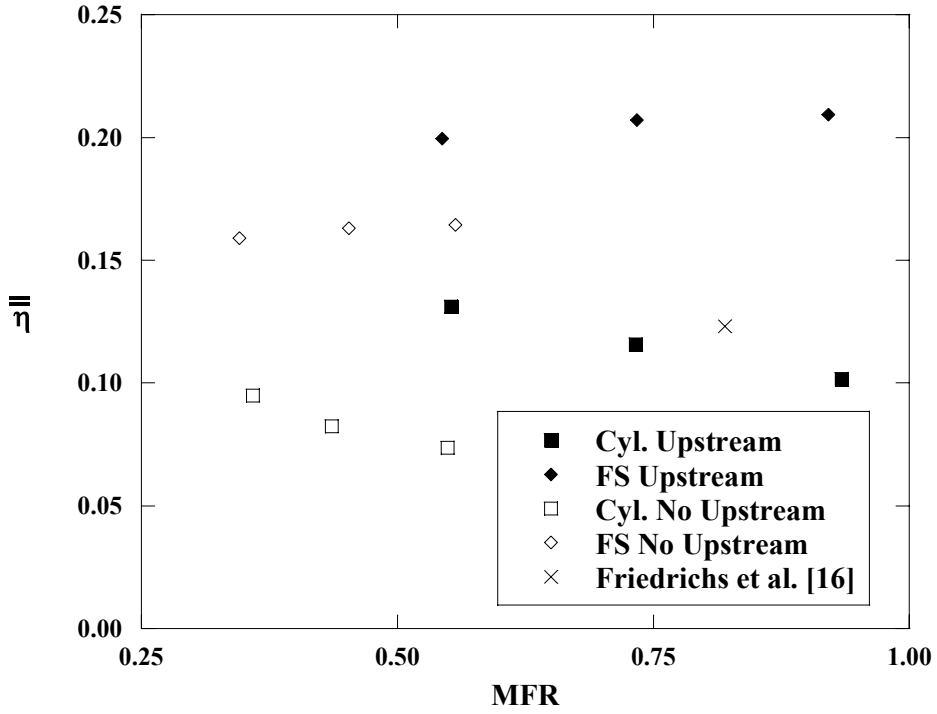

Figure 4.16. Area-averaged film-cooling effectiveness for all cases including results from Friedrichs et al. [16].

coolant injection from this study. The difference in hole layout between the two studies suggests that even though the local effectiveness footprint may vary significantly, perhaps there is an insensitivity of area-averaged effectiveness to certain aspects of the hole layout.

Conclusions

As mentioned previously, the goals of this study were to evaluate the effect of upstream coolant injection on the exit plane flowfield for both cylindrical and fan-shaped holes, and also to quantify the effect of upstream coolant injection on the cooling performance of film-cooling holes located within the vane passage on the endwall. To accomplish the first goal, a five-hole total pressure probe was used to measure the exit plane flowfield with and without upstream injection for passages featuring cylindrical and fan-shaped holes. The effect of upstream coolant injection on endwall film-cooling effectiveness was examined by using an infrared camera to measure adiabatic film-cooling effectiveness for both fan-shaped and cylindrical passages with and without upstream injection.

The flowfield results indicated that cylindrical hole film-cooling increased the total pressure losses generated by the passage vortex. Cylindrical hole film-cooling did reduce the strength of the cross-passage flow, shifting the location of the passage vortex towards the pressure side. The coolant separation in the cylindrical passage, which was evident from the effectiveness contours, generated high mixing losses with the freestream. The fan-shaped holes did not separate from the endwall, but the shear layer between the coolant and the freestream still generated significant losses.

Both passages showed increased mixing and shear losses with upstream injection relative to no upstream injection. Overall mass-averaged losses for the cylindrical passage were much higher than the uncooled case because of the increase in passage vortex losses and the added mixing losses. Overall mass-averaged losses for the fan-shaped passage were nearly the same as for the uncooled case because the added shear layer losses were counteracted by the reduction in losses generated by the passage vortex. The flowfield results showed that fan-shaped holes generated less total pressure loss than cylindrical holes, especially with no upstream blowing.

The adiabatic film-cooling effectiveness measurements showed that the coolant from the upstream holes had little immediate cooling benefit to the endwall in the region just downstream of the upstream injection, with the coolant separating entirely from the endwall because of the high injection angle. However, further downstream in the passage, effectiveness levels for the cases with upstream coolant were much higher, the reason being that there was a large amount of coolant in the passage region from the upstream injection. This coolant mixed with the freestream and lowered the temperature of the near-wall fluid, resulting in higher effectiveness levels downstream in the passage. The flow field results also indicated an influence on the passage flowfield by the upstream coolant injection, which could have also contributed to the higher effectiveness levels. The effect of increased MFR was to decrease $\overline{\eta}$ in the cylindrical passage because of jet separation. In the fan-shaped passage the effect of increased MFR was to increase $\overline{\eta}$ because the fan-shaped coolant jets stayed attached to the endwall surface.

The results of this study further illustrate the complexity of the film-cooling design process. The addition of film-cooling holes on a turbine endwall has aerodynamic consequences in addition to the thermal benefit that might be gained. Incorrect

placement of film-cooling holes can also prove wasteful. It is critical that engine designers be aware of both the thermal and aerodynamic consequences of their film-cooling hole designs. The results of this study are clear in their recommendation of fan-shaped holes over cylindrical holes from both an aerodynamic and thermal perspective. Fan-shaped holes showed lower total pressure losses, while at the same time providing better film-cooling effectiveness than cylindrical holes.

Acknowledgments

The authors are grateful to Siemens Power Generation for their funding and support of this project.

Nomenclature

C true vane chord

D film-cooling hole diameter

I local momentum flux ratio, $I = \rho_{cool}U_{cool}^2/\rho_{in}U_{in}^2$

k thermal conductivity

$\dot{m}$ mass flow rate

M local blowing ratio, $M = \rho_{cool}U_{cool}/\rho_{in}U_{in}$

MFR % total coolant mass flow per total passage mass flow

P pressure, vane pitch

PS pressure side

Re Reynolds number, $Re = U_{in}C/\nu$

S distance along the surface of the vane, measured from the vane stagnation

SS suction side

t hole breakout distance

T temperature

U velocity

V_n velocity normal to the streamwise direction, $V_n = V_s\sin(\Psi_{ms} - \Psi)$

V_s streamwise velocity

V_z spanwise component of velocity, $V_n = V_s\sin(\Phi)$

X axial coordinate measured from the vane stagnation

Y	pitchwise coordinate
Y_o	total pressure loss coefficient, $Y_o = (P_{o,ref} - P_{o,exit})/ (P_{o,ref} - P_{s,exit})$
Z	spanwise coordinate

Greek

α	inclination angle
ν	kinematic viscosity
η	adiabatic film-cooling effectiveness, $\eta = (T_\infty - T_{surf})/(T_\infty - T_{cool})$
ρ	density
φ_1	lateral diffusion angle
φ_2	forward expansion angle
Φ	pitch angle
Ψ	yaw/flow turning angle

Subscripts

∞	freestream
base	baseline case without any film-cooling
cool	coolant
cyl	cylindrical holes
exit	exit plane
fs	fan-shaped holes
in	inlet condition
max	maximum value
ms	mid-span
no up	no upstream injection
o	total, uncooled effectiveness for conduction correction
plen	plenum
ps	pressure side
ref	reference value
s	static
ss	suction side

surf surface

up upstream injection

Overbar

– lateral/pitchwise average

= area average or mass average

References

[1] Morris A. W. H. and Hoare, R. G., "Secondary Loss Measurements in a Cascade of Turbine Vanes with Meridional Wall Profiling," 75-WA/GT-13, 1975.

[2] Kercher, D. M., *Film-Cooling Bibliography: 1940-2002*: Private publication, 2003.

[3] Kercher, D. M., *Film-Cooling Bibliography Addendum: 1999-2004*: Private publication, 2005.

[4] Goldstein, R. J., "Film Cooling," *Advances in Heat Transfer*, vol. 7, pp. 321-379, 1971.

[5] Bogard, D. G. and Thole, K. A., "Gas Turbine Film Cooling," *to appear in the AIAA Journal of Propulsion*, 2006.

[6] Bunker, R. S., "A Review of Shaped Hole Turbine Film-Cooling Technology," *ASME Journal of Heat Transfer*, vol. 127, pp. 441-453, 2005.

[7] Blair, M. F., "An Experimental Study of Heat Transfer and Film Cooling on Large-Scale Turbine Endwalls," *ASME Journal of Heat Transfer*, vol. 96, pp. 524-529, 1974.

[8] Granser, D. and Schulenberg, T., "Prediction and Measurement of Film Cooling

Effectiveness for a First Stage Turbine Vane Shroud," 90-GT-95, 1990.

[9] Colban, W., Thole, K. A., and Zess, G., "Combustor Turbine Interface Studies - Part 1: Endwall Effectiveness Measurements," *ASME Journal of Turbomachinery*, vol. 125, pp. 193-202, 2003.

[10] Knost, D. G. and Thole, K. A., "Computational Predictions of Endwall Film-Cooling for a First Stage Vane," GT2003-38252, 2003.

[11] Knost, D. G. and Thole, K. A., "Adiabatic Effectiveness Measurements of Endwall Film-Cooling for a First Stage Vane," *ASME Journal of Turbomachinery*, vol. 127, pp. 297-305, 2005.

[12] Harasgama, S. P. and Burton, C. D., "Film Cooling Research on the Endwall of a Turbine Nozzle Guide Vane in a Short Duration Annular Cascade: Part 1-Experimental Technique and Results," *ASME Journal of Turbomachinery*, vol. 114, pp. 734-740, 1992.

[13] Nicklas, M., "Film-Cooled Turbine Endwall in a Transonic Flow Field: Part II - Heat Transfer and Film-Cooling Effectiveness," 2001-GT-0146, 2001.

[14] Langston, L. S., Nice, M. L., and Hooper, R. M., "Three-Dimensional Flow Within a Turbine Cascade Passage," *ASME Journal of Engineering Power*, vol. 99, pp. 21-28, 1977.

[15] Sieverding, C. H. and Wilputte, P., "Influence of Mach Number and Endwall Cooling on Secondary Flows in a Straight Nozzle Cascade," *ASME Journal of Engineering for Gas Turbines and Power*, vol. 103, pp. 257-264, 1981.

[16] Friedrichs, S., Hodson, H. P., and Dawes, W. N., "Distribution of Film-Cooling Effectiveness on a Turbine Endwall Measured Using the Ammonia and Diazo

Technique," *ASME Journal of Turbomachinery*, vol. 118, pp. 613-621, 1995.

[17] Kost, F. and Nicklas, M., "Film-Cooled Turbine Endwall in a Transonic Flow Field: Part I - Aerodynamic Measurements," 2001-GT-0145, 2001.

[18] Barigozzi, G., Benzoni, G., Franchini, G., and Perdichizzi, A., "Fan-Shaped Hole Effects on the Aero-Thermal Performance of a Film Cooled Endwall," GT2005-68544, 2005.

[19] Friedrichs, S., Hodson, H. P., and Dawes, W. N., "Aerodynamic Aspects of Endwall Film-Cooling," *ASME Journal of Turbomachinery*, vol. 119, pp. 786-793, 1997.

[20] Oke, R. A., Burd, S. W., Simon, T. W., and Vahlberg, R., "Measurements in a Turbine Cascade over a Contoured Endwall: Discrete Hole Injection of Bleed Flow," 2000-GT-214, 2000.

[21] Zess, G. and Thole, K. A., "Computational Design and Experimental Evaluation of Using a Leading Edge Fillet on a Gas Turbine Engine," *ASME Journal of Turbomachinery*, vol. 124, pp. 167-175, 2002.

[22] Lethander, A. T. and Thole, K. A., "Optimizing the Vane-Endwall Junction to Reduce Adiabatic Wall Temperatures in a Turbine Vane Passage," GT2003-38940, 2003.

[23] Becz, S., Majewski, M. S., and Langston, L. S., "Leading Edge Modification Effects on Turbine Cascade Endwall Loss," GT2003-38898, 2003.

[24] Mahmood, G. I., Gustafson, R., and Acharya, S., "Experimental Investigation of Flow Structure and Nusselt Number in a Low-Speed Linear Blade Passage With and Without Leading-Edge Fillets," *ASME Journal of Heat Transfer*, vol. 127, pp.

499-512, 2005.

[25] Zhang, L. J. and Jaiswal, R. S., "Turbine Nozzle Endwall Film Cooling Study Using Pressure-Sensitive Paint," *ASME Journal of Turbomachinery*, vol. 123, pp. 730-738, 2001.

[26] Zhang, L. and Moon, H. K., "Turbine Nozzle Endwall Inlet Film Cooling - The Effect of a Back-Facing Step," GT2003-38319, 2003.

[27] Colban, W., Thole, K. A., and Haendler, M., "A Comparison of Cylindrical and Fan-Shaped Film-Cooling Holes on a Vane Endwall at Low and High Freestream Turbulence Levels," GT2006-90021, 2006.

[28] Colban, W., Gratton, A., Thole, K. A., and Haendler, M., "Heat Transfer and Film-Cooling Measurements on a Stator Vane with Fan-Shaped Cooling Holes," GT2005-68258, 2005.

[29] Colban, W., Thole, K. A., and Haendler, M., "Experimental and Computational Comparisons of Fan-Shaped Film-Cooling on a Turbine Vane Surface," IMECE2005-79596, 2005.

[30] Moffat, R. J., "Describing the Uncertainties in Experimental Results," *Experimental Thermal and Fluid Science*, vol. 1, pp. 3-17, 1988.

Summary of Findings and Recommendations for Future Work

This research focused on the performance of fan-shaped film-cooling holes on the critical vane and endwall surfaces in a gas turbine vane. The first two papers dealt with the vane results, while the last two papers dealt with the endwall results. The vane results were split into single row measurements, discussed in the first paper, and multiple row results and comparisons to computational predictions, which were discussed in the second paper. A comparison of fan-shaped and cylindrical holes on the endwall at both high and low freestream turbulence was given in the third paper. The fourth and final paper gave a summary of the effect of upstream injection on the endwall for both hole geometries, and examined the aerodynamic performance of both hole shapes for the endwall.

The first paper described in detail the high-resolution single-row adiabatic film-cooling effectiveness measurements on the vane with fan-shaped holes. A number of critical regions were identified, including the first pressure side row and the first suction side row. The first pressure side row was located in a region of concave curvature. The coolant partially separated before reattaching further along the surface. The reattachment acted as an impingement, spreading the coolant laterally and raising effectiveness levels. The first suction side row was located in a region of convex curvature. The coolant from this row separated from the surface because of the strong curvature, with lower blowing ratios offering better cooling for this region. Showerhead measurements also revealed significant lift-off with higher blowing ratios, resulting from the high surface angles of the showerhead holes.

The second paper was meant to be a parallel paper to the first, offering film-cooling measurements on the vane with multiple rows of cooling holes. Overall, effectiveness levels increased with blowing ratio for the multiple row configurations, as compared to a reduction in cooling effectiveness with blowing ratio for most of the single rows of holes as reported in the first paper. The CFD predictions offered mixed results, with the RNG-kε model coming closer to the averaged film-cooling effectiveness levels, while the v^2-f model gave a better prediction of the separation at the leading edge. The v^2-f model, however, had trouble predicting the lateral spreading of the coolant, which

resulted in an over-prediction of film-cooling effectiveness.

The third paper gave a direct comparison of fan-shaped holes to cylindrical holes on the endwall surface with high and low freestream turbulence. The major finding from that study was to show that fan-shaped holes offered an increase in film-cooling effectiveness of 75% percent over cylindrical holes at low freestream turbulence. The reason was that the fan-shaped holes spread out more in the lateral direction and stayed attached to the surface, while the cylindrical cooling holes showed little lateral spreading and separated off of the surface. The effect of high freestream turbulence was to reduce the effectiveness by 6% in the fan-shaped passage and to change the dependency of effectiveness on flow rate for the cylindrical passage.

The fourth and final paper examined the effect of upstream coolant injection on the film-cooling performance for both cooling hole geometries on the endwall. The aerodynamic performance of each cooling hole shape on the endwall was also investigated using a five-hole probe to measure total pressure losses through the passage. While upstream coolant injection offered little immediate cooling benefit in the near-hole region, it saturated the near-wall region with coolant and increased effectiveness levels in the endwall region downstream. Flowfield measurements showed that the highest losses in the exit plane were generated by the passage vortex. Cylindrical film-cooling tended to reduce the strength of the cross-passage flow and increase the strength of the losses generated by the passage vortex. High losses resulted from separated film-cooling mixing with the freestream in the cylindrical passage. For the fan-shaped passage, the coolant remained near the wall, and the shear layer between the coolant and freestream generated additional losses. For both passages, upstream coolant injection generated additional mixing losses.

One other major achievement of this work was related to the data processing. A unique transformation routine was developed to unwrap distorted surface images into rectangular coordinates. The transformation routine was necessary to yield quantifiable results on the vane surface. The unique approach taken to measure film-cooling effectiveness from below the test section allowed previously unobtainable high resolution measurements on the vane surface.

Recommendations for Future Work

Although this study offered a comprehensive examination of fan-shaped film-cooling in the turbine vane passage, there is still a significant amount of work that could be done to better understand the behavior of film-cooling in the extremely complex region. There are a number or areas in which additional research could be performed, including vane heat transfer with film-cooling.

In a study that paralleled this research, Gratton [1] measured heat transfer coefficients on the vane surface for the same airfoil shape. Although a great amount was learned from that work, the original desire was to also measure heat transfer coefficients with vane film-cooling. The measurement of surface heat transfer coefficients with film-cooling should be performed.

The computational predictions shown in paper 2 of this study were not as close as hoped for. Obviously there is significant room for improvement in the area of full-scale multiple-row film-cooling predictions. Many current computational film-cooling studies involve the modeling of only a single hole, or very few holes. Although the capability exists to accurately model those more simple situations, often accurate solutions require time-dependent models with resolution down to $y^+ < 1$. Obviously those types of computations cannot be done yet for the full vane, although because of the complexity of film-cooling flow, perhaps time-dependent calculations will be required for the multiple-row configuration as well to obtain more accurate predictions.

For the endwall measurements, although a lot of information can be extracted from surface measurements, there is still the need for field measurements, both thermal and flowfield. It is possible to determine whether or not a cooling jet separates from the surface from surface measurements of adiabatic film-cooling effectiveness. However, the surface measurements offer no indication of how the separated film migrates through the passage. Also, more flowfield measurements within the passage would provide a glimpse of the secondary flow development through the passage. There is still much to learn as to how the upstream injection affects the passage flow development.

One other investigation that would be particularly interesting would be a combined vane and endwall film-cooling study. During engine operation both the vane and endwall surfaces are film-cooled. In the presence of secondary flows, which sweep

flow down the vane pressure side surface and onto the endwall, perhaps some of the vane film-cooling near the vane-endwall junction has some cooling benefit for the endwall surface. The current facility was constructed with this particular investigation in mind for future researchers.

References

[1] Gratton, A., 2004, "Measurements and Predictions of Heat Transfer for a First Vane Design," Master's Thesis, Virginia Polytechnic and State University.

Appendix A:
Design and Construction of Experimental Facilities

Vane Construction

There were many considerations that went into designing the film-cooling vane, some of which were hole layout, plenum division, material selection, manufacturing technique, and instrumentation. This section describes the development of the film-cooling vane design in detail, describing each of the considerations listed above. The first step in the design process was determined by the exit width from the combustor simulator test section in the VTExCCL wind tunnel. In order to have two passages with a center film-cooled vane, the maximum possible scaling parameter was 3X from the airfoil geometry given by Siemens.

The design of the vane was in large part dictated by the sponsor, and a considerable effort was made to maintain the integrity of the engine design in the large-scale wind tunnel facility. The hole geometry, the surface locations on the vane of each row of holes, the wall thickness, and the relative hole spacing were all taken from the Siemens engine design and applied to the 3X scale experimental vane. The actual Siemens vane is shown in Figure A.1a, alongside the vane design for this study at 3X scale (Figure A.1b). The airfoil profile shape is identical for both designs, as well as the hole placement of each row that was modeled.

Slight adjustments were made to the hole spacing in the spanwise direction in order to obtain a periodic hole pattern every 6 cm (11% span). The pattern periodicity was vital to accurate and meaningful lateral averaging, as well as later computational fluid dynamics (CFD) simulations. Figure A.2 shows the hole pattern for the Siemens engine design in red, with the current 3X periodic hole pattern outlined in black showing both patterns being very similar. The exact hole spacing values are shown in Table A.1 for both the engine and experimental designs.

It was desired to match as closely as possible the blowing ratios at engine conditions for the experimental vane. Blowing ratios at engine conditions for each row of holes were calculated from the information provided by Siemens. To correctly match the engine blowing ratios, the vane interior was divided into plenums. Because the

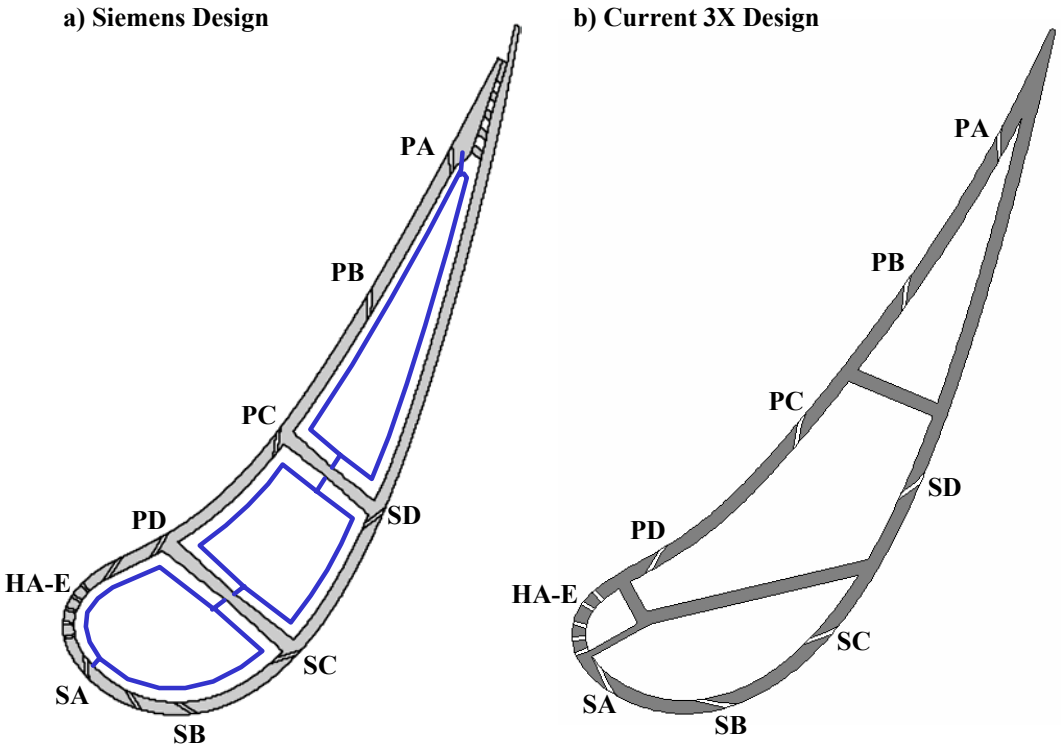

Figure A.1 Film-cooling vane layouts for (a) the Siemens engine design and (b) the current 3X vane design.

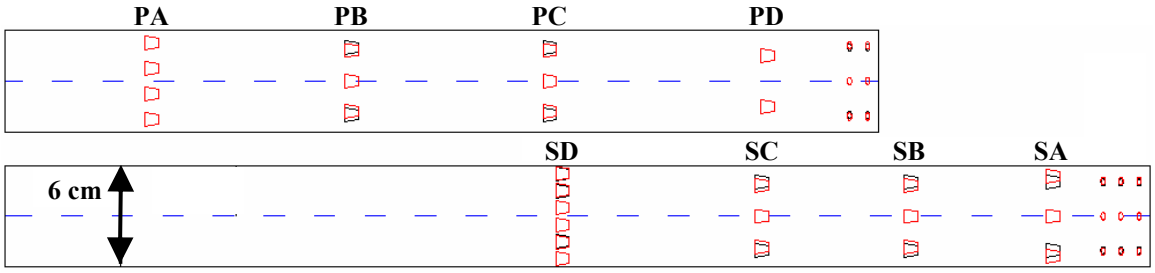

Figure A.2 The hole layout for the Siemens engine vane is shown in red, while the current 3X hole layout is shown in black. The current design is periodic every 11% span (inlet span).

exterior flow conditions and pressure ratios were not the same as the engine, and there were no impingement plates in the 3X scale vane, the plenum division had to be determined by matching predicted blowing ratios at low speed conditions to the engine blowing ratios.

The plenum supply pressure needed to achieve the correct blowing ratio was determined for each row of holes for the film-cooling vane. Plenum locations were

Table A.1 Hole Spacing Parameter for Engine Vane and Design Vane

Hole Location	Siemens	Current
	t/P	t/P
PA	0.54	0.54
PB	0.45	0.41
PC	0.45	0.41
PD	0.27	0.27
HA	0.21	0.22
HB	0.21	0.22
HC	0.21	0.22
HD	0.21	0.22
HE	0.21	0.22
SA	0.34	0.41
SB	0.45	0.41
SC	0.45	0.41
SD	0.80	0.81

decided on by grouping rows together based on their location on the vane and their calculated necessary supply pressures. Figure A.1b shows the four plenum divisions that were chosen for the interior of the experimental vane. A comparison of the engine local blowing ratios with the predicted local blowing ratios based on the plenum division in the experimental vane is shown in Table A.2. With the plenum division that was chosen, the predicted blowing ratios compared well to those at engine conditions. The four independent plenums required four independently controlled inlet flow feeds.

A number of different methods were considered from which to construct the film-cooling vane. The three requirements for the test vane were the following: (1) a material with a low thermal conductivity to minimize lateral and radial conduction losses, (2) a material that would be strong enough such that it would support the interior plenum pressure, and (3) a material that would maintain the geometric integrity of the hole shaped after the manufacturing process. The final design was chosen based on the results of a conduction loss analysis, the manufacturing difficulty, and the cost.

Table A.2 Comparison Between Engine Blowing Ratios to Predicted Values

Hole Location	Siemens	Predicted
	M	M
PA	2.1	1.9
PB	2.8	2.9
PC	3.9	3.8
PD	5.9	5.9
SA	3.0	3.0
SB	1.8	1.8
SC	1.5	1.5
SD	1.2	1.1

In all, four designs were considered for the film-cooling vane, all of which are shown schematically from the side cross-section in Figures A.3a through d. The first design considered, shown in Figure A.3a, was to construct the vane from a medium density with a thermal conductivity of k = 0.028 W/m·K. Although the foam was ideal for the film-cooling vane from a thermal conductivity standpoint, it was very difficult to machine for intricate geometries such as the shaped holes. The second design, shown in Figure A.3b, was to have the vane made using the rapid prototype process of stereo-lithography (SLA). The SLA process would allow precise geometrical definition and was relatively quick (a vane can be manufactured within a week). However, the SLA material had a much higher thermal conductivity value than foam (k = 0.180 W/m·K). With that in mind, the third design, shown in Figure A.3c, was developed with an air gap between two walls of SLA. This design was intended to minimize the conduction losses through the wall. The fourth design, shown in Figure A.3d, was developed as a composite of the SLA, which would provide strength and geometrical definition, and the foam, which would minimize lateral conduction losses. A skeleton of the vane and the hole shapes would be manufactured with SLA. Foam would then be poured around the SLA skeleton using an SLA casting. This design process had been proven in a previous experimental project in this research group.

The conduction analysis involved comparing adiabatic effectiveness levels for a

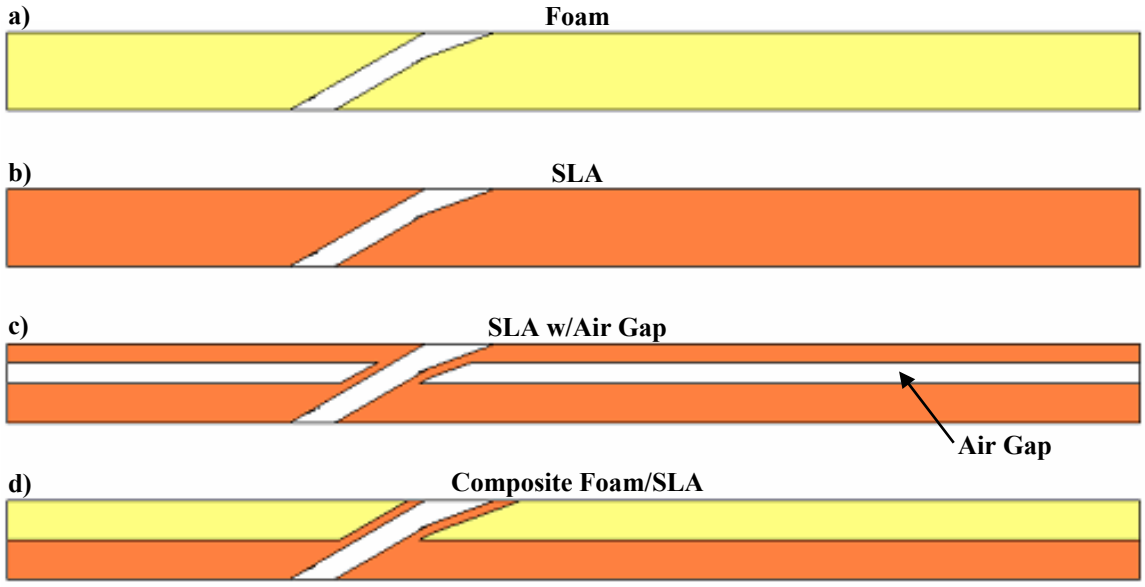

Figure A.3 Possible methods of manufacturing the film-cooling vane.

flat plate with a single fan-shaped hole using computational predictions of the conduction losses done with a solid model in FLUENT. The analysis was done with the different materials and composite vane walls that were being considered for constructing the vane. First, the adiabatic wall temperature on the outer wall, which simulated the outer surface convective boundary condition on the vane, was calculated using Fluent. The domain geometry is shown in Figure A.4. The geometry for row PD (Figure A.1b) was used for the analysis because that row had the largest pitch, and therefore would be subject to the highest lateral conduction effects. The freestream velocity predicted in the inviscid flow calculations and the calculated coolant mass flow rate necessary to match blowing ratios were used as inlet conditions. There were periodic boundary conditions along the width of the plate. For the baseline computation, the walls were set to be adiabatic. Approximately 300,000 cells were used in the simulation, and the RNG-kε turbulence model was used. The adiabatic effectiveness from this simulation is shown in Figure A.5a.

The conduction through the vane wall was then computed for each of the construction possibilities in Figure A.3 by forming each geometry into a solid model. The material properties and geometry of each configuration were modeled in FLUENT, and the energy equation was solved in the solid model using the computed adiabatic

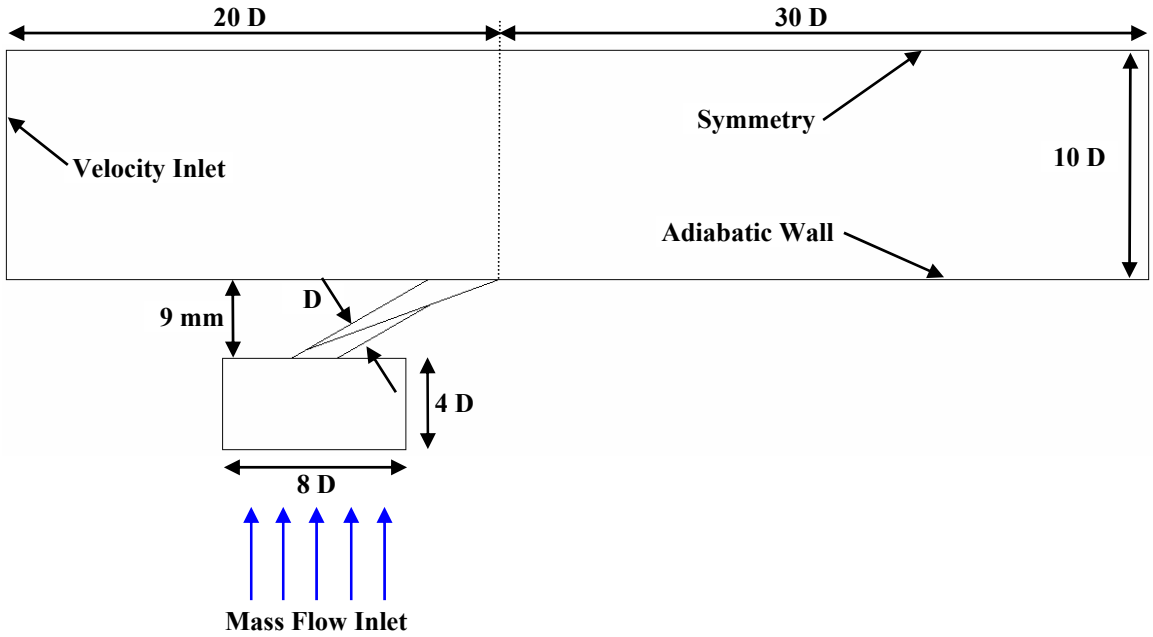

Figure A.4 Domain used for the baseline adiabatic effectiveness predictions used for the conduction correction.

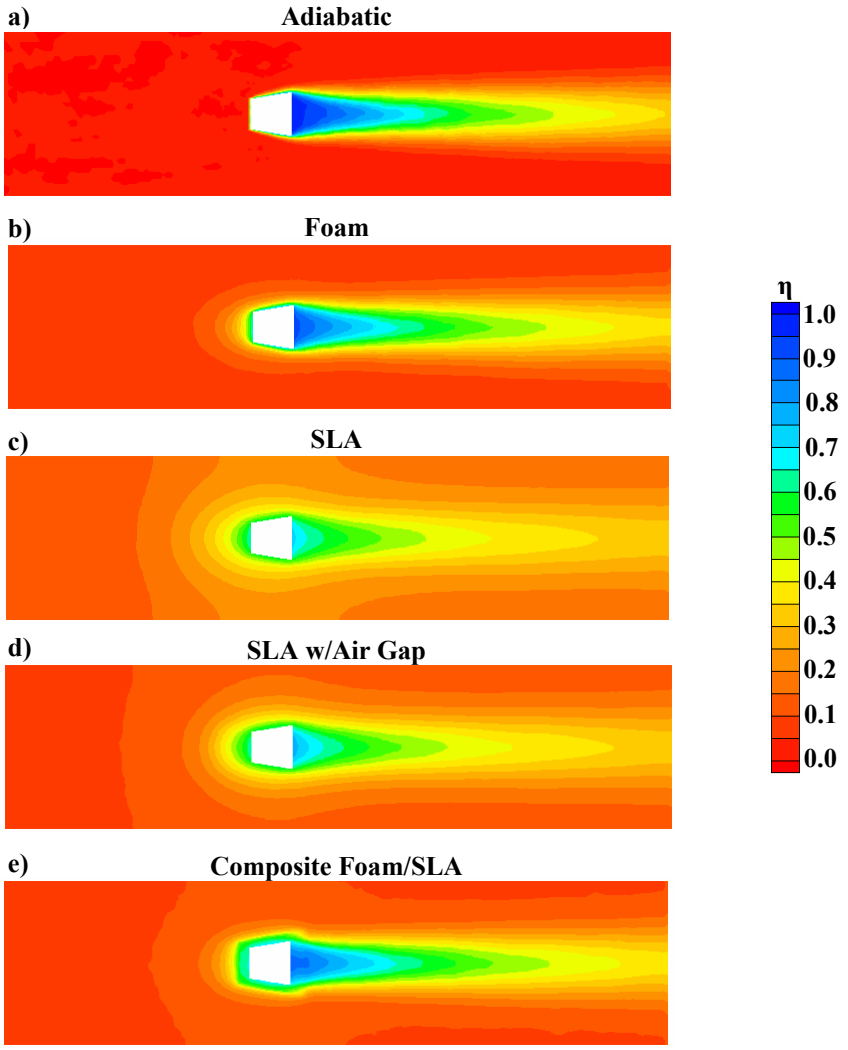

Figure A.5 Results of the preliminary CFD and solid model conduction analysis.

effectiveness results as the exterior wall boundary condition. The external heat transfer coefficients were calculated using TEXSTAN, while the Dittus-Boelter equation (Equation A.1) was used to calculate the Nusselt number for the interior hole surface,

$$Nu_D = 0.023 Re_D^{4/5} Pr^n \tag{A.1}$$

where n = 0.4 because $T_{cool} < T_{surf}$. The heat transfer coefficient was then calculated using Equation A.2,

$$h = \frac{Nu_D k}{D} \tag{A.2}$$

and used along with the coolant temperature as a convective boundary condition for the interior hole surface. The inner vane wall (plenum wall) also had a convective boundary condition with a low heat transfer coefficient (5 W/mK) and the coolant temperature.

Numerical computations were then done for each case to calculate the outer wall temperature. The calculated wall temperatures are shown in Figures A.5b through e, in terms of non-dimensional adiabatic effectiveness. The difference between the calculated surface temperature and the adiabatic surface temperature (Figure A.5a) was the conduction loss for that particular vane design. The pitch averaged change in η from the adiabatic case for each case is shown in Figure A.6 where X/D = 0 is located at the trailing edge of the cooling hole. This graph clearly shows that the best design from a thermal standpoint was the case with a solid foam wall. The foam itself was purchased from General Plastics Manufacturing Corporation. The specific type of foam used was FR-6700 at 6 lbs/ft^3. The difficulty then became how to manufacture the vane out of foam, while maintaining the correct hole shape.

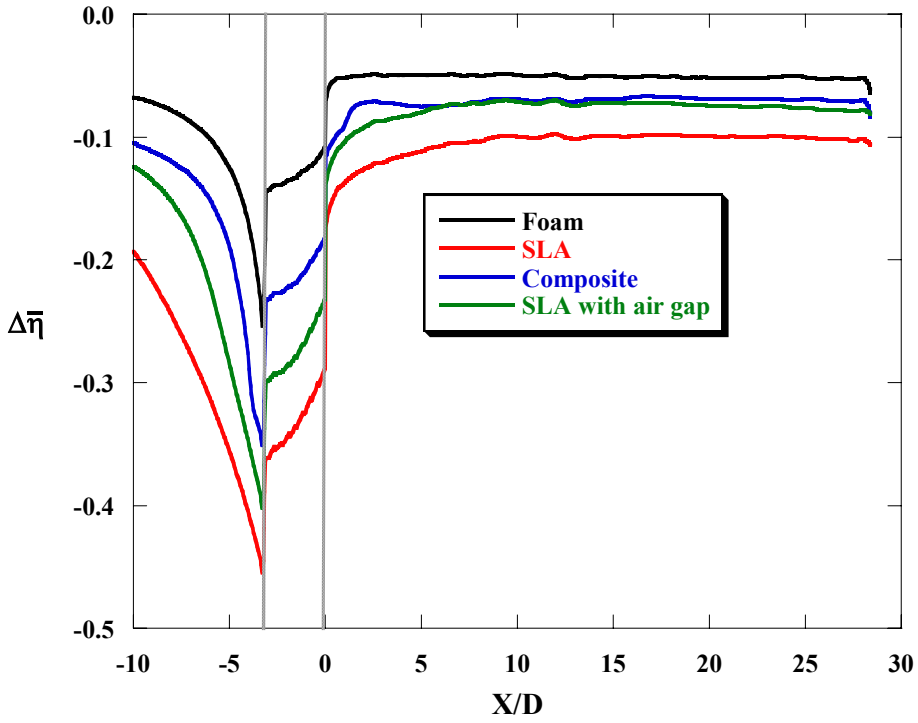

Figure A.6 The pitch-averaged difference in η for each case from the adiabatic case (the hole position is indicated with dashed lines).

The construction of the vane from medium density foam was a two part process. First, the airfoil profile, complete with the contoured endwall contraction, was machined using a computer numerically controlled (CNC) mill. Next, the airfoil shell was sent to a 5-axis waterjet company, where the film-cooling holes were manufactured. The 5-axis waterjet allowed a high geometrical integrity for the fan-shaped holes, although there were some inconsistencies in hole diameter and hole shape and these irregularities were accounted for (see Appendix D).

Finally, the interior and exterior of the vane were instrumented with numerous thermocouples and pressure taps. Type E thermocouples were placed flush with the vane surface in order to accurately calibrate the infrared (IR) images. Thermocouples were also located in each plenum to measure the coolant temperature during tests. Static pressure taps were located around the vane surface to measure the flow distribution around the vane prior to testing. Total pressure taps were also located in each plenum to measure pressure ratios and set blowing ratios during tests.

Endwall Construction

Construction of the endwall was very similar in approach and technique to the vane design. The Siemens endwall film-cooling pattern for the engine is shown in Figure A.7a. The holes that were chosen to be incorporated into the experimental endwall are highlighted in Figure A.7a. The engine endwall design featured separate plenums for different groups of holes and also included an impingement plate. These features were not included in the 3X scale design, as all of the holes were fed from a single plenum. The 3X scale endwall design is shown in Figure A.7b, and featured two passages, one with cylindrical cooling holes in the passage and the other with fan-shaped cooling holes in the passage. For both passages, a double row of staggered 60º cylindrical holes were located upstream of the passage.

Also, the manufacturing fillet was included in the experimental model. The fillet was an elliptical design, and extended vertically to a height of 12D and radially to a distance of 10D. The fillet was made by SLA and was secured to the vane-endwall junction circumferentially around the base of the vane.

A single supply plenum was located beneath the test section, which supplied

a) Siemens Endwall Design

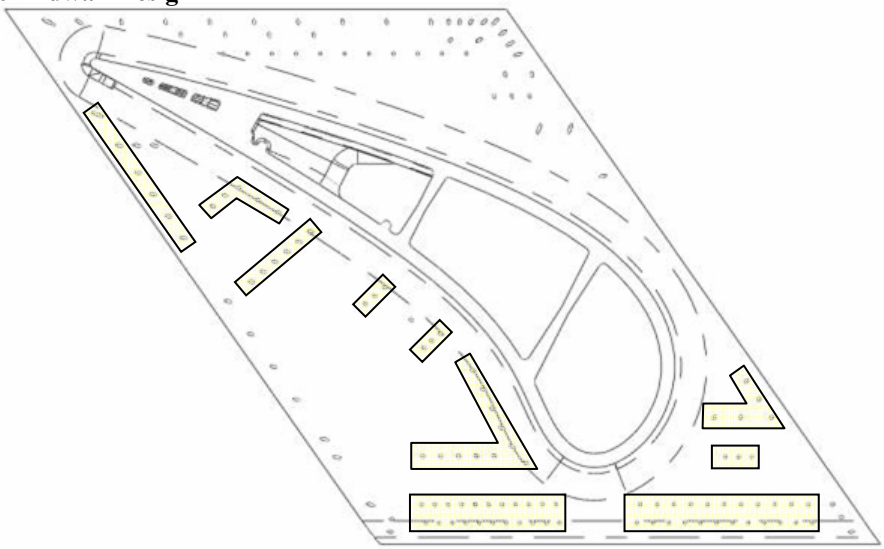

b) 3X Scale Design

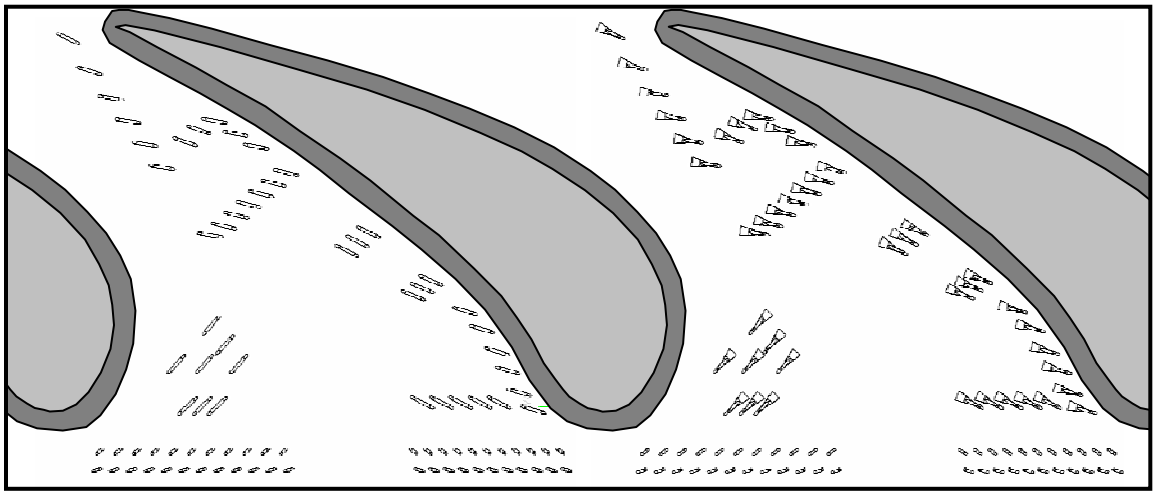

Figure A.7 Siemens engine endwall film-cooling hole layout and the 3X scale hole layout (showing both the cylindrical and fan-shaped passage).

coolant flow to each passage. Tests were performed on only a single passage at a time, and the flow to the non-tested passage was always blocked from inside the plenum during testing. To accurately measure the coolant mass flow to each passage during testing, a laminar flow element was located upstream of the endwall plenum.

Just as with the vane, the same medium density, low thermal conductivity foam was used for the endwall. Again, a 5-axis water jet machine was used to machine the film-cooling holes in each passage. Because the endwall surface was flat, as opposed to the curved vane surface, a higher degree of accuracy and uniformity in cooling hole geometry was noticed for the endwall design.

Prior to testing, the endwall surface and plenum interior were instrumented with thermocouples and pressure taps to record pertinent temperature and pressure data during testing. Nine type E thermocouples were placed flush with the endwall surface in each passage with which to calibrate the IR images. Thermocouples were also placed within the plenum to monitor coolant temperatures during the endwall tests. Pressure taps were placed upstream of the vane passage on the endwall to measure the upstream static pressure on the endwall, and provide a reference with which to calculate local blowing ratios using the static pressure distribution on the endwall obtained from CFD for the uncooled case. Pressure taps were also located within the plenum to measure the pressure ratio within the plenum.

Nomenclature

D film-cooling hole diameter

h heat transfer coefficient, $h = Nu_D K/D$

k thermal conductivity

M local blowing ratio, $M = \rho_{cool} U_{cool} / \rho_{in} U_{in}$

n power for the Dittus-Boelter equation, $n = 0.4$ for $T_{cool} < T_{surf}$

Nu Nusselt number, for this study, $Nu_D = 0.023 Re_D^{4/5} Pr^n$ ($n = 0.4$, Dittus-Boelter)

P spacing between adjacent holes

Pr Prandtl number

t hole breakout width

T temperature

U velocity

X axial coordinate measured from the vane stagnation

Greek

η adiabatic film-cooling effectiveness, $\eta = (T_\infty - T_{surf})/(T_\infty - T_{cool})$

ρ density

Subscripts

∞ freestream

cool coolant

D diameter

in inlet condition

surf surface

Overbar

– lateral/pitchwise average

Appendix B:
Data Analysis

Adiabatic Film-Cooling Effectiveness Measurements

To obtain any quantitative results for the adiabatic effectiveness on the vane surface, the infrared (IR) images needed to undergo a rigorous post-processing analysis including the following: a three-dimensional surface transformation, a calibration to ensure accurate temperatures on the surface, and a one-dimensional conduction correction to account for conduction losses through the vane wall. The transformation process is illustrated in Figure B.1, showing the initial raw IR image, and the subsequent transformation, calibration, and conduction correction. The following three sub-sections describe each of these tasks in detail.

Three-Dimensional Surface Transformation

The test section for the vane surface measurements is shown in Figure B.2. Because of the adjacent vanes on either side of the center vane, it was not possible to place the IR camera perpendicular to the vane surface. For this reason, it was chosen to locate the IR camera underneath the test section as shown in Figure B.3. Images were taken at approximately 45º to the vane surface. There were ten different locations that were required to get a complete contour map of the vane surface. Each image station was constructed such that the IR camera could be removed and then replaced in the exact same spot, resulting in a repeatable image location. Repeatable image locations greatly simplified the data reduction process.

Not only were the images taken at a 45º angle with respect to the surface, but the surface was also highly curved. The curvature and picture distortion required a transformation procedure that would transform the IR image into rectangular coordinates. A fully interactive image transformation program was written in MATLAB that allowed transformation of a uniform grid that was distorted in some way as to look non-uniform in the image. In addition, another interactive program was written in MATLAB to apply the same image transformation to an image taken at the same location, for instance a picture taken during testing.

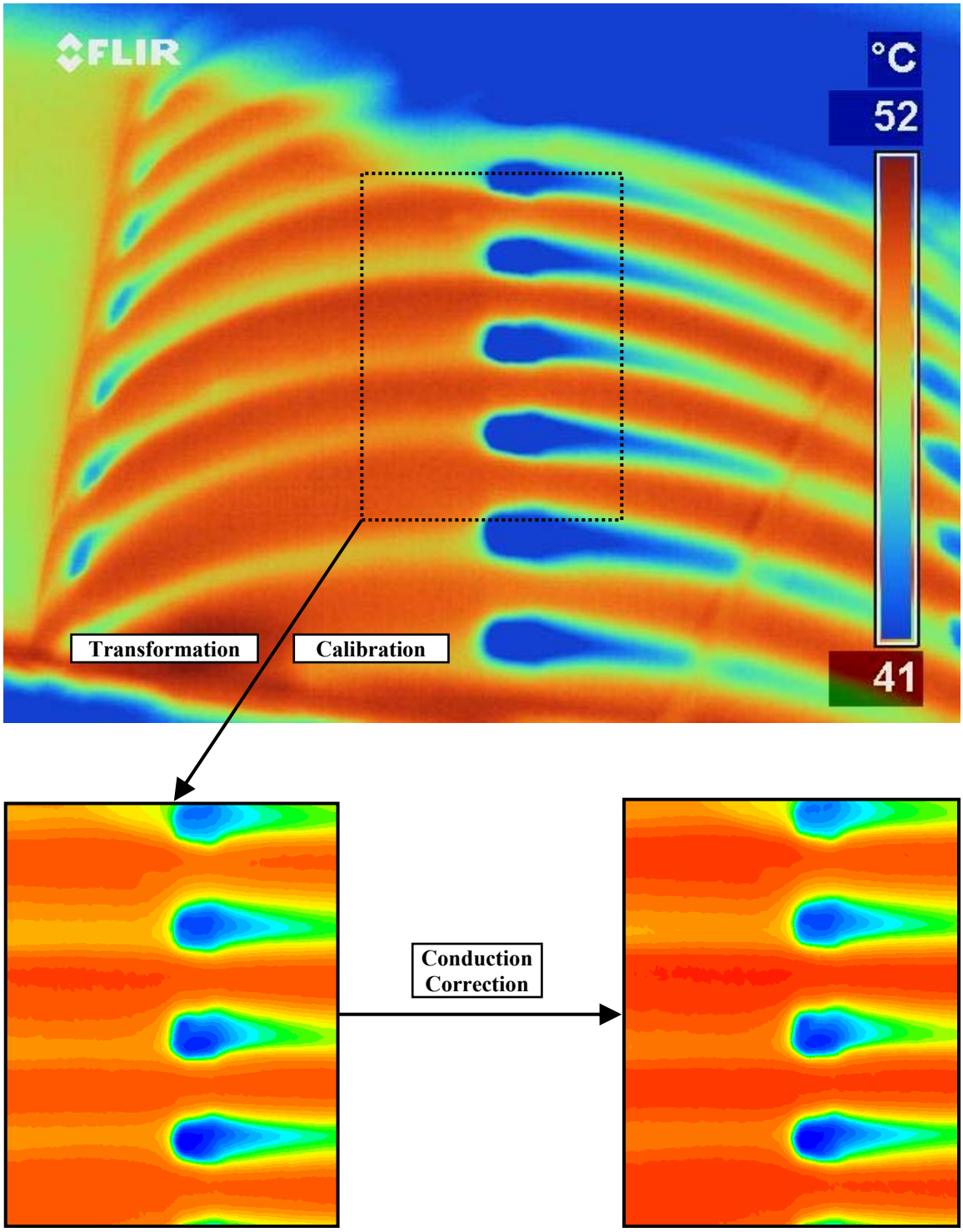

Figure B.1 Schematic of the data reduction procedures for the adiabatic effectiveness measurements.

A uniform grid was made from a thin inconel sheet. The inconel sheet was spray painted with a black paint, allowed to dry, and then a 1 cm x 1 cm grid was etched into the paint exposing the inconel below. The grid was then placed onto the vane at

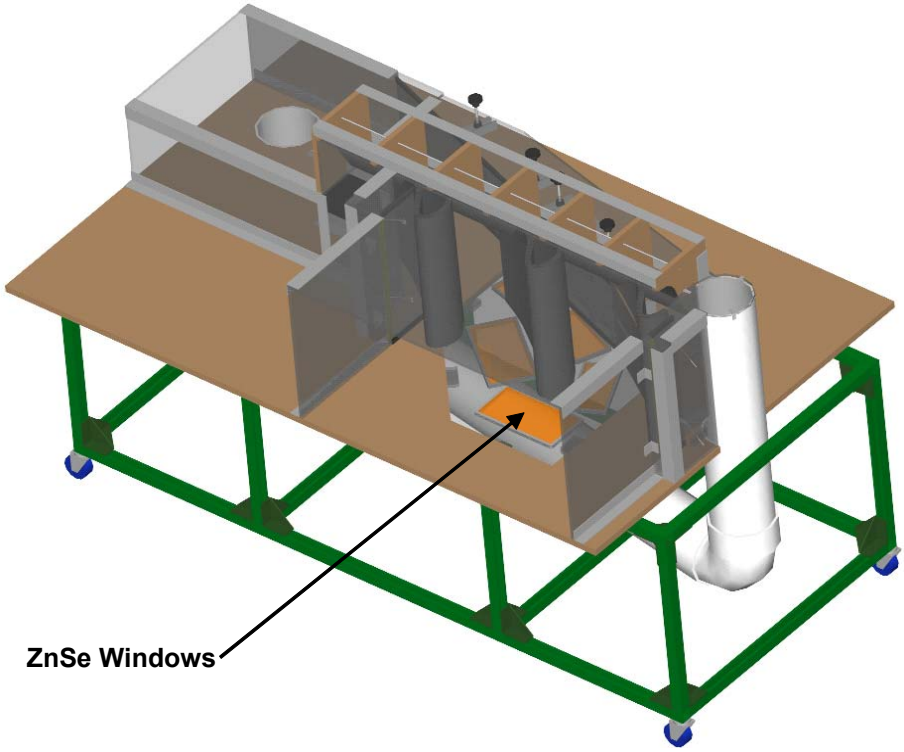

Figure B.2 Test section showing ZnSe windows through which images of the vane were taken.

Figure B.3 IR camera setup below the test section.

each image location. An IR image was taken of the grid at each image location, such as the one shown in Figure B.4, which was taken of the suction side near the leading edge.

The grid image was then loaded into the MATLAB program shown in Figure B.5. Upon loading the image file, information regarding the number of grid vertices and an approximate value for number of pixels per inch were required. The number of grid vertices in the horizontal and vertical directions determined how many cross-hairs must be placed on the image, and subsequently how much of the image was deemed useful for final data. The approximate number of pixels per inch was vital, because that determined the size of the final rectangular grid upon which the distorted data was to be interpolated. In interpolating data, it is important not to project too many points onto too small of a grid, because data will be lost in the change of resolution. Similarly, interpolating too few points onto a grid with a much higher resolution will result in generating extraneous data that is beyond the resolution of the initial image.

Points were located on the image vertices using the cursor and cycling through all of the points that were entered into the program initially. Once all of the cross-hairs were

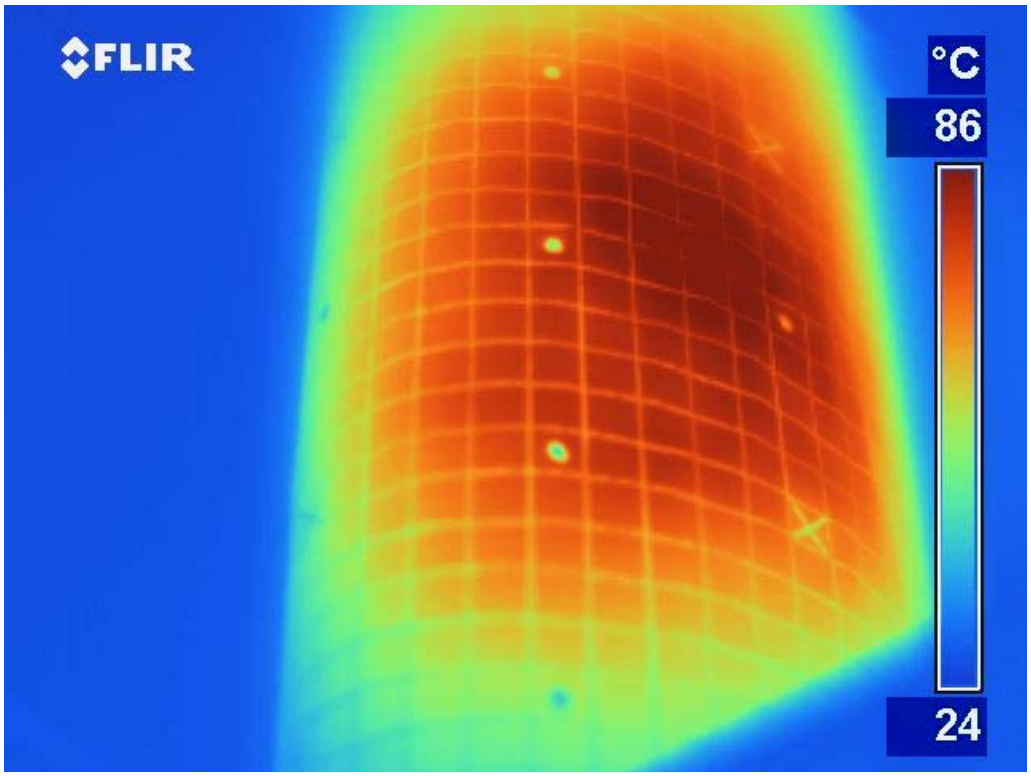

Figure B.4 Example of an image taken with the uniform grid on the vane surface.

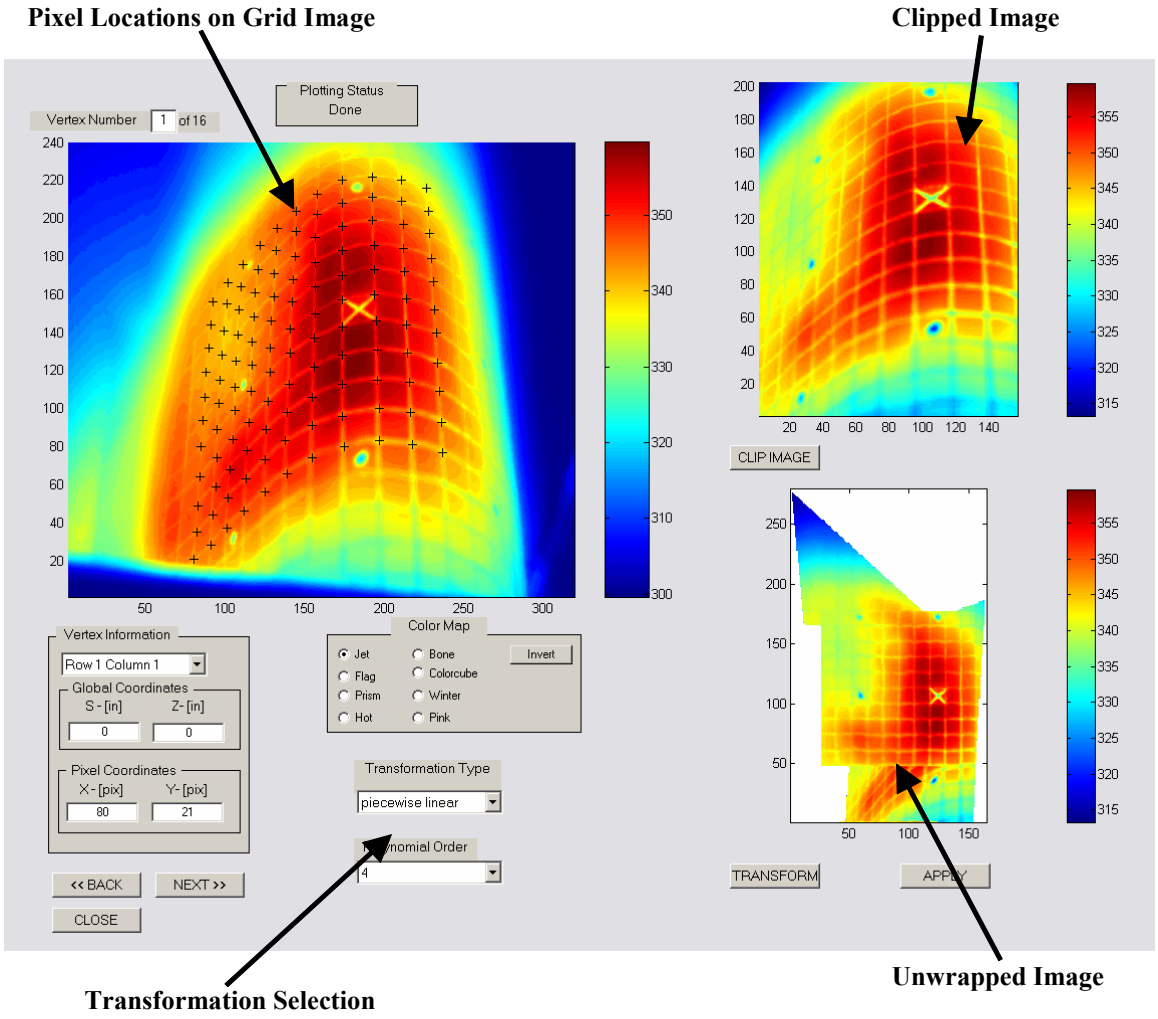

Figure B.5 Grid image transformation program.

located correctly on a grid vertex, the image was cropped based on the minimum and maximum extents of the cross-hairs placed on the grid image. The clipped image is shown in the upper right-hand corner of Figure B.5. The reason the image was cropped is that the following transformation was valid only in the region where the cross-hairs were located, so it wasn't necessary to apply the transformation to the entire image.

Several options were available for the transformation procedure. The transformation can be understood by imaging the distorted grid image to be placed on the surface of a balloon. The rectangular grid would then be obtained by stretching the material in such a way to make the grid image appear rectangular. The different transformation techniques were essentially different ways of stretching the image. The 3rd and 4th order polynomial and piecewise linear transformations were used for the vane.

The polynomial transformation involved fitting polynomial curves to the rows and columns of selected points on the image, and then projecting those polynomial curves onto a uniform grid. That transformation routine worked well for the vane surface because of the orientation of the camera coupled with the surface curvature. The piecewise linear transformation was used in the leading edge region. The piecewise linear transformation involved segmenting the image into different sections and performing a linear transformation in each section. This routine worked well in the leading edge region, where the curvature was perhaps too great for the polynomial transformations, which did not yield good rectangular transformed grids for that region.

Once the distorted grid image had been transformed into a rectangular grid, the same transformation routine could then be applied to subsequent images taken during testing at that same location. Figure B.6 shows the MATLAB program that was developed to apply the transformation to non-grid images. First, the grid image was loaded, and the region of interest (essentially the rectangular data region) was selected on the grid image using the cursor. The corresponding global coordinates of the region on the vane surface were entered into the program. Finally, a raw image file with test data taken at the same image location was chosen, and the final transformed image appeared on the program for visual inspection. If the final image, shown on the right-hand-side of Figure B.6 looked acceptable, it was saved for calibration.

Surface Calibration

Following the image transformation, the image required calibration to ensure accurate temperature values. The IR camera essentially measured the radiation emitted from the surface according to Equation B.1,

$$Q_{surf} = \sigma\varepsilon T_{surf}^4 + \sigma(1-\varepsilon)T_{amb}^4 \tag{B.1}$$

where σ is the Stefan-Boltzmann constant, ε is the surface emissivity, T_{surf} is the temperature of the surface, and T_{amb} is the average temperature of the surroundings observed by the surface. By setting $\varepsilon = 1$, the surface heat flux could be calculated directly from the surface temperatures displayed in the IR image reduction software using Equation B.2,

$$Q_{surf} = \sigma T_{surf}^4 \tag{B.2}$$

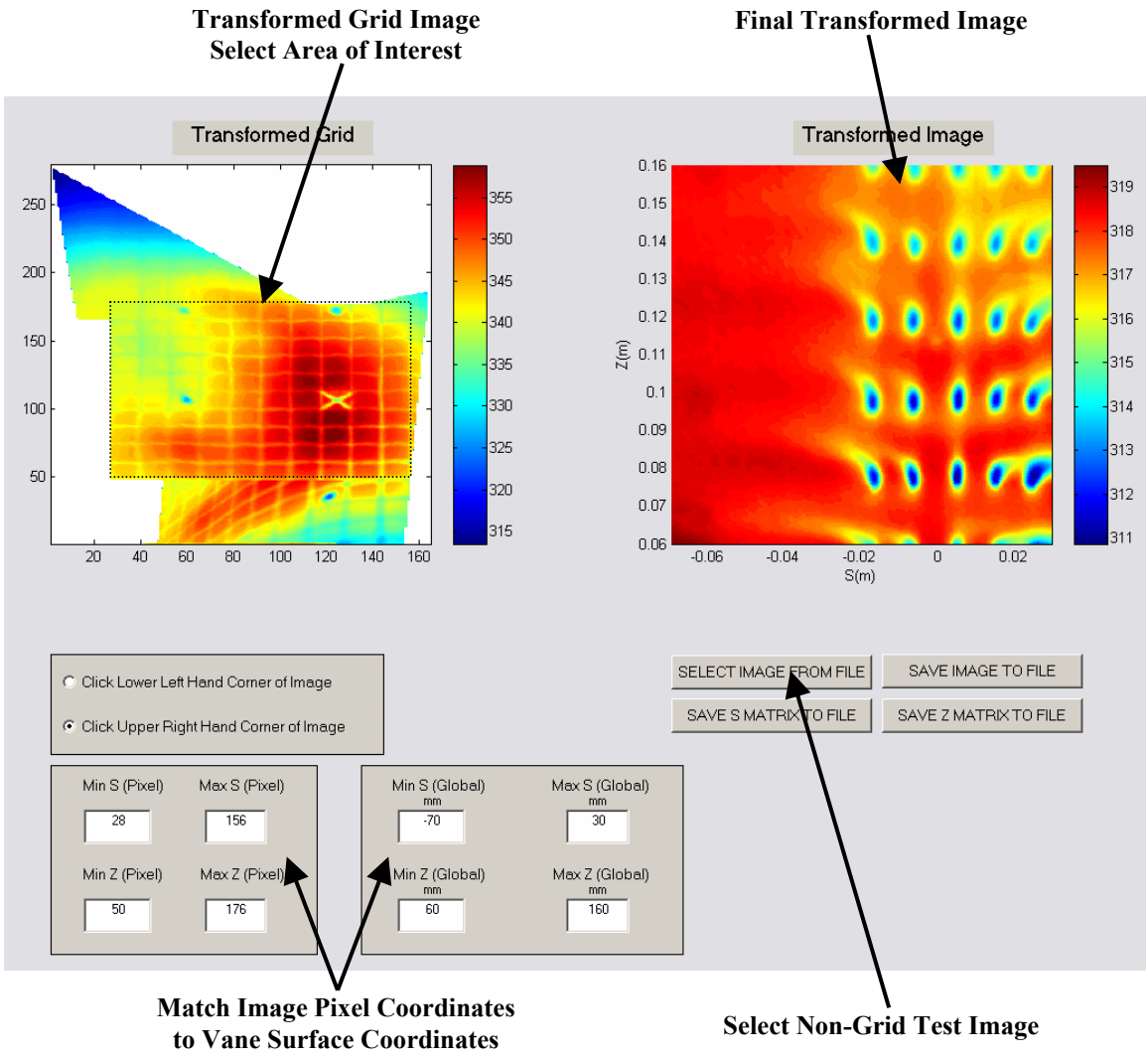

Figure B.6 Grid image transformation program.

Once Q_{surf} is known, the correct surface temperature can then be calculated using Equation B.3 by correctly choosing ε and T_{amb},

$$T_{surf} = \sqrt[4]{\frac{1}{\sigma\varepsilon}\left[Q_{surf} + \sigma(\varepsilon - 1)T_{amb}^4\right]} \qquad (B.3)$$

where Equation B.3 is essentially a rearrangement of Equation B.1.

Rather than guessing the values of ε and T_{amb}, they were calculated directly by forcing T_{surf} to equal known temperatures at certain locations on the image which were instrumented with thermocouples. It was also desired to calibrate the image over the full range of expected temperatures, from the freestream temperature to the coolant temperature. For this reason, an image was taken without film-injection (shown in Figure

B.7a) such that the surface thermocouple would read the freestream temperature. The film-injection was then turned on, and another image was taken at the same location once a steady state had occurred. The cooled image is shown in Figure B.7b, with the thermocouple located just downstream of the hole exit measuring the coolant temperature. An algorithm was developed to minimize the difference between T_{surf} in Equation B.3 and the measured thermocouple temperatures at the locations shown in Figure B.7 based on varying ε and T_{amb}. In this way, the optimum values of ε and T_{amb} were obtained, with an average difference $|T_{surf} - T_{TC}| < 0.05$ºC. Typical values of ε were between 0.6 and 0.7, and they varied with image location. Typical values of T_{amb} were on the order of 50º C, which considering the freestream temperature (and subsequently the temperature of the surrounding surfaces) was roughly 60º and the room temperature was nominally 30º C, the value of T_{amb} was acceptable.

Conduction Correction

Following the calibration, the image was corrected for conduction losses through the surface using a one-dimensional correction developed at the University of Texas by Dr. David Bogard's research group. In order to apply the correction, the surface temperatures must be measured at test conditions with no flow. In other words, the external freestream flow was heated to the normal testing temperature of roughly 60º C, while the interior plenum was filled with coolant at nominally 40º C, which was also

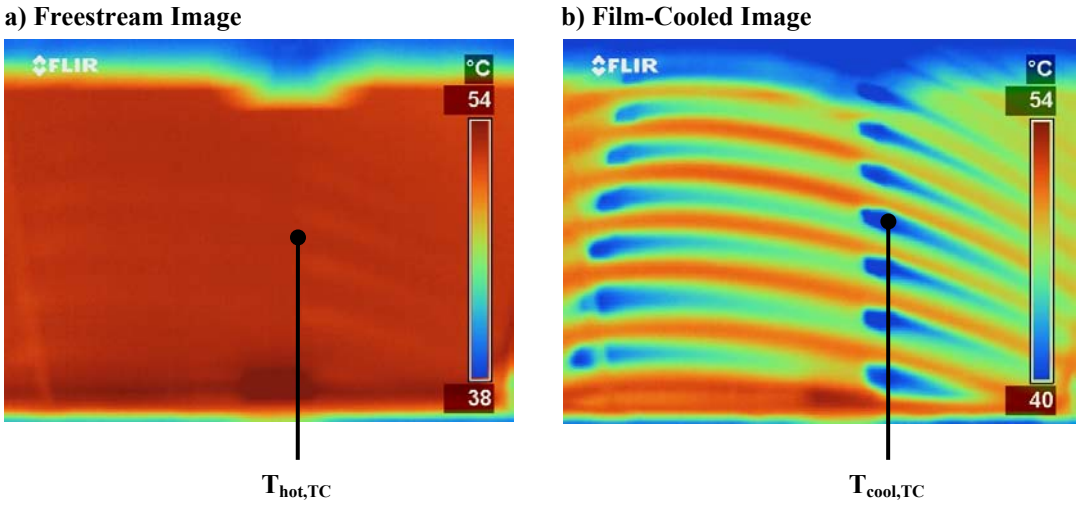

Figure B.7 Sample of images used for calibration.

typical of the film-cooling tests. The holes in the test region on the vane surface were plugged, although coolant was ejected through holes at a different span location, such that the plenum could be filled with coolant. The surface temperatures were then measured in the test region of the vane surface. Any reduction in surface temperature in this configuration could then be assumed a result of one-dimensional conduction through the surface of the vane into the plenum.

The results of the uncooled measurements yielded an uncooled surface effectiveness as a function of S, the surface distance around the vane. The uncooled surface effectiveness was calculated using Equation B.4,

$$\eta_o = \frac{T_\infty - T_{surf,o}}{T_\infty - T_{cool}} \tag{B.4}$$

where T_∞ is the measured freestream temperature, T_{cool} is the measured coolant temperature flowing through the interior plenum, and $T_{surf,o}$ is the uncooled surface temperature measured and calibrated with the IR camera. The conduction corrected adiabatic film-cooling effectiveness could then be calculated using Equation B.5,

$$\eta_{aw} = \frac{\eta_{meas} - \eta_o}{1 - \eta_o} \tag{B.5}$$

where η_o is given by Equation B.4, and η_{meas} is the measured film-cooling effectiveness calculated using Equation B.6,

$$\eta_{meas} = \frac{T_\infty - T_{surf}}{T_\infty - T_{cool}} \tag{B.6}$$

where T_{surf} is the surface temperature with film-cooling measured with the IR camera. Values of η_o varied from 0.04 to 0.12, depending on the surface location.

An image before and after the conduction correction described above is shown in Figure B.1. The conduction correction affected regions of low η_{aw} more strongly than regions of high η_{aw}. The reason for this was that regions with low η_{aw} corresponded to areas with higher temperatures, meaning that the temperature difference from the exterior surface to the interior surface was higher. The higher temperature difference generated higher conduction losses in those locations, hence the stronger correction.

Total Pressure Loss Measurements

Total pressure loss measurements were made using a United Sensor DC-095 five-hole total pressure probe. The probe head, shown in Figure B.8 from the front and side view, had a diameter was 2.4 mm, which allowed for relatively non-intrusive measurements. The probe was inserted through a slot in the upper endwall downstream of the contraction in order to measure the exit plane (shown schematically in Figure 4.2). The five-hole probe measured the total pressure of the flow (P_t), the yaw angle (Ψ), the pitch angle (Φ), and the magnitude of the velocity (V_s). The total pressure was always measured relative to the constant reference value of the vane stagnation pressure (P_{stag}).

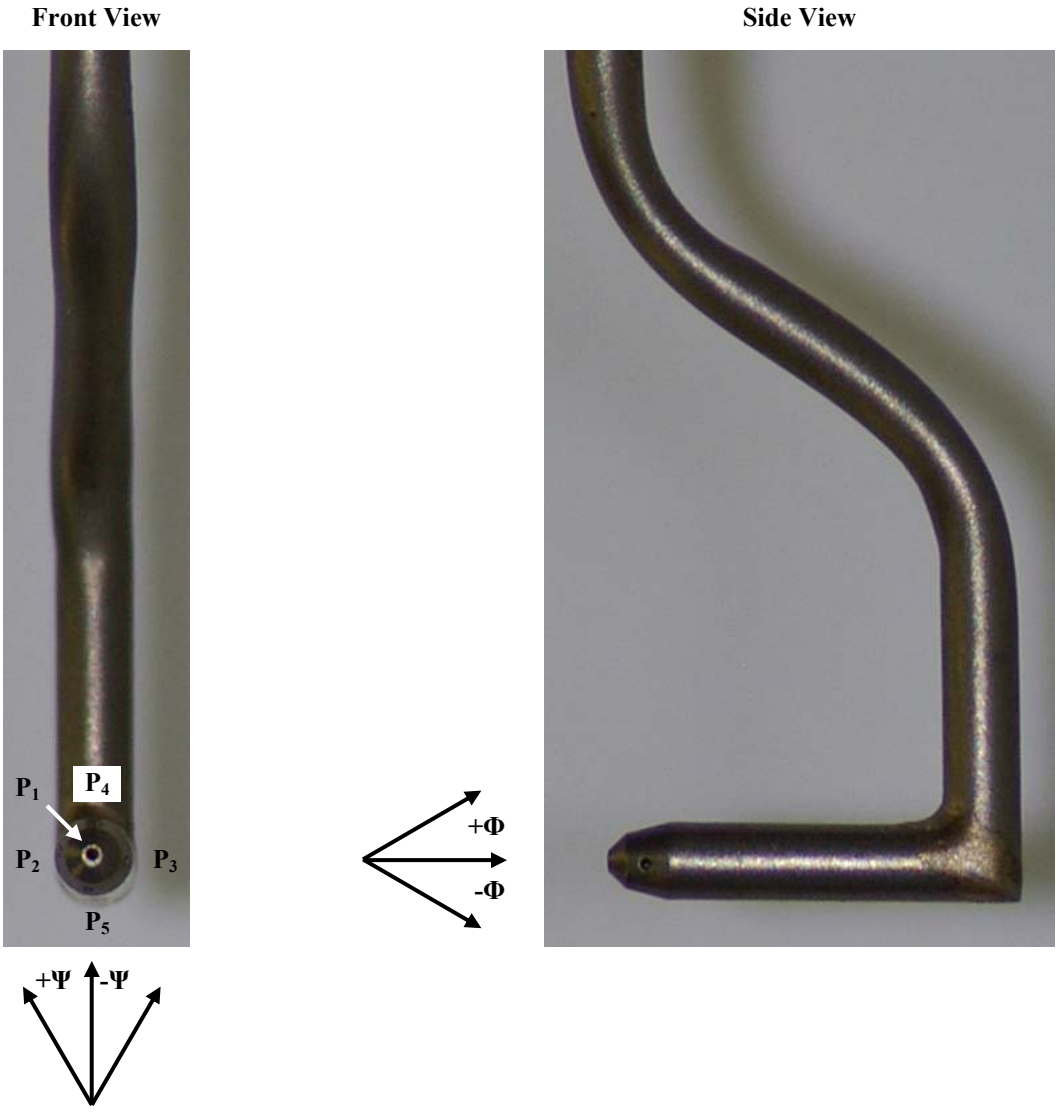

Figure B.8 A front and side view of the five-hole total pressure probe.

The yaw and pitch angles were used along with velocity magnitude to infer all three components of velocity at the exit plane. The probe was calibrated by the manufacturer, United Sensor, for the range of velocities that were expected in the exit plane.

There were a total of four pressure transducers necessary for the flow field measurements when using the five-hole probe. The pressure designations for each of the five holes on the probe tip are shown in Figure B.8. The five pressure lines coming from each of those holes issuing from the top of the probe are shown in Figure B.9. The five-hole probe was calibrated by the manufacturer, and that information (shown in Figure B.10) was used along with the measured pressure differences to calculate the flow values at each data location. A program was written in LabVIEW to interface with the probe and the pressure transducers while taking data, which reduced the data in real-time with the experiment. A screen shot of the program is given in Figure B.11, showing the required entries for each measurement in red text, and the location of the current data

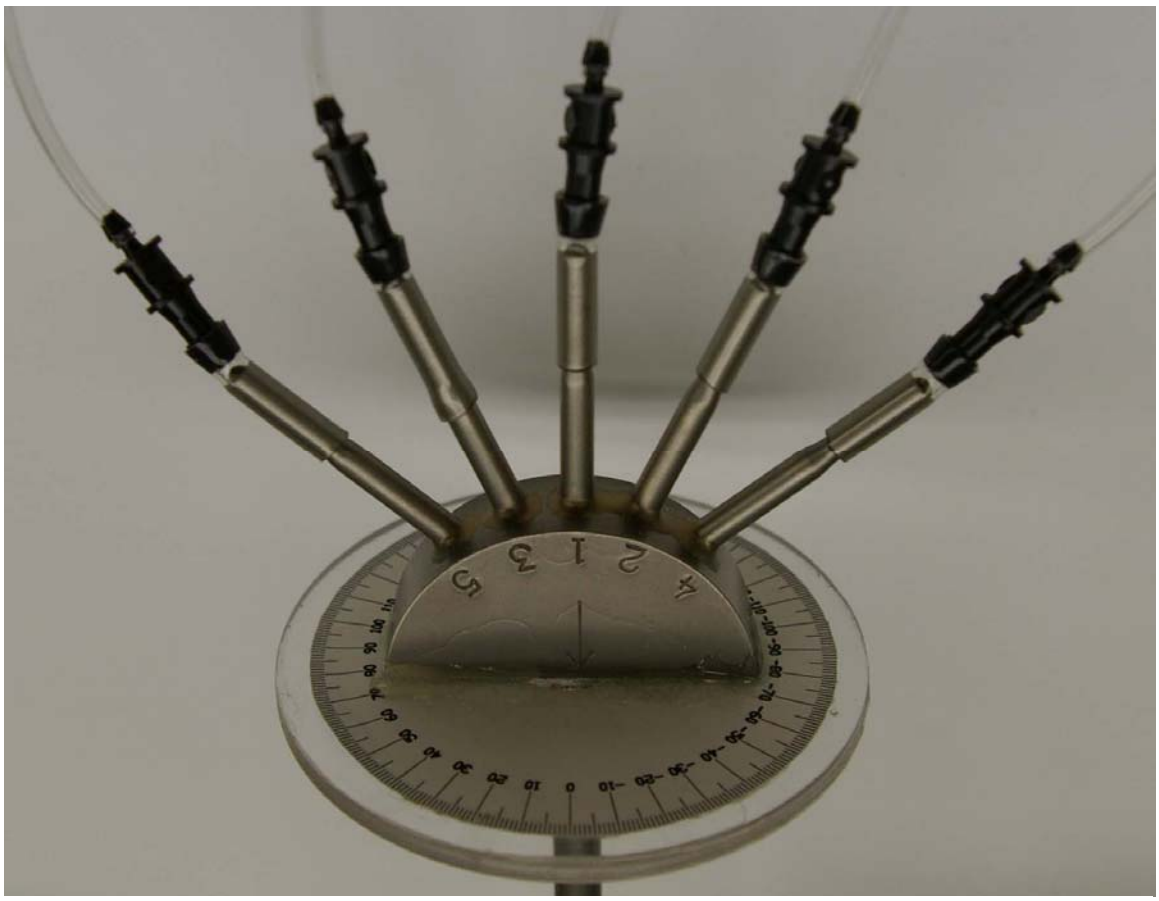

Figure B.9 A close-up of the top view of the five-hole total pressure probe, showing the protractor used to determine yaw angle.

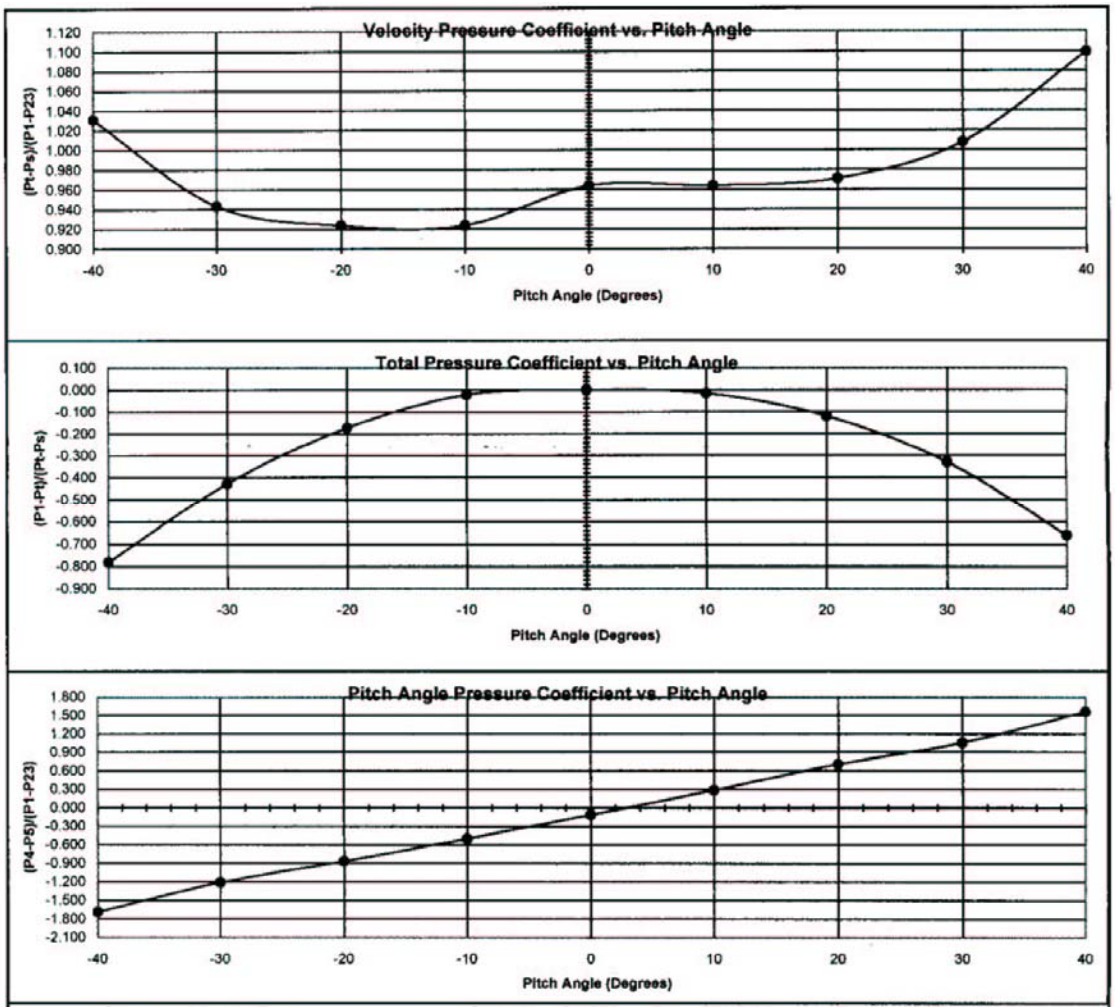

Customer: Virginia Tech | Serial No.: C-4578 | Date: 07/12/05 | Temp =80 °F
Probe Type: DC-095 | Operator: AR | Patm= 29.9 In Hg | Rel Humid= 63 %

1	2	3	4	5	6	7	8	9	10	11	12
Pt - Ps	P1 - Pt	P23 - Ps	P4 - P5	Patm - Pt	Pitch	2/1	3/1	4/1	1.0+7-8	9/10	1.0/10
13.3	-10.4	-10.0	-21.8	3.0	-40.0	-0.782	-0.752	-1.639	0.970	-1.690	1.031
13.3	-5.7	-6.5	-17.1	3.0	-30.0	-0.429	-0.489	-1.286	1.060	-1.213	0.943
13.3	-2.3	-3.4	-12.5	3.0	-20.0	-0.173	-0.256	-0.940	1.083	-0.868	0.924
13.3	-0.3	-1.4	-7.2	3.0	-10.0	-0.023	-0.105	-0.541	1.083	-0.500	0.924
13.3	0.0	-0.5	-1.6	3.0	0.0	0.000	-0.038	-0.120	1.038	-0.116	0.964
13.3	-0.2	-0.7	3.9	3.0	10.0	-0.015	-0.053	0.293	1.038	0.283	0.964
13.3	-1.6	-2.0	9.6	3.0	20.0	-0.120	-0.150	0.722	1.030	0.701	0.971
13.3	-4.4	-4.3	13.9	3.0	30.0	-0.331	-0.323	1.045	0.992	1.053	1.008
13.3	-8.8	-7.6	18.8	3.0	40.0	-0.662	-0.571	1.414	0.910	1.554	1.099

All Pressure Units in cm of Water

United Sensor Corporation

Figure B.10 Five-hole calibration data provided by United Sensor.

point on the three calibration curve plots.

The first step in the data taking process was to determine the correct yaw (or flow turning) angle. This was done manually by rotating the probe until the pressure

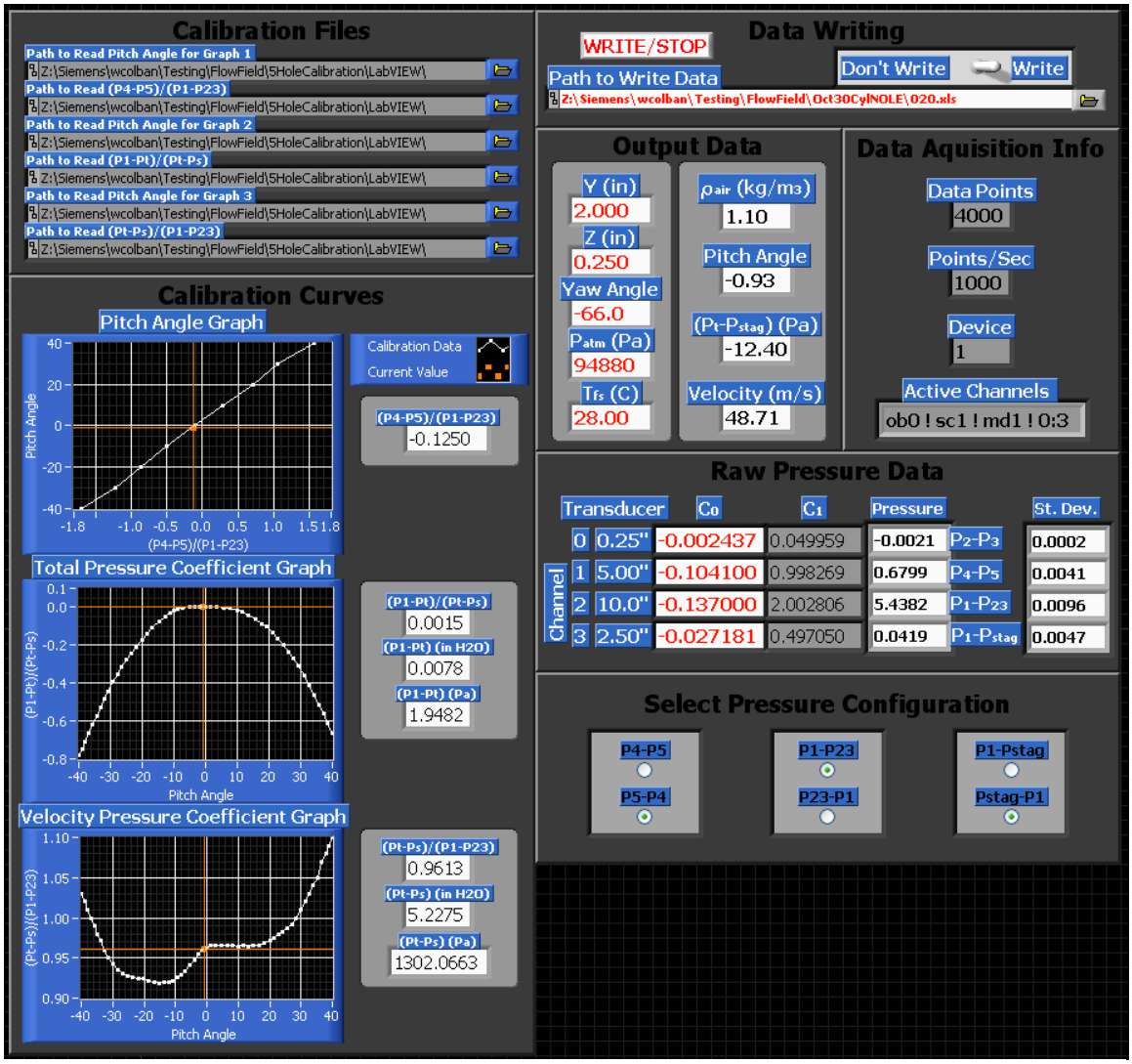

Figure B.11 A screen-shot of the LabVIEW program written to take the five-hole probe measurements.

difference ($P_2 - P_3$) was equal to zero and reading the protractor attached to the top of the probe (shown in Figure B.9). The yaw angle was manually entered into the LabVIEW program, and used later to calculate secondary flow vectors.

After the correct yaw angle had been set, the pitch angle could then be calculated from the ratio of measured pressure differences $(P_4 - P_5)/(P_1 - P_{23})$ using the calibration data in Figure B.12. The pressure P_{23} was the average between P_2 and P_3, however, since those two pressures are equalized in the first step to determine yaw angle, only P_2 was used for that pressure.

The pitch angle was then used to determine the velocity pressure coefficient using

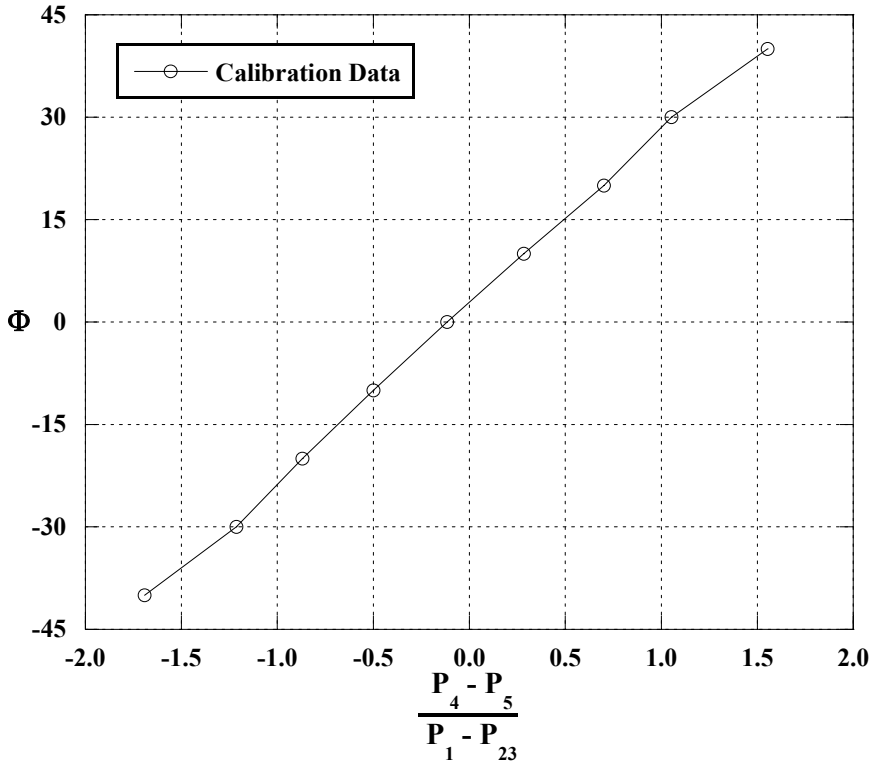

Figure B.12 The calibration data used to determine the pitch angle from the measured pressure differences.

the calibration data given in Figure B.13, where the velocity pressure coefficient is given by Equation B.7,

$$C_{vp} = \frac{P_t - P_s}{P_1 - P_{23}} \tag{B.7}$$

The velocity pressure coefficient, C_{vp} and the measured pressure difference ($P_1 - P_{23}$) were in turn used to calculate the dynamic pressure of the flow ($P_t - P_s$). The streamwise velocity magnitude was then calculated from Equation B.8, a simplification of Bernoulli's Equation,

$$V_s = \sqrt{\frac{2(P_t - P_s)}{\rho}} \tag{B.8}$$

where ρ was the freestream flow density, calculated by measuring the freestream temperature and the atmospheric pressure and using the Ideal Gas Law.

Finally, the total pressure coefficient was determined using the pitch angle and the calibration data shown in Figure B.14, where the total pressure coefficient was given by Equation B.9,

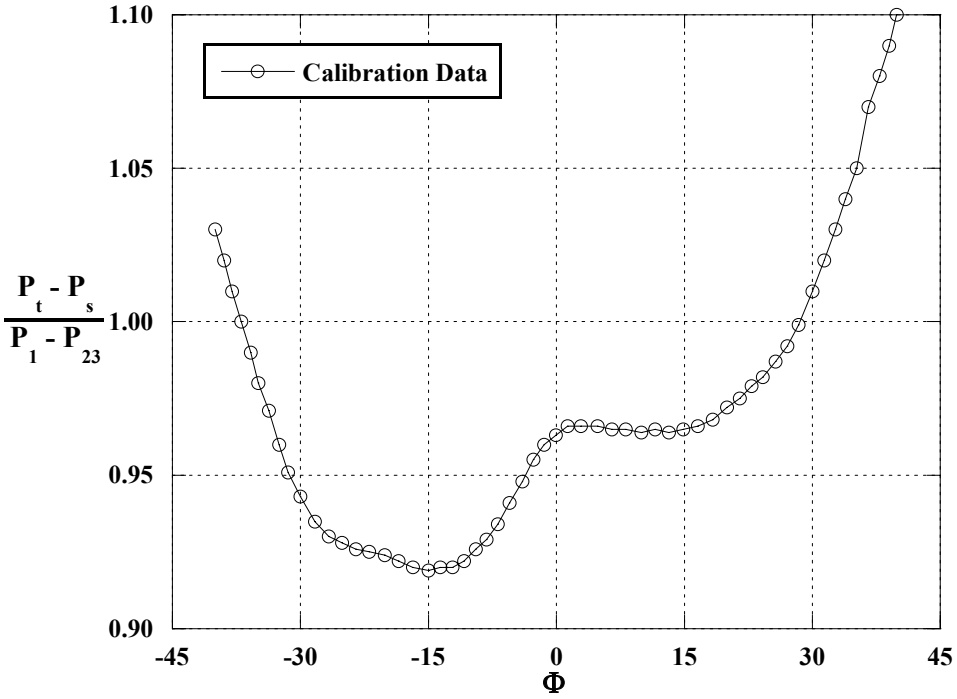

Figure B.13 The calibration data used to determine the velocity pressure coefficient from the measured pressure differences.

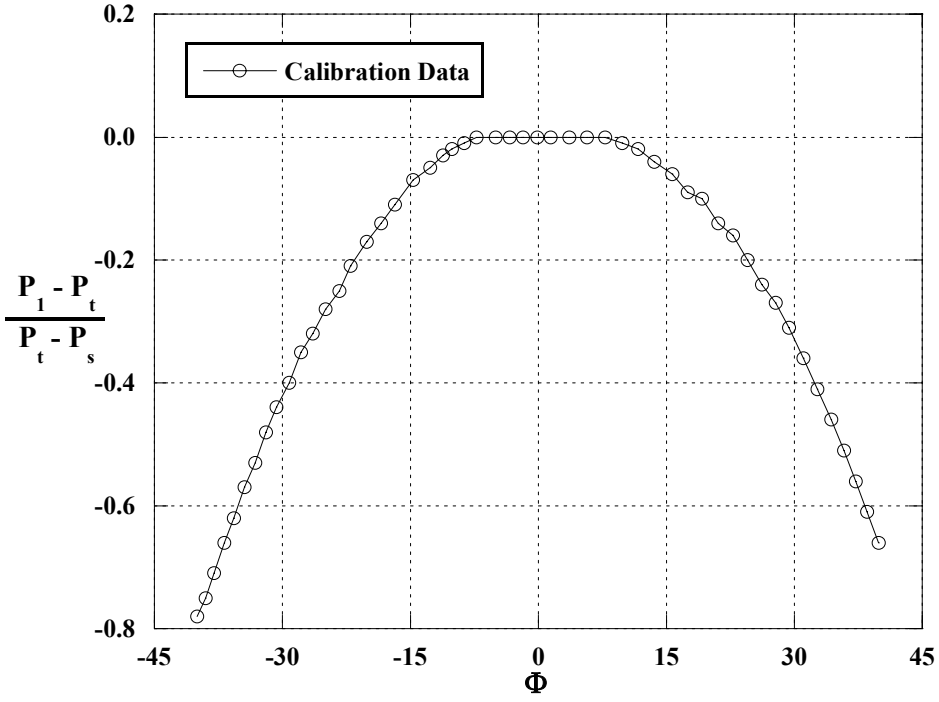

Figure B.14 The calibration data used to determine the total pressure coefficient from the measured pressure differences.

$$C_{tp} = \frac{P_1 - P_t}{P_t - P_s} \tag{B.9}$$

The total pressure coefficient, C_{tp}, dynamic pressure of the flow, $(P_t - P_s)$, and the measured difference between P_1 and the vane stagnation pressure (P_{stag}) were then used to determine the pressure difference between the total pressure and the vane stagnation pressure using Equation B.10,

$$P_t - P_{stag} = \left(P_1 - P_{stag}\right) - \left[C_{tp}\left(P_t - P_s\right)\right] \tag{B.10}$$

Nomenclature

C coefficient of pressure

P pressure

Q radiation emitted from the surface measured by the infrared camera

S the surface distance around the vane, measured from the stagnation point

T temperature

V velocity

Greek

ε emissivity

η adiabatic film-cooling effectiveness, $\eta = (T_\infty - T_{surf})/(T_\infty - T_{cool})$

ρ density

σ Stefan-Boltzmann constant ($\sigma = 5.67 \times 10^{-8}$ W·m^2/K^4)

Φ pitch angle

Ψ yaw angle

Subscripts

1 hole 1 on the five-hole probe

2 hole 2 on the five-hole probe

3 hole 3 on the five-hole probe

4 hole 4 on the five-hole probe

5 hole 5 on the five-hole probe

∞ freestream

amb	ambient/surroundings
aw	adiabatic wall
cool	coolant
meas	measured
o	uncooled
s	streamwise
stag	vane stagnation
surf	surface
t	total
TC	thermocouple
tp	total pressure coefficient
vp	velocity pressure coefficient

Appendix C:
Uncertainty Analysis of Experimental Results

Approach

The uncertainty calculations for the experimental data presented in this dissertation were performed using the method presented by Moffat [1]. This method took into account the contribution of each variable used to calculate the reported value in terms of its partial derivative. The parameter R was a reported value which was calculated from measured values X_i and can be represented as shown in Equation C.1,

$$R = R(X_1, X_2, \cdots, X_n) \tag{C.1}$$

The error in parameter R from any individual measured value X_i was given by Equation C.2,

$$\delta R_i = \frac{\partial R}{\partial X_i}\delta X_i \tag{C.2}$$

Similarly, the total error in R as a function of all of the errors in the measured values used to calculate R was just the root-sum-square of the individual errors associated with each measured value (Equation C.3).

$$\delta R = \left[\sum_{i=1}^{N}\left(\frac{\partial R}{\partial X_i}\delta X_i\right)^2\right]^{1/2} \tag{C.3}$$

The total uncertainty for the measurement of X_i was given by δX_i, where δX_i was the root-sum-square of the bias uncertainty and the precision uncertainty in X_i. The bias uncertainty for a measurement was defined as the capability of the measurement device to accurately measure the true value. The precision uncertainty was defined as the capability of the measurement device to repeat the same measurement of a property that remained at the same value. The precision uncertainty was typically calculated by measuring a single unchanging quantity a number of times, and taking the standard deviation of those measurements.

Adiabatic Effectiveness – η

The measured film-cooling effectiveness for both the vane and the endwall

surfaces was calculated using Equation C.4,

$$\eta_{meas} = \frac{T_\infty - T_{surf}}{T_\infty - T_{cool}} \tag{C.4}$$

The freestream temperature, T_∞, was measured at the test section inlet using type E thermocouples. The coolant temperature, T_{cool}, was also measured using type E thermocouples inside either the vane or endwall plenums. The bias error associated with type E thermocouples was taken as ± 0.2 K, which was the value listed by the manufacturer. The precision uncertainty for the freestream and coolant thermocouples was determined by taking a reading every 10 seconds while the images were being taken. The standard deviation of those readings, during an assumed steady state for the test section, was taken as the precision uncertainty. The precision uncertainty for the freestream temperature was ± 0.25 K, while the precision uncertainty in the coolant temperature measurements was ± 0.03 K.

The surface temperature in Equation C.4 was measured with an infrared (IR) camera. The temperature recorded by the IR camera was calibrated to readings taken by type E thermocouples mounted flush with the measurement surface. Because the IR images were forced onto the measured thermocouple temperatures, one can assume that the bias error for the IR data was the root-sum-square of the thermocouple bias (± 0.2 K) and the average difference between the calibrated IR data and the thermocouple measurement (± 0.12 K). In this way, the bias error for the surface temperature measurements was ± 0.23 K. The precision error for the IR surface temperature measurements was found by taking the standard deviation of the same points in 10 images taken at steady state at the same location. From this method, the precision error for the IR surface temperature measurements was found to be ± 0.27 K, which make the total uncertainty for the IR surface temperature measurements ± 0.35 K.

The bias, precision, and total uncertainties of all the measured temperatures which were used to calculate η_{meas} are summarized in Table C.1. The equations used in the calculation of total uncertainty in η_{meas}, $\delta\eta_{meas}$, are summarized in Table C.2. The total uncertainty for a value of $\eta_{meas} = 0.9$ was ± 0.0189, while for a lower reported value of $\eta_{meas} = 0.2$, the calculated total uncertainty was ± 0.0208.

Table C.1 Equations for Calculation of Total Uncertainty in η

$R = R(X_1, X_2, \cdots, X_n)$	$\frac{\partial R}{\partial X_i}$
$\eta_{meas} = \frac{T_\infty - T_{surf}}{T_\infty - T_{cool}}$	$\frac{\partial \eta}{\partial T_\infty} = \frac{T_{surf} - T_{cool}}{(T_\infty - T_{cool})^2}$ $\frac{\partial \eta}{\partial T_{surf}} = \frac{1}{T_{cool} - T_\infty}$ $\frac{\partial \eta}{\partial T_{cool}} = \frac{T_\infty - T_{surf}}{(T_\infty - T_{cool})^2}$
$\delta R = \left[\sum_{i=1}^{N} \left(\frac{\partial R}{\partial X_i} \delta X_i \right)^2 \right]^{1/2}$	
$\delta\eta = \sqrt{\left(\frac{\partial \eta}{\partial T_\infty} \cdot \delta T_\infty \right)^2 + \left(\frac{\partial \eta}{\partial T_{surf}} \cdot \delta T_{surf} \right)^2 + \left(\frac{\partial \eta}{\partial T_{cool}} \cdot \delta T_{cool} \right)^2}$	

Table C.2 Uncertainty Values of Measured Quantities for Calculation of η

Measured Value	Bias Uncertainty	Precision Uncertainty	Total Uncertainty
T_∞	± 0.20 K	± 0.25 K	± 0.32 K
T_{surf}	± 0.23 K	± 0.27 K	± 0.35 K
T_{cool}	± 0.20 K	± 0.03 K	± 0.20 K

Mass Flow Rate – MFR

The mass flow rate (MFR) was reported for each endwall case. It was defined as the ratio of coolant flow to the total freestream flow and was calculated nominally by Equation C.5,

$$MFR = \frac{\rho_{cool} Q_{LFE}}{\rho_{hot} U_{inlet} A} \tag{C.5}$$

where ρ_{cool} and ρ_{hot} were the coolant and freestream densities, Q_{LFE} was the coolant flowrate measured through the laminar flow element (LFE), U_{inlet} was the velocity at the test section inlet, and A was the inlet area for one vane pitch. Each of the terms in Equation C.4 were calculated from measured quantities using Equations C.6 through C.9,

$$Q_{LFE} = 2.48 \cdot 10^{-4} \Delta P_{LFE} - 4.30 \cdot 10^{-10} \Delta P_{LFE} \tag{C.6}$$

$$\rho_{cool} = \frac{P_{atm}}{RT_{cool}} \tag{C.7}$$

$$\rho_{hot} = \frac{P_{atm}}{RT_{hot}} \tag{C.8}$$

$$U_{inlet} = \sqrt{\frac{2\Delta P_{Pitot}}{\rho_{hot}}} \tag{C.9}$$

The atmospheric pressure, P_{atm}, was measured with a digital Setra pressure transducer with a range from 800 mbar to 1100 mbar. The bias uncertainty in the reading was ± 0.0206% of the full scale (also ± 0.0681 mbar or ± 6.81 Pa). The precision uncertainty was determined by measuring the same pressure 20 times, once every 10 seconds and determined from the standard deviation of that data to be ± 1.88 Pa. That makes a total uncertainty in the measurement of atmospheric pressure of ± 7.06 Pa.

The freestream temperature, T_{hot}, was measured with type E thermocouples at the inlet. Again, the manufacturer specified value for bias uncertainty in type E thermocouples was ± 0.2 K. The precision uncertainty was determined from the raw data file which records temperatures continuously during testing and was ± 0.27 K. The total uncertainty was therefore ± 0.34 K.

The coolant temperature, T_{cool}, was measured with two type E thermocouples located inside the endwall plenum and positioned just below the entrance to the holes. The precision uncertainty was determined from the raw data file which records temperatures continuously during testing and was ± 0.08 K. The total uncertainty was therefore ± 0.22 K.

The pressure drop through the LFE was measured using a 5.0" Setra pressure transducer, which had a bias uncertainty of ± 0.206% of the full scale (or ± 0.64 Pa). The precision error was not measured; however, it could be inferred from the Pitot probe measurements made with the 0.25" transducer as ± 0.78 Pa, which makes the total uncertainty ± 1.01 Pa.

The inlet velocity was measured indirectly by measuring the inlet dynamic pressure at the inlet with a Pitot probe. A 0.25" Setra pressure transducer was used to make the measurements. The pressure transducer has a bias error of ± 0.206% of the full scale (or ± 0.13 Pa). The inlet profile was used to calculate a precision error of ± 0.18 Pa.

The total uncertainty was therefore ± 0.22 Pa.

The bias, precision, and total uncertainties of all the measured values which were used to ultimately calculate MFR are summarized in Table C.3. The equations used in the calculation of total uncertainty in MFR, δMFR, are summarized in Table C.4. For the nominal case with MFR = 0.73% in the cylindrical passage at low freestream turbulence, the uncertainty was calculated to be ± 0.0024%.

Table C.3 Equations for Calculation of Total Uncertainty in MFR

$R = R(X_1, X_2, \cdots, X_n)$	$\frac{\partial R}{\partial X_i}$
$MFR = \frac{\left(1.75\cdot10^{-5}\Delta P_{LFE} - 3.04\cdot10^{-10}\Delta P_{LFE}^2\right)}{AT_{cool}\sqrt{\frac{\Delta P_{Pitot} R_{air}}{T_{hot} P_{atm}}}}$	$\frac{\partial MFR}{\partial P_{atm}} = \frac{\left(8.77\cdot10^{-6}\Delta P_{LFE} - 1.52\cdot10^{-10}\Delta P_{LFE}^2\right)}{AT_{cool}\sqrt{\frac{\Delta P_{Pitot} P_{atm} R_{air}}{T_{hot}}}}$ $\frac{\partial MFR}{\partial T_{hot}} = \frac{\left(8.77\cdot10^{-6}\Delta P_{LFE} - 1.52\cdot10^{-10}\Delta P_{LFE}^2\right)}{AT_{cool}\sqrt{\frac{\Delta P_{Pitot} T_{hot} R_{air}}{P_{atm}}}}$ $\frac{\partial MFR}{\partial T_{cool}} = \frac{\left(-1.75\cdot10^{-5}\Delta P_{LFE} + 3.04\cdot10^{-10}\Delta P_{LFE}^2\right)}{AT_{cool}^2\sqrt{\frac{\Delta P_{Pitot} R_{air}}{T_{hot} P_{atm}}}}$ $\frac{\partial MFR}{\partial \Delta P_{LFE}} = \frac{\left(1.75\cdot10^{-5} - 6.08\cdot10^{-10}\Delta P_{LFE}\right)}{AT_{cool}\sqrt{\frac{\Delta P_{Pitot} R_{air}}{T_{hot} P_{atm}}}}$ $\frac{\partial MFR}{\partial \Delta P_{Pitot}} = \frac{\left(-8.77\cdot10^{-6}\Delta P_{LFE} + 1.52\cdot10^{-10}\Delta P_{LFE}^2\right)}{AT_{cool}\Delta P_{Pitot}\sqrt{\frac{\Delta P_{Pitot} R_{air}}{T_{hot} P_{atm}}}}$
$\delta R = \left[\sum_{i=1}^{N}\left(\frac{\partial R}{\partial X_i}\delta X_i\right)^2\right]^{1/2}$	
$\delta MFR = \sqrt{\left(\frac{\partial MFR}{\partial P_{atm}}\cdot\delta P_{atm}\right)^2 + \left(\frac{\partial MFR}{\partial T_{hot}}\cdot\delta T_{hot}\right)^2 + \left(\frac{\partial MFR}{\partial T_{cool}}\cdot\delta T_{cool}\right)^2 + \left(\frac{\partial MFR}{\partial \Delta P_{LFE}}\cdot\delta\Delta P_{LFE}\right)^2 + \left(\frac{\partial MFR}{\partial \Delta P_{Pitot}}\cdot\delta\Delta P_{Pitot}\right)^2}$	

Table C.4 Uncertainty of Measured Quantities for Calculation of MFR

Measured Value	Bias Uncertainty	Precision Uncertainty	Total Uncertainty
P_{atm}	± 6.81 Pa	± 1.88 Pa	± 7.06 Pa
T_{hot}	± 0.20 K	± 0.27 K	± 0.34 K
T_{cool}	± 0.20 K	± 0.08 K	± 0.22 K
ΔP_{LFE}	± 0.64 Pa	± 0.78 Pa	± 1.01 Pa
ΔP_{Pitot}	± 0.13 Pa	± 0.18 Pa	± 0.22 Pa

Total Pressure Loss – Y_o

Total pressure losses were measured using a five-hole total pressure probe at the exit plane. The total pressure loss coefficient was defined as given in Equation C.10,

$$Y_o = \frac{P_{o,ref} - P_{o,exit}}{P_{o,ref} - P_{s,exit}} \tag{C.10}$$

where $P_{o,ref}$ was either the mass-averaged total pressure measured at the inlet plane, $P_{o,in}$, or $P_{o,ref}$ included the total pressure addition from the film coolant as defined in Equation C.11,

$$P_{o,ref} = \frac{P_{o,in}\,\dot{m}_{in} + P_{o,cool}\,\dot{m}_{cool}}{\dot{m}_{in} + \dot{m}_{cool}} \tag{C.11}$$

The exit static pressure given in Equation C.10 was the difference between the measured total pressure and the dynamic pressure, which was calculated using the measured streamwise velocity.

The exit total pressures were measured using a 5.0" Setra pressure transducer, which had a bias uncertainty of ± 0.019% of the full scale (or ± 0.24 Pa). At the exit plane the precision error for P_o was found to be ± 0.41 Pa by averaging 20 data points taken at one location. The inlet total pressures, $P_{o,in}$, were measured using a 0.5" Setra pressure transducer, which had a bias uncertainty of ± 0.079% of the full scale (or ± 0.10 Pa). The precision uncertainty at the inlet was measured by taking the standard deviation of 25 data points taken in the same location and was ± 0.42 Pa. This uncertainty value was used as the uncertainty in $P_{o,ref}$.

The bias, precision, and total uncertainties of all the measured values which were used to ultimately calculate Y_o are summarized in Table C.5. The equations used in the calculation of total uncertainty in Y_o, δY_o, are summarized in Table C.6. For a value of $Y_o = 0.15$ measured in the cylindrical passage with upstream cooling, the uncertainty was calculated to be ± 0.001.

Table C.5 Equations for Calculation of Total Uncertainty in Y_o

$R = R(X_1, X_2, \cdots, X_n)$	$\frac{\partial R}{\partial X_i}$
$Y_o = \frac{P_{o,ref} - P_o}{P_{o,ref} - P_{s,exit}}$	$\frac{\partial Y_o}{\partial P_{atm}} = \frac{\frac{1}{2}(P_o - P_{o,ref})RTV_s^2}{(P_{o,ref}RT - P_oRT + \frac{1}{2}P_{atm}V_s^2)^2}$ $\frac{\partial Y_o}{\partial T} = -\frac{\frac{1}{2}P_{atm}(P_o - P_{o,ref})RV_s^2}{(P_{o,ref}RT - P_oRT + \frac{1}{2}P_{atm}V_s^2)^2}$ $\frac{\partial Y_o}{\partial P_o} = -\frac{\frac{1}{2}P_{atm}RTV_s^2}{(P_{o,ref}RT - P_oRT + \frac{1}{2}P_{atm}V_s^2)^2}$ $\frac{\partial Y_o}{\partial P_{o,ref}} = \frac{\frac{1}{2}P_{atm}RTV_s^2}{(P_{o,ref}RT - P_oRT + \frac{1}{2}P_{atm}V_s^2)^2}$ $\frac{\partial Y_o}{\partial V_s} = \frac{P_{atm}(P_o - P_{o,ref})RTV_s}{(P_{o,ref}RT - P_oRT + \frac{1}{2}P_{atm}V_s^2)^2}$
$\delta R = \left[\sum_{i=1}^{N}\left(\frac{\partial R}{\partial X_i}\delta X_i\right)^2\right]^{1/2}$	
$\delta Y_o = \sqrt{\left(\frac{\partial Y_o}{\partial P_{atm}}\cdot\delta P_{atm}\right)^2 + \left(\frac{\partial Y_o}{\partial T}\cdot\delta T\right)^2 + \left(\frac{\partial Y_o}{\partial P_o}\cdot\delta P_o\right)^2 + \left(\frac{\partial Y_o}{\partial P_{o,ref}}\cdot\delta P_{o,ref}\right)^2 + \left(\frac{\partial Y_o}{\partial V_s}\cdot\delta V_s\right)^2 +}$	

Table C.6 Uncertainty Values of Measured Quantities for Calculation of Y_o

Measured Value	Bias Uncertainty	Precision Uncertainty	Total Uncertainty
P_{atm}	± 6.81 Pa	± 1.88 Pa	± 7.06 Pa
T	± 0.20 K	± 0.27 K	± 0.34 K
P_o	± 0.24 Pa	± 0.41 Pa	± 0.47 Pa
$P_{o,ref}$	± 0.10 Pa	± 0.42 Pa	± 0.43 Pa
V_s	± 0.184 m/s	± 0.0335 m/s	± 0.187 m/s

Nomenclature

A inlet area for one passage

$\dot{m}$ mass flow rate

MFR % total coolant mass flow per total passage mass flow

P pressure

Q volumetric flowrate

R a reported parameter calculated from measured values/ideal gas constant

T temperature

U velocity

V_s streamwise velocity

X any measured value

Y_o total pressure loss coefficient, $Y_o = (P_{o,ref} - P_{o,exit})/ (P_{o,ref} - P_{s,exit})$

Greek

δ experimental error

Δ change in

η adiabatic film-cooling effectiveness, $\eta_{meas} = (T_\infty - T_{surf})/(T_\infty - T_{cool})$

ρ density

Subscripts

1 the first index number

2 the second index number

∞ freestream

atm atmospheric

cool coolant

exit exit plane

hot hot gas

i an index number

in inlet condition

inlet inlet condition

LFE laminar flow element

meas measured value

n the n^{th} index number

N the total number of measured values that are included in calculating R

o total

Pitot measured with a Pitot probe

ref reference value

s static

surf surface

References

[1] Moffat, R. J., 1988, "Describing the Uncertainties in Experimental Results," *Experimental Thermal and Fluid Science*, vol. 1, pp. 3-17.

Appendix D:
Measurements of Film-Cooling Hole Diameters and Flow Setting Procedures

Hole Discharge Coefficient Measurements

Prior to making measurements of adiabatic effectiveness on the vane surface, discharge coefficients were measured for each row of fan-shaped holes. There were four plenums on the vane interior, and each one fed more than one row of holes. The rows were grouped based on the desired blowing ratios and estimating the blowing ratio for each hole based on an inviscid Bernoulli calculation. Blowing ratios were determined for each row by calculating the ideal jet velocity exiting a hole, using the interior plenum total pressure and the exterior static pressure at the exit location on the vane. However, this was just an approximation and it was necessary to measure discharge coefficients prior to testing to know the actual blowing ratios of each row during the multiple row configuration testing.

Discharge coefficients were calculated using the following equation,

$$C_D = \frac{\dot{m}_{actual}}{\dot{m}_{ideal}} \tag{D.1}$$

where $\dot{m}_{actual}$ was measured directly using a laminar flow element (LFE) and $\dot{m}_{ideal}$ was calculated using Equation D.2.

$$\dot{m}_{ideal} = A_{holes}\sqrt{2\rho_{cool}\left(P_{o,cool} - P_{s,exit}\right)} \tag{D.2}$$

The measured discharge coefficients for each fan-shaped hole are shown in Figure D.1. A comparison was made to existing data with a similar hole geometry published by Gritsch et al. [1], and the agreement was quite good for the range of pressure ratios that were measured. Showerhead discharge coefficients are shown in Figure D.2. Note that the discharge coefficients were much lower for the showerhead holes, perhaps because of the much longer L/D ratio of 9, compared to the fan-shaped hole L/D ratio of 2.

Initially, the measured values for the discharge coefficients were greater than 1, which happened to be the theoretical limit for discharge coefficients. After much

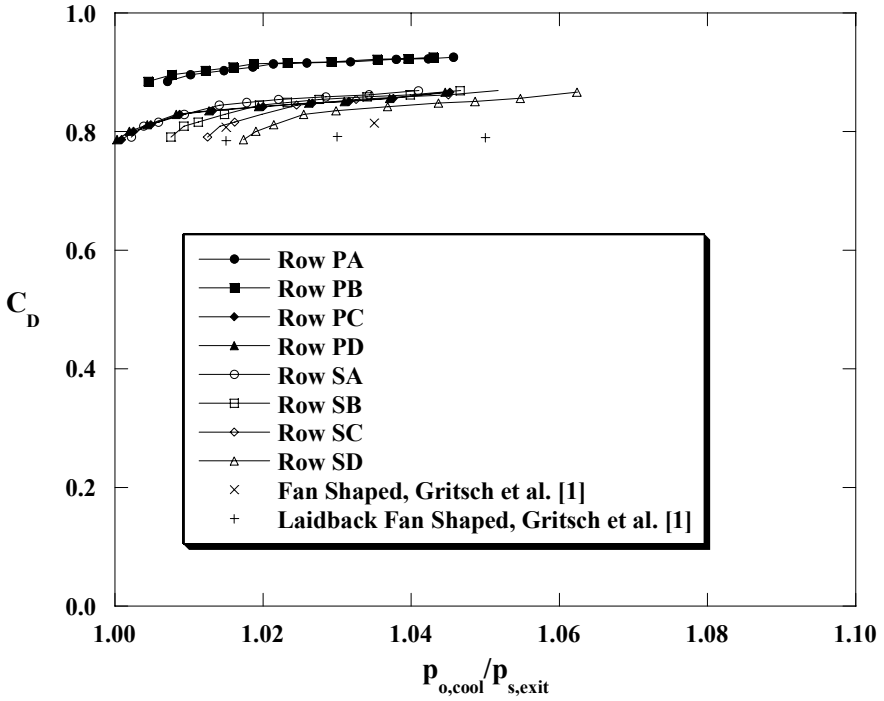

Figure D.1 Fan-shaped hole discharge coefficients.

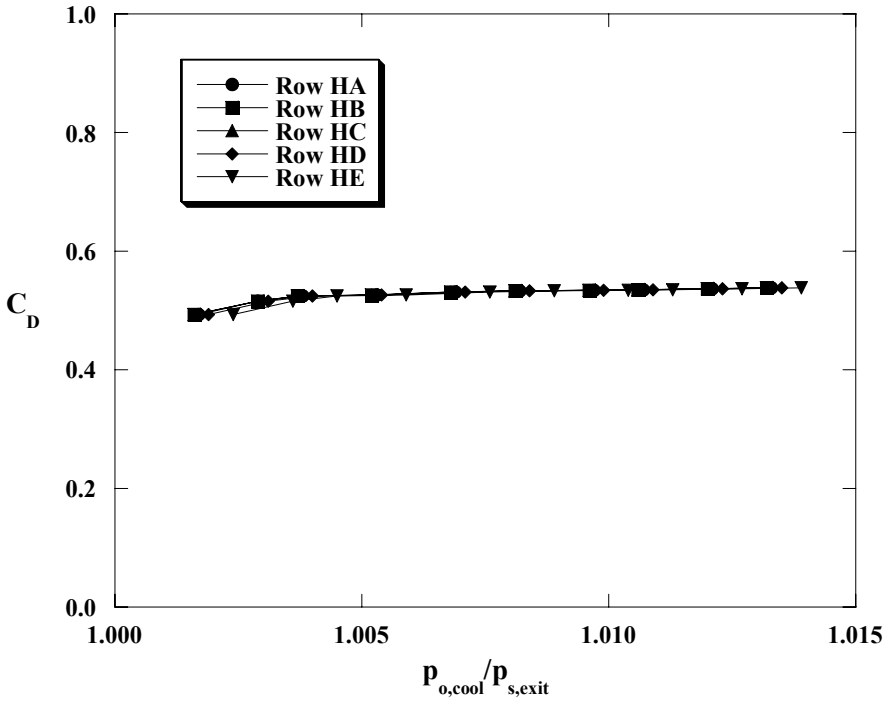

Figure D.2 Showerhead hole discharge coefficients.

investigation for leakage through the piping and plenum interior, the problem was determined to be inaccurate knowledge of the cooling hole diameter. The term A_{holes} in Equation D.2 was defined as the metering area, so the specified value given to the

manufacturer was used for the calculations. Upon closer examination, it was determined that some of the holes were slightly larger, however, at the experimental scale of the vane it had a large effect on the outcome of C_D. In addition, some of the holes did not have circular cross-sections at the metering area (Figure D.3). The irregularities were most likely a result of either the manufacturing or the instrumentation process.

Hole Diameter Measurements

In order to get correct values for the average discharge coefficient of each row, every hole was measured with extremely accurate pin gages. The circular pins increased in diameter in increments of approximately 0.03 mm. The non-circular irregularities were also accounted for, both the distorted corners and the ovular hole shapes. The distorted corners were approximated by assuming any irregular shape in a quadrant of the circular cross-section to have a square corner. The area of any ovular hole was calculated by measuring the major (D_1) and minor (D_2) axis, and using Equation D.3,

$$A_{oval} = \frac{\pi}{4} D_1 D_2 \tag{D.3}$$

Both irregularities are illustrated schematically in Figure D.4.

The final results for the hole diameter measurement process are listed in Table D.1. In summary, the specified fan-shaped hole diameter in the circular entrance length region was given as 2.61 mm. The average measured diameter in that same region for the

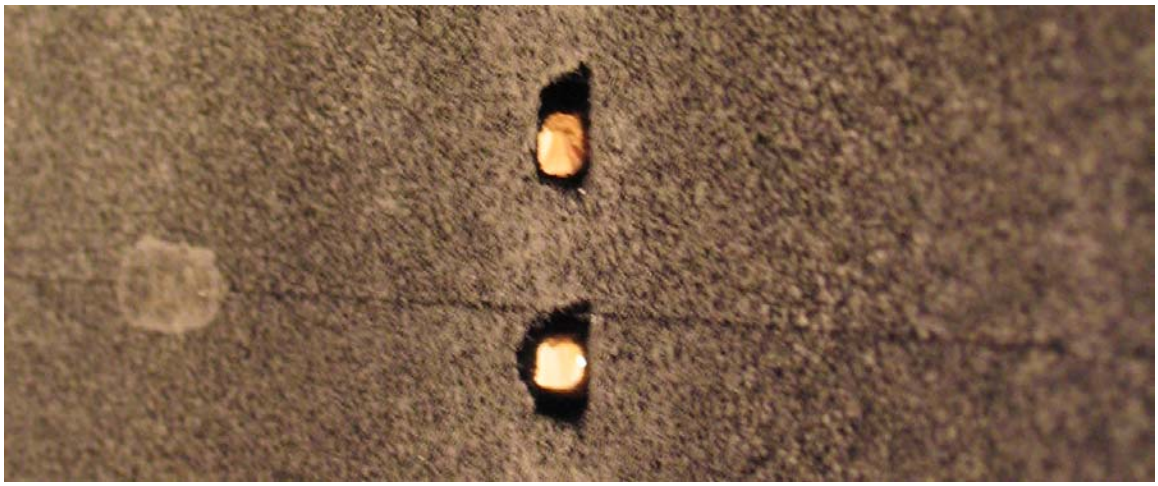

Figure D.3 Example of two non-circular holes at the metering area. The upper hole has an ovular shape, while the lower left-hand quadrant of the lower hole was approximated as a square.

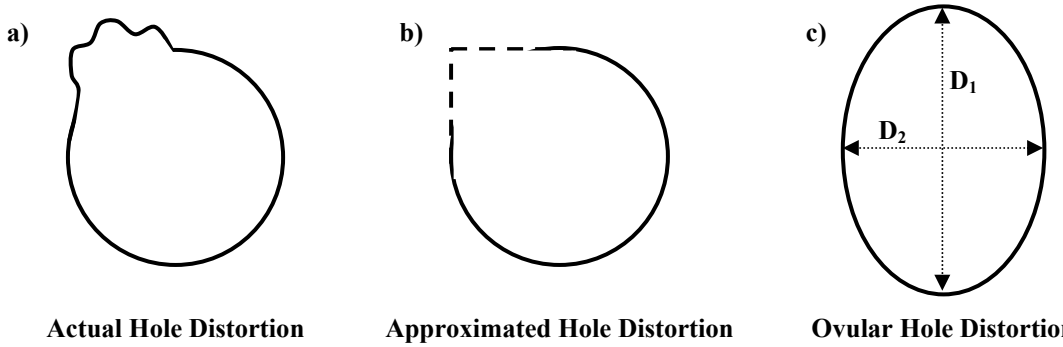

Figure D.4 Schematic illustration of an example of (a) a non-circular distortion and (b) how it was approximated, and also (c) an ovular shaped hole.

Table D.1 Summary of Hole Diameter Measurements on the Vane.

Cooling Hole Diameters (mm)	
Design Fan-Shaped	2.61
Average Measured Fan-Shaped	3.78 ± 0.15
Design Showerhead	2.16
Average Measured Showerhead	2.39 ± 0.08
Individual Row Measurements	**D (mm)**
PA	3.82
PB	3.92
PC	3.81
PD	3.85
HA-HE	2.39
SA	3.77
SB	3.82
SC	3.68
SD	3.61

fan-shaped holes was 3.78 mm. For the showerhead holes, the same procedure was followed, with the final measured average diameter being 2.39 mm as opposed to the originally specified 2.16 mm.

Flow Setting Procedure for the Vane Film-Cooling Tests

The experimental film-cooling vane was separated into four plenums on the interior. Each plenum was supplied with coolant by a pipe at the base of the vane from below. The four pipes (shown in Figure D.5) were all fed from the same source, and each individual pipe had a valve installed with which to regulate the flow delivered to each plenum. The main supply pipe, from which the other four supply pipes were fed, contained a 100 cfm capacity Meriam model 50MC2-2 laminar flow element (LFE) for

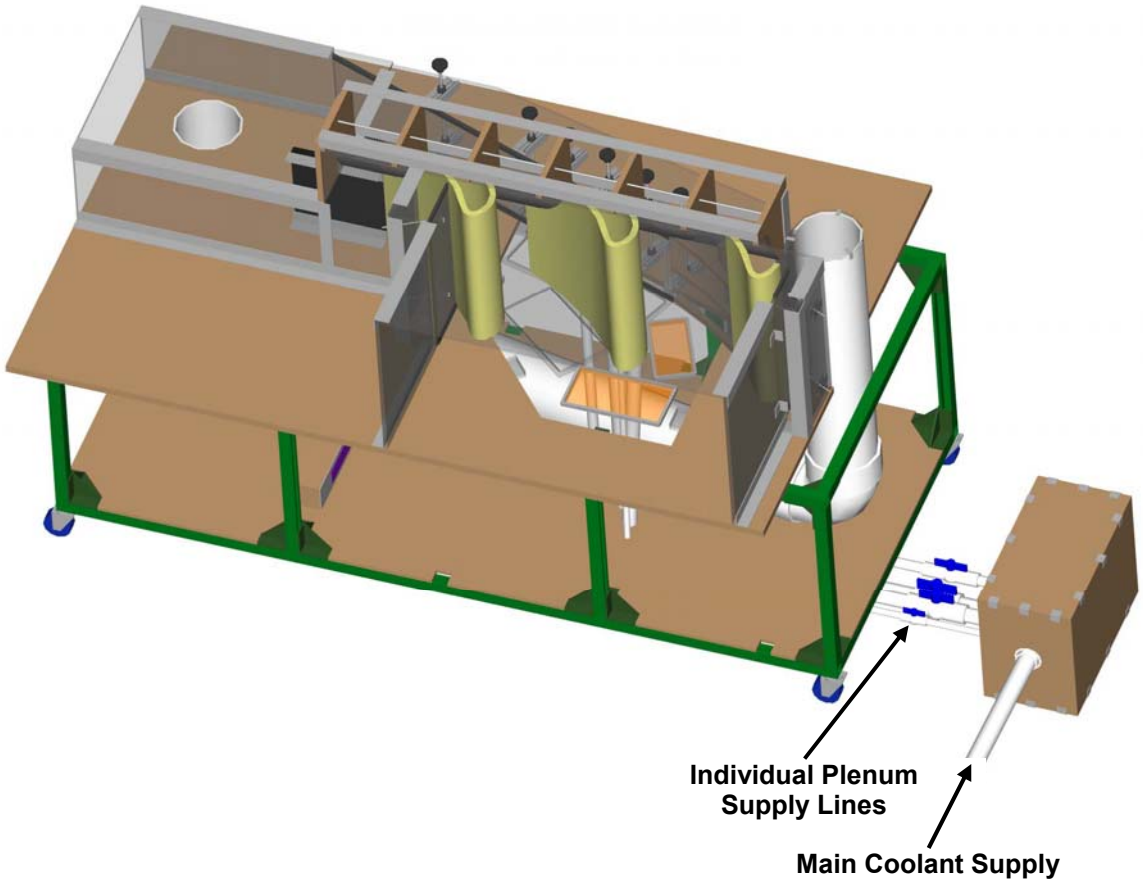

Figure D.5 Diagram illustrating the coolant supply distribution to the film-cooling vane.

measuring the total volumetric flowrate of the coolant.

For the single row film-cooling tests on the vane, the mass flow rate was set for each case using only the LFE. However, since each individual plenum supply line did not have an LFE, the discharge coefficients were necessary (see Figures D.1 and D.2) to set the flow rates for the multiple row film-cooling tests. Once the test had begun and the coolant had been turned on, the plenum-to-surface pressure ratios were measured for each plenum, where the vane surface pressure was the static pressure measured at the midspan. Then, the discharge coefficients for each row of holes was determined from Figures D.1 and D.2. Next, the jet velocity for each row of holes was calculated using Equation D.4,

$$U_{jet} = C_D \sqrt{\frac{2\left(P_{o,plen} - P_{s,exit}\right)}{\rho_{cool}}} \qquad (D.4)$$

where the static pressure on the surface of the vane at the hole exit location, $P_{s,exit}$, was interpolated from the measured midspan static pressure distribution around the vane.

Pressure taps were located within each plenum with which to measure the plenum total pressure, $P_{o,plen}$. The blowing ratios at each hole were then calculated using Equation D.5,

$$M = \frac{\rho_{cool} U_{jet}}{\rho_{\infty} U_{local}} \tag{D.4}$$

where the local velocity near the surface of the vane at the hole exit, U_{local}, was calculated using the measured static pressure distribution around the vane.

The measured blowing ratios at each hole location were then compared to the desired values. The valves for each coolant supply pipe were then adjusted to minimize the difference between the calculated blowing ratios and the desired blowing ratios. Once the flows had been set, the total coolant mass flow to the vane measured with the LFE was compared with the calculated total mass flow rate using the measured pressure ratios and discharge coefficients. The difference between the actual measured value and the predicted calculated value was always less than 2% for all multiple row vane film-cooling experiments.

Flow Setting Procedure for the Endwall Film-Cooling Tests

The endwall film-cooling tests required a plenum to be built underneath the lower flat film-cooled endwall. The plenum is shown in Figure D.6, along with the single coolant supply pipe for the plenum. Each coolant passage could be totally blocked from inside the plenum, with specially designed Lexan plates which covered the hole entrances. The coolant supply pipe contained the same Meriam model 50MC2-2 LFE, so the mass flow rate for each test could be measured directly, as long as the passage that was not being tested was blocked from within the plenum.

Similarly, for the tests without upstream coolant injection, the upstream film-cooling holes were selectively blocked from within the plenum on the passage to be tested. In addition, the holes for the untested passage were also blocked. The pressure ratio taken from within the plenum relative to static pressure taps located 0.6 C upstream of the vane stagnation was matched to the cases with upstream injection. In this way, the unblocked cooling holes within the passage had the same coolant flow regardless of the status of the upstream cooling holes.

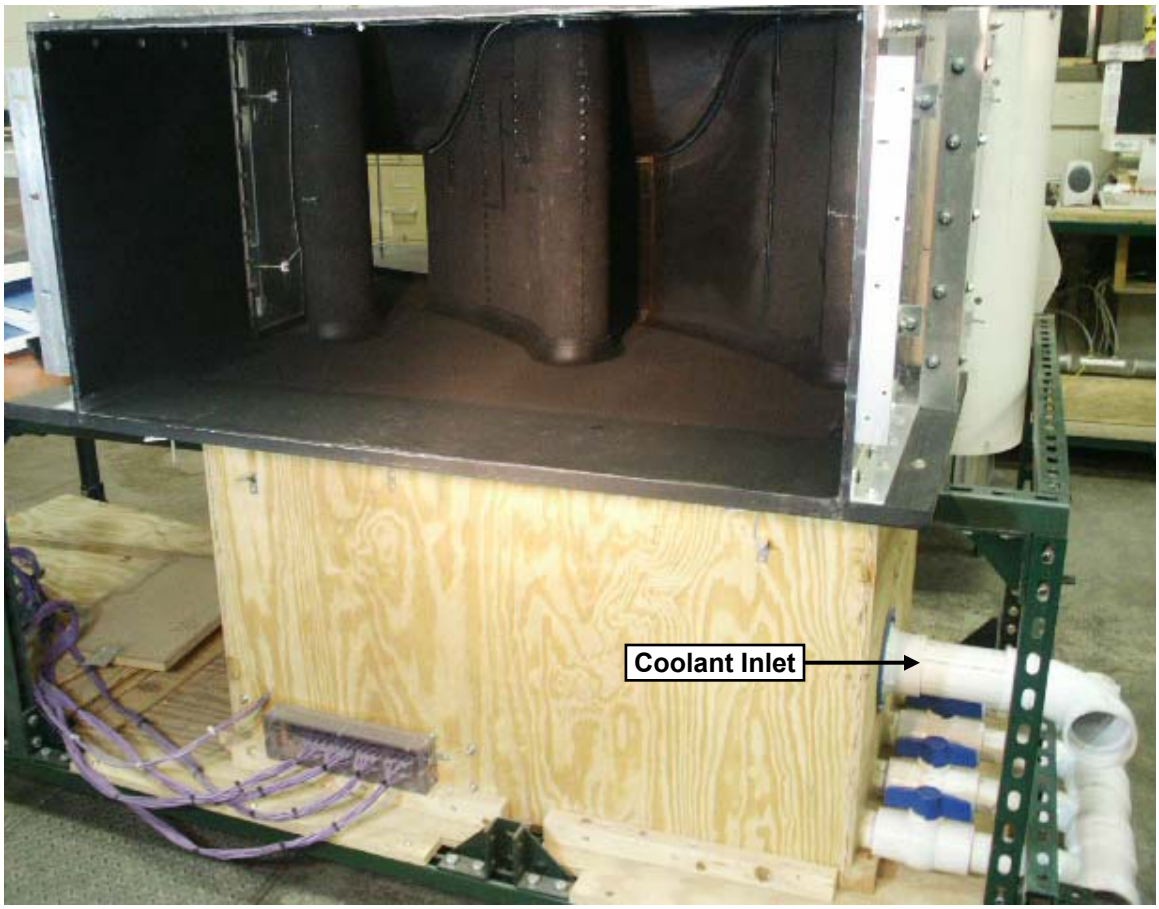

Figure D.6 Illustration of the endwall coolant plenum showing the single coolant supply line (the other inlet pipes that are shown were blocked and not used).

Nomenclature

A	inlet area for one passage
C	true vane chord
C_D	discharge coefficient, $C_D = \dot{m}_{actual} / \dot{m}_{ideal}$
D	diameter at the hole inlet
L	metering length of the hole
$\dot{m}$	mass flow rate
P	pressure
U	velocity

Greek

ρ	density

Subscripts

1	the major axis of an oval
2	the minor axis of an oval
actual	the actual flowrate that occurs through the hole because of losses
cool	coolant
exit	exit of the hole
holes	all film-cooling holes in an individual row
ideal	the ideal flow rate through the hole as predicted by the Bernoulli Equation
jet	film-cooling jet at the metering area
o	total
oval	the cross-sectional area of an oval
plen	plenum
s	static

References

[1] Gritsch, M., Schulz, A., and Wittig, S., 1997, "Discharge Coefficient Measurements of Film-Cooling Holes with Expanded Exits," 97-GT-165.

Vita

William Frederick Colban IV

Will was born on November 6, 1980 in Beaufort, SC, son of Michelle Pauline Colban-Hill and William Frederick Colban III. On May 25, 1992, Will's brother Ellis 'EJ' Hill II was born. Will went to high school in Richmond, VA at the Governor's School, graduating in 1997. Wanting to study mechanical engineering, Will decided to attend renowned Virginia Tech.

Four years later, in May 2001, Will graduated with a BSME from Virginia Tech. Because of his insatiable thirst to understand the physical world around him, Will continued on as a graduate student, receiving his MSME in the January 2002. During that time, in the fall of 2001, he met the girl that he would ultimately ask to marry him, the beautiful Lauren Elizabeth Ross.

The following spring in 2002, Will went to Baden, Switzerland to work as an intern for ALSTOM Power. Will had always wanted to go live and travel in Europe, and he got the opportunity to see many different countries and meet people from all over the world. During that time, Will decided he would return to Virginia Tech to work on a PhD in mechanical engineering under Dr. Karen A. Thole. Will's research centered on the examination of fan-shaped film-cooling holes in a gas turbine vane, and he learned a great deal.

On July 3, 2005 Will asked Lauren to marry him at the Middleton Inn in Charleston, SC. The following December, Will received his PhD in mechanical engineering from the great Virginia Polytechnic Institute and State University.